Yangsoo Kim
Infrared-Ultraviolet Double Resonance Spectroscopy of NO-Ne and NO-Ar Complexes.
(Under the direction of Henning Meyer)

Van der Waals forces play an important role in the interaction at large molecular separation. It is responsible for the existence of liquid states. The interest in the van der Waals complexes originates from the prospect of understanding the transition from the gas phases to the condensed phases. Even though many van der Waals complexes involving closed-shell atoms and molecules have been studied, only few systems involving open-shell molecules have been studied. As a bench mark system for the interaction of an open shell molecule with a closed shell atom, a great focus has been on the NO-Ar system both experimentally and theoretically for the past two decades. The major source of experimental information on the interaction of NO with Ar relied on collision studies. So far, no spectroscopic information about the rovibrational levels of the electronic ground state of the NO-Ar complex is available. It is a goal of this dissertation to investigate the interaction potential of the electronic ground state of NO-Ar and NO-Ne complexes through IR spectroscopy. As a state specific detection scheme of molecules, (2+1) resonance enhanced multiphoton ionization(REMPI) has been used to the Rydberg state spectroscopy of van der Waals complexes, such as NO-Ar, NO-Ne, and CH_3CHO-Ar. These studies provide information about the structure of the potential surface correlating with electronically excited NO. To explore the structure of the electronic ground state, REMPI detection was combined with IR spectroscopy. For the first time, observed are intermolecular vibration spectra of NO-Ar and NO-Ne built on the first overtone transition of NO. For both complexes, the agreement with Alexander's new results (J. Chem. Phys. **111**,7435 (1999); J. Phys. Chem. **114**, 5588 (2001)) based on his coupled-cluster (CCSD(T)) *ab initio* calculation of the two potential energy surfaces is excellent. Additional physical insight can be obtained by using a heuristic

Hamiltonian based on perturbation theory. The results of this thesis opens new possibilities in exploring weak interactions involving van der Waals complexes using IR-REMPI double resonace technique.

INDEX WORDS: molecular beam, infrared spectroscopy,
ultraviolet spectroscopy, van der Waals complex,
open-shell complex, laser spectroscopy, REMPI spectroscopy,
IR-UV double resonance spectroscopy, NO-Ar, NO-Ne

Infrared-Ultraviolet Double Resonance Spectroscopy of NO-Ne and NO-Ar Complexes.

by

Yangsoo Kim

B.S., Seoul National University, 1989

A Dissertation Submitted to the Graduate Faculty
of The University of Georgia in Partial Fulfillment
of the
Requirements for the Degree

Doctor of Philosophy

Athens, Georgia

2001

Infrared-Ultraviolet Double Resonance Spectroscopy of NO-Ne and NO-Ar Complexes.

by

Yangsoo Kim

Approved:

Major Professor: Henning Meyer

Committee: Nigel G. Adams
Michael A. Duncan
Alan K. Edwards
Phillip C. Stancil

Electronic Version Approved:

Gordhan L. Patel
Dean of the Graduate School
The University of Georgia
August 2001

To my parents

Acknowledgements

It would not have been possible to finish this dissertation without the help from lots of people. First of all, I would like to express special gratitude to my mentor Henning Meyer. His enthusiasm on science gave me a deep impression. His tenacity toward a new result will have a great influence on me throughout my future. He showed me great patience to make me a spectroscopist.

I would also like to thank all members of committee, Profs. Nigel G. Adams, Alan K. Edward, Michael A. Duncan, and Phillip C. Stancil for their interests in my research and helpful feedbacks.

For theoretical cooperation during the research, I should acknowledge Millard H. Alexander at the University of Maryland, Paul J. Dagdigian at the Johns Hopkins University, and Timothy G. Wright at the University of Sussex in England.

Dean Guyer deserves my acknowledgement for his endless help in operating the OPO (MIRAGE 3000) and understanding the system. At early stage of my work, I called him countless times to get his advice and he gladly spared some time to help me out.

I would like to thank Loris Magnani for being a nice supporter and for encouraging me to comeback after a few years of break.

I would like to share this honor with all my friends both in Korea and in the U.S. Their great support should not be forgotten. I also would like to thank Boyoung Park for her silent support.

Finally, I must recognize the encouragement and support of my parents, sisters and brother. I would like to express my gratitude to my two grandmothers. I also

thank my relative including aunts, uncles, and cousins. I would not have finished my degree without them.

Table of Contents

List of Figures

List of Tables

Chapter 1

Introduction

Most elementary bimolecular reactions relevant to atmospheric or combustion chemistry involve at least one free radical. While the dynamics at small intermolecular distance is clearly governed by chemical forces, at large intermolecular separations the orientation of the approaching reactants can be influenced critically by van der Waals forces. Great advances in the study of van der Waals systems have been achieved over the past two decades. The chemistry of individual molecules is generally dominated by covalent bonding. However, van der Waals forces not only govern the interaction within collections of molecules, but they are also responsible for the stability of intermolecular complexes and for the existence of the condensed liquid states. Van der Waals clusters are very prolific model systems for the study of the details and of the origin of intermolecular forces as well as for the study of their effects on most fundamental chemical, physical, and biochemical processes from a molecular point of view. Because all life-forms may be viewed as a matter of supramolecular chemistry in which van der Waals forces play a central role, the understanding of these interactions is important for any progress, for example, in the synthesis of new drugs. Another interest in van der Waals complexes originates from the prospect of understanding in detail the transition from the gas phase to the condensed phase. Properties of clusters due to their finite size are of particular interest. For many systems, cluster properties can be explained in terms of pairwise interactions while three-body and other higher-order terms contribute only small

corrections. Considerable progress has been made in understanding these interactions and several excellent reviews on both experimental and theoretical works have been reported [1, 2, 3].

During the past 15 years, rotationally resolved infrared (IR) spectra of many complexes involving closed shell atoms and molecules have been recorded through different absorption techniques in combination with IR sources like diode [4], color center [5] or difference frequency lasers [6]. While continuous lasers allow us to detect weak absorption signals, they provide only modest power, therefore limiting its application to systems with relatively strong IR transitions. On the other hand, by applying different nonlinear optical processes, pulsed lasers can provide high power IR radiation over a wide spectral range. Although the large pulse-to-pulse fluctuations prevent extremely sensitive direct absorption measurements, several groups have succeeded in measuring IR absorption spectra of some aromatic molecules and their complexes using ion-dip spectroscopy in combination with resonant two-photon ionization [7, 8, 9]. Another possibility to overcome the poor signal-to-noise ratio resulting from the large pulse-to-pulse fluctuations is the application of cavity ring down spectroscopy. This technique has been used successfully by Liu *et al.* to measure the first overtone spectrum of the HCl dimer with rotational resolution [10]. Very recently, Infrared-ultraviolet(IR-UV) double resonance techniques have been employed to measure rotationally resolved spectra for the open-shell complexes OH-Ar using laser induced fluorescence (LIF) detection [11] and in this lab for the NO-Ar and NO-Ne complex using (2+1) resonant enhanced multi-photon ionization (REMPI) detection [12, 13, 14, 15].

The extreme sensitivity of the employed (2+1) REMPI process make it possible to measure the IR spectrum associated with the very weak first overtone transition in NO of complexes with Ar [12, 13] and Ne [14, 15]. The high sensitivity is achieved by detecting the IR absorption through a (2+1) REMPI process for the

hot band transition to a low lying Rydberg state in the complex. An important advantage of the REMPI approach over LIF detection is the ability to discriminate against a possible large monomer background. This makes it an ideal candidate to detect vibrationally excited van der Waals complexes in an IR-UV double resonance experiment. In the case of NO containing complexes, the fact can be utilized that the NO monomer is characterized by a rich UV and vacuum ultraviolet (VUV) electronic spectrum consisting of transitions to many different low lying Rydberg states or valence states which can be accessed from the electronic ground state via strong nonresonant two-photon absorption processes [16].

Many van der Waals complexes involving closed shell atoms and molecules have been studied [3, 17, 18], but only a few systems involving open shell molecules have been investigated. These complexes are of special interest since most of the chemically active systems involve atoms or molecules with one or more unpaired electrons. For example, van der Waals complexes comprising an open-shell diatomic molecule and a rare gas atom have four sources of angular momentum: electron orbital motion, electron spin, internal rotation of the diatomic molecule and overall rotation of the complex. These systems are ideal for studying how these angular momenta and their couplings influence the bound level structure or the collision dynamics without interference from reactive interactions.

Systems involving the $^2\Pi$ radicals OH($X\ ^2\Pi$) and NO($X\ ^2\Pi$) have emerged as important benchmarks for the understanding and quantitative description of the collision dynamics and the bound state structure. In these complexes, the electronic degeneracy of the Π-state is lifted giving rise to two adiabatic potential surfaces of A' and A'' symmetry with respect to reflection in the triatomic plane(see Fig. **??**). In contrast to an isolated diatom open shell molecule, the electronic orbital angular momentum is quenched giving rise to Renner-Teller type splittings. The degree of quenching can be viewed as a measure for the extent of chemical bonding

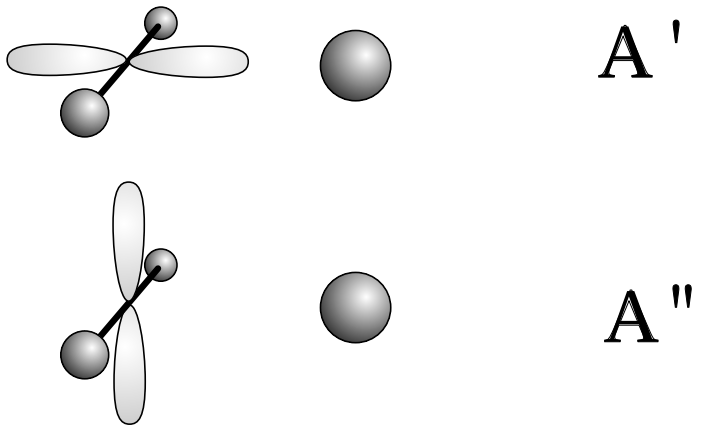

Figure 1.1: A' and A'' symmetry with respect to reflection in the triatomic plane.

involved in the formation of the complex. Mills *et al.* have developed a model for various angular momentum couplings by treating the complex as a rigid rotor [19]. Fawzy and Hougen have extended a rigid rotor model to include transitions between states with different electronic orbital angular momenta [20]. Their model involves angular momenta due to three types of motions except internal rotation and hence the complex is treated as a semirigid rotor. The Hamiltonian derived by these authors includes a full treatment of the asymmetric top or linear molecule rotation as well as the effects of spin-orbit interaction and Renner-Teller orbital angular momentum quenching. On the other hand, the complex as a near-free rotor has been studied theoretically by Dubernet *et al.* [21]. They considered three types of coupling cases depending on the size of the anisotropy of the intermolecular potential. In their work, they have established the relation between the bending energy level and the intermolecular potential anisotropy. In this model, no treatment of the effects of the van der Waals stretching motion, end-over-end rotation or electron spin was included.

The OH-Rg (Rg=rare gas atom) van der Waals complexes have been thoroughly investigated over the last few years by experiment and theory. The OH radical has a triply filled π-orbital. As a hydride, its rotational constant is comparable in magnitude with the intermolecular interaction. To a first approximation, the OH can be regarded as freely rotating in the complex with an approximately linear equilibrium structure. The complexes with Ar or Ne have been detected through laser induced fluorescence(LIF) spectroscopy in the vicinity of the respective monomer transition A-X [22, 23, 24, 25, 26, 27, 28]. Endo *et al.* has reported the pure rotational microwave spectrum of the OH-Ar complex [29, 30]. Chakravarty *et al.* have calculated bound states for the electronic ground and the electronically excited states [26, 31] using the *ab initio* potential energy surfaces of Degli-Eposti and Werner [32]. Complexes of OH with other closed shell molecules have been studied by Lester and co-workers employing various spectroscopic techniques [33, 34].

Among the various complexes involving NO, the NO-Ar system has served as the paradigm for understanding and characterizing the interaction of an open shell diatom with a closed shell atom for more than two decades. The first theoretical study of the van der Waals interaction in its electronic ground state was performed by Nielson *et al.* [35, 36] who had applied the electron gas model to calculate the first set of potential energy surfaces. They also emphasized the advantage of working with two adiabatic potential surfaces and thus keeping the electronic degree of freedom instead of introducing a single potential surface with an additional angle dependence [37]. A similar approach was followed by Alexander who has shown that the potential surfaces relevant to the collision dynamics can be derived from the two Born-Oppenheimer surfaces in the form of an average and a difference potential [38, 39]. Alexander and co-workers studied extensively the dynamics for collisions of NO with different rare gas atoms and the applicability of different decoupling approximations [40, 41, 42, 43, 44]. While most of these earlier studies relied on semiempirical

potential surfaces, high-level *ab initio* calculations during the 1990s have produced multi-dimensional surfaces for several NO-rare gas systems [42, 43, 45, 46, 47, 48]. Our recent spectroscopic studies have confirmed the great accuracy of these potential surfaces [12, 15, 49].

Experimentally, the NO-Ar system has been studied in different collision experiments. Integral cross sections without final state resolution for the scattering of NO from different rare gas partners have been measured by Thuis *et al.* [50, 51]. Their measurements indicated a near T-shaped equilibrium structure of the complex and gave the first quantitative information about the equilibrium distance. Employing LIF detection in combination with IR excitation in the first overtone region of NO, Sudbø and Loy were able to measure state-to-state relaxation rates [52]. Joswig and co-workers determined state-resolved integral cross-sections for the NO-Ar system for the first time [53, 54]. Jons *et al.* reported first state resolved differential scattering cross sections [55, 56] which were later compared with the results of a full quantum mechanical close coupling calculation by Alexander [42]. The new *ab initio* PES based on the correlated electron pair (CEPA) approximations used in this study yielded better agreement with the experimental data. Recently, Alexander calculated an improved *ab initio* PES at the CCDS(T) (coupled cluster singlet doublet(triplet)) level of theory [45, 46]. At this level of theory, the dispersion energy is reproduced more reliably while features of the repulsive region are affected only very little. Even with these latest improvements, the earlier discrepancies with experimental scattering data are not completely resolved. The remaining discrepancies are not likely related to deficiencies of the *ab initio* potential surfaces. Another important test of the quality of the PESs will be the comparison of bound states with spectroscopic information.

While numerous scattering experiments involving NO have been performed, until recently very little information on the bound levels of the corresponding van der

Waals complexes was known. Again, most attention has been focused on the NO-Ar complex. The existence of the complex was first inferred from molecular beam deflection studies [57]. The first spectroscopic observation of the complex was reported by Langridge-Smith *et al.* [58, 59]. In the LIF spectrum of an Ar molecular beam expansion containing NO, these authors found a broad feature to the blue of the band origin of the $A - X$ transition in the monomer. This feature was attributed to transitions from the electronic ground state of the complex terminating on the repulsive wall of the excited state surface. Recently, REMPI and LIF spectra for the $A\ ^2\Sigma^+ - X\ ^2\Pi$ transition terminating in the bound region of the $\tilde{A}$-state have been reported by several groups for complexes with Ar [60, 61, 62, 63], Kr [64], and Xe [64]. After the study of Levy and co-workers [58, 59], spectra correlating with other low lying Rydberg states of NO have been observed by several groups. The first spectrum for NO($C\ ^2\Pi$)-Ar was reported by Sato *et al.* applying (2+1) REMPI detection [65]. Later, Miller and Cheng extended these experiments towards higher vibrational levels of the C-state manifold and towards complexes with Ne, Kr, and Xe [66, 67]. Complex spectra correlating with the NO Rydberg states $D\ ^2\Sigma^+$ [67, 68], $E\ ^2\Sigma^+$ [69, 70, 71], $F\ ^2\Delta$ [70, 72] and $H\ ^2\Sigma^+$,$H'\ ^2\Pi$ [70, 72] have been reported more recently.

Since the complexes can only be generated in the extremely cold molecular beam or jet environments, hot band transitions or combination bands involving internuclear vibrations are rarely observed. Thus, the electronic spectra provide mainly information on molecular interactions in the electronically excited state. In the case of OH-Ar, important structural information for the electronic ground state is derived from microwave studies [29] while information on the electronic ground state potential surface has been obtained by combining laser induced fluorescence spectroscopy with stimulated emission pumping [74], stimulated Raman pumping [33] or infrared absorption [11, 75].

The first direct observation of bound rotational levels of the electronic ground state surface of NO-Ar was accomplished by Mills *et al.* in their pioneering study using a molecular beam electronic resonance spectrometer [19, 73]. The rotational structure of the observed spectrum was analyzed by these authors assuming a rigid rotor Hamiltonian. This analysis provided precise structural information confirming the near T-shaped structure of the complex originally deduced from collision studies [50, 51]. As part of this thesis, bound levels of the complex involving intermolecular vibrations for the electronic ground state have been observed for the first time in an IR-REMPI double resonance experiment for NO-Ar [12, 13] and NO-Ne [14, 15] built on the first overtone transition of the NO monomer. The positions of the observed bands and their rotational structure are extremely sensitive to different features of the potential surface.

This thesis is organized as follows: In Chapter 2, the different apparatus and the experimental setups are described in detail. The theoretical background for understanding of the spectroscopy of an open shell diatom and a van der Waals complex is covered in Chapter 3. Chapter 4 describes the experimental results and discussions. Finally, conclusions are given in Chapter 5.

Chapter 2

Experiments

2.1 Experimental Apparatus

This section describes the molecular beam machine and laser systems used in the experiments.

2.1.1 Molecular Beam Machine

A schematic of the molecular beam machine is shown in Fig. 2.1 [76]. Two chambers, the source chamber and the detection chamber, are differentially pumped with two diffusion pumps. The 500 mm diameter source chamber is mounted on top of a diffusion pump (P1) (BALZERS DIF 500) whose pumping speed is 11000 l/s. Inside the source chamber a 400 mm diameter cylindrical chamber is mounted from the top of the 500 mm flange. Two sides of the inner chamber facing the molecular beam source are flat walls with a skimmer opening. The other two sides are connected to flanges with bellows. One flange has a window (CaF_2) to give access for the laser beam to the molecular beam. The other flange is connected to one side of a T cross. On the other side is mounted a plexiglass flange with a window which is used for the laser beam and visual alignment. The bottom flange of the cross is connected to a water baffled 3000 l/s diffusion pump (P2) (LEYBOLD 3000). The upper flange is connected to a liquid N_2 baffle. The detection chamber is completely separated from the source chamber except for the skimmer openings. The two diffusion pumps are backed by a roots-rotary pump combination (EDWARDS

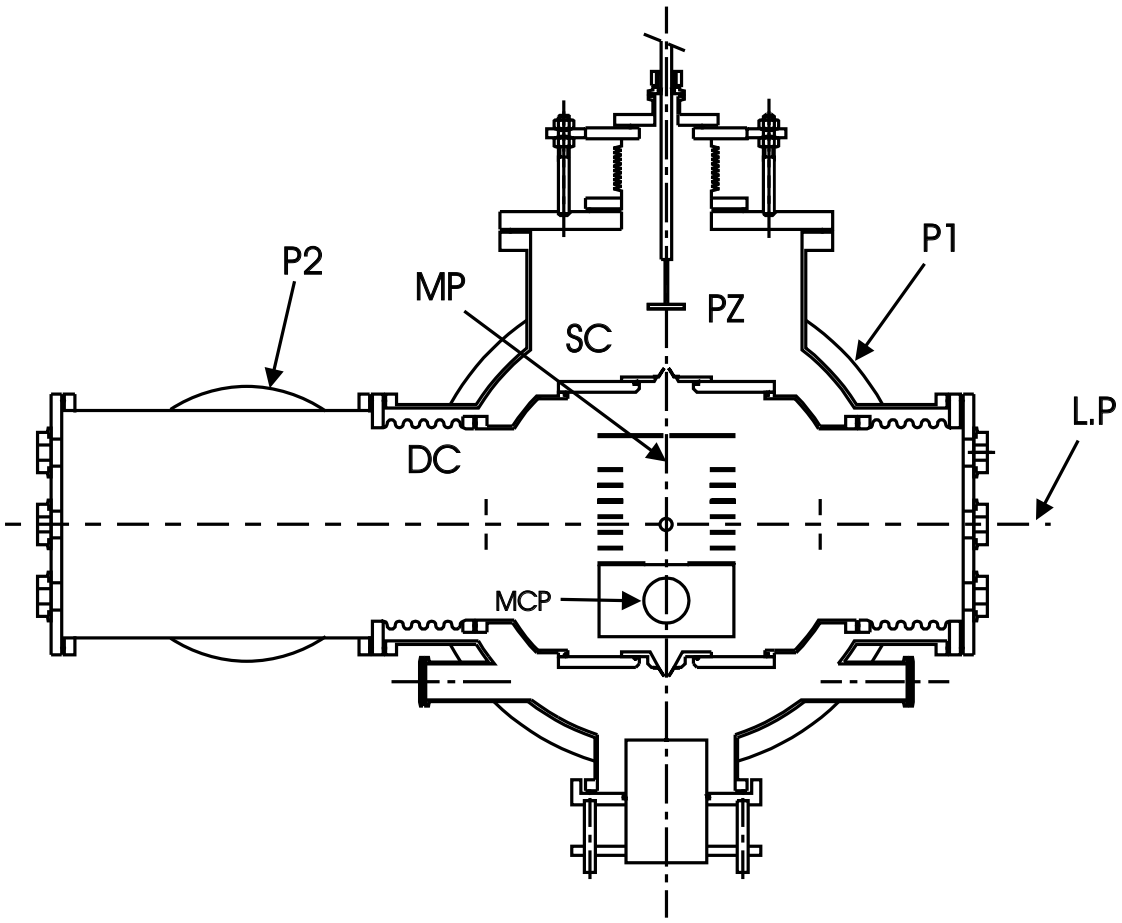

Figure 2.1: Cross-section of the molecular beam machine. SC=source chamber, DC=detection chamber, PZ=piezoelectric valve, MCP=microchannel plate detector, P1,P2=diffusion pumps, MP=molecular beam path, LP=laser beam path.

E2M40 as mechanical pump and EDWARDS EH250 as booster). The base pressure in the source chamber is 5×10^{-7} mbar and rises to 10^{-5} mbar when the molecular beam is operating. The base pressure in the detection chamber is 5×10^{-7} mbar and rises to 10^{-6} mbar when the molecular beam is operating. At the top of the 500 mm flange a liquid N_2 trap is mounted to reduce oil contamination.

As a molecular beam source, a homebuilt piezoelectric valve is mounted in the source chamber and is operated at 10 Hz. Beam pulses of about 70 μs duration are

generated in the source chamber with this valve. When the molecules are delivered into the vacuum by supersonic expansion, they are cooled to an extremely cold temperature in an adiabatic process. Typical rotational temperatures are less than 2 K when the piezoelectric valve is operated at a backing pressure of 2 bar. Higher rotational temperatures are measured when the valve is operated at other backing pressures or when the laser beam probes the beginning or the end of the molecular beam pulse. The molecules pass from the source chamber into the detection chamber through a skimmer with 5 mm diameter. Due to the dimension of the molecular beam machine, the 300 mm lens for the UV laser is mounted inside the molecular beam machine. To facilitate the alignment of the laser beam two 5 mm guiding apertures are mounted 10 cm before and after the expected focal spot. In order to avoid oil contamination of the lens, a copper pipe is mounted to block the oil vapor from the diffusion pump.

The schematic of the drift field arrangement of the time-of-flight (TOF) mass spectrometer is depicted in Fig. 2.2 [77]. The constant electric field in the accelerating region is defined using seven metal electrodes (150 mm $\times$150 mm $\times$1.6 mm) with a circular opening of 100 mm in diameter. The electrodes are separated by 16 mm and interconnected with 1 MΩ resistors. At the entrance of the drift region, a metal plate is mounted with a 10 mm diameter hole to let the molecular beam pass. On the other side of the drift region, an electrostatic mirror is mounted so that it deflects the ions towards a 25 mm diameter microchannel plate (MCP) detector (GALLILEO FTD2500). The mirror has two electrodes which are 20 mm apart. The front electrode has a wire mesh of 90% transmission (WIRE WEAVING CO NJ). The ions are deflected by 90° off the beam axis, pass another wire mesh and are accelerated into the MCP. A dc power supply provides 100 V for the drift voltage (V_d), 144 V for the front plate (V_f), and 82 V for the mirror (V_m) (typically

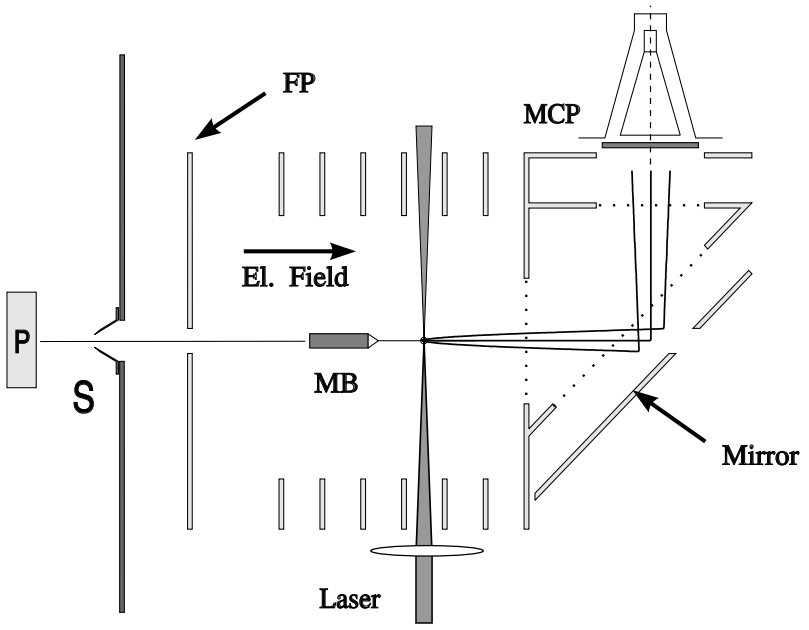

Figure 2.2: Schematic of the drift field arrangement. MCP=microchannel plate detector, P=piezoelectric valve, FP=front plate, MB=molecular beam pulse, S=skimmer.

$V_f = 1.44V_d$, $V_m = 0.82V_d$).

2.1.2 Ultraviolet Laser System

The ultraviolet laser system consists of two grazing incidence dye lasers (LASER ANALYTICAL SYSTEM (LAS) LDL205 and RADIANT DYES RDP02N) pumped by the second harmonic of a Nd:YAG laser (SPECTRA PHYSICS GCR170-10) operated at a repetition rate 10 Hz. The 532 nm beam is generated from the 1064 nm fundamental. The effective linewidth of the Nd:YAG laser is about 1 cm^{-1} and its polarization is horizontal. With type II doubling (see page 21), a vertically polarized 532 nm beam is generated by second harmonic generation in a KDP (potassium dihydrogen phosphate) crystal.

An optical layout of the dye laser is shown in Fig. 2.3. The cavity of the dye lasers is composed of an output coupler (M1), an oscillator/preamplifier cell (C1), a prism beam expander (PBE), a grating (G), and a tuning mirror (M2) [78]. The 532 nm beam is introduced into C1 where a dye solution is circulating. The lower part of C1 is the active medium for the oscillator. C1 is tilted 6° from the vertical direction so that undesired radiation due to lasing from the walls of C1 leaves the normal beam path. M1 reflects the part of the light deriving from C1 and sends it back towards C1. The beam travels through PBE, which magnifies the beam in its vertical direction (by a factor of 12) and translates the beam downwards (by 11 mm). The beam hits the grating (G) which diffracts the first order towards the tuning mirror (M2). M2 can be rotated around an axis which runs through the center of the grating surface towards the grating grooves. The wavelength (λ) of the outgoing laser beam is determined by the angle according to the grating equation:

$$\lambda = d(\sin\alpha + \sin\beta). \tag{2.1}$$

where α stands for the angle between the normal of the grating and M2 and β is the angle of incidence on the grating. d is the spacing between grooves of the grating. The light reflected by M1 travels the described path in reversed direction through G, PBE, C1, and to M1, where the outcoupled part leaves the oscillator. The brewster plates filter the proper polarization of the output beam. The pump beams for the pre-amplifier and the amplifier stages are delayed before reaching the amplifier so that the output of the previous stage overlaps with the pump beam in time. The beam from the oscillator is pre-amplified once in C1 and amplified in a second cell (C2). The lenses T1 and T2 shift the beam path.

The visible output of the dye lasers is frequency-doubled in a KDP crystal resulting in tunable UV radiation. When DCM dye is being used with 30 mJ pump power of 532 nm, typical output energies of the dye laser stages are 160 μJ, 1.5 mJ,

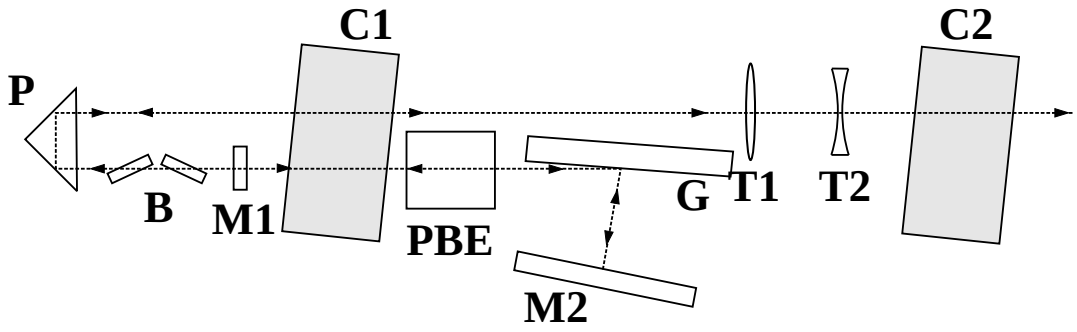

Figure 2.3: Layout of the dye laser (LSL205 and RDP02N) oscillator cavity and beam path. P=reflection prism, B=brewster plates, M1=output coupler, M2=tuning mirror, G=grating, C1=oscillator/preamplifier cell, C2=main amplifier cell, PBE=prism beam expander, T1,T2=telescope lenses.

and 10 mJ for the oscillator, the pre-amplifier, and the amplifier beam, respectively. After doubling in KDP, a UV power of 1.5 mJ is obtained. The efficiency varies depending on the dye used. With DCM dye, an efficiency of 30% is achieved. For the present experiments, DCM, Pyridine 1, and Pyridine 2 are used as dyes.

2.1.3 Infrared Laser System

IR radiation is generated with an optical parametric oscillator pumped by an injection seeded Nd:YAG laser.

Nd:YAG

The pump laser Nd:YAG (CONTINUUM POWERLITE 7010) is operated at a repetition rate of 10 Hz. Typical pulse energies at 1064 nm are 145 mJ for the oscillator output and 500 mJ for the amplified beam with unseeded operation. The

linewidth is 1 cm^{-1} (FWHM) unseeded and the pulsewidth is 5-7 ns (FWHM). A layout of the Nd:YAG laser system is shown in Fig. 2.4. The laser cavity consists of a highly reflecting rear mirror (RM), a Pockel cell (Q-switch), a polarizer (P), three quarter-wave ($\lambda/4$) plates, a Nd:YAG rod, and an output coupler (OC). The system has one flash lamp but two Nd:YAG rods: one for the oscillator and the other for the amplifier.

When the two $\lambda/4$ plates (before and after the laser head) are not present, the lasing mechanism can be explained as follows (Fig. 2.5(a) and (b)) [79]. The beam propagating within the oscillator cavity makes a double pass through the Q-switch (QSW) and a $\lambda/4$ plate. With high voltage applied to the Pockel cell, the QSW adds a phase shift of 45° and the $\lambda/4$ plate adds an additional phase shift of 45° with each pass, giving a total phase shift of of 180°. Thus, the horizontal beam transmitted through the plate polarizer (P) is rotated vertical and back to horizontal so that it is transmitted by the polarizer allowing oscillation to occur (Fig. 2.5(b)). Diagram (a) illustrates the closed cavity where there is no lasing. When no voltage is applied to the Pockel cell, only the $\lambda/4$ plate adds a phase shift of 45° with each pass giving a total phase shift of 90°. The horizontal beam is rotated to vertical and is rejected by the polarizer preventing laser oscillation.

Additional two quarter-wave ($\lambda/4$) plates are mounted on each side of the oscillator Nd:YAG rod so that they produce counter-rotating circularly polarized light within the Nd:YAG rod suppressing spatial hole burning. The horizontal beam passing through the polarizer becomes circularly polarized after L2. Then, L3 transforms circular polarization into vertical polarization. The reflected beam from OC travels in reversed direction. After L3, the beam becomes circularly polarized again, but counter-rotating with respect to the incoming beam. After L2, it becomes horizontally polarized again. The Nd:YAG laser has a resonator length of 60 cm which

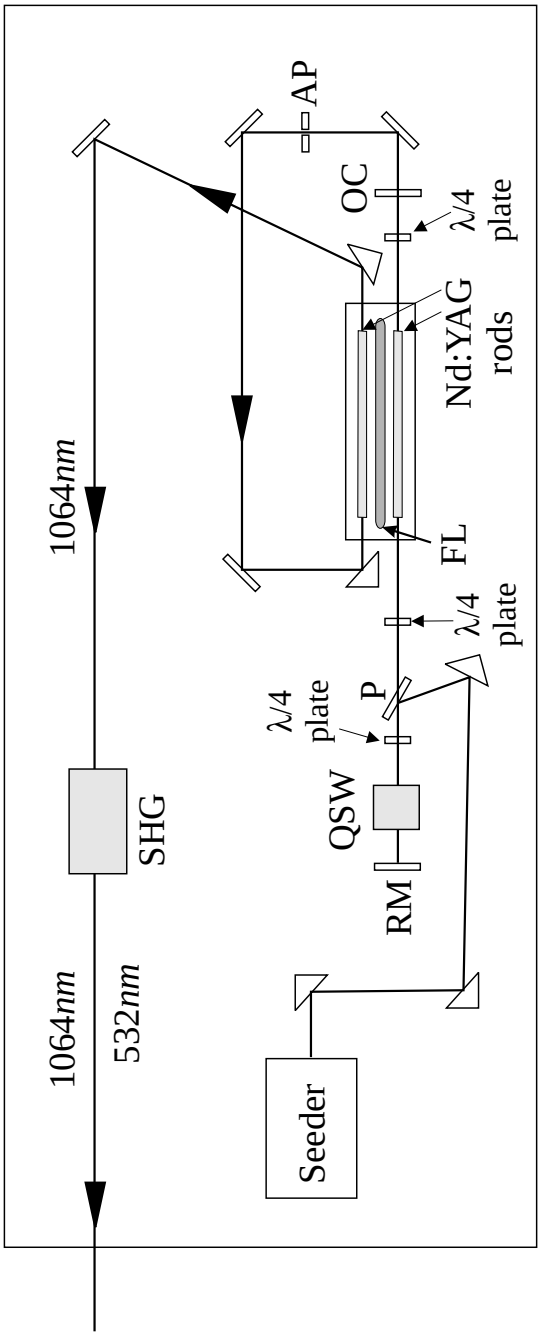

Figure 2.4: Layout of the Nd:YAG laser (POWERLITE 7010). AP=aperture, FL=flash lamp, OC=output coupler, QSW=Q-switch, RM=rear mirror, SHG=second harmonic generator

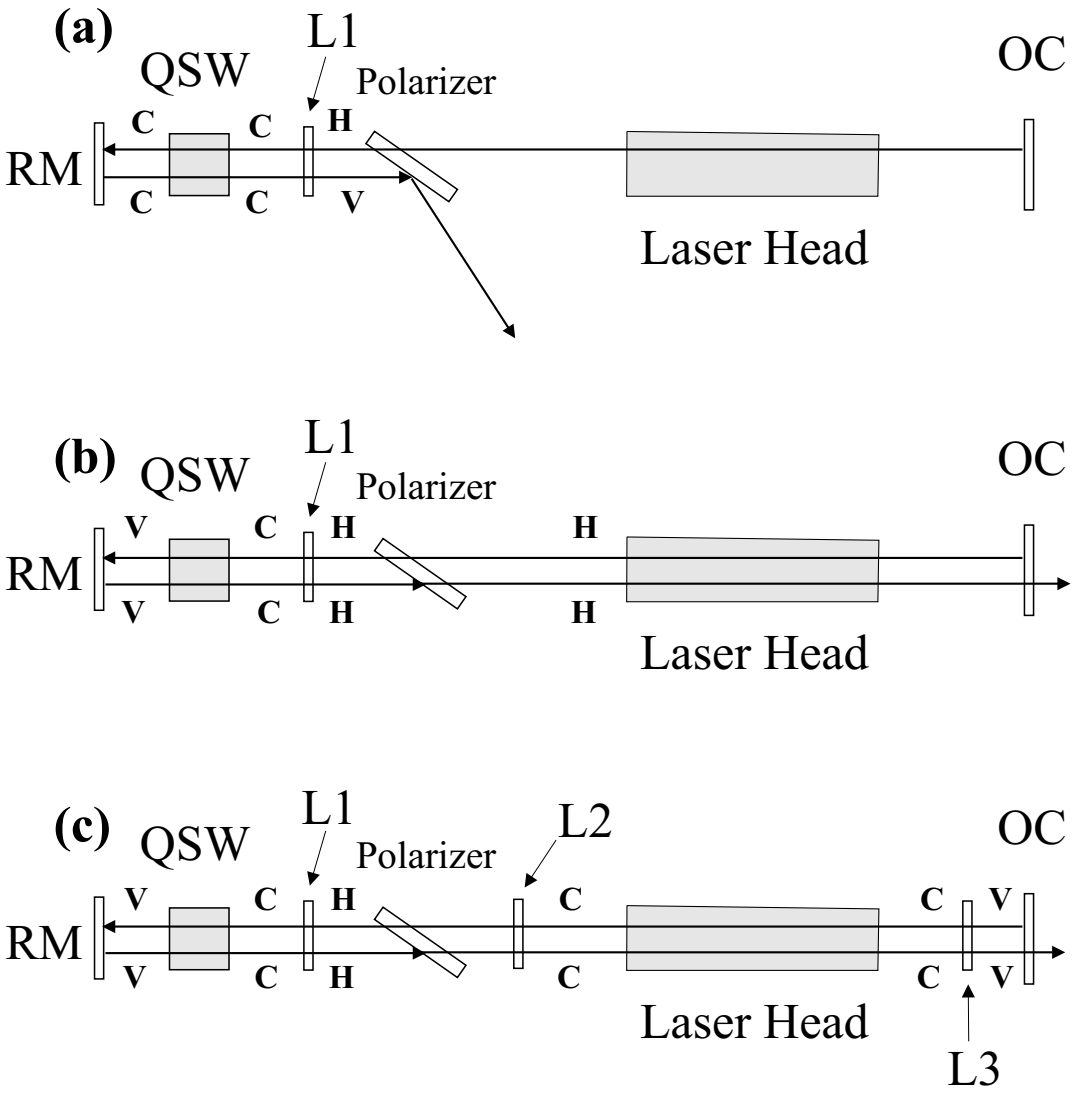

Figure 2.5: Cavity diagrams for the Nd:YAG laser (POWERLITE 7010). OC=output coupler, QSW=Q-switch, RM=rear mirror. L1,L2,L3=$\lambda/4$ plates, C : circular polarization, H : horizontal polarizaton, V : vertical polarization. Part (a) shows a diagram when the cavity is open whereas part (b) show one when the cavity is closed. In part (c), the beams from left to right and from right to left are both circularly polarized but they are counter-rotating in order to suppress the spatial hole burning.

yields the spacing between adjacent longitudinal modes,

$$\Delta\nu = c/2nL = 3 \times 10^{10}/\ 2 \times 1 \times 60\ (\text{cm}) = 250\ \text{MHz}.$$

Though the gain curve for the Nd:YAG is approximately 120 GHz (FWHM), due to mode competition longitudinal modes closest to the center of the gain curve get hold of most of the available energy at the expense of longitudinal modes further from the gain center. This results in a typical unseeded linewidth of 1 cm^{-1} for the host laser. In order to achieve single longitudinal mode output, a seed laser is coupled to the Nd:YAG laser cavity.

Single Frequency Injection Seeding Laser

Injection seeding refers to the process of achieving single longitudinal mode operation of a pulsed laser by injecting radiation from a very narrow linewidth, continuous-wave (cw) seed laser into the pulsed host (Nd:YAG) laser cavity during the time the Q-switch opens. If the seed emission is near the frequency of a host laser longitudinal mode, it will be resonantly amplified by the host when the Q-switch opens. The seed emission is more than 6 orders of magnitude stronger than the spontaneous noise and all the energy stored in a homogeneously broadened gain element is depleted by the pulse developed from the seed laser emission resulting in single mode output from the pulsed laser [80]. Furthermore, the Q-switched pulses build up sooner out of the seeded emission than out of the spontaneous emission. The seed beam which is introduced into the YAG cavity by a beam splitter polarizer needs to be aligned along the YAG laser beam. The best way of aligning the seeder is by monitoring the QBTR (Q-switch build-up time reduction) from a fast oscilloscope and keeping it as large as possible. The voltage readout for the QBT (Q-switch build-up time) and the voltage of the piezoelectric element are monitored during experiments. The lowest

output of the QBT corresponds to the largest QBTR. Thus, it must be maintained as low as possible. The voltage output of the piezo provides information about the dither magnitude, the rate of host laser frequency drift, and the piezoelectric reset.

Optical Parametric Oscillator (OPO)

In this section, the theoretical background of an optical parametric oscillator is given. Details relevant to the alignment and operation of each component of the OPO (CONTINUUM MIRAGE 3000) are also described.

(1) Theoretical Background

Optical parametric oscillator (OPO) and optical parametric amplifier (OPA) devices have long been recognized as useful sources of wide-range tunable, coherent radiation for spectroscopic purposes yielding high peak and average powers in the nanosecond regime [81, 82, 83, 84, 85, 86, 87, 88]. Their solid-state character and high efficiency offer substantial advantages in several respects over the dye laser. Moreover, the wide tuning range of many OPOs opens up the prospect for laser spectroscopy in otherwise inaccessible spectral regions such as the near- and mid-infrared. The intrinsic process which allows an OPO or an OPA to operate is a nonlinear optical process.

In the process, coherent pump radiation interacts with the second-order nonlinear-optical susceptibility tensor $\boldsymbol{\chi}^{(2)}$ of a suitable noncentrosymmetric crystal and generates two additional radiation fields. These are referred to as the signal and idler waves with frequencies ω_1 and ω_2, respectively. Here, it is customary to take $\omega_1 \geq \omega_2$. The pump, signal, and idler waves in an optical parametric device are subject to two conservation conditions. The first condition corresponds to energy

conservation:

$$\omega_3 = \omega_1 + \omega_2 \tag{2.2}$$

where ω_3 is the frequency of the pump wave. The second conservation condition corresponds to momentum conservation and takes the form of a phase-matching condition. This is expressed in terms of the three wave vectors $\boldsymbol{k}_j$, with $j = 1, 2,$ and 3. These have magnitude of $k_j = n_j\omega_j/c = 2\pi n_j/\lambda_j$ where n_j is the refractive index at vacuum wavelength λ_j and c is the speed of light. The wave vectors combine vectorially,

$$\boldsymbol{k}_3 = \boldsymbol{k}_1 + \boldsymbol{k}_2 + \Delta\boldsymbol{k} \tag{2.3}$$

where $\Delta\boldsymbol{k}$ is a phase-mismatch increment. Although typically small, $\Delta\boldsymbol{k}$ causes the signal and idler waves to have an intrinsically broad bandwidth.

Phase-matching conditions can be fulfilled in birefringent crystals which have two different refractive indices n_o and n_e for the ordinary and the extraordinary waves, respectively. While the ordinary index n_o does not depend on the propagation direction, the extraordinary index n_e depends on both directions of the electric field $\boldsymbol{E}$ and $\boldsymbol{k}$. In uniaxial birefringent crystals where two of the principal axes are equal at a given wavelength, the n_e is given by

$$\frac{1}{n_e^2(\theta)} = \frac{\cos^2\theta}{n_o^2} + \frac{\sin^2\theta}{n_e^2(\theta = 90°)}. \tag{2.4}$$

Here, θ is the direction of propagation with respect to the optic axis. If it is assumed that the three waves are collinear and that $\Delta\boldsymbol{k}$ is zero, then Eq. (2.3) becomes

$$\omega_3 n_3 = \omega_1 n_1 + \omega_2 n_2. \tag{2.5}$$

Then, the signal frequency can be expressed simply in terms of the refractive indices n_j:

$$\omega_1 = \frac{\omega_3(n_3 - n_2)}{n_1 - n_2}. \tag{2.6}$$

By changing one or more of the refractive indices (for example, by rotating a birefringent crystal or by variation of the temperature), the signal and the idler wavelength can be tuned. If the signal and the idler have the same polarization, the interaction is referred to as a Type I interaction. On the other hand, if the signal and the idler have different polarizations (by 90°), the interaction is referred to as a Type II interaction.

The polarization P of a dielectric medium with nonlinear susceptibility $\boldsymbol{\chi}$, subject to an electric field $\boldsymbol{E}$, can be written as an expansion in terms of powers of $\boldsymbol{E}$

$$\boldsymbol{P} = \epsilon_0 \left(\boldsymbol{\chi}^{(1)} \boldsymbol{E} + \boldsymbol{\chi}^{(2)} \boldsymbol{E}\boldsymbol{E} + \boldsymbol{\chi}^{(3)} \boldsymbol{E}\boldsymbol{E}\boldsymbol{E} \cdots \right), \tag{2.7}$$

where $\boldsymbol{\chi}^{(k)}$ is the k-th order susceptibility tensor of rank k. If the electric field

$$\boldsymbol{E} = \boldsymbol{E}_1 \cos(\omega_1 t - k_1 z) + \boldsymbol{E}_2 \cos(\omega_2 t - k_2 z) \tag{2.8}$$

is composed of two components incident on the nonlinear medium. The induced polarization at a fixed position (z=0, for example) in the medium is generated by the combination of the two components. The second order term is of interest giving the contributions

$$\begin{aligned} \boldsymbol{P}^{(2)} &= \varepsilon_0 \boldsymbol{\chi}^{(2)} \boldsymbol{E}^2 (z = 0) \\ &= \varepsilon_0 \boldsymbol{\chi}^{(2)} \Big\{ \frac{1}{2} (\boldsymbol{E}_1^2 + \boldsymbol{E}_2^2) + \frac{1}{2} \boldsymbol{E}_1^2 \cos 2\omega_1 t + \frac{1}{2} \boldsymbol{E}_2^2 \cos 2\omega_2 t \\ &\quad + \boldsymbol{E}_1 \cdot \boldsymbol{E}_2 \big[\cos(\omega_1 + \omega_2) t + \cos(\omega_1 - \omega_2) t \big] \Big\}. \end{aligned} \tag{2.9}$$

The second and third terms correspond to the second harmonics $2\omega_1$, $2\omega_2$ and the last term corresponds to the sum or difference frequencies $\omega_1 \pm \omega_2$. The second order term is expressed in terms of tensor notation as

$$P_i^{(2)} = \varepsilon_0 \sum_{j,k=1}^{3} \chi_{ijk}^{(2)} E_j E_k. \tag{2.10}$$

The above equation depicts the fact that the components of the induced polarization $\boldsymbol{P}^{(2)}$ are determined by the tensor components χ_{ijk} and the components of the

incident fields. The components χ_{ijk} are written in the reduced Voigt notation in order to reduce the number of indices, as $\chi_{ijk} = d_{im}$ [89]. Here,

$$\begin{array}{ccccccc} (\mathrm{jk}) & = & 11 & 22 & 33 & 23 & 13 & 12 \\ \mathrm{m} & = & 1 & 2 & 3 & 4 & 5 & 6. \end{array}$$

And it is found that the effective nonlinear-optical coefficient d_{eff} is

$$d_{\mathit{eff}} = d_{31} \sin\theta - d_{22} \sin 3\phi \cos\theta \tag{2.11}$$

where the optic axis (Z) of the crystal is at an angle θ to the propagation direction of the phase-matched optical wave whereas the crystal's X-axis is at the azimuthal angle ϕ (which may be set to an optimal value by the cut of the crystal) [84, 90, 91]. Then, the second order polarizations are expressed as

$$\begin{aligned} P_1^{(2)} &= 2\varepsilon_0 d_{\mathit{eff}}\, E_3 E_2^* \\ P_2^{(2)} &= 2\varepsilon_0 d_{\mathit{eff}}\, E_3 E_1^* \\ P_3^{(2)} &= 2\varepsilon_0 d_{\mathit{eff}}\, E_1 E_2. \end{aligned} \tag{2.12}$$

The generated polarization acts as a driving term in the wave equation

$$\nabla \times (\nabla \times \boldsymbol{E}_j) + \frac{\partial}{\partial t}(\sigma \mu_0 \boldsymbol{E}_j) + \mu_0 \varepsilon \frac{\partial^2 \boldsymbol{E}_j}{\partial t^2} = -\mu_0 \frac{\partial^2 \boldsymbol{P}_j^{(2)}}{\partial t^2} \tag{2.13}$$

where

$$\boldsymbol{E}_j(\boldsymbol{r}, t) = \frac{1}{2}\big\{\boldsymbol{E}_j(\boldsymbol{r}) \exp[i(\boldsymbol{k}\cdot\boldsymbol{r} - \omega t)] + \boldsymbol{E}_j^*(\boldsymbol{r}) \exp[-i(\boldsymbol{k}\cdot\boldsymbol{r} - \omega t)]\big\} \tag{2.14}$$

and

$$\boldsymbol{P}_j^{(2)}(\boldsymbol{r}, t) = \frac{1}{2}\big\{\boldsymbol{P}_j^{(2)}(\boldsymbol{r}) \exp[i(\boldsymbol{k}\cdot\boldsymbol{r} - \omega t)] + \boldsymbol{P}_j^{(2)*}(\boldsymbol{r}) \exp[-i(\boldsymbol{k}\cdot\boldsymbol{r} - \omega t)]\big\}. \tag{2.15}$$

Here, σ_i is the conductivity of the medium. The suffix j takes on the value of 1,2 or 3.

The combination of Eqs. (2.14), (2.15), and (2.12) with Eq. (2.13) yields a set of coupled equations for the three frequency parametric interaction,

$$\begin{aligned} \frac{d}{dz}E_1 + \alpha_1 E_1 &= i\kappa_1 E_3 E_2^* \exp(i\Delta k z) \\ \frac{d}{dz}E_2 + \alpha_2 E_2 &= i\kappa_2 E_3 E_1^* \exp(i\Delta k z) \\ \frac{d}{dz}E_3 &= i\kappa_3 E_1 E_2 \exp(-i\Delta k z) \end{aligned} \tag{2.16}$$

where $\kappa_j = \omega_j d/n_j c$ and $\alpha_j = \frac{1}{2}\mu_0\sigma_j c$ is the round trip electric field loss [83]. Neglecting loss, the equations lead to a photon conservation relation

$$\frac{1}{\omega_1}\frac{dI_1}{dz} = \frac{1}{\omega_2}\frac{dI_2}{dz} = -\frac{1}{\omega_3}\frac{dI_3}{dz} \tag{2.17}$$

where

$$I(\boldsymbol{r},\omega) = \frac{1}{2}nc\varepsilon_0|E(\boldsymbol{r},\omega)|^2$$

is the intensity and z is the direction of propagation.

For every photon converted from the pump field, a signal and a corresponding idler photon are generated. For parametric generation in a crystal of length l, the solutions of Eq. (2.16) can be assumed in the form

$$E_1^* = E_1^* \exp\left[(\Gamma' - \frac{1}{2}i\Delta k)z\right] \quad \text{and} \quad E_2 = E_2 \exp\left[(\Gamma' + \frac{1}{2}i\Delta k)z\right]. \tag{2.18}$$

The solution of the equations

$$\begin{aligned} E_1^*\left(-\frac{i\omega_2 d E_3}{n_2 c}\right) + E_2\left(\Gamma' + \alpha_1 + \frac{i\Delta k}{2}\right) &= 0 \\ E_1^*\left(\Gamma' + \alpha_2 - \frac{i\Delta k}{2}\right) + E_2\left(\frac{i\omega_d E_3^*}{n_2 c}\right) &= 0 \end{aligned} \tag{2.19}$$

is

$$\begin{aligned} \Gamma'_{\pm} &= -\frac{(\alpha_1+\alpha_2)}{2} \\ &\pm\frac{1}{2}\left[(\alpha_1-\alpha_2)^2 + \frac{i\Delta k}{2}(\alpha_1-\alpha_2) - 4\left(\frac{\Delta k}{2}\right)^2 + \frac{4\omega_1\omega_2|d|^2|E_3|^2}{n_1 n_2 c^2}\right]^{1/2}. \end{aligned} \tag{2.20}$$

The parametric gain coefficient is defined as [92]

$$\Gamma = \left| \frac{\omega_1 \omega_2 |d|^2 |E_3|^2}{n_1 n_2 c^2} \right|^{1/2} = \left| \frac{2\omega_1 \omega_2 |d|^2 I_3}{n_1 n_2 \varepsilon_0 c^3} \right|^{1/2} \tag{2.21}$$

where I_3 is the pump intensity. Therefore, the general solution is

$$\begin{aligned} E_1^*(z) &= (E_{1+}^* e^{gz} + E_{1-}^* e^{-gz}) e^{-\alpha z} \exp(-i\Delta k z/2) \\ E_1(z) &= (E_{2+} e^{gz} + E_{2-} e^{-gz}) e^{-\alpha z} \exp(+i\Delta k z/2) \end{aligned} \tag{2.22}$$

where $\alpha_1 = \alpha_2 = \alpha$ and the total gain coefficient is defined as [86]

$$g = \left[\Gamma^2 - \left(\frac{1}{2} \Delta k \right)^2 \right]^{1/2}. \tag{2.23}$$

There are several generic forms of optical parametric devices, all sharing the same nonlinear-optical basis. In an optical parametric generator (OPG) there is sufficiently high gain to amplify spontaneous optical noise to the level of the incident pump radiation in the same sense as superfluorescent laser emission. The corresponding optical parametric oscillator (OPO) requires an optical cavity to amplify at least one of the generated waves, as in a conventional laser. The resulting output beams have laserlike monochromaticity and coherence. An OPO cavity may be operated as a doubly resonant oscillator (DRO) in which resonant optical feed back occurs at both ω_1 and ω_2, a singly resonant oscillator (SRO) with feedback at only one frequency (either ω_1 or ω_2), or a nonresonant oscillator (NRO) in which neither ω_1 nor ω_2 are resonated in the cavity. The MIRAGE 3000 has an NRO in the first amplification stage. An optical parametric amplifier (OPA) requires coherent input at either ω_1 or ω_2 which is amplified by coherent interaction with the pump radiation through the same form of a nonlinear optical process as in an OPG or an OPO.

As mentioned earlier, the frequency (or the wavelength) tuning in parametric oscillation is achieved by rotating the nonlinear crystal. Theoretically the angle tuning of the type II crystal can be calculated as follows (the calculation for the

type I crystal is described in Ref. [93]). Consider a parametric oscillator pumped by an extraordinary pump wave at ω_3. ω_1 is an ordinary wave and ω_2 is an extraordinary wave. At some crystal orientation θ_0, oscillation takes place at ω_{10} and ω_{20} where the indices of refraction are n_{10} and n_{20}, respectively. At $\theta = \theta_0$, according to Eq. (2.5),

$$\omega_3 n_{30}(\theta_0) = \omega_{10} n_{10} + \omega_{20} n_{20}. \tag{2.24}$$

The crystal is rotated by $\Delta\theta$. This causes the index n_3 to change so that the need to satisfy the phase-matching condition causes ω_1 and ω_2 to change slightly. The new oscillation takes place with the following changes relative to oscillation at θ_0:

$$\begin{aligned}
\omega_3 &\longrightarrow \omega_3 \\
n_{30} &\longrightarrow n_{30} + \Delta n_3 \\
n_{10} &\longrightarrow n_{10} + \Delta n_1 \\
n_{20} &\longrightarrow n_{20} + \Delta n_2 \\
\omega_{10} &\longrightarrow \omega_{10} + \Delta\omega_1 \\
\omega_{20} &\longrightarrow \omega_{20} + \Delta\omega_2 \\
\Delta\omega_2 &= -\Delta\omega_1.
\end{aligned} \tag{2.25}$$

Since the phase-matching conditions need to be satisfied at the new set of frequencies, then

$$\omega_3(n_{30} + \Delta n_3) = (\omega_{10} + \Delta\omega_1)(n_{10} + \Delta n_1) + (\omega_{20} - \Delta\omega_2)(n_{20} + \Delta n_2). \tag{2.26}$$

Neglecting second-order terms $\Delta n \Delta\omega$ and using the energy conservation condition yields

$$\Delta\omega_1|_{\theta=\theta_0} = \frac{\omega_3 \Delta n_3 - \omega_{10}\Delta n_1 - \omega_{20}\Delta n_2}{n_{10} - n_{20}}. \tag{2.27}$$

Since the pump and the idler are extraordinary, n_3 and n_2 are functions of θ. The index n_1 of the ordinary wave depends on frequency but not on θ. Then,

$$\begin{aligned} \Delta n_1 &= \left.\frac{\partial n_1}{\partial \omega}\right|_{\omega_{10}} \Delta\omega_1 \\ \Delta n_2 &= \left.\frac{\partial n_2}{\partial \theta}\right|_{\theta} \Delta\theta \\ \Delta n_3 &= \left.\frac{\partial n_3}{\partial \theta}\right|_{\theta} \Delta\theta \end{aligned} \tag{2.28}$$

$$\frac{\partial \omega_1}{\partial \theta} = \frac{\omega_3 \frac{\partial n_3}{\partial \theta} - \omega_{20} \frac{\partial n_2}{\partial \theta}}{n_{10} - n_{20} + \omega_{10} \frac{\partial n_1}{\partial \omega}}. \tag{2.29}$$

Using Eq. (2.3) and the differentiation relation $\frac{d}{dx}\left(\frac{1}{x^2}\right) = -\frac{2}{x^3}$, it turns out that

$$\frac{\partial n_j}{\partial \theta} = -\frac{n_j^3}{2} \sin 2\theta \left[\left(\frac{1}{n_e^{(\omega_j)}} \right)^2 - \left(\frac{1}{n_o^{(\omega_j)}} \right)^2 \right] \tag{2.30}$$

where $j = 2,\ 3$. Then, the final result becomes

$$\frac{\partial \omega_1}{\partial \theta} = \frac{-\omega_3 \frac{n_3^3}{2} \sin 2\theta \left[\left(\frac{1}{n_e^{(\omega_3)}} \right)^2 - \left(\frac{1}{n_o^{(\omega_3)}} \right)^2 \right] + \omega_{20} \frac{n_2^3}{2} \sin 2\theta \left[\left(\frac{1}{n_e^{(\omega_2)}} \right)^2 - \left(\frac{1}{n_o^{(\omega_2)}} \right)^2 \right]}{n_{10} - n_{20} + \omega_{10} \frac{\partial n_1}{\partial \omega}}. \tag{2.31}$$

(2) OPO Laser System: MIRAGE 3000

The MIRAGE 3000 has three stages: a single-frequency optical parametric oscillator (or master oscillator), a nonresonant oscillator (NRO), and a parametric amplifier (OPA) [95, 96]. The core of the OPO is the master oscillator(MO) which is pumped by the second harmonic of the injection seeded Nd:YAG. A layout of the OPO is shown in Fig. 2.6. The MO generates the near-infrared radiation in the wavelength range between 710 nm and 840 nm. The mid-infrared radiation (1.45

μm - 2.12 μm) is generated by two stages of optical parametric amplification. The first amplification stage is an NRO seeded by the near-IR beam from the MO. It is pumped by 532 nm and amplifies the injected near-IR radiation from the MO while simultaneously producing an idler beam with wavelength 1.45 μm - 2.12 μm. Now, the idler photons from the NRO act as seed radiation for the second stage which is pumped by the Nd:YAG fundamental at 1064 nm. The second stage mixes the idler from the NRO with the 1064 nm pump beam resulting in amplified output between 2.12 μm to 1.45 μm (the signal) and a difference-frequency output between 2.12 μm to 4 μm (the idler). For the convenience, λ_1, λ_2, and λ_3 denote photons of wavelength 710 nm - 840 nm, 1.45 μm - 2.12 μm, and 2.12 μm - 4 μm, respectively. In the following, each stage is described in detail.

The MO consists of a KTP (potassium titanyl phosphate) crystal, a near grazing-incidence diffraction grating, a rear mirror, and a tuning mirror (see dotted box in Fig. 2.6). The two mirrors define the optical resonator. The cavity length is about $5cm$ yielding a free spectral range of 3 GHz. The grating of length 5 cm has 1800 lines/mm. Wavelength tuning is achieved by simultaneously rotating the tuning mirror and the KTP crystal. Rotating the tuning mirror selects a wavelength from the grating whereas rotating the KTP crystal allows one to maintain the phase-matching condition for the specific wavelength (Eq. (2.31)). The rear mirror mounted on a piezo-driven translator allows the fine adjustment of the cavity length. As described in the previous section, single frequency pump radiation of the injection-seeded SLM Nd:YAG is required for single-frequency OPO operation. Typically, 18 mJ of 532 nm pump radiation is introduced into the cavity producing about 0.7 mJ of near-IR radiation. The threshold input pump energy for lasing is about 12 mJ per pulse. Since the polarization of the near-IR beam is horizontal, less than 1% of the MO beam output is reflected from window (W1) and injected into the NRO. To attain single longitudinal mode (SLM) operation, it is important to

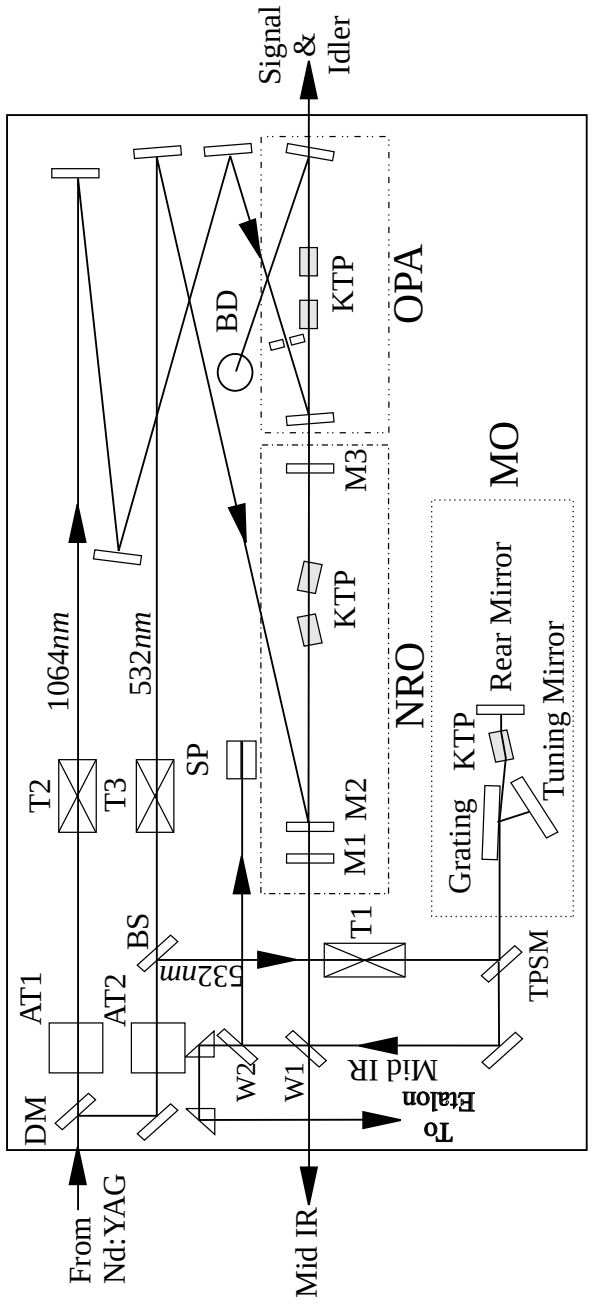

Figure 2.6: Layout of the OPO laser. DM=dichorioc mirror, AT1,AT2=attenuators, T1,T2,T3=telescopes, BS=beam splitter, W1,W2=windows, M1,M2,M3=mirrors, SP=split photodiode, TPSM=translating pump steering mirror. Dotted $(\cdots)$ box represents the MO (master oscillator). Dash-dot-dash $(-\cdot-)$ box refers to the NRO (nonresonant oscillator). Finally, dash-dot-dot-dash $(-\cdot\cdot-)$ box refers to the OPA (optical parametric oscillator).

maintain the cavity length precisely. The reflection from a second window (W2) is directed towards a split photodiode (SP) for feedback. Most of the near-IR radiation from the MO is transmitted and is sent to an etalon for monitoring single frequency operation. The NRO amplifies the signal radiation of the MO beam and generates idler photons at the difference frequency while maintaining spectral properties of the MO beam.

The NRO consists of three mirrors and a pair of KTP crystals (see dash-dot-dash ($-\cdot-$) box in Fig. 2.6), which are identical to the one in the MO. They are mounted so that their optical axes are reversed in order to compensate for the beam displacement as the crystals are angle-tuned. The three mirrors are differently coated according to their purposes: M1 is highly reflective for λ_2 and highly transmissive for λ_1, M2 is highly reflective for the 532 nm pump and transmissive for both λ_1 andλ_2, and M3 is highly transmissive for λ_2 and highly reflective for both the 532 nm pump beam and λ_1. The signal and idler (λ_1 and λ_2) exit to opposite ends of the NRO. About 65 mJ of the 532 nm pump radiation is introduced into the NRO cavity to generate about 15 mJ of the signal beam (λ_1) in the experiment. The idler beam of the NRO stage (λ_2) is sent to the last stage (OPA). It is important to note that the polarization of the signal (λ_1) is horizontal with respect to the laser bench and the polarization of the idler (λ_2) is vertical.

The OPA pumped by the Nd:YAG fundamental beam amplifies the idler output (λ_2) of the NRO which acts as the signal beam and generates a new idler beam (λ_3). The OPA consists of a pair of KTP crystals and two dichroic mirrors (see dash-dot-dot-dash ($-\cdot\cdot-$) box in Fig. 2.6). 160 mJ of the 1064 nm radiation measured after an aperture (AP) is introduced into the OPA yielding about 10 mJ of the signal and 5 mJ of the idler radiation. The polarization of the signal (λ_2) is vertical with respect to the laser bench and that of the idler (λ_3) is horizontal in this stage.

Since the first overtone transition of the NO monomer is at 3724 cm^{-1} (or 2.685 μm), from the energy conservation

$$\frac{1}{1.064\ \mu\text{m}} = \frac{1}{2.685\ \mu\text{m}(\lambda_3)} + \frac{1}{\lambda_2}$$

$$\frac{1}{532\ \text{nm}} = \frac{1}{\lambda_1} + \frac{1}{\lambda_2}$$

$\lambda_1 = 762$ nm and $\lambda_2 = 1.762$ μm are obtained. In this wavelength region of the MO, surface lasing due to normal incidence of the pump beam onto the KTP crystal which is cut at $\theta = 57°$ makes it impossible for the OPO to operate in SLM. Although the crystal is mounted slightly tilted at the factory ($\tan^{-1}(0.5/15.2) = 1.88°$ slanted) (see Fig. 2.7(a)), this off-horizontal configuration is not sufficient to enable single mode operation in this wavelength range. For the best performance of the OPO, all beams must be 50 mm above the laser bench everywhere in order for the pump beam to be parallel to the grating. In other words, the pump beam must be perpendicular to the grooves of the grating. In order to avoid normal incidence for the present experiment, the pump beam is lowered on the translating pump steering mirror (TPSM) and then directed up towards the rear mirror. The elevation is about 0.25° upward which results in an angle of 2.13° between the crystal and the pump beam path (see Fig. 2.7(b)). Figure 2.7 is a side view of the MO cavity. Part (a) is the configuration for normal horizontal alignment of the MO with the pump beam horizontal to laser bench and grating. In part (b), the pump beam is pointing up. The rear mirror is tilted so that the reflection coincides with the incoming beam. This setup avoids the surface lasing under normal incidence of the pump beam.

(3) Frequency Stabilization

For the measurement of the hot band transition, the IR laser frequency is fixed to a specific monomer line. Therefore, it is important to stabilize the OPO output to

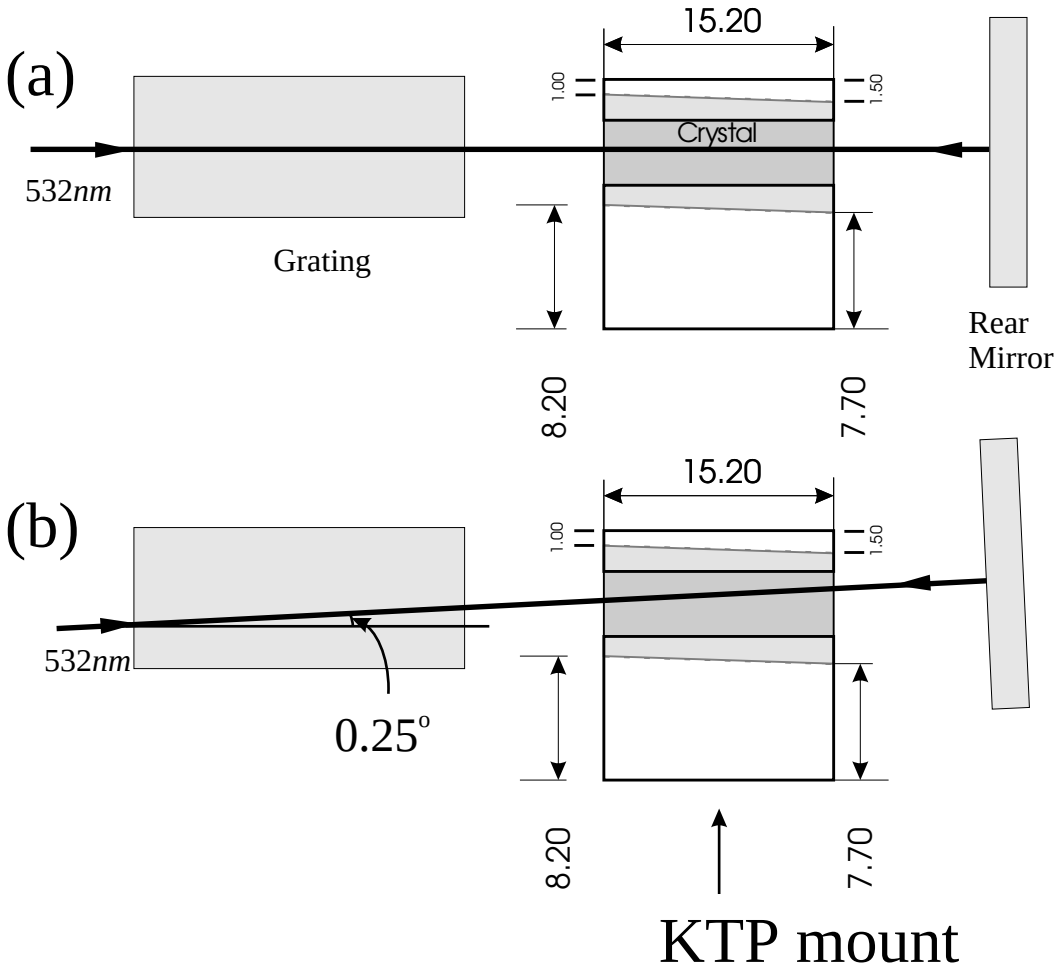

Figure 2.7: Side view of the MO cavity. The units for the dimension are millimeters (mm). The KTP mount is drawn from the actual measurement but displayed in reduced scale. The 532 nm pump beam follows the solid line and is reflected from the rear mirror. Part (a) is the configuration for the normal horizontal alignment of the MO. The crystal is slightly slanted from the factory to avoid normal incidence of the pump beam. In part (b), the pump beam is pointing up to avoid severe surface lasing. The rear mirror is tilted so that the reflection coincides with incoming beam. The angle in (b) is exaggerated for clarity.

this particular frequency. This is accomplished by a frequency stabilization feature (LASER VISION). Active frequency stabilization of the OPO is achieved by the addition of a piezoelectric element to the tuning mirror actuator for fine adjustment of the tuning mirror angle with respect to the grating [97]. Shifts in frequency are detected as drift of the fringes of an external etalon monitored with a CCD array. The voltage applied to the piezo element is changed correspondingly to correct the direction of frequency drift determined from the analysis of the etalon fringe image. Furthermore, the accuracy is enhanced by stabilizing the temperature of the external etalon.

2.2 Multiphoton Ionization Spectroscopy

To study the structure of the electronically excited state potential energy surface of van der Waals complexes (e.g. NO-Ar, NO-Ne, acetaldehyde-Ar), (2+1) resonance enhanced multiphoton ionization (REMPI) has been employed [70, 98]. In the (2+1) REMPI process the molecule undergoes two-photon excitation to a sufficiently long-lived intermediate electronic state (resonance) followed by the absorption of a third photon resulting in the ionization of the molecule (see Fig. 2.8(a)). When one-photon excitation is combined with ionization detection, the extraction of population densities from the measured intensity is complicated often by partial saturation of the resonant excitation step. Furthermore, electronic spectra of small molecules lie frequently in the vacuum ultraviolet region which is not easily accessible using commercially available laser systems. Two-photon spectroscopy is less troubled by saturation phenomena and, using commercially available laser systems, even small molecules can be detected with high sensitivity. Due to the reduced transition probability in comparison to allowed one-photon transitions, it is necessary to focus

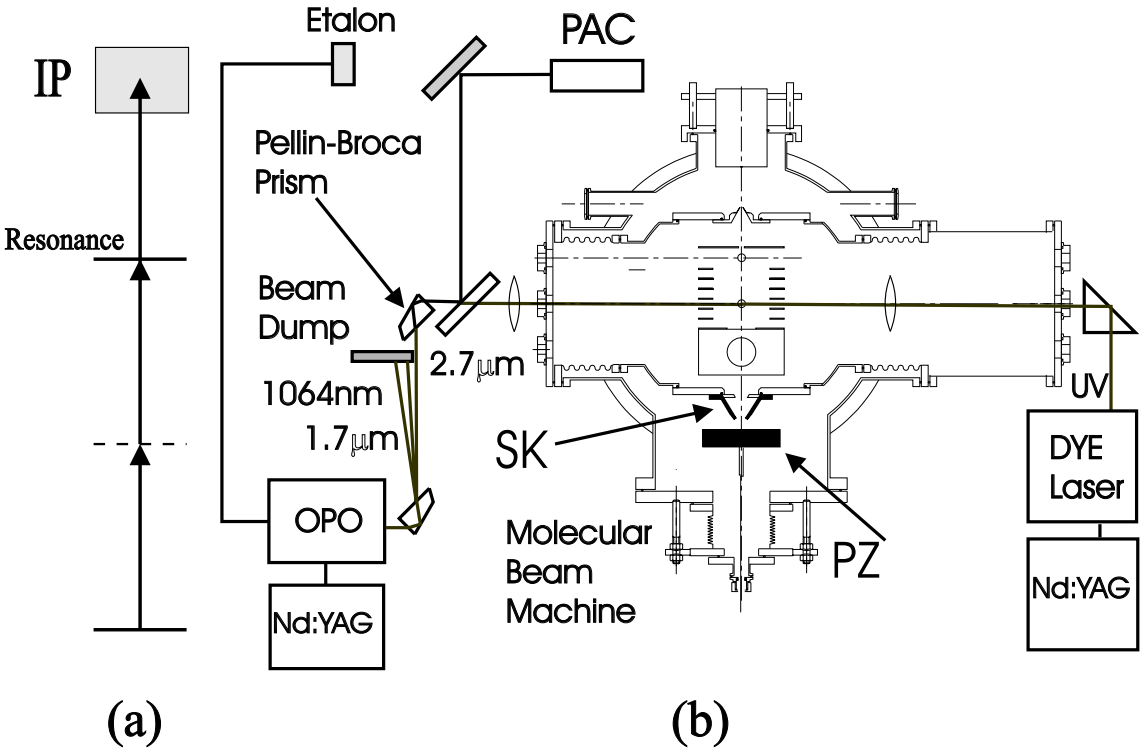

Figure 2.8: (a) (2+1) REMPI scheme. IP=ionization potential. (b) Setup for the (2+1) REMPI experiment and IR-REMPI double resonance experiment. SK=skimmer, PZ=piezoelectric valve, PAC=photoacoustic cell.

the laser beam resulting in extremely small probe volumes, typically on the order of 10^{-6} cm^3. Since the product densities in molecular beam scattering experiments are on the order of 10^6-10^{10} cm^{-3} per quantum state, only the strongest two-photon transitions realizing detection efficiencies as high as 10% can be employed. This enables us to use molecules with a strong two-photon resonance as a two-photon chromophore in a van der Waals complex. Using this technique, complexes involving NO have been studied as part of this thesis.

Figure 2.8(b) shows a schematic diagram of the molecular beam experiment. The molecular beam machine was described in Section 2.1. For a single color (2+1) REMPI excitation, a focused UV laser intersects the molecular beam at right angles

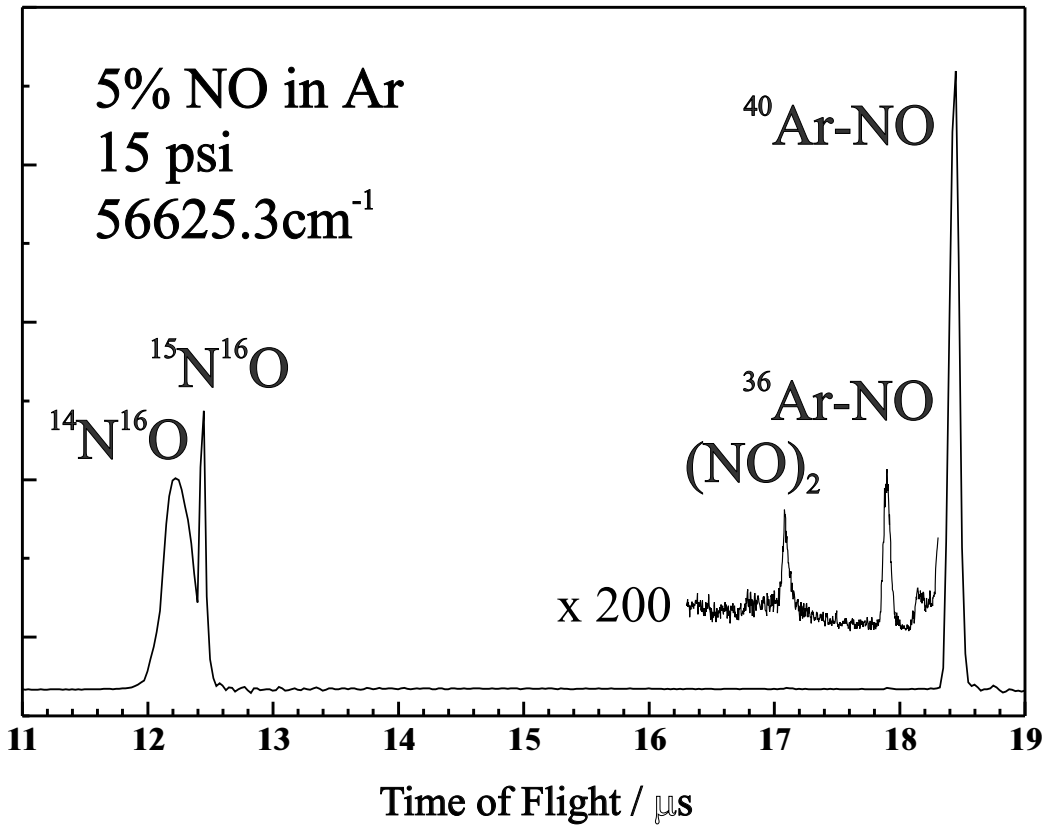

Figure 2.9: Time-of-flight mass spectrum recorded at the indicated two-photon frequency. The inset represents a spectrum taken with significantly increased sensitivity

in the acceleration region of a time-of-flight (TOF) mass spectrometer. Molecules are excited and ionized via REMPI. The resulting ions are accelerated and mass analyzed. Frequency spectra are recorded by monitoring the signal on a particular ion mass. Figure 2.9 shows a typical TOF mass spectrum measured at the indicated two-photon wavenumber. The spectrum is dominated by a sharp peak due to the complex $^{14}N^{16}O$-^{40}Ar. In the region of the expected NO monomer arrival time, two features are observed: A sharp peak due to the isotope $^{15}N^{16}O$ and a broad distribution around the flight time expected for the regular $^{14}N^{16}O$ isotope. The broad feature results from fragmentation processes of larger clusters. The inset

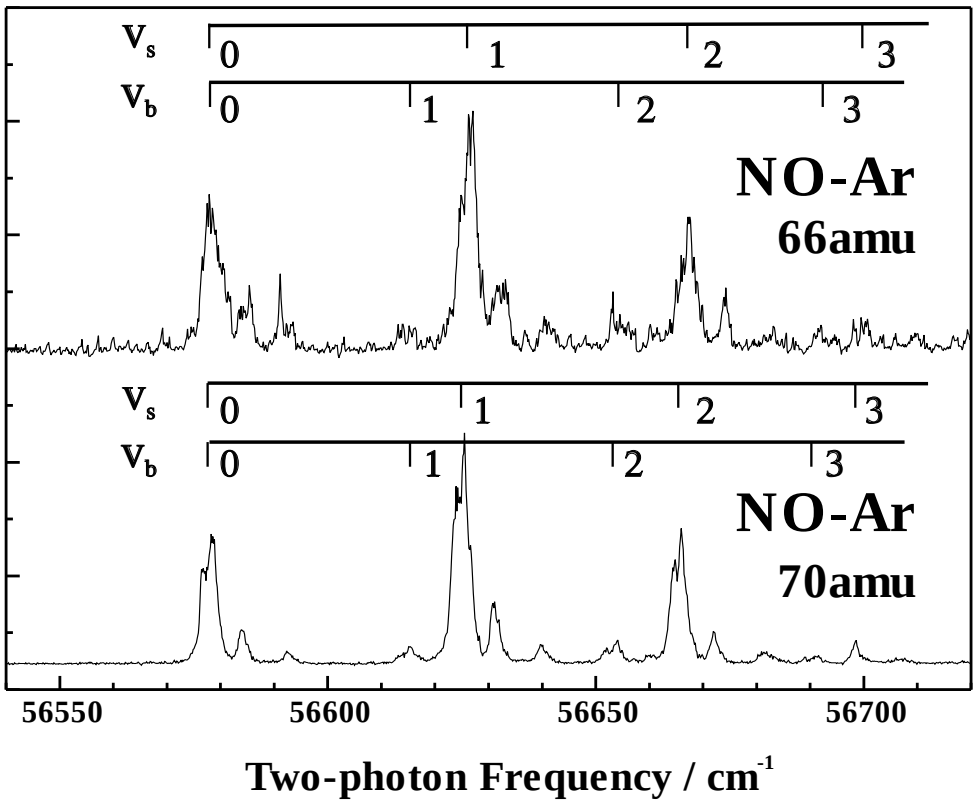

Figure 2.10: Comparison of spectra for the NO-Ar complex recorded on mass 66 amu and 70 amu in the wavelength region of the $\tilde{C}\,^2\Pi(v' = 2) - \tilde{X}\,^2\Pi(v'' = 0)$ transition.

shows a mass spectrum recorded with significantly increased sensitivity. Small signals are attributed to the isotope ^{14}N^{16}O-^{36}Ar and the NO dimer. While the dimer spectrum does not show a frequency dependence, a typical NO-Ar $\tilde{C}\,^2\Pi(v' = 2)$ state spectrum is measured for the NO-^{36}Ar isotope. The comparison of the spectra for the complexes involving the two different isotopes of Ar is shown in Fig. 2.10. Both spectra are dominated by a progression in the intermolecular stretching vibration labeled v_s. On the low frequency side of the stretching progression, there is a progression in the bending vibration denoted v_b. The overall structure is almost identical except for a small increase in the stretching frequency due to the isotope

effect. Considering the fact that the natural abundance of ^{36}Ar is only 0.36%, the spectrum recorded for the isotopic complex demonstrates the extreme sensitivity of the applied REMPI detection process.

2.3 Infrared-Ultraviolet Double Resonance Spectroscopy: I. The NO monomer

In order to excite the first overtone transition of NO containing complexes, the IR laser is used. In comparison with fundamental vibrational transitions, the intensity of an overtone band is decreased by up to two orders of magnitude. Unlike a closed shell molecule like HCl, the intensity per rotational line in NO($X\,^2\Pi$) is reduced even further because of the large number of rotational states due to the smaller rotational constant and its open shell nature. With the IR laser alone, the transition cannot be detected since the molecules cannot reach their ionization limit. In this case, the IR absorption is detected via a (2+1) REMPI process with an accompanying UV laser. In this IR-UV double resonance experiment, the UV laser acts like an IR absorption detector. In this project, two variations of the double resonance experiment have been performed. In a depletion experiment, the UV laser probes a ground state level while the IR laser is scanned over an IR resonance. IR photons are absorbed by the molecule depleting the UV signal. In a second type of experiment, a positive signal is detected by the UV laser tuned to a hot band transition. When the lifetime of the vibrational state is long enough, the UV laser probes the vibrationally excited molecules promoting them to the excited electronic state. To compensate for the small absorption cross section of the first overtone transition and to detect the IR absorption efficiently, both laser beams are focused onto the molecular beam inside the vacuum chamber rendering their alignment very difficult. In addition to these

problems, the Nd:YAG laser system itself needs to be aligned, occasionally. After each Nd:YAG alignment, the three stages of the OPO must be aligned as well. As a consequence, all following optics including two Pellin-Broca prisms and the diode laser need to be realigned. Besides the temporal and the spatial alignment, both lasers must be tuned to the correct frequencies in order to find a double resonance signal.

The feasibility of this type of experiment is tested by measuring a double resonance spectrum for the NO monomer prior to an experiment with the NO-X (X=Ar, Ne) complexes. Once the NO monomer double resonance signal is found, this signal becomes an effective reference for the spatial and temporal alignment. Due to the complicated alignment procedure, the verification of the optimum alignment is crucial before searching for a resonance for the NO-X complexes. In verifying the alignment via a double resonance signal of the NO monomer, the following procedure is adopted to minimize the number of unknown parameters at each step.

1. Photoacoustic Spectroscopy

   In this experiment, a room temperature photoacoustic spectrum of the NO monomer provides information on resonance frequencies for the IR absorption.

2. Discharge Source

   With the help of a molecular beam discharge source, the UV frequencies for probing vibrationally excited monomers are determined.

3. REMPI Cell Experiment

   The first double resonance signal is recorded with the help of a REMPI cell. In this case, the spatial and temporal alignment is achieved in a straightforward manner. These spectra confirm the UV frequencies for the hot band transitions.

4. Molecular Beam Experiment

   With the IR and UV frequencies found from the previous steps, the spatial and temporal alignment can be verified before searching for a signal due to the NO-X complexes.

For a better understanding of the procedure, each step is described in detail in the following subsections.

2.3.1 Photoacoustic Spectroscopy

This sensitive technique for measuring small absorptions is mainly applied when minute concentrations of molecular species have to be detected in the presence of other components at higher pressure. If the laser is tuned to the absorbing molecular transition $E_i \rightarrow E_k$, a fraction of the molecules in the lower level E_i will be excited into the upper level E_k. In collisions with other molecules in the cell, these excited molecules may transfer their excitation energy completely or partly into translational, rotational, or vibrational energy of the collision partners, causing a local increase of temperature and pressure [92].

This temperature change results in a pressure change which is detected with a sensitive microphone placed inside the cell. Therefore, the output signal of the microphone is proportional to the pressure change induced by the absorbed radiation power. The signal decreases with increasing quantum efficiency for radiative relaxation . Since the quantum efficiency is determined by the ratio of spontaneous to collision-induced deactivation of the excited level, it decreases with increasing spontaneous lifetime and gas pressure. Therefore, the photoacoustic method is particularly favorable to monitor vibrational spectra of molecules in the infrared region

(because of the long lifetimes of excited vibrational levels) and to detect small concentrations of molecules in the presence of other gases at higher pressures (because of the large collisional deactivation rate). With IR lasers, the molecules are generally excited into higher vibrational levels of the electronic ground state. It is even possible to use this technique for measuring rotational spectra in the microwave region and also electronic molecular spectra in the visible or ultraviolet range although the sensitivity in these spectral regions is not quite as high and there are other superior methods. Laser light reflected from the cell windows or scattered by aerosols in the cell may partially be absorbed by the walls contributing to the temperature increase. The resulting pressure is modulating at the laser repetition frequency and is therefore detected as background signal. Anti-reflection coatings on the cell windows or a wedged window may reduce this background.

The photoacoustic cell used in the experiment is equipped with an electret microphone (PANASONIC P9970-ND). Signals from the microphone are amplified with an operational amplifier (op-amp). The circuit diagram of the microphone and the op-amp is shown in Fig. 2.11. One of the windows of the photoacoustic cell is a plane window made of CaF_2 to ensure IR transmission. The other window is a wedge to avoid the modulation described above. The cell is filled with $50mbar$ of NO. The portion of the idler IR output ($\sim$ 2.7 μm) of the OPO reflected from a wedge (CaF_2) is sent through the cell. The experimental arrangement is shown in Fig. 2.12. Etalon fringes for the signal output of the NRO are recorded for frequency calibration. An overview spectrum of the first overtone region of NO is displayed in Fig. 2.13. The top part shows a room temperature photoacoustic spectrum while the bottom part represents a calculated spectrum using the constants (Table 2.1) from Amiot *et al.* with an effective linewidth of about 1 GHz [99]. Since the spin-orbit splitting for the ground state is about 123 cm^{-1}, at room temperature both spin-orbit components (F_1 and F_2 with F_1 having lower energy) are populated.

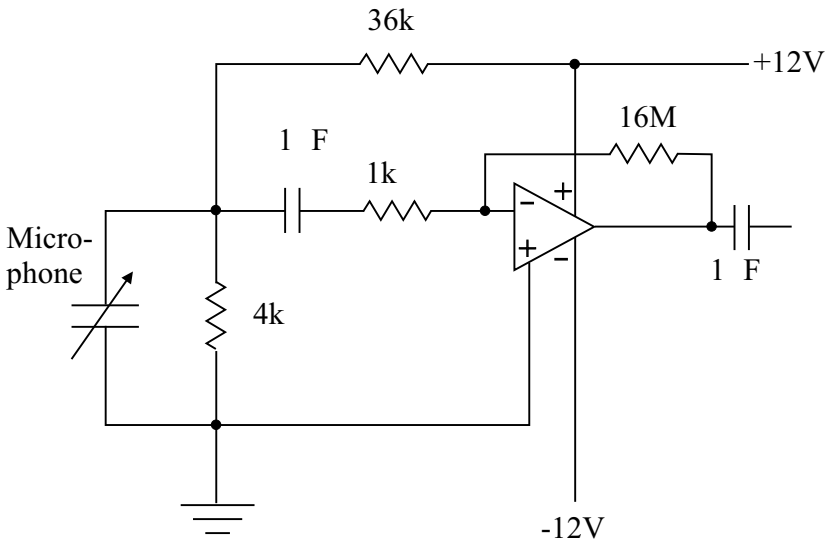

Figure 2.11: Circuit diagram for the microphone and the operational amplifier(op-amp).

The ratio of the population of the F_2 component to that of the F_1 component is approximately 0.5 ($\exp(-\Delta E/kT) = \exp(-123\ \mathrm{cm}^{-1}/\ 203\ \mathrm{cm}^{-1}) \simeq 0.5$). The spectrum which shows doublets in P- and R-branches with the intensity ratio of 0.5 confirms the ratio of the population estimates. Since the resolution of the OPO linewidth is limited by pressure broadening, the λ-doubling (this will be discussed theoretically later in Chapter 3) is only resolved for lines of the Q_{11} branch (Fig.

Table 2.1: Molecular constants (in cm^{-1}) of NO for $v = 0$ and $v = 2$ level from Ref. [99]. A_v : spin-orbit constant, B_v : rotational constant.

	$v = 0$	$v = 2$
ν_0	0	3723.85256
A_v	123.13361	122.63486
B_v	1.6961483	1.6609632

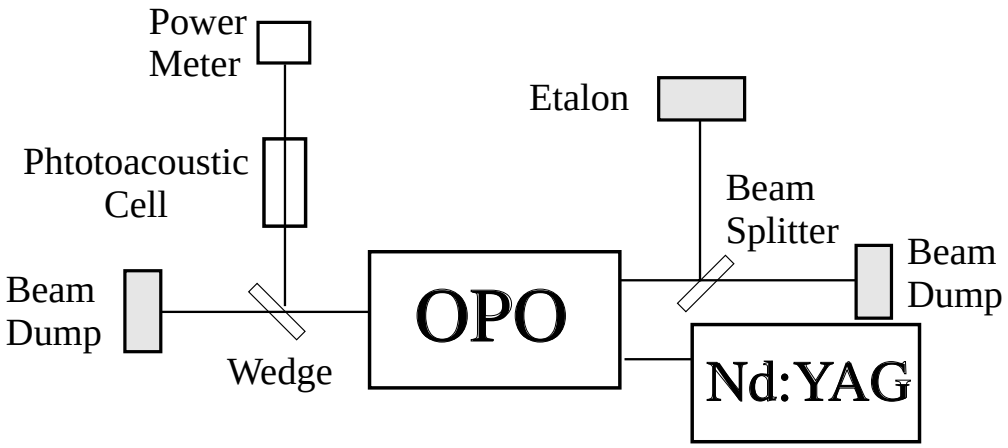

Figure 2.12: Setup for the photoacoustic cell experiment.

2.14) when the scanning speed of the OPO is slow (0.00018 nm/s in Fig. 2.14 vs. 0.0018 nm/s in Fig. 2.13). As will be discussed in Section 3.1, the selection rule for e/f levels is $e \leftrightarrow f$ for Q-branches and $e(f) \leftrightarrow e(f)$ for P- and R-branches. Therefore, the spacing of λ-doublets is larger in the Q-branch than in the P- and R-branches, especially for high j values (j is the total angular momentum of the NO monomer). P- and R-branch lines are composed of unresolved doublets with a typical spacing of 300 MHz. The observed linewidth of 1 GHz well exceeds the Doppler linewidth of 250 MHz. This indicates that the observed lines are actually unresolved doublets. In the bottom part of Fig. 2.15, two center sticks with identical intensity are separated by 0.01 cm^{-1}. For reference, two additional sticks are located at ± 0.3 cm^{-1}. The top part shows the spectrum convoluted with a linewidth of a 400 MHz Lorentzian component and a 250 MHz Gaussian component. Figure 2.15 shows how two sticks with equal intensity separated by 0.01 cm^{-1} result in two unresolved lines. The confirmation of the existence of two unresolved lines can also be seen in the UV spectrum where the detection process is λ doublets specific (Fig. 2.16). The $R_{11}(\frac{1}{2})$

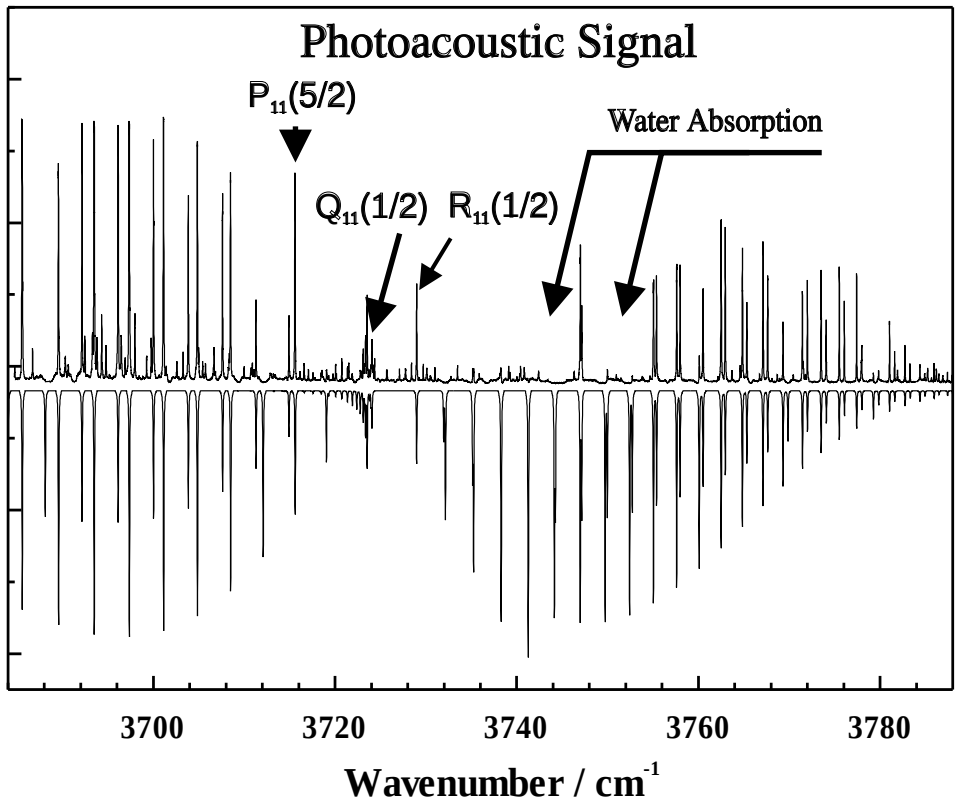

Figure 2.13: Photoacoustic spectrum of the first overtone band in NO. The marked IR transitions are used in different double resonance schemes. The top spectrum is recorded in the cell and the bottom spectrum is calculated using the constants from Ref. [99]. The spectrum is recorded without purging the laser beam path with N_2. The scanning speed is 0.0018 nm/s.

observed under molecular beam conditions is found to be displaced slightly from the center of the corresponding photoacoustic lines.

In the region of the first overtone transition of NO, there is strong absorption due to water vapor in the air. The missing lines in the measured spectrum in Fig. 2.13 are due to water absorption. This is consistent with the fact that the laser power drops dramatically when it is measured just before the photoacoustic cell. These problems are avoided by purging the entire beam path and the OPO system with dry

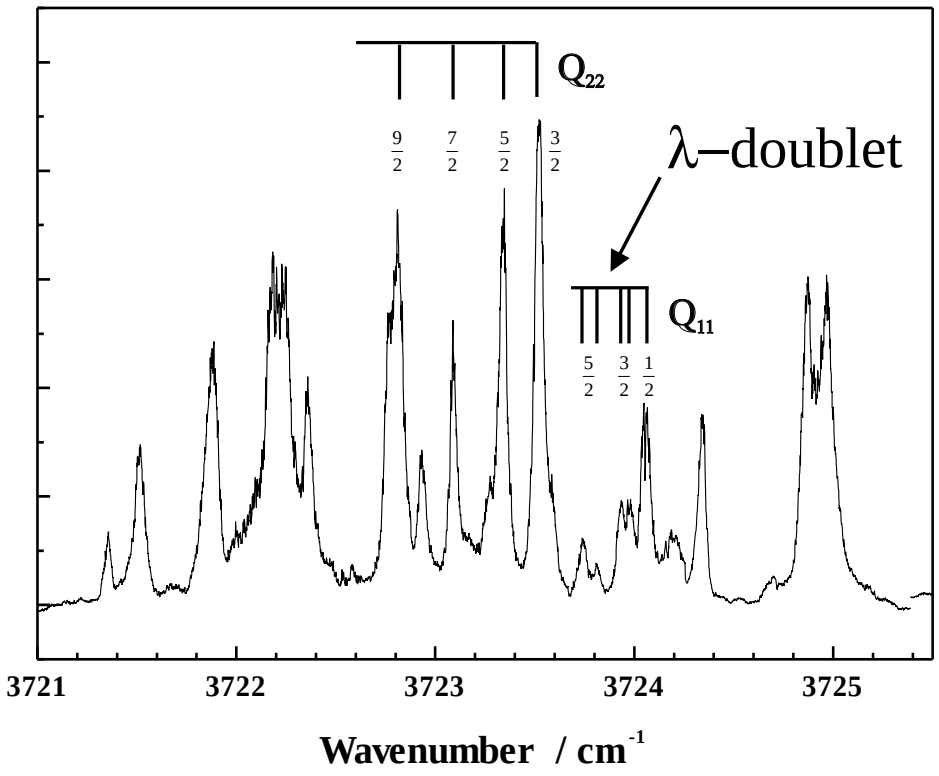

Figure 2.14: Photoacoustic spectrum recorded with a reduced scanning speed of 0.00018 nm/s. The Q_{11} branch lines with $j = \frac{3}{2}$ and $j = \frac{5}{2}$ show λ-doublets. Lines not assigned are due to water impurities in the photoacoustic cell.

N_2. In the experimental spectrum, weak lines which do not appear in the calculated spectrum of Fig. 2.13 are due to a small water impurity in the photoacoustic cell. In Fig. 2.17, trace (b) shows a spectrum after several hours of purging. The purging process recovers lines which are not detected in part (a) which is measured without purging. On the other hand, the increased laser power results in even stronger water signals (marked with asterisks). The photoacoustic spectrum and the well matched simulated spectrum confirm the assignments of the various lines. In this way the photoacoustic spectrum not only provides the IR frequency for the double

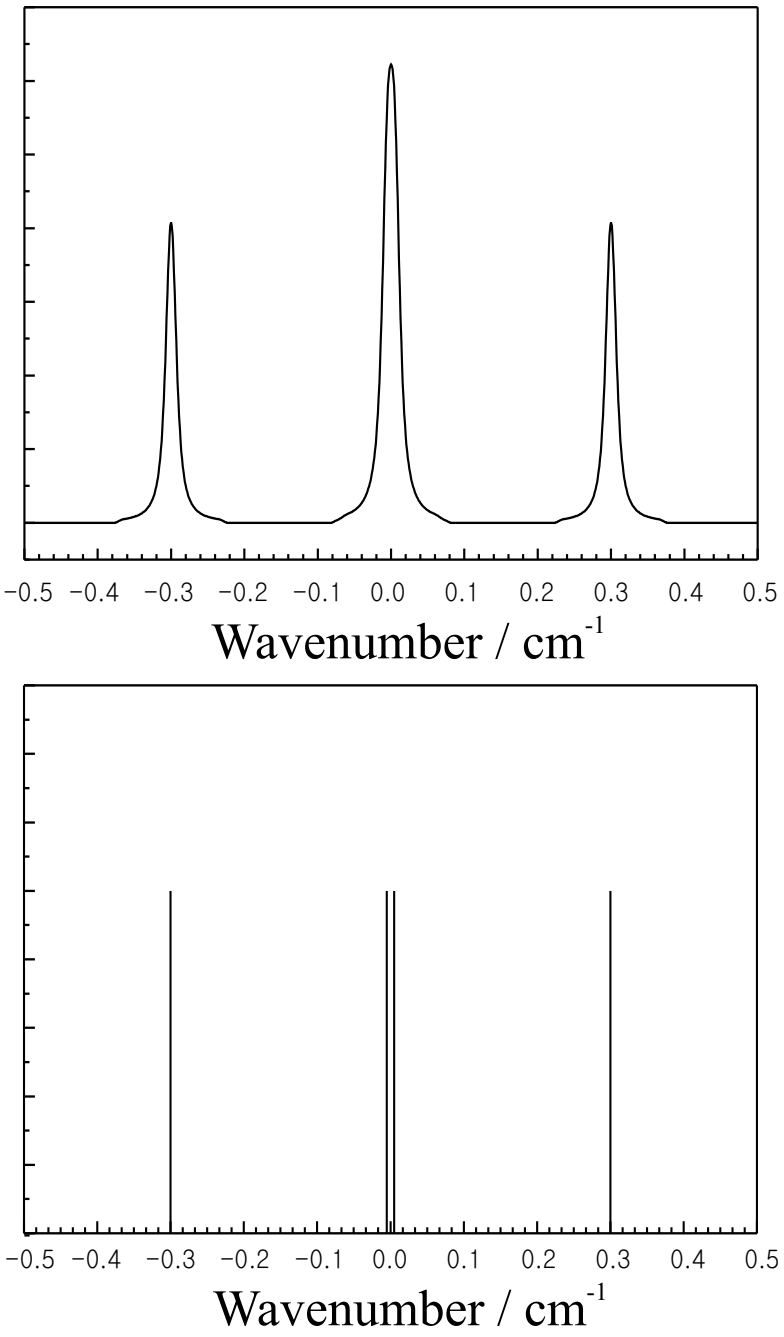

Figure 2.15: Illustration of two unresolved lines by convoluting a stick spectrum. In the bottom inset, the center sticks with identical intensity are separated by 0.01 cm^{-1}. For reference, two additional sticks are located at ± 0.3 cm^{-1}. The top part shows the convoluted spectrum with a linewidth of a 400 MHz Lorentzian component and a 250 MHz Gaussian component.

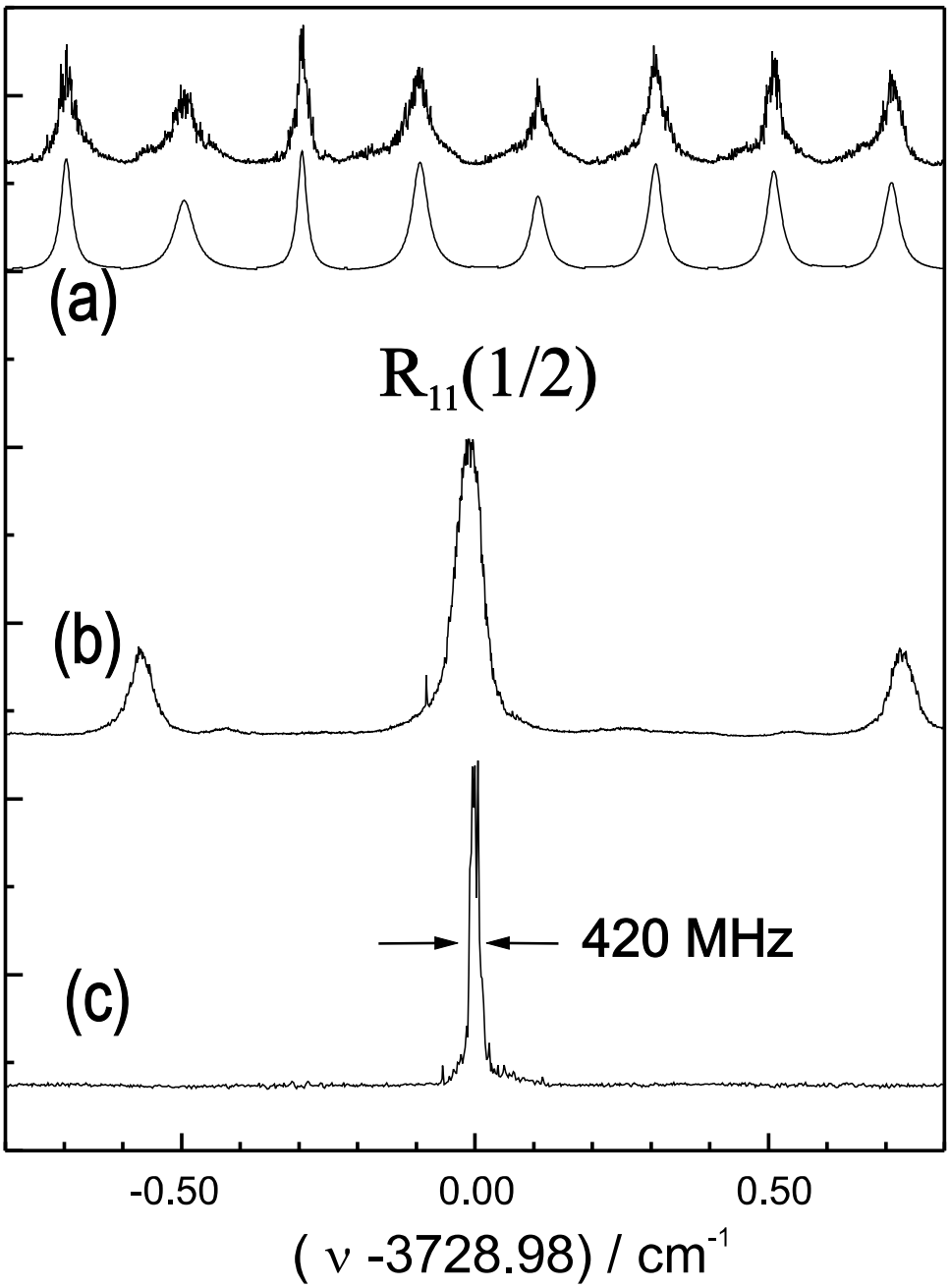

Figure 2.16: Double resonance spectrum of NO recorded under molecular beam conditions. The IR laser is scanned over the $R_{11}(\frac{1}{2})$ line while the UV laser is fixed to the line $Q_{21d}(\frac{3}{2})$ of the $H - X$ hot band transition. Trace (a) shows etalon fringes (top:measured, bottom:calculated), trace (b) and trace (c) display spectra measured under molecular beam condition with and without focusing the IR laser beam, respectively. The latter shows an effective linewidth (FWHM) of 420 MHz. See page 56.

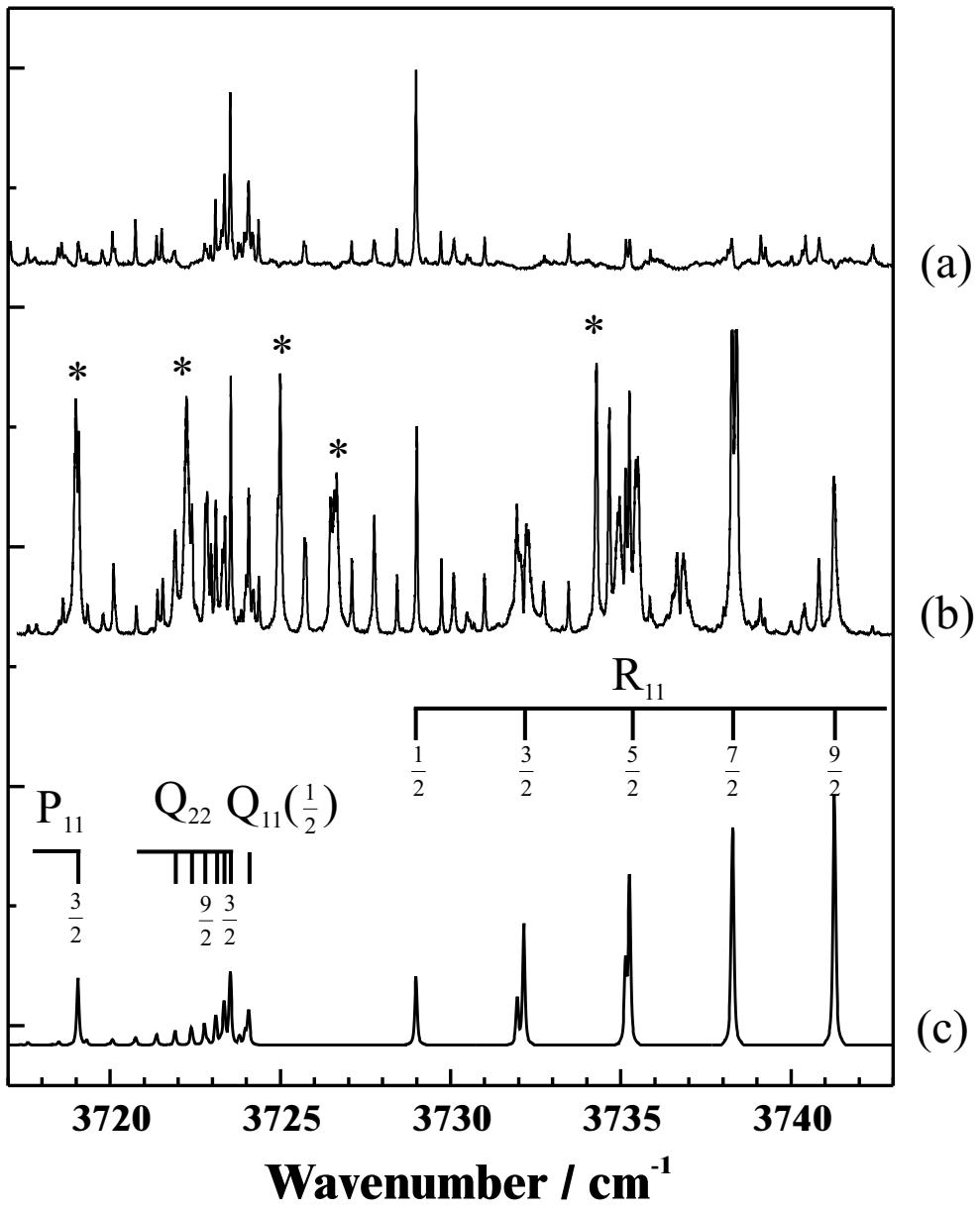

Figure 2.17: Photoacoustic spectra of NO without (a) and with (b) purging with N_2. Trace (c) is calculated using the constants of Ref. [99]. Rotational lines are labeled with $(j - \frac{1}{2})$.

resonance experiment but also serves as a fingerprint for the specific region in the IR.

Frequency Calibration

Due to mechanical imperfections of several motors and the piezo-driven stage of the OPO, the frequency readouts from the OPO are not accurate and the scan speed of the OPO is not constant. In order to measure accurate frequencies, the readouts must be calibrated. In doing so, it is important to record etalon fringes and a photoacoustic signal as well as the frequencies of the OPO output. A photoacoustic signal is used to provide absolute frequencies while etalon fringes are used to produce accurate relative frequencies. The latter requires the accurate measurement of the free spectral range (FSR) of the etalon (see Fig. 2.16(a)). A photoacoustic spectrum was recorded from 3685 cm^{-1} to 3778 cm^{-1} together with etalon fringes. Table 2.2 shows the data used for finding the FSR. Lines of the photoacoustic spectrum are assigned to those from the literature [99] (see the first column of Table 2.2). Setting $Q_{11}(\frac{1}{2})$ at 3724.06693 cm^{-1} as a reference, the number of etalon fringes corresponding to each photoacoustic line is counted from $Q_{11}(\frac{1}{2})$ up to the second decimal point (the second column). The third column represents the frequency relative to the $Q_{11}(\frac{1}{2})$ line.

The FSR of the etalon was determined by a least squares fitting method which minimizes the quantity

$$\sum_i p_i \big[n_i \Delta + b - \nu_i \big]. \tag{2.32}$$

Here, p_i is a weight, n_i is the number of etalon fringes relative to $Q_{11}(\frac{1}{2})$, Δ is the FSR, b is an offset and ν_i is the relative frequency with respect to $Q_{11}(\frac{1}{2})$. To minimize the above quantity, Eq. (2.32) is differentiated with respect to Δ and b,

Table 2.2: Data table for finding the FSR. Assigned lines are calculated using the constants from Ref. [99]. n_i=number of etalons, ν_i=relative frequencies from $Q_{11}(\frac{1}{2})$ line, p_i=weights.

Assigned line	n_i	ν_i	$\lvert n_i \rvert$	p_i
3685.56307	-191.66	-38.50386	191.66	0.03417
3689.55825	-171.87	-34.50868	171.87	0.03064
3692.14795	-158.90	-31.91898	158.90	0.02833
3693.48484	-152.21	-30.58209	152.21	0.02714
3696.12122	-139.10	-27.94571	139.10	0.02480
3700.02432	-119.69	-24.04261	119.69	0.02134
3701.13224	-114.26	-22.93469	114.26	0.02037
3703.85696	-100.62	-20.20997	100.62	0.01794
3704.85308	-95.68	-19.21385	95.68	0.01706
3707.61889	-81.93	-16.44804	81.93	0.01461
3708.50536	-77.55	-15.56157	77.55	0.01383
3711.30985	-63.59	-12.75708	63.59	0.01134
3714.92955	-45.53	-9.13738	45.53	0.00812
3715.60434	-42.15	-8.46259	42.15	0.00752
3723.53005	-2.65	-0.53688	2.65	0.00047
3724.06693	0	0	0	0
3728.98004	24.48	4.91311	24.48	0.00436
3755.05885	154.30	30.99192	154.30	0.02751
3755.38959	155.90	31.32266	155.90	0.02781
3757.61142	166.98	33.54449	166.98	0.02977
3757.98714	168.84	33.92021	168.84	0.03010
3760.51032	181.42	36.44339	181.42	0.03235
3762.50798	191.34	38.44105	191.34	0.03412
3762.95903	193.59	38.89210	193.59	0.03452
3764.85164	203.00	40.78471	203.00	0.03619
3765.33312	205.38	41.26619	205.38	0.03662
3767.12528	214.24	43.05835	214.24	0.03820
3767.63250	216.75	43.56557	216.75	0.03864
3769.32874	225.21	45.26181	225.21	0.04015
3771.46180	235.83	47.39487	235.83	0.04205
3772.00675	238.58	47.93982	238.58	0.04254
3773.52427	246.10	49.45734	246.10	0.04388
3774.08143	248.84	50.01450	248.84	0.04437
3775.51593	256.00	51.44900	256.00	0.04564
3776.08103	258.82	52.01410	258.82	0.04615
3777.43656	265.56	53.36963	265.56	0.04735

yielding the two equations:

$$\begin{aligned} \Big[\sum_i p_i n_i^2\Big]\,\Delta + \Big[\sum_i p_i n_i\Big]\,b &= \sum_i p_i \nu_i n_i \\ \Big[\sum_i p_i n_i\Big]\,\Delta + \Big[\sum_i p_i\Big]\,b &= \sum_i p_i \nu_i . \end{aligned} \tag{2.33}$$

After solving for Δ, the FSR was found to be 0.200917 cm^{-1}.

A computer program was developed to determine relative frequencies of the etalon fringes based on the measured value of the FSR. With this program the relative frequency scale for the measured spectra is determined by linear interpolation between adjacent etalon fringes. This is shown in trace (a) of Fig. 2.16. The top line within trace (a) represents the measured etalon fringes and the bottom spectrum represents the calculated fringes using the program. With this method, the spectra are reproducible within 0.015 cm^{-1} which is comparable to the effective resolution of the OPO. Absolute frequencies are determined from the known resonances in the photoacoustic spectrum of the NO monomer [99].

2.3.2 Discharge Source

The first attempt to find the UV frequencies for various hot band transitions in NO under molecular beam conditions was performed in a newly designed molecular beam apparatus in which a discharge molecular beam source is operated [100]. The discharge source generates vibrationally excited *but* rotationally cold species of molecules. As an example, Fig. 2.18 shows the REMPI spectrum recorded in the wavelength region for the hot band transitions $E - X(v'' = 1)$ and $H - X(v'' = 2)$. Since the discharge source generates vibrationally excited species, it makes it possible to find the UV frequencies for the hot band transition without using the IR laser. In this case, parameters such as the spatial alignment, the temporal alignment and IR frequency are not critical.

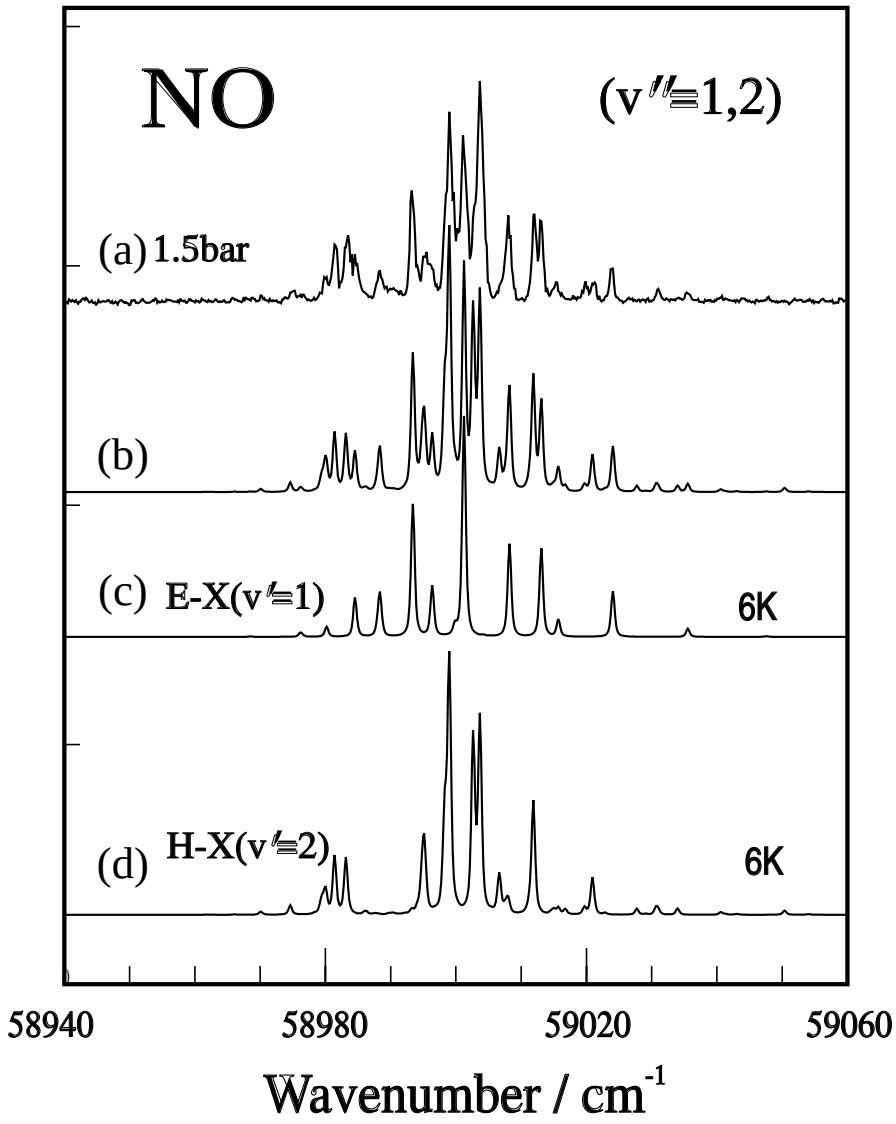

Figure 2.18: REMPI spectra from the discharge source. Trace (a) is a measured spectrum with a backing pressure of 1.5 bar. Trace (c) and (d) are calculated spectra of $E - X(v'' = 1)$ and $H - X(v'' = 2)$, respectively. Trace (b) is the superposition of (c) and (d) with a population ratio of $[\mathrm{NO}(v'' = 2)]/[\mathrm{NO}(v'' = 1) = 0.5]$.

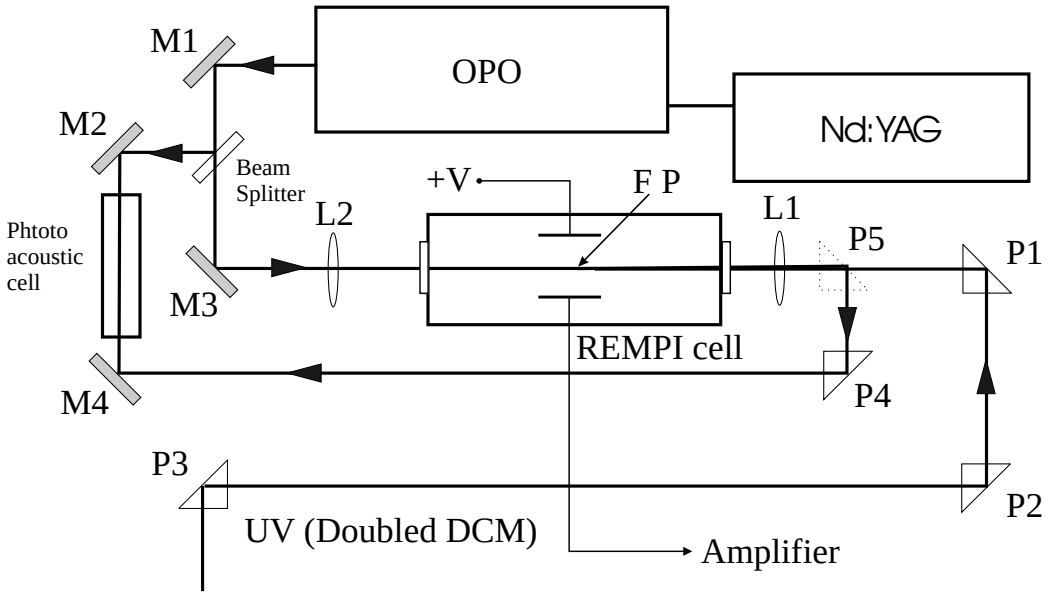

Figure 2.19: Setup of the REMPI cell experiment. M1-M4: gold mirrors, P1-P3: infrasil prisms, P4,P5: CaF_2 prisms. L1: 300mm focal length CaF_2 lens, L2: 300 mm focal length quartz lens, FP=focal point. When aligning the two counterpropagating laser beams, a pin hole is placed in place of the REMPI cell.

2.3.3 REMPI Cell Experiment

Once IR and UV frequencies for the double resonance experiment are determined, the first double resonance experiment is performed using a REMPI cell. A schematic of the REMPI cell experiment is shown in Fig. 2.19. Inside the REMPI cell, two electrodes are mounted: one for detecting ions and the other for applying a positive voltage. The resulting electric field accelerates the ions toward the detection electrode. The REMPI cell is filled with 0.1 mbar of NO. As typical voltages, 20 V - 70 V are applied to the electrode. In order to steer the IR beam,

gold mirrors (EDMUND SCIENTIFIC) are used. A lens made of CaF_2 is used for focusing the IR beam. For spatial overlap of two counterpropagating laser beams, a pinhole burned into a razor blade with the focused laser beam is prepared. The pinhole is placed at the focal point of the two counterpropagating laser beams. The UV laser focused with a 300 mm lens is aligned so that it passes through the pinhole. The counterpropagating IR laser beam is focused with a 300 mm lens (CaF_2) and aligned through the same hole. The final OPO output consists of four different frequencies: the signal (1.7 μm), the idler (2.7 μm), the residual 532 nm beam, and the residual 1.064 μm beam. For rough alignment of the IR laser beam, the residual 532 nm beam was used. Due to the imperfect alignment of the OPO amplifier stage (in other words, the phase-mismatch ($\Delta \boldsymbol{k}$) is not equal to zero in Eq. (2.3)), the four different beams are not collinear. Therefore, it is important to verify that the idler beam goes through the pinhole. For this verification, prism P5 is placed between lens L1 and prism P1 so that the IR beam which passes through the pinhole can be directed to the photoacoustic cell. A photoacoustic signal on the oscilloscope screen is optimized by adjusting the mirror M3. In this way, the spatial alignment is verified. Although the lifetime of the vibrationally excited NO is sufficiently long, it is important that the UV laser beam excites vibrationally excited molecules before they move out of the focal region of the UV laser beam. By using $v_{rms} = \sqrt{\frac{2kT}{m}} \simeq 400$ m/s and the size of the two laser beam spots ($\simeq 30$ μm), it is estimated that the delay between the two lasers must be at least within 75 ns ($= 30 \times 10^{-6}$ m $\div$ 400 m/s). The optimum delay is around 10 ns. The temporal alignment is verified using two fast photodiodes with the same length BNC cables. By monitoring the photodiode signals on the oscilloscope, the delay between the two pulsed lasers is adjusted with two delay generators (STANFORD RESEARCH SYSTEMS DG535), each of which triggers one Nd:YAG laser. After the temporal and spatial alignment is optimized, the pinhole is removed and the REMPI cell is placed

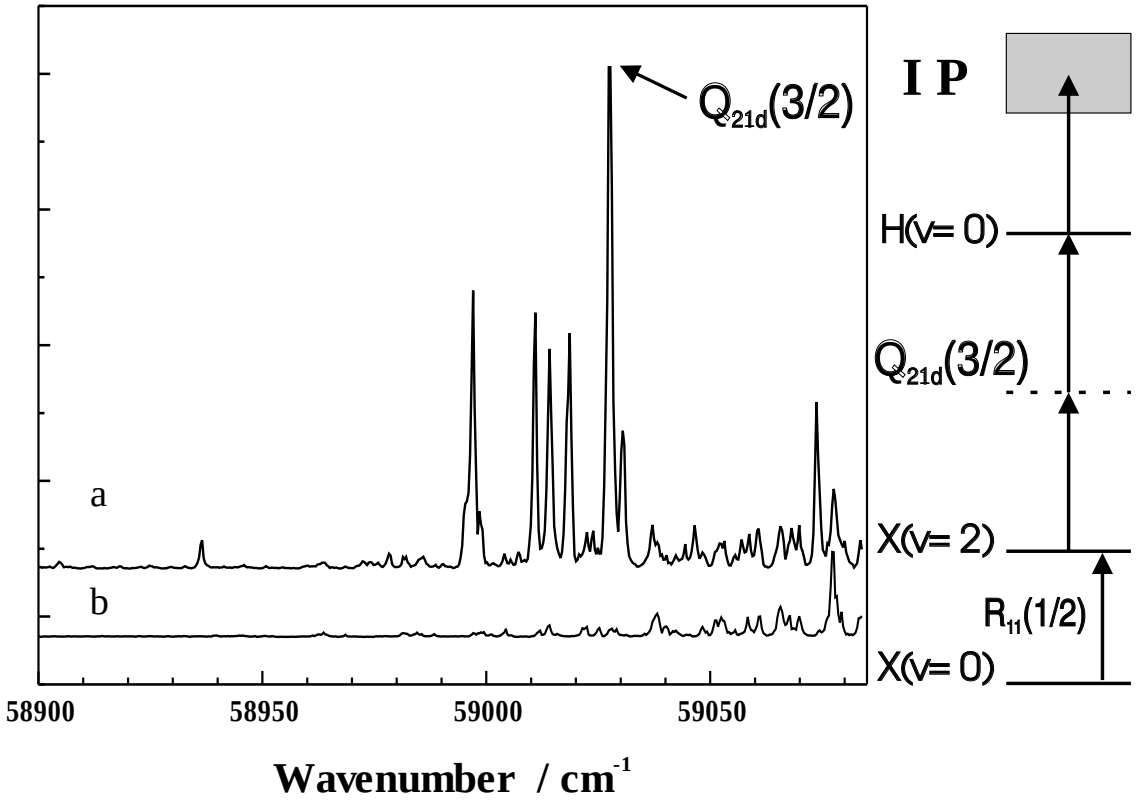

Figure 2.20: Double resonance spectrum under cell conditions (top). The bottom spectrum is a background spectrum taken without the IR laser beam. While the IR laser frequency is fixed to the $v' = 2$ $R_{11}(\frac{1}{2})$ line, the UV laser is scanned over the hot band region of the $H - X$ transition.

so that the two laser beams are focused in the detection region inside the REMPI cell. To measure the double resonance spectrum, the IR frequency is fixed to the first overtone transition while the UV probe laser is scanned over the appropriate hot band region in search of a positive double resonance signal. In Fig. 2.20, the UV laser is scanned over the hot band region of the $H\,^2\Pi - X\,^2\Pi$ transition while the IR frequency is fixed to the $R_{11}(\frac{1}{2})$ transition. The top spectrum is the double resonance signal whereas the bottom spectrum is the background signal without the

IR laser beam confirming that the signal results from the double resonance scheme.

2.3.4 Molecular Beam Experiment

The next step is to perform the double resonance experiment under molecular beam conditions. For the double resonance experiment, two counterpropagating laser beams are focused onto the molecular beam. While the temporal alignment is easily optimized using two fast photodiodes, the spatial overlap of the two laser spots inside the vacuum chamber is a difficult task. From the photoacoustic cell and the discharge experiments, the correct IR and UV frequencies for the double resonance experiment are obtained. For directing the IR beam into the molecular beam machine, the residual green (532 nm) is used (later, the spatial alignment of the IR beam is aided by the output of a red laser diode). Gold mirrors are used to direct the IR beam. Other optical components like lenses and windows are made of CaF_2. In the double resonance experiment, the counterpropagating UV beam exiting the molecular beam machine is likely to be focused onto one of the gold mirrors causing damage. To avoid burning mirrors, one of the two beams is sent slightly displaced from the collinear axis. In this way, the UV beam can be blocked mechanically before reaching any gold mirror and without obstructing the IR beam.

To see if the idea of separating the two beams is possible, an algebraic calculation was done using simple thin-lens equations. As shown in Fig. 2.21, the IR beam is travelling from the right to the left along the lens-axis which connects the centers of both lenses that are separated by $f_1^{UV} + f_2^{IR}$. Here, f_1^{UV}, f_2^{UV}, and f_2^{IR} denote the focal length of lens $L1$ for the UV, the focal length of lens 2 ($L2$) for the UV, and the focal length of lens $L2$ for the IR, respectively. Then, from the left the UV beam enters lens $L1$ at height h_1 parallel to the lens-axis. The beam is focused on the UV focal point P of $L1$, making an angle θ between the lens-axis and the UV

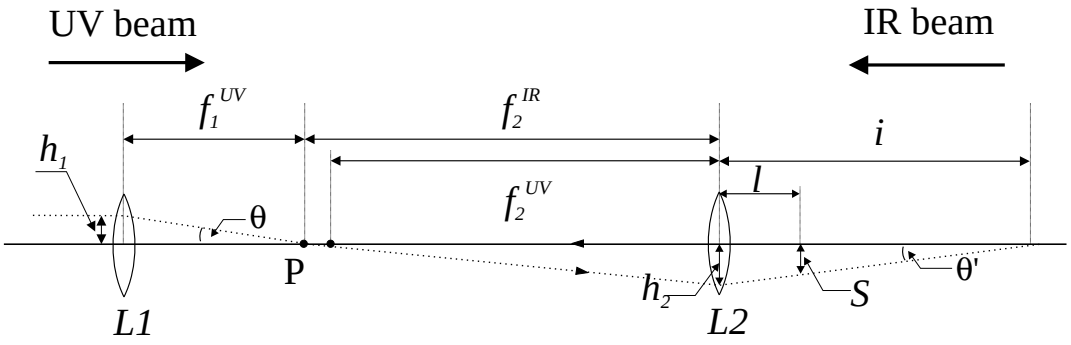

Figure 2.21: Configuration of lenses. The IR beam(solid line) follows the lens-axis from the right to the left. The UV beam follows the dotted line from the left to the right. f_1^{UV}: focal length of lens $L1$ for the UV, f_2^{UV}: focal length of lens $L2$ for the UV, f_2^{IR}: focal length of lens $L2$ for the UV, P: focal point of both laser beams, S: separation.

beam path. The relationship

$$h_1 = f_1^{UV}\theta.$$

holds if θ is sufficiently small. The focal point P becomes the object for the second lens($L2$). The position of the image will be determined by solving the thin-lens equation:

$$\frac{1}{f_2^{IR}} + \frac{1}{i} = \frac{1}{f_2^{UV}},$$
$$\Longrightarrow \quad i = \frac{f_2^{UV} f_2^{IR}}{f_2^{IR} - f_2^{UV}}\ . \tag{2.34}$$

The UV beam passes $L2$ slightly low (h_2) with an angle θ'. If θ' is the angle between the lens-axis and the UV beam path after $L2$, then from

$$h_2 = f_2^{IR}\theta = i\theta' = \frac{f_2^{UV} f_2^{IR}}{f_2^{IR} - f_2^{UV}}\ \theta'$$

θ' becomes

$$\theta' = \frac{f_2^{IR} - f_2^{UV}}{f_2^{UV}}\ \theta. \tag{2.35}$$

If the beam block is placed at a distance l from $L2$, the separation S between the IR and the UV beam will be

$$\begin{aligned} S &= \theta' \, (i - l) \\ &= \left(f_2^{IR} - \frac{f_2^{IR} - f_2^{UV}}{f_2^{UV}} \, l \right) \theta. \end{aligned} \tag{2.36}$$

Finally, substituting $h_1 = f_1^{UV}\theta$ into the above equation, then

$$S = \frac{h_1}{f_1^{UV}} \left(f_2^{IR} - \frac{f_2^{IR} - f_2^{UV}}{f_2^{UV}} \, l \right) \tag{2.37}$$

As expected, to achieve a large separation S, h_1 must be large. In the experiment, the focal lengths are 280 mm, 600 mm, and 640 mm for f_1^{UV}, f_2^{UV}, and f_2^{IR}, respectively. The distance l is about 1000 mm and h_1 is estimated as 5 mm. Then, the estimated separation S is 10.3 mm. In the experiment, a separation of about 7 mm was achieved.

After the IR laser is aligned using the residual $532nm$ beam through the molecular beam machine, the next step is to search for a double resonance signal. Since under molecular beam conditions only the lowest rotational level of NO $j = \frac{1}{2}$ is populated, the IR laser is stabilized onto the $R_{11}(\frac{1}{2})$ line and the UV laser probes the state X($v'' = 2, j = \frac{1}{2}$) state. Even if both laser beams overlap only slightly, a small signal can be detected when the MCP is operated at its maximum sensitivity (see Fig. 2.22). This small signal can easily be optimized by steering the laser beams and changing the delay between the two lasers. After the spatial and the temporal alignment is optimized, typical signal-to-noise ratios in the order of 10^4-10^5 are achieved.

In order to measure the linewidth of the OPO, the UV laser frequency was fixed at the $Q_{21d}(\frac{3}{2})$ line and the IR laser was scanned over the $R_{11}(\frac{1}{2})$ line. In Fig.(2.16) on page 45, trace (b) shows the molecular beam spectrum recorded using a 500 mm lens to focus the IR laser and a 300 mm lens for the UV beam while trace (c)

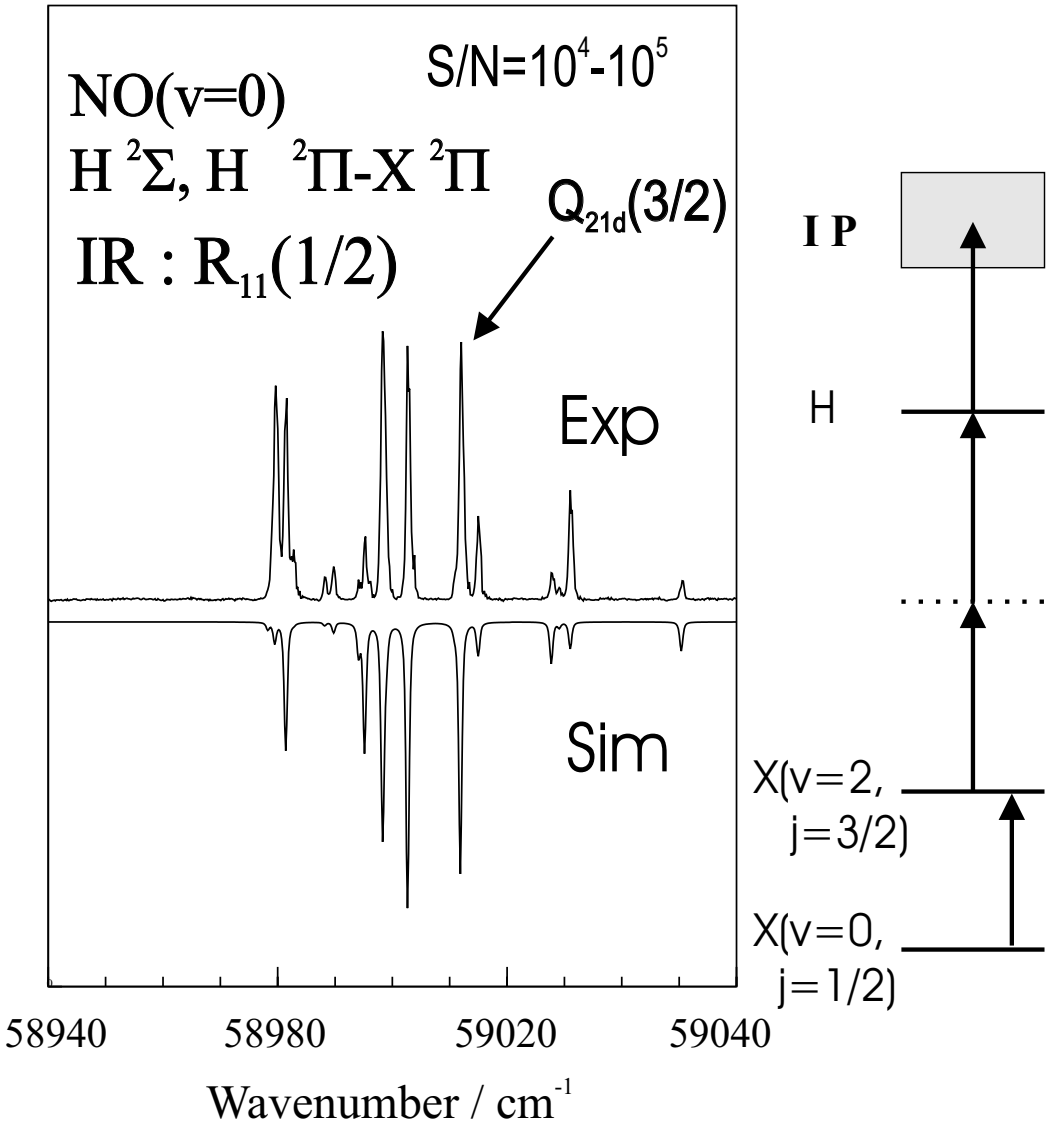

Figure 2.22: IR-UV double resonance hot band spectrum. The IR laser excites the $R_{11}(\frac{1}{2})$ transition and the UV laser probes the $H - X$ transition. The top spectrum is measured under molecular beam conditions and the bottom one is a calculated spectrum.

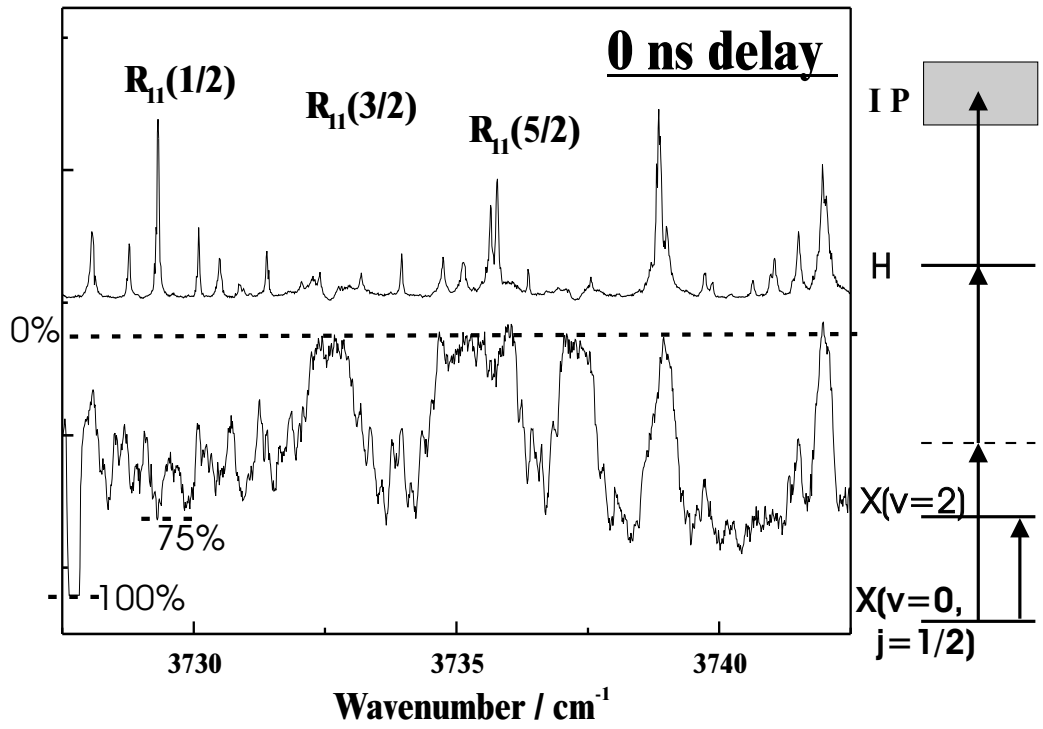

Figure 2.23: Depletion spectrum recorded with the UV laser fixed to the $H - X$ transition without separating the signal and the idler. The top spectrum is a photoacoustic signal whereas the bottom spectrum is an ion signal. Where there is no water absorption, a depletion up to 75% is measured.

displays the molecular beam spectrum without the 500 mm lens. The measured linewidth is about 420 MHz. In trace (b), the observed line is not symmetric and there are small peaks on each side (around -0.4 cm^{-1} and 0.7 cm^{-1}). These peaks are not measurable without the 500 mm lens. It is reckoned that this may be caused by not separating the signal and the idler beam. The strong signal beam might have shifted the potential surface due to the AC Stark effect. This behavior becomes more prominent for the corresponding depletion spectrum. Figure 2.23 shows a depletion spectrum where the depletion does not depend on the frequency. The depletion occurs everywhere except at frequencies where there is strong water

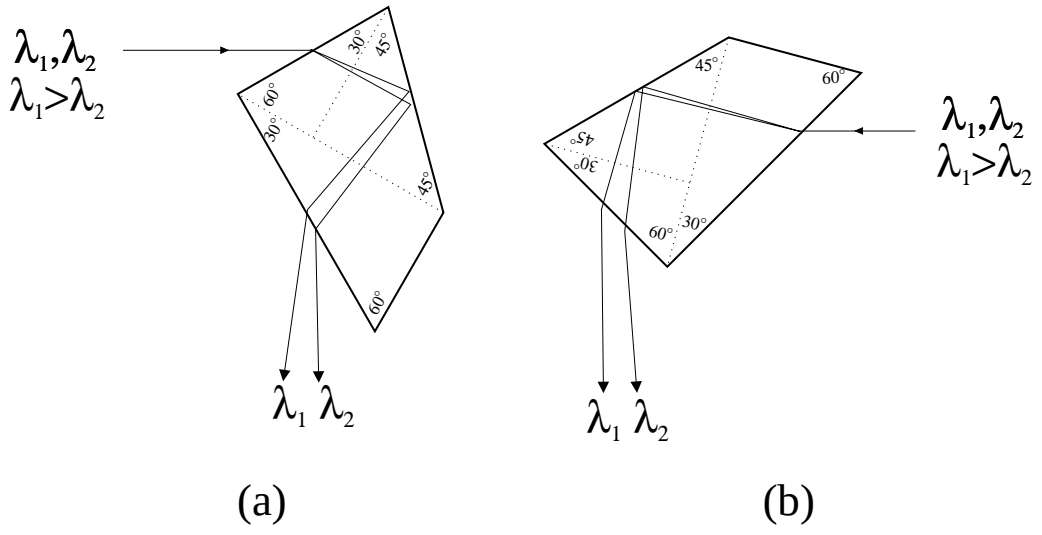

Figure 2.24: Pellin-broca prism. Part (a) shows 'enter short side' configuration and part (b) displays 'enter long side' configuration

absorption. Furthermore, up to 75% of the REMPI signal is lost. In order to avoid this, the idler output beam must be separated from the signal beam using a pair of Pellin-Broca (PB) prisms. Although the PB prisms are single blocks, they can be visualized as consisting of two 30°-60°-90° prisms and one 45°-45°-90° prism [101]. When two beams with different wavelengths collinearly superimposed enter a PB prism, the beams are deflected differently according to the wavelength and depending on which side of the prism the laser beams enter. Figure 2.24 shows 'enter short side'(a) and 'enter long side'(b) configurations. The 'enter short side' configuration deflects the longer wavelength more while the reverse is true for the 'enter long side' configuration. In the experiment, one PB prism is used to separate four outputs of the OPO (the signal beam, the idler beam, residual 532 nm beam, and 1064 nm beam) and the other is used to compensate for the displacement of the

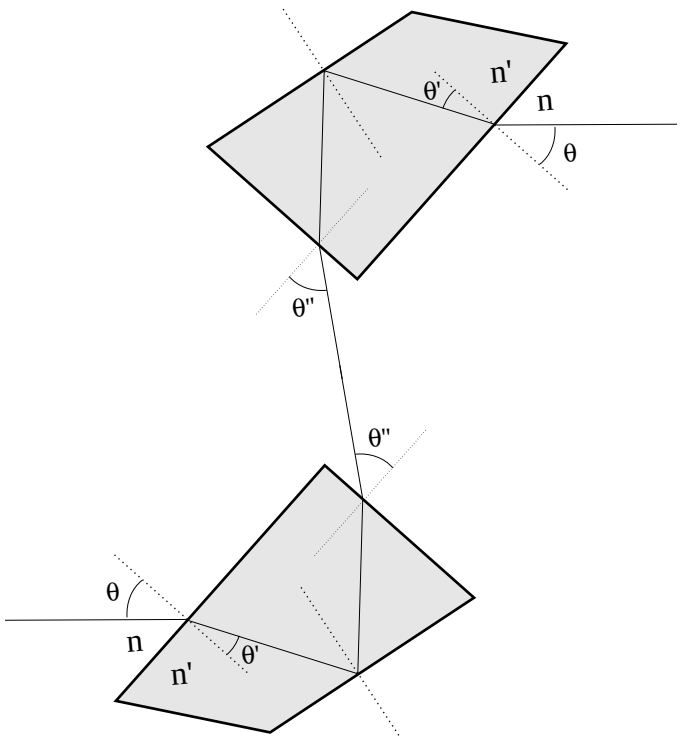

Figure 2.25: The pair of Pellin-Broca prism configuration used to separate the signal beam and the idler beam. A beam dump is placed just before the second prism to block the signal beam.

beam during scans. In order to verify that a pair of PB prisms does not displace the beam path during a scan, a calculation is done using Snell's law. n and n' denote refractive indices of air and the prism, respectively. θ, θ' and θ'' denote the incident, the refracted and the outgoing angles, respectively. Then, the relationship

$$\begin{aligned} n\sin\theta &= n'\sin\theta' \\ n\sin\theta'' &= n'\sin(\frac{\pi}{3}-\theta') \end{aligned} \tag{2.38}$$

is found. A schematic is shown in Fig. 2.25. This relationship also applies to the second PB prism in the reverse way. A simple computer code proves that the beam path does not move after passing through the pair of PB prisms when the wavelength of the IR beam is scanned. In the experiment, the two PB prisms are separated by

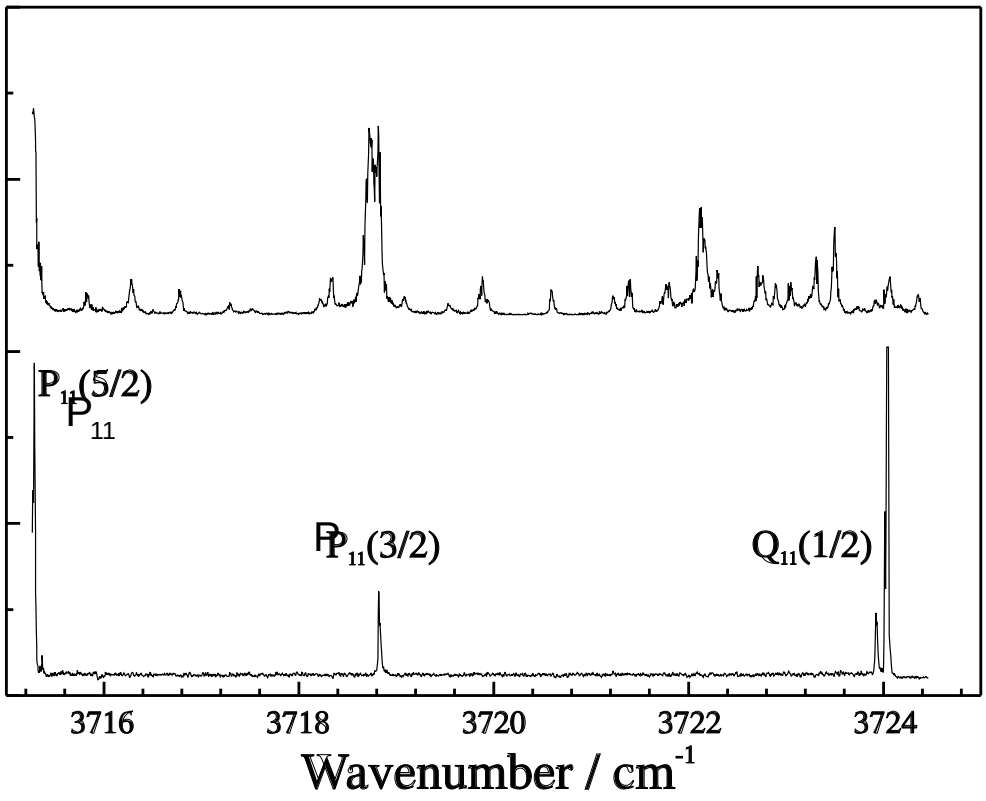

Figure 2.26: Double resonance spectrum to verify that a pair of Pellin-Broca prisms does not displace the beam path during a scan over a range of 10 cm^{-1}.

about 1 m yielding a 5 mm separation just before the second prism. A beam dump is used to block the signal beam as well as the residual 532 nm and 1064 nm beams. In order to verify this experimentally, a double resonance spectrum is measured with a wide range scan of the OPO as shown in Fig. 2.26.

Since with the beam dump the residual green (532 nm) is blocked, it is desirable to have a visible light source as a guide to align the IR beam into the molecular beam machine. For this purpose, a visible laser diode beam (WS TECH LC3-3.5G-650) operating at 650 nm is aligned parallel with the IR laser beam. This beam is coupled onto the IR beam path with the help of a wedge (CaF_2). Now, the UV laser beam and the diode beam are aligned onto the molecular beam inside the molecular

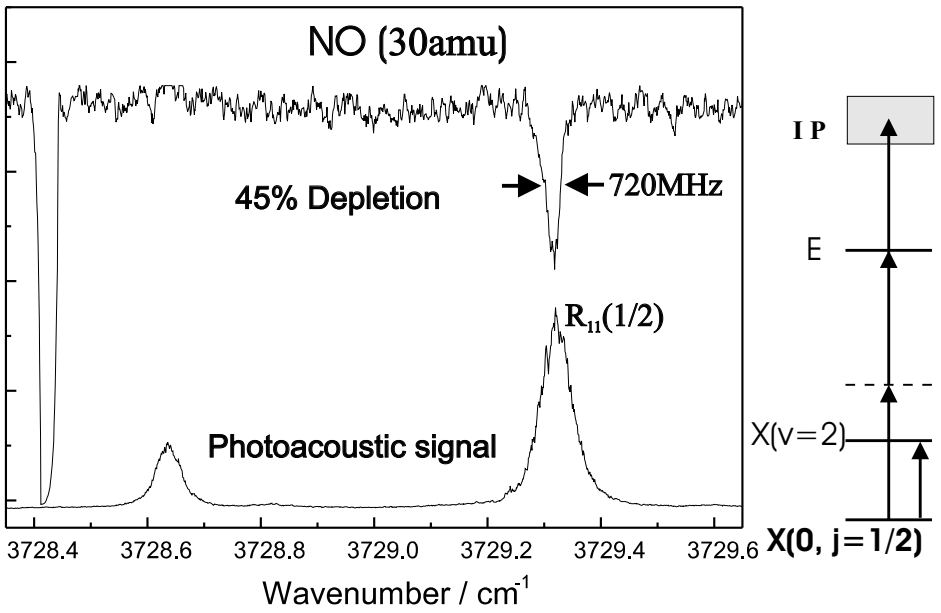

Figure 2.27: NO monomer depletion after the signal beam is blocked. The UV laser probes the $E - X$ transition while the IR laser is scanned over the $R_{11}(\frac{1}{2})$ line to measure a depletion signal. The top spectrum is a depletion signal of the NO monomer while the bottom spectrum is the photoacoustic signal. The linewidth of the IR laser is measured to be 720 MHz when it is focused with a 500 mm lens.

beam apparatus to achieve the double resonance. As described earlier, the UV beam needs to be sent slightly displaced from the IR beam path to avoid damage of the gold mirrors.

Figure 2.27 shows a NO monomer depletion spectrum recorded with only the idler beam being present. As compared to Fig. 2.23, this spectrum shows clearly a frequency dependent depletion up to 45% with a linewidth of 720 MHz. In the spectrum, the UV laser probes the $E - X$ transition and the IR pump laser is fired 10 ns earlier than the UV laser to deplete the population of the lower level. In this case the IR laser acts as a hole-burning laser removing population of the lower

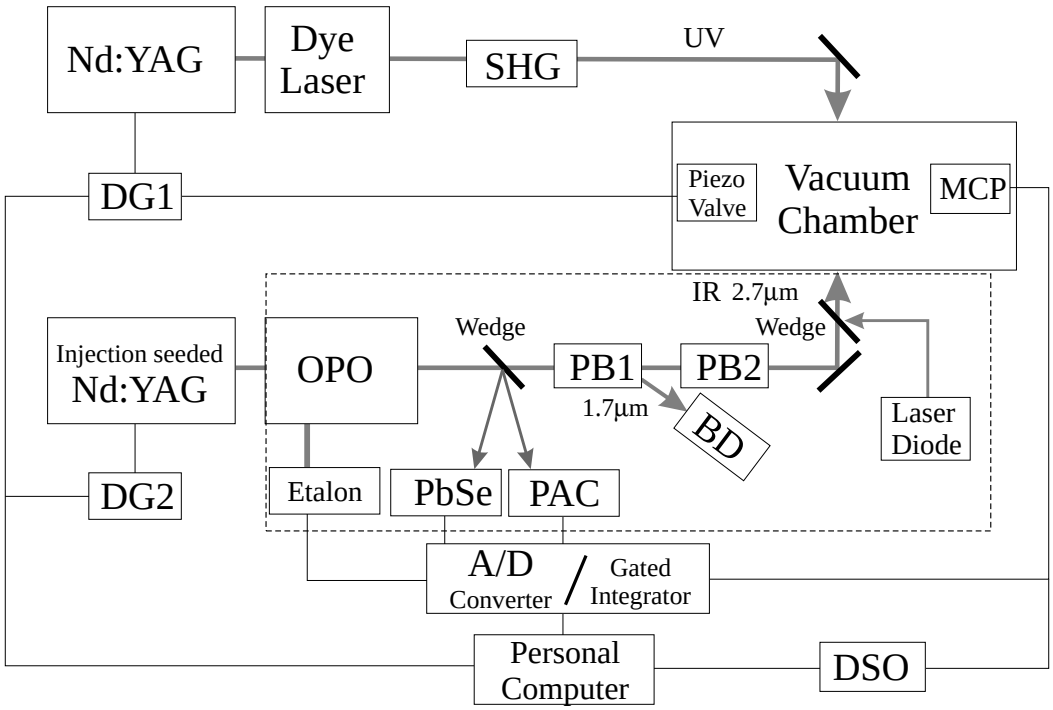

Figure 2.28: Schematic of the experimental setup for the IR-REMPI double resonance experiments. DG1,DG2: delay generators, DSO=digital storage oscilloscope, PB1,PB2=Pellin-Broca prisms, BD=beam dump, PAC=photoacoustic cell.

level. Then, the UV laser probes the hole which manifests itself as a reduction in the signal.

The final schematic diagram is displayed in Fig. 2.28. The setup is summarized as follow. A delay generator (DG1) triggers the Nd:YAG laser which pumps the dye laser. The UV radiation from the second harmonic generation is focused onto the molecular beam. The second delay generator (DG2) triggers the injection seeded Nd:YAG laser to pump the OPO. The OPO generates the IR radiation (the signal and the idler) which are separated by a pair of PB prisms. The near-IR radiation from the NRO output is sent to an etalon for the purpose of calibration. The two reflections of the idler beam from a wedge are sent to a photoacoustic cell for

reference and to a PbSe detector (CAL SENSORS MODEL BP25) for monitoring the IR output power. For alignment purposes, a laser diode beam is introduced to copropagate with the IR laser beam. The IR laser beam travelling anti-parallel to the UV laser beam is focused onto the molecular beam. Signals from the MCP are recorded with a gated integrator and transferred to a PC via an A/D converter. The signals from the etalon, the PbSe detector, and the photoacoustic cell are also recorded with box car integrators and stored in the PC. To avoid water absorption in air, all optics are mounted inside a plexiglass housing which is purged with dry N_2. The dotted box in Fig. 2.28 indicates the plexiglass housing. In order to verify the double resonance character of a signal, a mechanical shutter is used to block the IR beam under computer control.

2.4 Infrared-Ultraviolet Double Resonance Spectroscopy: II. Application to NO-X (X=Ar, Ne) Complex

So far, a technique has been developed to search for double resonance signals of the NO monomer under molecular beam conditions. Now, this technique is applied to measure spectra for the NO-X (X=Ar, Ne) complex. The detection gate is fixed at the appropriate cluster mass (70 amu for NO-Ar, 50 amu for NO-Ne). In order to find the IR resonance frequency for the first overtone transition of the complex, a depletion signal must be detected first. In search of the depletion, the UV frequency is fixed to a known cluster resonance while the IR laser is scanned. For example, in the case of NO-Ar, the UV laser is fixed to the second feature (56624.7 cm^{-1}) of the $\tilde{C}\,^2\Pi(v' = 2) - \tilde{X}\,^2\Pi(v'' = 0)$ transition as seen in Fig. 2.10 and the IR laser is scanned over the wavelength region of the first NO overtone. For NO-Ar, a resonance is discovered at 3723.4 cm^{-1}. In this case, the cluster band is redshifted

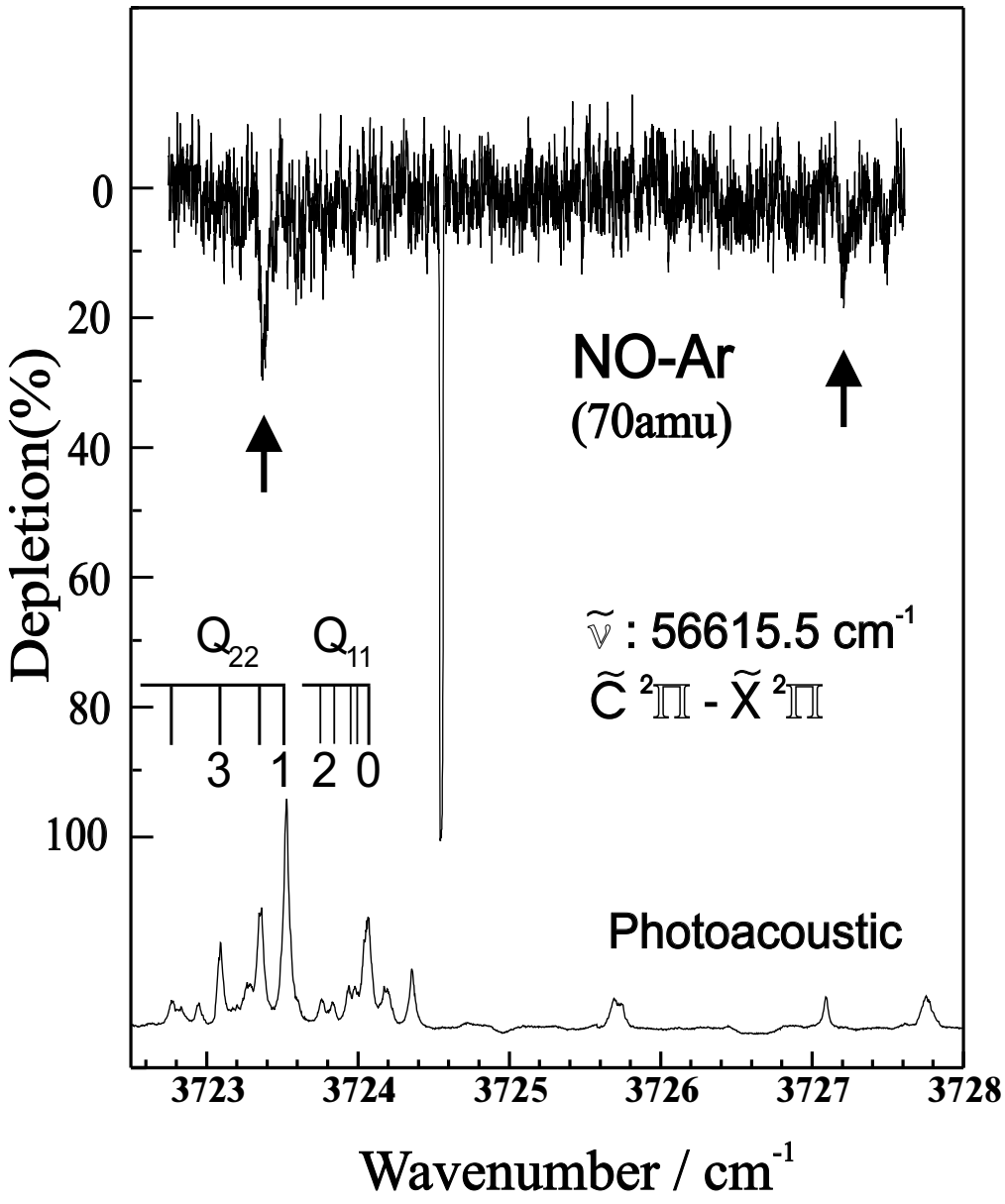

Figure 2.29: IR depletion spectrum of the NO-Ar complex in the vicinity of the origin of the first overtone transition of the NO monomer. At 3723.4 cm^{-1} and 3727.2 cm^{-1}, deletion features are detected.

about 0.5 cm^{-1} from the corresponding origin band of the NO monomer. The shift implies a small increase in the binding energy. As can be seen in Fig. 2.29, the depletion signal has a poor signal-to-noise ratio. REMPI signals involving a two-photon process suffer from large pulse-to-pulse fluctuations. In spite of that, a depletion signal of about 20% is detected. This signal is greatly reduced as compared to the NO monomer depletion. This reduction may be caused by the mismatch in the linewidths of the two lasers. In the case of the monomer, the linewidth of the UV laser is sufficiently small for detecting a single rovibronic level. On the other hand, for the case of the complex, it covers several levels due to the higher level density of the complex. Thus, the narrow linewidth of the IR laser causes only one level to be depleted while the UV laser probes additional levels resulting in the reduced depletion. If the lifetime of the vibrationally excited state of the NO-X complex is comparable to or larger than the laser pulse duration of 5 ns, it should be possible to detect vibrationally excited complexes. To check this, the IR frequency is tuned to the observed depletion features while the UV laser is scanned over the region of the second hot band transition.

For NO-Ar, a positive IR-REMPI double resonance spectrum is shown in Fig. 2.30. With the IR laser beam fixed to the depletion feature, the UV laser beam is scanned over the $\tilde{E}\,^2\Sigma(v' = 0) - \tilde{X}\,^2\Pi(v'' = 2)$ band of the NO-Ar complex. Trace (a) is a spectrum recorded with the IR fixed to the frequency of the maximum depletion signal while trace (b) is recorded without the IR laser. To confirm that the assignment is attributed to the hot band transition to the $\tilde{E}$ state, the corresponding spectrum for the origin band system is shown in trace (c) shifted by 3723.4 cm^{-1}. Lines marked with an asterisk result from baseline shifts due to strong monomer resonances.

Once the hot band transition has been found, an IR absorption spectrum is recorded to see rotational structures of the first overtone transition. In this case

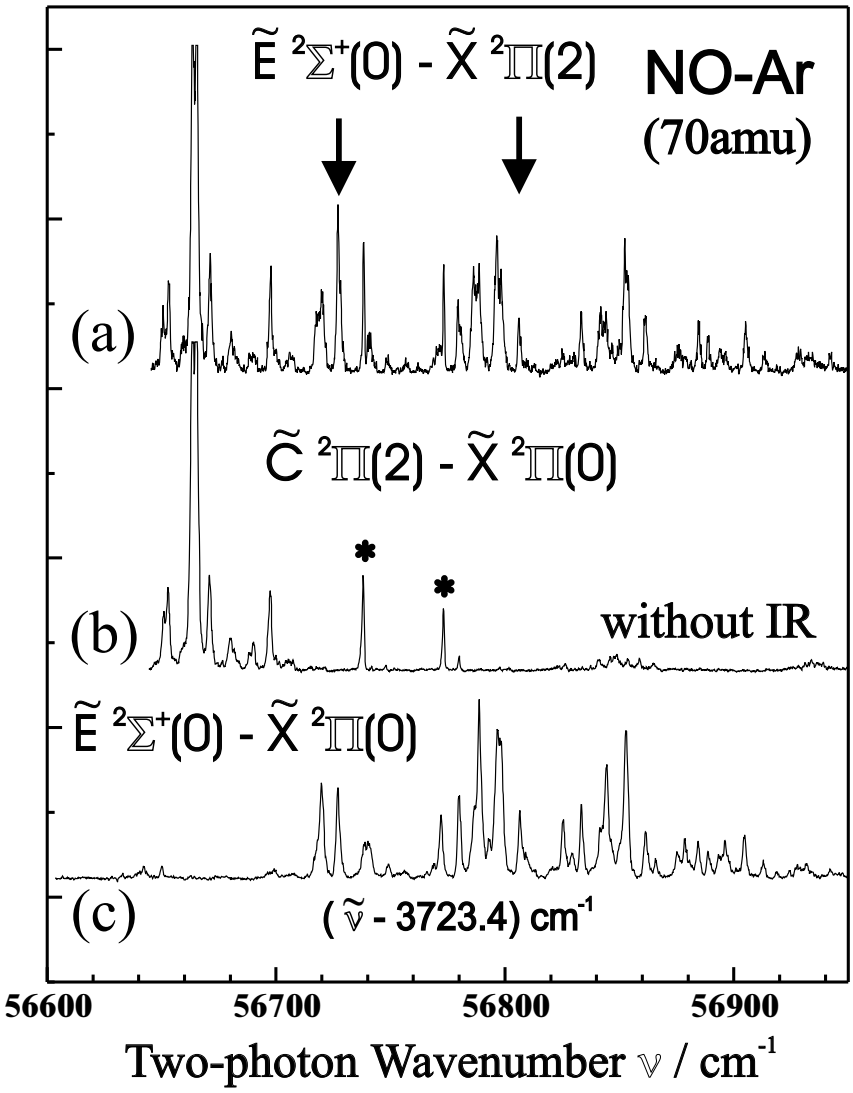

Figure 2.30: IR-REMPI double resonance spectrum of NO-Ar. In trace (a) the UV laser is scanned over the region of the hot band transition $\tilde{E}\,^2\Sigma^+(v'=0) - \tilde{X}\,^2\Pi(v''=2)$ of the complex while the IR laser is fixed to the maximum depletion signal. Trace (b) is recorded without the IR laser. Signals in this range are assigned to the cluster transition $\tilde{C}\,^2\Pi(v'=2) - \tilde{X}\,^2\Pi(v''=0)$. The spectrum in trace (c) shows the (2+1) REMPI spectrum of NO-Ar for the excitation from the electronic ground state to its $\tilde{E}\,^2\Sigma^+$ state shifted by 3723.4 cm^{-1} to the lower frequency. Lines marked with an asterisk are caused by a baseline shift due to strong monomer resonance.

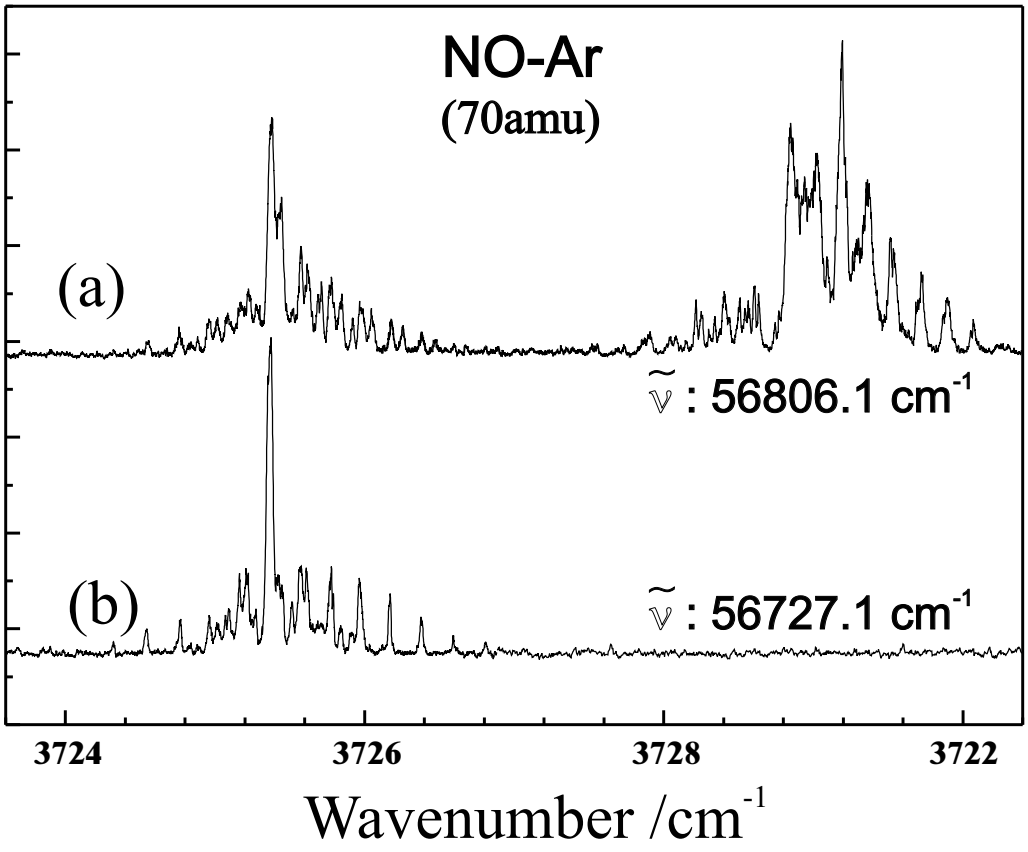

Figure 2.31: IR-REMPI double resonance spectra. The IR laser is scanned while the UV laser is fixed to the indicated UV frequencies which are marked as arrows in Fig. 2.30.

the mismatch in the linewidth acts as an advantage. The larger linewidth of the UV laser makes it possible to detect a great number of rovibrational levels of the complex populated by the IR laser during the scan. Figure 2.31 displays the IR spectra measured with the UV laser tuned to the bands marked with arrows in Fig. 2.30. The top spectrum shows two bands while the bottom one shows only one band. This difference is ascribed to the fact that the UV laser is kept fixed during the IR scan. When the UV frequency is fixed to 56727.1 cm^{-1} (Fig. 2.31(b)), during the IR scan the UV laser frequency is out of resonance with the levels populated for

the second band. On the other hand, when the UV frequency is fixed to 56806.1 cm^{-1} (Fig. 2.31(a)), the UV laser frequency still remains within the resonance.

Chapter 3

Theoretical Background

3.1 Theory of the NO Monomer

3.1.1 Low-Lying Rydberg States

The ground state electron configuration of NO is given in terms of molecular orbitals:

$$(1s\sigma)^2\ (1s\sigma^*)^2\ (2s\sigma)^2\ (2s\sigma^*)^2\ (2p\sigma^*)^2\ (2p\pi)^4\ (2p\pi^*)^1.$$

14 electrons are in closed shells while the 15th electron is in an anti-bonding π^* orbital. This contribution gives rise to the $X\ ^2\Pi$ ground state. The electronic spectrum of the NO molecule has been studied in absorption and emission by many authors [16, 99, 102, 103, 104]. Excitation of the electron in the anti-bonding π^* orbital to a Rydberg orbital generates Rydberg states characterized by nl where n is the principal quantum number and l is the orbital angular quantum number. This leaves the remaining 14 electrons in the $NO^+\ ^1\Sigma^+$ state. This closed shell configuration is little influenced by the Rydberg electron. Several Rydberg series with different l converge to the Σ^+ ground state of the cation NO^+ located at about 9.6 eV. The vibrational frequencies and rotational constants for the Rydberg states are almost identical with the ones of the cation: $\nu_{NO^+} = 2376$ cm^{-1} and $B_v = 2.06$ cm^{-1} [105]. Atomic orbitals split into molecular orbitals characterized by λ which is the projection of the orbital angular momentum $\boldsymbol{l}$ onto the diatom axis. The energetic ordering of the low-lying Rydberg states is shown in Fig. 3.1. These are

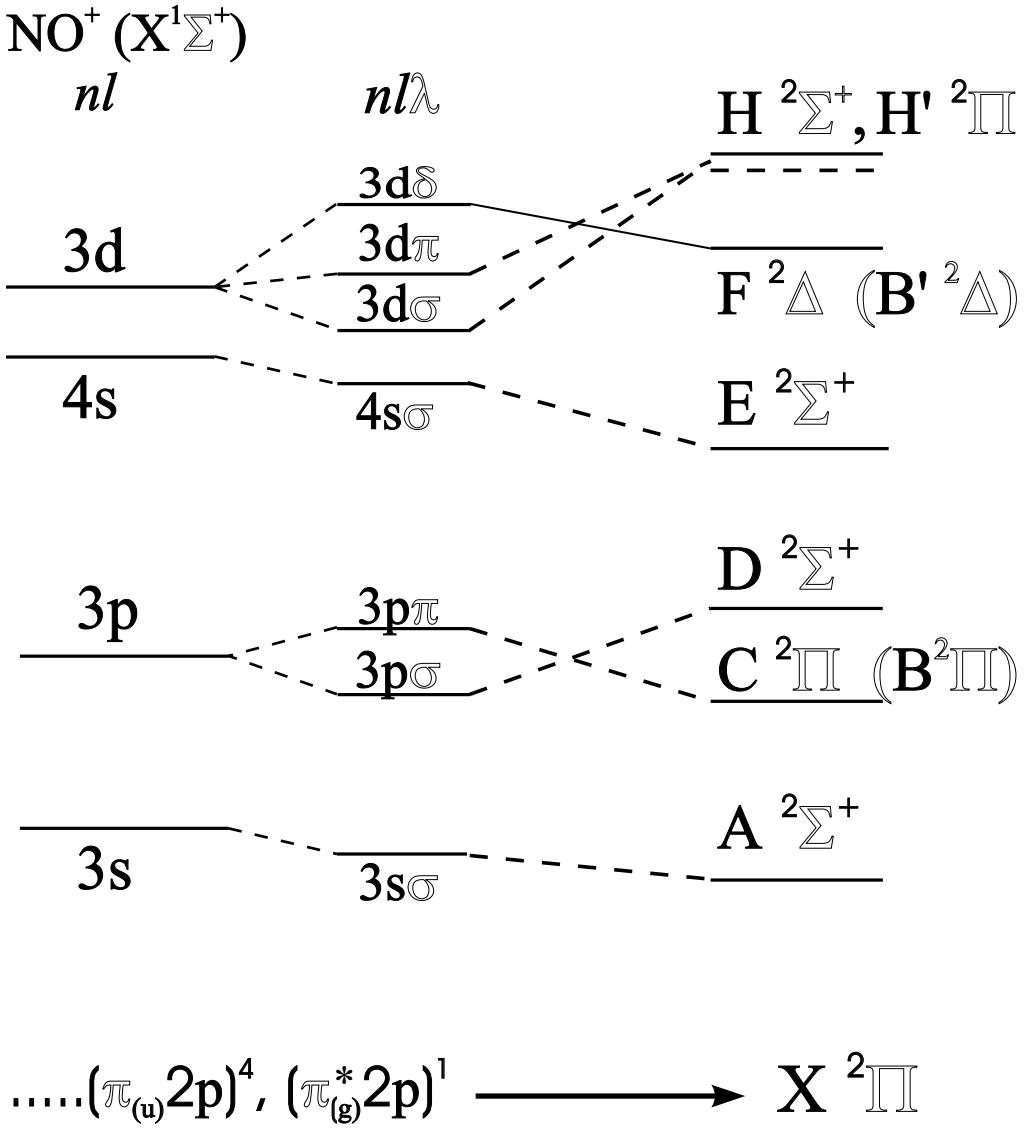

Figure 3.1: The energetic ordering of the low-lying Rydberg states. The states in parentheses are valence states.

derived from orbitals like $3s$, $3p$, $3d$, and $4s$. An ns complex gives rise to a Σ^+ state such as $A\ ^2\Sigma^+$ $(3s)$ and $E\ ^2\Sigma^+$ $(4s)$. The $3p$ orbital splits into a non-degenerate $3p\sigma$-orbital and a doubly degenerate $3p\pi$-orbital giving rise to the states $D\ ^2\Sigma^+$ and $C\ ^2\Pi$, respectively. The $3d$ orbital splits into $3d\sigma$ $(H\ ^2\Sigma^+)$, $3d\pi(H'\ ^2\Pi)$, and $3d\delta$ $(F\ ^2\Delta)$ components.

The characteristics of the Rydberg orbitals depend on the effective quantum number n^* rather than n. n^* can be calculated from the relative distance of the observed energy level T_n to the ionization limit I_p:

$$n^* = n - \delta = \left(\frac{R_\infty}{I_p - T_n}\right)^{1/2} \tag{3.1}$$

Here, δ is the quantum defect, and R_∞ is the Rydberg constant. The large quantum defect of the orbitals $(n+1)s$ is responsible for a near-degeneracy with the nd orbital which have a small quantum defect. As a result, the $nd\sigma$ orbitals are strongly mixed with the $(n+1)s\sigma$ orbitals [104]. Excitation of an electron out of a closed shell into the anti-bonding orbital π^* leads to non-Rydberg (valence) states. These valence states have significantly reduced vibrational frequencies and rotational constants (see Table 3.1). Important homogeneous ($\Delta\Omega = 0$) interactions have been found between several Rydberg states and valence states (e.g. $C\ ^2\Pi \sim B'\ ^2\Delta$ and $F\ ^2\Delta \sim B\ ^2\Pi$). The strength of the interaction varies with the vibrational level. For example, it reaches a maximum at $C\ ^2\Pi(v = 3)$ and $B\ ^2\Pi(v = 15)$ for the $C\ ^2\Pi \sim B'\ ^2\Delta$ interaction. Furthermore, the degree of state mixing depends on the rotational energy which tunes the overall energy in or out of resonance [106].

3.1.2 Diatomic Hamiltonian

In order to understand the NO monomer, the diatomic Hamiltonian is derived in this subsection. In this derivation, the spin is first neglected. It will be included

Table 3.1: Low-Lying Rydberg States and valence states [16]. A_v: spin-orbit constant, B_v: rotational constant, δ: quantum defect, r_{nl}: radius of Rydberg orbital.

	State	T_0	A_v	B_v	δ	r_{nl}/Å
$3d\pi$	$H\,'^2\Pi$	62,721.1			-0.02	5.65
$3d\sigma$	$H\,^2\Sigma^+$	62,705.3				
$3d\delta$	$F\,^2\Delta$	62,051.1			0.06	5.28
$4s\sigma$	$E\,^2\Sigma^+$	60,862.8			1.19	6.27
Non-Rydberg	$B\,'^2\Delta$	60030.	-2.2	1.321		
$3p\sigma$	$D\,^2\Sigma^+$	53,290.9			0.74	3.52
$3p\pi$	$C\,^2\Pi$	52,373.2	+3.0		0.78	3.38
Non-Rydberg	$B\,^2\Pi$	45,482.0	+30	1.115		
$3s\sigma$	$A\,^2\Sigma^+$	44,198.9		1.987	1.10	2.86
	$X\,^2\Pi$	0.0	+123.2	1.697		

later when the energy eigenvalues are calculated in the next subsection. After the derivation of the eigenenergies, 'λ-doubling' is derived theoretically.

The total energy of the diatom is comprised of the kinetic energy and the electrostatic potential energy. The kinetic energy of the diatom is the sum of the kinetic energies of all particles (two nuclei and N_{bc} electrons). The electrostatic potential energy is the sum of the electron-electron, electron-nucleus, and nucleus-nucleus Coulomb interaction energies. The total energy of the diatom is written as

$$\begin{aligned} H &= T + V \\ &= \frac{1}{2}m_b\dot{\boldsymbol{R}}_b^2 + \frac{1}{2}m_c\dot{\boldsymbol{R}}_c^2 + \frac{1}{2}\sum_{k_{bc}=1}^{N_{bc}} m_e\dot{\boldsymbol{R}}_{k_{bc}}^2 \\ &\quad + \frac{Z_bZ_ce^2}{|\boldsymbol{R}_b - \boldsymbol{R}_c|} - \sum_{k_{bc}=1}^{N_{bc}} \frac{Z_be^2}{|\boldsymbol{R}_b - \boldsymbol{R}_{k_{bc}}|} - \sum_{k_{bc}=1}^{N_{bc}} \frac{Z_ce^2}{|\boldsymbol{R}_c - \boldsymbol{R}_{k_{bc}}|} + \sum_{j_{bc}<k_{bc}} \frac{e^2}{|\boldsymbol{R}_{j_{bc}} - \boldsymbol{R}_{k_{bc}}|}. \end{aligned} \tag{3.2}$$

In the above expression, the subscript b and c denote the two nuclei and the subscripts j_{bc} or k_{bc} denote the electrons. Accordingly, $\boldsymbol{R}_b$ and $\boldsymbol{R}_c$ represent the position vectors of the two nuclei and $\boldsymbol{R}_{k_{bc}}$ the position vector of an electron with respect to an arbitrary laboratory frame. m_b, m_c, and m_e denote the masses of the nuclei and an electron. $Z_b e$ and $Z_c e$ are charges of the nuclei. In the absence of external fields, the center-of-mass (cm) of a molecule moves along a straight line with constant velocity. Then, the cm motion can be separated off by defining the following new coordinates:

$$\boldsymbol{R}_b = \boldsymbol{R}_{cm} + \boldsymbol{r}_b, \quad \boldsymbol{R}_c = \boldsymbol{R}_{cm} + \boldsymbol{r}_c, \quad \text{and} \quad \boldsymbol{R}_{k_{bc}} = \boldsymbol{R}_{cm} + \boldsymbol{r}_{k_{bc}}. \tag{3.3}$$

Here, $\boldsymbol{R}_{cm}$ is defined as the cm of all particles:

$$M\boldsymbol{R}_{cm} = m_b\boldsymbol{R}_b + m_c\boldsymbol{R}_c + \sum_{k_{bc}=1}^{N_{bc}} m_e\boldsymbol{R}_{k_{bc}} \tag{3.4}$$

where M is the total mass of the diatom. The coordinates $\boldsymbol{r}_b$, $\boldsymbol{r}_c$, and $\boldsymbol{r}_{k_{bc}}$ are related according to the cm condition:

$$m_b\boldsymbol{r}_b + m_c\boldsymbol{r}_c + \sum_{k_{bc}=1}^{N_{bc}} m_e\boldsymbol{r}_{k_{bc}} = 0. \tag{3.5}$$

Using Eq. (3.3) the kinetic energy is expressed as

$$T = \frac{1}{2}M\dot{\boldsymbol{R}}_{cm}^2 + \frac{1}{2}m_b\dot{\boldsymbol{r}}_b^2 + \frac{1}{2}m_c\dot{\boldsymbol{r}}_c^2 + \frac{1}{2}\sum_{k_{bc}=1}^{N_{bc}} m_e\dot{\boldsymbol{r}}_{k_{bc}}^2. \tag{3.6}$$

In these new coordinates, the potential energy becomes

$$V = \frac{Z_b Z_c e^2}{|\boldsymbol{r}_b - \boldsymbol{r}_c|} - \sum_{k_{bc}=1}^{N_{bc}} \frac{Z_b e^2}{|\boldsymbol{r}_b - \boldsymbol{r}_{k_{bc}}|} - \sum_{k_{bc}=1}^{N_{bc}} \frac{Z_c e^2}{|\boldsymbol{r}_c - \boldsymbol{r}_{k_{bc}}|} + \sum_{j_{bc}<k_{bc}} \frac{e^2}{|\boldsymbol{r}_{j_{bc}} - \boldsymbol{r}_{k_{bc}}|}. \tag{3.7}$$

Since the potential does not depend on $\boldsymbol{R}_{cm}$, the cm motion can be separated off and its contribution to the kinetic energy will be discarded from now on:

$$T = \frac{1}{2}m_b\dot{\boldsymbol{r}}_b^2 + \frac{1}{2}m_c\dot{\boldsymbol{r}}_c^2 + \frac{1}{2}\sum_{k_{bc}=1}^{N_{bc}} m_e\dot{\boldsymbol{r}}_{k_{bc}}^2. \tag{3.8}$$

In the above expression, the variables are not completely independent of each other since they are related by Eq. (3.5). In order to have a set of generalized coordinates, it is convenient to define a space fixed (sf) frame whose origin is located at the cm of the nuclei, $\boldsymbol{r}_{cm}$. The position of the electrons are determined with respect to the nuclear cm:

$$m_{bc}\boldsymbol{r}_{cm} = m_b\boldsymbol{r}_b + m_c\boldsymbol{r}_c, \quad \boldsymbol{r} = \boldsymbol{r}_b - \boldsymbol{r}_c \ \text{ and } \ \boldsymbol{\xi}_{k_{bc}} = \boldsymbol{r}_{k_{bc}} - \boldsymbol{r}_{cm}, \tag{3.9}$$

where m_{bc} is the total mass of the two nuclei. The kinetic energy and the potential energy are expressed in terms of the sf frame:

$$T = \frac{1}{2}M\dot{\boldsymbol{r}}_{cm}^2 + \frac{1}{2}\mu_{bc}\dot{\boldsymbol{r}}^2 + \dot{\boldsymbol{r}}_{cm}\cdot\sum_{k_{bc}=1}^{N_{bc}} m_e\dot{\boldsymbol{\xi}}_{k_{bc}} + \frac{1}{2}\sum_{k_{bc}=1}^{N_{bc}} m_e\dot{\boldsymbol{\xi}}_{k_{bc}}^2, \tag{3.10}$$

and

$$V = \frac{Z_bZ_ce^2}{r} - \sum_{k_{bc}=1}^{N_{bc}}\frac{Z_be^2}{|\frac{m_c}{m_{bc}}\boldsymbol{r} - \boldsymbol{\xi}_{k_{bc}}|} - \sum_{k_{bc}=1}^{N_{bc}}\frac{Z_ce^2}{|\frac{m_b}{m_{bc}}\boldsymbol{r} + \boldsymbol{\xi}_{k_{bc}}|} + \sum_{j_{bc}<k_{bc}}\frac{e^2}{|\boldsymbol{\xi}_{j_{bc}} - \boldsymbol{\xi}_{k_{bc}}|}. \tag{3.11}$$

Here, μ_{bc} is the reduced mass of two nuclei. It is clear that the potential energy does not depend on $\boldsymbol{r}_{cm}$. On the other hand, the kinetic energy contains terms with $\boldsymbol{r}_{cm}$. Since the third term in the kinetic energy couples the nuclear center of mass motion to the electron motion, it is not possible to separate off the former motion. However, from the condition in Eq. (3.5) the nuclear center of mass is balanced by the electrons:

$$m_b\boldsymbol{r}_b + m_c\boldsymbol{r}_c = -\sum_{k_{bc}=1}^{N_{bc}} m_e\boldsymbol{r}_{k_{bc}} \quad\Leftrightarrow\quad m_{bc}\boldsymbol{r}_{cm} = -\sum_{k_{bc}=1}^{N_{bc}} m_e\boldsymbol{\xi}_{k_{bc}} - N_{bc}m_e\boldsymbol{r}_{cm}. \tag{3.12}$$

Solving for $\boldsymbol{r}_{cm}$ yields

$$\boldsymbol{r}_{cm} = -\frac{m_e}{M}\sum_{k_{bc}=1}^{N_{bc}} m_e\boldsymbol{\xi}_{k_{bc}}. \tag{3.13}$$

Substituting the above result into the Eq. (3.10), the kinetic energy takes on the form [107]:

$$T = \frac{1}{2}\mu_{bc}\dot{\boldsymbol{r}}^2 + \frac{1}{2}\sum_{k_{bc}=1}^{N_{bc}} m_e\dot{\boldsymbol{\xi}}_{k_{bc}}^2 - \frac{1}{2}\frac{m_e^2}{M}\left(\sum_{j=1}^{N_{bc}}\dot{\boldsymbol{\xi}}_{j_{bc}}\right)^2. \tag{3.14}$$

Now, the kinetic energy is given in terms of a set of independent variables.

In classical mechanics, the Hamiltonian needs to be expressed in terms of generalized coordinates and their conjugate momenta. The momenta conjugate to the generalized coordinates are found according to:

$$\boldsymbol{p}_r = \nabla_{\dot{r}} T = \mu_{bc} \dot{\boldsymbol{r}}, \tag{3.15}$$

$$\boldsymbol{p}_{k_{bc}} = \nabla_{\dot{\xi}_{k_{bc}}} T = m_e \dot{\boldsymbol{\xi}}_{k_{bc}} - \frac{m_e^2}{M} \sum_{j_{bc}=1}^{N_{bc}} \dot{\boldsymbol{\xi}}_{j_{bc}}. \tag{3.16}$$

Then, the kinetic energy becomes

$$T = \frac{1}{2\mu_{bc}} \boldsymbol{p}_r^2 + \sum_{k_{bc}=1}^{N_{bc}} \frac{1}{2m_e} \boldsymbol{p}_{k_{bc}}^2 + \frac{1}{2m_{bc}} \left(\sum_{k_{bc}=1}^{N_{bc}} \boldsymbol{p}_{k_{bc}} \right)^2. \tag{3.17}$$

The first term in the above equation is the nuclear kinetic energy T_N whereas the second terms represents the electron kinetic energy T_e. The third term is referred to as the mass polarization.

In describing the rotational motion of the molecule, it is convenient to introduce a molecule fixed (mf) frame which is defined in such a way that its z-axis coincides with the direction of the internuclear axis (parallel to the vector $\boldsymbol{r}$). In the sf frame the orientation of the diatom axis is determined by two polar angles, α and β. The components of $\boldsymbol{r}$ in these two frames are

$$\boldsymbol{r}^{sf} = r \begin{pmatrix} \sin\beta\cos\alpha \\ \sin\beta\sin\alpha \\ \cos\beta \end{pmatrix} \quad \text{and} \quad \boldsymbol{r}^{mf} = r \begin{pmatrix} 0 \\ 0 \\ 1 \end{pmatrix}. \tag{3.18}$$

The above coordinates are related by a matrix $\mathsf{C}(\alpha, \beta)$:

$$\boldsymbol{r}^{mf} = \mathsf{C}(\alpha, \beta) \boldsymbol{r}^{sf} \tag{3.19}$$

where

$$\mathsf{C}(\alpha, \beta) = \begin{pmatrix} \cos\beta & 0 & -\sin\beta \\ 0 & 1 & 0 \\ \sin\beta & 0 & \cos\beta \end{pmatrix} \begin{pmatrix} \cos\alpha & \sin\alpha & 0 \\ -\sin\alpha & \cos\alpha & 0 \\ 0 & 0 & 1 \end{pmatrix}. \tag{3.20}$$

The electronic coordinates in the mf frame which are denoted $\boldsymbol{\eta}_{j_{bc}}$ will be transformed in a similar way:

$$\boldsymbol{\eta}_{k_{bc}} = \mathsf{C}(\alpha,\beta)\boldsymbol{\xi}_{k_{bc}}. \tag{3.21}$$

Since a rotation does not change the lengths of a vector, the potential energy does not change appearance under the rotation:

$$V = \frac{Z_b Z_c e^2}{r} - \sum_{k_{bc}=1}^{N_{bc}} \frac{Z_b e^2}{|\frac{m_c}{m_{bc}}\boldsymbol{r} - \boldsymbol{\eta}_{k_{bc}}|} - \sum_{k_{bc}=1}^{N_{bc}} \frac{Z_c e^2}{|\frac{m_b}{m_{bc}}\boldsymbol{r} + \boldsymbol{\eta}_{k_{bc}}|} + \sum_{j_{bc}<k_{bc}}^{N_{bc}} \frac{e^2}{|\boldsymbol{\eta}_{j_{bc}} - \boldsymbol{\eta}_{k_{bc}}|}. \tag{3.22}$$

Note that in the above expression, $\boldsymbol{r}$ represents the vector in the molecule fixed frame and henceforth a vector without superscript is regarded as a vector in the mf frame unless otherwise stated. An arbitrary velocity $\dot{\boldsymbol{a}}$ defined in the sf frame but projected onto the mf frame is written as

$$\begin{aligned} \mathsf{C}(\alpha,\beta)\dot{\boldsymbol{a}}^{sf} &= \dot{\boldsymbol{a}}^{mf} + \mathsf{C}(\alpha,\beta)\dot{\mathsf{C}}^{\dagger}(\alpha,\beta)\boldsymbol{a}^{mf} \\ &= \dot{\boldsymbol{a}}^{mf} + \boldsymbol{\omega}\times\boldsymbol{a}^{mf} \end{aligned} \tag{3.23}$$

where

$$\boldsymbol{\omega} = \begin{pmatrix} -\sin\beta\ \ \dot{\alpha} \\ \dot{\beta} \\ \cos\beta\ \ \dot{\alpha} \end{pmatrix}. \tag{3.24}$$

Using Eq. (3.23) the expression of the kinetic energy Eq. (3.14) is found to be

$$\begin{aligned} T &= \frac{1}{2}\mu_{bc}\big(\dot{\boldsymbol{r}} + \boldsymbol{\omega}\times\dot{\boldsymbol{r}}\big)^2 \\ &\quad + \frac{1}{2}m_e \sum_{k_{bc}=1}^{N_{bc}} \big(\dot{\boldsymbol{\eta}}_{k_{bc}} + \boldsymbol{\omega}\times\dot{\boldsymbol{\eta}}_{k_{bc}}\big)^2 + \frac{1}{2}\frac{m_e^2}{M}\left(\sum_{k_{bc}=1}^{N_{bc}} \big(\dot{\boldsymbol{\eta}}_{k_{bc}} + \boldsymbol{\omega}\times\dot{\boldsymbol{\eta}}_{k_{bc}}\big)\right)^2. \end{aligned} \tag{3.25}$$

In terms of the generalized coordinates $(r,\ \alpha,\ \beta,\ \boldsymbol{\eta}_{j_{bc}})$, the kinetic energy is rewritten as

$$\begin{aligned} T &= \frac{1}{2}\mu_{bc}\big(\dot{r}^2 + r^2\dot{\beta}^2 + r^2\dot{\alpha}^2\sin^2\beta\big) \\ &\quad + \frac{1}{2}m_e \sum_{k_{bc}=1}^{N_{bc}} \big(\dot{\boldsymbol{\eta}}_{k_{bc}} + \boldsymbol{\omega}\times\dot{\boldsymbol{\eta}}_{k_{bc}}\big)^2 + \frac{1}{2}\frac{m_e^2}{M}\left(\sum_{k_{bc}=1}^{N_{bc}} \big(\dot{\boldsymbol{\eta}}_{k_{bc}} + \boldsymbol{\omega}\times\dot{\boldsymbol{\eta}}_{k_{bc}}\big)\right)^2. \end{aligned} \tag{3.26}$$

Now, the kinetic energy must be expressed in terms of generalized coordinates and their conjugate momenta. The momentum conjugate to $\boldsymbol{\eta}_{k_{bc}}$ is calculated as

$$\boldsymbol{p}_{k_{bc}} = \nabla_{\dot{\eta}_{k_{bc}}} T = m_e\big(\dot{\boldsymbol{\eta}}_{k_{bc}} + \boldsymbol{\omega} \times \boldsymbol{\eta}_{k_{bc}}\big) - \frac{m_e^2}{M} \sum_{k_{bc}=1}^{N_{bc}} \big(\dot{\boldsymbol{\eta}}_{k_{bc}} + \boldsymbol{\omega} \times \boldsymbol{\eta}_{k_{bc}}\big). \tag{3.27}$$

The momentum conjugate to r is determined as

$$p_r = \frac{\partial T}{\partial \dot{r}} = \mu_{bc}\dot{r}. \tag{3.28}$$

For the generalized coordinates α and β, the conjugate momenta are given by

$$j_\alpha = \frac{\partial T}{\partial \dot{\alpha}} = \frac{\partial T_N}{\partial \dot{\alpha}} + \sum_{i=x,y,z} \frac{\partial T_e}{\partial \omega_i}\frac{\partial \omega_i}{\partial \dot{\alpha}} = \frac{\partial T_N}{\partial \dot{\alpha}} + \big(\nabla_\omega T_e\big) \cdot \frac{\partial \boldsymbol{\omega}}{\partial \dot{\alpha}} \tag{3.29}$$

and

$$j_\beta = \frac{\partial T}{\partial \dot{\beta}} = \frac{\partial T_N}{\partial \dot{\beta}} + \sum_{i=x,y,z} \frac{\partial T_e}{\partial \omega_i}\frac{\partial \omega_i}{\partial \dot{\beta}} = \frac{\partial T_N}{\partial \dot{\beta}} + \big(\nabla_\omega T_e\big) \cdot \frac{\partial \boldsymbol{\omega}}{\partial \dot{\beta}}. \tag{3.30}$$

j_α and j_β are expressed using the gradient of the electronic part of the kinetic energy with respect to the components of the vector $\boldsymbol{\omega}$. The gradient of the electronic kinetic energy is found to be

$$\nabla_{\boldsymbol{\omega}} T_e = m_e \sum_{k_{bc}=1}^{N_{bc}} \boldsymbol{\eta}_{k_{bc}} \times \left(\dot{\boldsymbol{\eta}}_{k_{bc}} + \boldsymbol{\omega} \times \boldsymbol{\eta}_{k_{bc}} - \frac{m_e}{M} \sum_{j_{bc}} \big(\dot{\boldsymbol{\eta}}_{j_{bc}} + \boldsymbol{\omega} \times \boldsymbol{\eta}_{j_{bc}}\big) \right). \tag{3.31}$$

Using Eq. (3.27), the above expression defines the electronic orbital angular momentum:

$$\nabla_{\boldsymbol{\omega}} T_e = \sum_{k_{bc}=1}^{N_{bc}} \boldsymbol{\eta}_{k_{bc}} \times \boldsymbol{p}_{k_{bc}} = \boldsymbol{l}. \tag{3.32}$$

Now, the conjugate momenta j_α and j_β take the form:

$$j_\alpha = \mu_{bc} r^2 \sin^2\beta\, \dot{\alpha} - \sin\beta\, l_x + \cos\beta\, l_z, \tag{3.33a}$$

$$j_\beta = \mu_{bc} r^2 \dot{\beta} + l_y. \tag{3.33b}$$

In order to avoid any confusion regarding the angular momentum vectors, it is convenient to note that those of the diatom are expressed in terms of small letters

such as $\boldsymbol{j}, \boldsymbol{l}$, and $\boldsymbol{s}$. On the other hand, the angular momentum vectors of the complex are expressed in terms of capital letters like $\boldsymbol{J}, \boldsymbol{L}$, and $\boldsymbol{S}$.

Solving the above equations for $\dot{\alpha}$ and $\dot{\beta}$ gives

$$\dot{\alpha} = \frac{j_\alpha + \sin\beta\, l_x - \cos\beta\, l_z}{\mu_{bc} r^2 \sin^2\beta} \tag{3.34a}$$

$$\dot{\beta} = \frac{j_\beta - l_y}{\mu_{bc} r^2}. \tag{3.34b}$$

Substituting $\dot{\alpha}$ and $\dot{\beta}$ into Eq. (3.26) yields the following expression for the kinetic energy in terms of the generalized coordinates and their conjugate momenta:

$$\begin{aligned} T = & \frac{p_r^2}{2} + \frac{1}{2\mu_{bc} r^2}\left(\left(j_\beta - l_y\right)^2 + \left(\csc\beta\, j_\alpha + l_x - \cot\beta\, l_z\right)^2\right) \\ & + \frac{1}{2m_e}\sum_{k_{bc}=1}^{N_{bc}} \boldsymbol{p}_{k_{bc}}^2 + \frac{1}{2m_{bc}}\left(\sum_{k_{bc}=1}^{N_{bc}} \boldsymbol{p}_{k_{bc}}\right)^2. \end{aligned} \tag{3.35}$$

By introducing a rotating coordinate frame, the nuclear kinetic energy couples the electronic coordinates and nuclear motion. This coupling involves the orbital angular momentum vector of the electrons, $\boldsymbol{l}$.

It is informative to calculate the total angular momentum of the diatom which is conserved in the sf center of mass frame (of all particles) and to express the Hamiltonian in terms of its components. From the definition of the total angular momentum in the sf frame (of all particles), $\boldsymbol{j}^{sf}$ is given by

$$\boldsymbol{j}^{sf} = m_b \boldsymbol{r}_b \times \dot{\boldsymbol{r}}_b + m_c \boldsymbol{r}_c \times \dot{\boldsymbol{r}}_c + m_e \sum_{k_{bc}} \boldsymbol{r}_{k_{bc}} \times \dot{\boldsymbol{r}}_{k_{bc}}. \tag{3.36}$$

Introducing the nuclear center mass $\boldsymbol{r}_{cm}$ as defined in Eq. (3.9), the total angular momentum becomes

$$\begin{aligned} \boldsymbol{j}^{sf} = & M\boldsymbol{r}_{cm} \times \dot{\boldsymbol{r}}_{cm} + \mu_{bc} \boldsymbol{r}^{sf} \times \dot{\boldsymbol{r}}^{sf} + \sum_{k_{bc}} m_e \boldsymbol{\xi}_{k_{bc}} \times \dot{\boldsymbol{\xi}}_{k_{bc}} \\ & + \left(\sum_{k_{bc}} m_e \boldsymbol{\xi}_{k_{bc}}\right) \times \dot{\boldsymbol{r}}_{cm} + \boldsymbol{r}_{cm} \times \left(\sum_{k_{bc}} m_e \boldsymbol{\xi}_{k_{bc}}\right). \end{aligned} \tag{3.37}$$

Substituting Eq.(3.13) into the above equation, $\boldsymbol{j}^{sf}$ becomes

$$\boldsymbol{j}^{sf} = \mu_{bc}\boldsymbol{r}^{sf} \times \dot{\boldsymbol{r}}^{sf} + \sum_{k_{bc}} m_e \boldsymbol{\xi}_{k_{bc}} \times \dot{\boldsymbol{\xi}}_{k_{bc}} - \frac{m_e^2}{M}\left(\sum_{j_{bc}} \boldsymbol{\xi}_{j_{bc}}\right) \times \left(\sum_{k_{bc}} \dot{\boldsymbol{\xi}}_{k_{bc}}\right). \tag{3.38}$$

Using Eq. (3.23), the total angular momentum in the mf frame, $\boldsymbol{j}^{mf}$, is obtained by projecting $\boldsymbol{j}^{sf}$ onto mf axes:

$$\begin{aligned}
\boldsymbol{j}^{mf} = \mathsf{C}(\alpha,\beta)\boldsymbol{j}^{sf} &= \mu_{bc}\boldsymbol{r} \times (\dot{\boldsymbol{r}} + \boldsymbol{\omega} \times \boldsymbol{r}) + \sum_{k_{bc}} m_e \boldsymbol{\eta}_{k_{bc}} \times \left(\dot{\boldsymbol{\eta}}_{k_{bc}} + \boldsymbol{\omega} \times \boldsymbol{\eta}_{k_{bc}}\right) \\
&\quad -\frac{m_e^2}{M}\left(\sum_{k_{bc}} \boldsymbol{\eta}_{k_{bc}}\right) \times \left(\sum_{j_{bc}} \dot{\boldsymbol{\eta}}_{j_{bc}} + \boldsymbol{\omega} \times \boldsymbol{\eta}_{j_{bc}}\right) \\
&= \mu_{bc}\boldsymbol{r} \times (\dot{\boldsymbol{r}} + \boldsymbol{\omega} \times \boldsymbol{r}) + \sum_{k_{bc}} \boldsymbol{\eta}_{k_{bc}} \times \boldsymbol{p}_{k_{bc}} \\
&= \mu_{bc} r^2 \begin{pmatrix} -\sin\beta\ \dot{\alpha} \\ \dot{\beta} \\ 0 \end{pmatrix} + \boldsymbol{l} \\
&= \begin{pmatrix} -\mu_{bc} r^2 \sin\beta\ \dot{\alpha} + l_x \\ \mu_{bc} r^2 \dot{\beta} + l_y \\ l_z \end{pmatrix}.
\end{aligned} \tag{3.39}$$

In order to express the Hamiltonian in terms of $\boldsymbol{j}^{mf}$, it is necessary to substitute Eq. (3.34) into Eq. (3.39) and to solve for j_α and j_β:

$$j_\alpha = -\sin\beta\ j_x^{mf} + \cos\beta\ l_z, \quad j_\beta = j_y^{mf}, \quad \text{and} \quad j_z^{mf} = l_z. \tag{3.40}$$

Then, the alternative form for the kinetic energy is

$$T = \frac{p_r^2}{2m_e} + \frac{1}{2\mu_{bc} r^2}\left[(j_x - l_x)^2 + (j_y - l_y)^2\right] + \frac{1}{2m_e}\sum_{k_{bc}} \boldsymbol{p}_{k_{bc}}^2 + \frac{1}{2m_{bc}}\left(\sum_{k_{bc}} \boldsymbol{p}_{k_{bc}}\right)^2. \tag{3.41}$$

The superscript *'mf'* has been dropped in the above equation. Unless otherwise stated, $\boldsymbol{j}$ represents the total angular momentum projected onto the axes of the mf frame.

The quantum mechanical Hamiltonian operator is obtained by applying the Podolsky trick [108]. With this method, it is possible to use the classical Hamiltonian in terms of generalized coordinates q_i and their conjugate momenta p_i and to replace the p_i by $\frac{\hbar}{i}\frac{\partial}{\partial q_i}$ to obtain the quantum mechanical Hamiltonian operator [109]. The classical Hamiltonian can be written in the form as

$$H_{cl} = \frac{1}{2}\sum_{i,j} p_i \left(\mathsf{G}^{-1}\right)_{ij} p_j + V(\cdots q_i \cdots) \tag{3.42}$$

Here, the matrix G^{-1} generates the quadratic form in the conjugate momenta p_i and p_j. Podolsky showed that by rewriting the classical Hamiltonian in the form

$$H_{qm} = \frac{1}{2} s^{-1/2} g^{-1/4} \sum_{i,j} p_i \; g^{1/2} \Big(\mathsf{G}^{-1}\Big)_{ij} p_j \; g^{-1/4} s^{1/2}, \tag{3.43}$$

the Hamiltonian operator is correctly obtained by replacing p_i by $\frac{\hbar}{i}\frac{\partial}{\partial q_i}$. Here, g is the determinant of the matrix G. s is the weight factor for the volume element involved in the coordinate transformation from Cartesian to general coordinates. After a straightforward algebra, the quantum mechanical Hamiltonian operator is obtained in the following form:

$$\begin{aligned} H &= -\frac{\hbar^2}{2\mu_{bc} r^2}\frac{\partial}{\partial r} r^2 \frac{\partial}{\partial r} + \frac{1}{2\mu_{bc} r^2}\left[(j_x - l_x)^2 + \frac{1}{\sin\beta}(j_y - l_y)\sin\beta\,(j_y - l_y)\right] \\ &\quad -\frac{\hbar^2}{2m_e}\sum_{k_{bc}} \nabla^2_{k_{bc}} - \frac{\hbar^2}{2m_{bc}} \sum_{j_{bc},k_{bc}} \nabla_{k_{bc}} \cdot \nabla_{j_{bc}} + V(r, \boldsymbol{\eta}_{k_{bc}}) \end{aligned} \tag{3.44}$$

A diatom (or a linear molecule) has only two rotational degrees of freedom corresponding to the two Euler angles α and β required to specify the direction of the diatom axis (z axis) in space. As a result of the absence of the third angle χ, the components of the angular momentum operator in the molecule fixed frame obey neither normal nor anomalous commutation relations. Furthermore, the rotational kinetic energy operator for a linear molecule is more complicated than that of a nonlinear molecule due to the presence of the extra angular factors $\sin\beta$ [109]. A method

has been devised for introducing the angle χ as an independent variable for a linear molecule. This is done by defining an isomorphic Hamiltonian [110, 111, 112, 113]. Since the isomorphic Hamiltonian has one more degree of freedom than the actual Hamiltonian, it has more eigenvalues which are not eigenvalues of the actual Hamiltonian. Therefore, a subset of the eigenfunctions to the isomorphic Hamiltonian must be chosen in order to derive the eigenfunctions to the actual Hamiltonian. The components of the angular momentum vector which appear in the mf axes follow anomalous commutation rules and thus the rotational kinetic energy operator is simplified. In this respect, the linear molecule can be treated in the same way as a nonlinear molecule.

Assuming that ψ is an eigenfunction of the Schrödinger equation

$$H\psi = E\psi,$$

the isomorphic Hamiltonian is derived by transforming the wavefunction with a unitary operator e^{iS}:

$$\tilde{\psi} = e^{iS}\psi \quad \text{with} \quad S = \frac{1}{\hbar} l_z \chi. \tag{3.45}$$

If the Hamiltonian commutes with l_z, then the transformed wavefunction differs only by a phase factor $e^{i\lambda\chi}$. Substituting $\tilde{\psi}$ for ψ and using the property of a unitary operator, a new Schrödinger equation is obtained:

$$He^{-iS}e^{iS}\psi = Ee^{-iS}e^{iS}\psi \quad \Longleftrightarrow \quad e^{iS}He^{-iS}\tilde{\psi} = E\tilde{\psi}. \tag{3.46}$$

In other words, the Hamiltonian is transformed to

$$\tilde{H} = e^{iS}He^{-iS} \tag{3.47}$$

which defines a new Schrödinger equation

$$\tilde{H}\tilde{\psi} = E\tilde{\psi} \tag{3.48}$$

with the same energy eigenvalues. In order to determine a transformed operator $\tilde{A}$, the operator e^{iS} is expanded into a Taylor series:

$$\begin{aligned}\tilde{A} &= e^{iS}Ae^{-iS} \\ &= A + i[S,A] + \frac{i^2}{2!}[S,[S,A]] + \frac{i^3}{3!}[S,[S,[S,A]]] + \cdots . \end{aligned} \tag{3.49}$$

With the normal commutation relation for $\boldsymbol{l}$ and the unusual commutation relation for the total angular momentum [109], it can be shown that the components of the transformed angular momentum operator $\tilde{\boldsymbol{j}} - \tilde{\boldsymbol{l}}$ have the following form:

$$\begin{aligned}(\tilde{j}_x - \tilde{l}_x) &= \cos\chi(j_x - l_x) + \sin\chi(j_y - l_y), \\ (\tilde{j}_y - \tilde{l}_y) &= -\sin\chi(j_x - l_x) + \cos\chi(j_y - l_y), \\ (\tilde{j}_z - \tilde{l}_z) &= (j_z - l_z). \end{aligned} \tag{3.50}$$

The Hamiltonian is transformed by Eq. (3.50) to the isomorphic Hamiltonian in the form of

$$\begin{aligned}\tilde{H} &= -\frac{\hbar^2}{2\mu_{bc}r^2}\frac{\partial}{\partial r}r^2\frac{\partial}{\partial r} + \frac{1}{2\mu_{bc}r^2}\Big[\left(\tilde{j}_x - \tilde{l}_x\right)^2 + \left(\tilde{j}_y - \tilde{l}_y\right)^2\Big] \\ &\quad -\frac{\hbar^2}{2m_e}\sum_{k_{bc}}\nabla^2_{k_{bc}} - \frac{\hbar^2}{2m_{bc}}\sum_{j_{bc},k_{bc}}\nabla_{k_{bc}}\cdot\nabla_{j_{bc}} + V(r,\boldsymbol{\eta}_{k_{bc}}). \end{aligned} \tag{3.51}$$

Remembering that the new mf frame is rotated by three angles (α,β,χ), it is safe to drop the tildes on $\boldsymbol{j}$, $\boldsymbol{l}$, and H. The final diatomic Hamiltonian is

$$H = H_{vib} + H_{rot} + H_{el} \tag{3.52}$$

where the electronic Hamiltonian, H^{el}, is defined as

$$H_{el} = -\frac{\hbar^2}{2m_e}\sum_{k_{bc}}\nabla^2_{k_{bc}} - \frac{\hbar^2}{2m_{bc}}\sum_{j_{bc},k_{bc}}\nabla_{k_{bc}}\cdot\nabla_{j_{bc}} + V(r,\boldsymbol{\eta}_{k_{bc}}), \tag{3.53}$$

the vibrational Hamiltonian, H_{vib}, as

$$H_{vib} = -\frac{\hbar^2}{2\mu_{bc}r^2}\frac{\partial}{\partial r}r^2\frac{\partial}{\partial r}, \tag{3.54}$$

and the rotational Hamiltonian, H_{rot}, as

$$H_{rot} = \frac{1}{2\mu_{bc}r^2}\Big[\,(j_x - l_x)^2 + (j_y - l_y)^2\,\Big] \tag{3.55}$$

The rotational Hamiltonian can also be expressed as

$$H_{rot} = \frac{1}{2\mu_{bc}r^2}\big[\;\Re_x^2 \;+\; \Re_y^2\;\big] \tag{3.56}$$

where $\boldsymbol{\Re} = \boldsymbol{j} - \boldsymbol{l}$ is the rotational angular momentum.

3.1.3 Energy Eigenvalues of NO

For an open shell diatom like NO, the spin must be included in the total angular momentum. The total angular momentum is defined as the sum of the nuclear rotational angular momentum, the electronic orbital angular momentum and the electronic spin angular momentum: $\boldsymbol{j} = \boldsymbol{\Re} + \boldsymbol{l} + \boldsymbol{s}$. This is equivalent to replacing $\boldsymbol{l}$ by $\boldsymbol{l} + \boldsymbol{s}$. The contribution to the energy caused by the nuclear rotation is expressed as

$$\begin{aligned} H_{rot} &= \frac{1}{2\mu_{bc}r^2}\big[\;\Re_x^2 \;+\; \Re_y^2\;\big] \\ &= \frac{1}{2\mu_{bc}r^2}\Big[\,(j_x - l_x - s_x)^2 + (j_y - l_y - s_y)^2\,\Big]. \end{aligned} \tag{3.57}$$

Eigenvalues and eigenfunctions are determined by solving the Schrödinger equation. In doing so, one must first determine a basis set which defines a matrix representation. Then, the complete solutions are determined by diagonalizing the Hamiltonian matrix. The eigenfunctions are represented by a linear combination of basis states. Within the validity of the Born-Oppenheimer approximation, the complete wavefunctions are products of wavefunctions describing the electronic and the nuclear motion. The nuclear motion involves the vibrational and the rotational

motion. Then, the total wavefunction can be written as a product of wavefunctions describing the electronic, vibrational, and rotational motion.

$$\Psi = \psi^{el}\psi^{vib}\psi^{rot}. \tag{3.58}$$

The electronic part of the wavefunction ψ^{el} is obtained from the electronic Schrödinger equation

$$H_{el}\psi^{el} = E_{el}\psi^{el}. \tag{3.59}$$

It can be shown that the z-component of the electron orbital angular momentum, l_z, commutes with the electronic Hamiltonian H_{el}. Then, it is possible to take a wavefunction ψ^{el} which is a simultaneous eigenfunction of the operators H_{el} and l_z. The index λ which is the quantum number of the l_z operator is added to the electronic wavefunction as ψ^{el}_{λ}. And for $|\lambda| > 0$, there are two eigenfunctions corresponding to λ and $-\lambda$ which are degenerate.

The rotational part of the Hamiltonian is partitioned into a diagonal part $H^{(0)}_{rot}$ and a coupling term $H^{(1)}_{rot}$,

$$\begin{aligned} H_{rot} &= \frac{1}{2\mu_{bc}r^2}\Big[(j_x - l_x - s_x)^2 + (j_y - l_y - s_y)^2\Big] \\ &= H^{(00)}_{rot} + H^{(0)}_{rot} + H^{(1)}_{rot} \end{aligned} \tag{3.60}$$

where

$$H^{(00)}_{rot} = \frac{1}{2\mu_{bc}r^2}(l^2 - l_z^2), \tag{3.61}$$

$$H^{(0)}_{rot} = \frac{1}{2\mu_{bc}r^2}\Big[(j^2 - j_z^2) + (l^2 - l_z^2) + (s^2 - s_z^2)\Big], \tag{3.62}$$

$$H^{(1)}_{rot} = \frac{1}{2\mu_{bc}r^2}\Big[(l^+s^- + l^-s^+) - (j^+l^- + j^-l^+) - (j^+s^- + j^-s^+)\Big]. \tag{3.63}$$

Here, the raising ($-$sign) and lowering ($+$sign) operators are defined as

$$j^{\pm} = j_x \pm ij_y, \;\; l^{\pm} = l_x \pm il_y, \;\; s^{\pm} = s_x \pm is_y.$$

The basis set is chosen in such a way that the operator $H_{rot}^{(0)}$ has only diagonal matrix elements while the operator $H_{rot}^{(1)}$ gives rise to the off-diagonal matrix elements. For the term $H_{rot}^{(00)}$, the electronic wavefunctions are generally not eigenfunctions of $\boldsymbol{l}^2$. But, the expectation value of $\boldsymbol{l}^2$ is a weakly R-dependent quantity for a given electronic state. Therefore, the quantity

$$\frac{\hbar^2}{2\mu_{bc}r^2}\Big[l(l+1)-\lambda^2\Big] \tag{3.64}$$

may be incorporated into the electronic energy. On the other hand, the zeroth order rotational contribution $H_{rot}^{(0)}$ commutes with the operators $j^2,\ j_z,\ j_z^{sf}$ and $s^2,\ s_z$. The eigenvalue equation of $H_{rot}^{(0)}$ defines the zeroth order rotational eigenfunctions:

$$H_{rot}^{(0)}\psi^{rot} = E_{rot}\psi^{rot}. \tag{3.65}$$

The normalized rotational eigenfunction including spin is

$$\tilde{\psi}^{rot}(\alpha,\beta,\chi) = \sqrt{\frac{2j+1}{8\pi^2}}\ D_{m\omega}^{(j)*}(\alpha,\beta,\chi)\ \Gamma_{s\sigma} = \big|jm\omega\big\rangle\big|s\sigma\big\rangle. \tag{3.66}$$

where $D_{m\omega}^{(j)*}(\alpha,\beta,\chi)$ is a Wigner D-function which represents an element of the rotation matrix [114]. $j,\ m$, and ω denote the quantum numbers for the total angular momentum and its projections onto the mf and sf z-axes, respectively. Now, the basis states without the vibrational part can be written in the form:

$$\begin{aligned}\tilde{\Psi}_j(\alpha,\beta,\chi,r,\boldsymbol{\eta}_{\boldsymbol{jbc}}) &= \sqrt{\frac{2j+1}{8\pi^2}}\ D_{m\omega}^{(j)*}(\alpha,\beta,\chi)\ \psi_\lambda^{el}\ \Gamma_{s\sigma} \\ &= \big|jm\omega\big\rangle\big|n\lambda\big\rangle\big|s\sigma\big\rangle. \end{aligned}\tag{3.67}$$

This basis set is used to set up the matrix representation of the isomorphic Hamiltonian resulting in only small off-diagonal elements. Basis states with well defined symmetry are constructed as

$$\begin{aligned}\tilde{\Psi}_{j,|\omega|,\epsilon}(\alpha,\beta,\chi,r,\boldsymbol{\eta}_{\boldsymbol{jbc}}) &= \frac{1}{\sqrt{2}}\sqrt{\frac{2j+1}{8\pi^2}}\Big[D_{m\omega}^{(j)*}(\alpha,\beta,\chi)\ \psi_\lambda^{el}\ \Gamma_{s\sigma} \\ &\qquad +\epsilon D_{m-\omega}^{(j)*}(\alpha,\beta,\chi)\ \psi_{-\lambda}^{el}\ \Gamma_{s-\sigma}\Big]. \end{aligned}\tag{3.68}$$

The eigenfunctions for the true Hamiltonian are found by imposing the following restriction on the eigenfunctions of the isomorphic Hamiltonian:

$$j_\chi \tilde{\Psi} = \frac{\hbar}{i}\frac{\partial}{\partial \chi}\left[e^{\frac{i}{\hbar}(l_z+s_z)\chi}\ \Psi\right] = (l_z+s_z)e^{\frac{i}{\hbar}(l_z+s_z)\chi}\ \Psi = (l_z+s_z)\ \tilde{\Psi}. \tag{3.69}$$

Among the eigenfunctions of the isomorphic Hamiltonian only those are accepted which satisfy the relation, $\omega = \lambda + \sigma$, where σ is the projection of the spin $\boldsymbol{s}$ onto the mf z-axis. The corresponding basis states to the original Hamiltonian are obtained by transforming Eq. (3.68).

$$\begin{aligned}\Psi_{j,|\omega|,\epsilon}(\alpha,\beta,r,\boldsymbol{\eta_{jbc}}) \;&=\; \frac{1}{\sqrt{2}}\sqrt{\frac{2j+1}{4\pi}}\Big[D^{(j)*}_{m\omega}(\alpha,\beta,0)\ \psi^{el}_{\lambda}\ \Gamma_{s\sigma} \\ &\qquad +\epsilon D^{(j)*}_{m-\omega}(\alpha,\beta,0)\ \psi^{el}_{-\lambda}\ \Gamma_{s-\sigma}\Big].\end{aligned} \tag{3.70}$$

Note that the normalization factor $\frac{1}{\sqrt{2\pi}}$ has been left out due to the lack of the angle χ. Using ket-vector notation, the basis functions can be written as

$$\big|njm|\omega|\epsilon\big\rangle = \frac{1}{\sqrt{2}}\Big\{\big|jm\omega\big\rangle\big|n\lambda\big\rangle\big|s\sigma\big\rangle + \epsilon\big|jm\ {-\omega}\big\rangle\big|n\ {-\lambda}\big\rangle\big|s\ {-\sigma}\big\rangle\Big\} \tag{3.71}$$

with $\omega = \lambda + \sigma$. These basis states describe the dependence of the complete wavefunction on all coordinates except the radial distant r. It is possible to expand the complete wavefunction in terms of the above basis set with an unknown, r-dependent coefficient $\big|v\big\rangle$. Hence, the complete basis states can be written in the form:

$$\Psi^{tot} = \frac{1}{\sqrt{2}}\big|v\big\rangle\Big\{\big|jm\omega\big\rangle\big|n\lambda\big\rangle\big|s\sigma\big\rangle + \epsilon\big|jm\ {-\omega}\big\rangle\big|n\ {-\lambda}\big\rangle\big|s\ {-\sigma}\big\rangle\Big\}. \tag{3.72}$$

The eigenvalues of the rotational Hamiltonian are obtained from

$$\frac{1}{2\mu_{bc}r^2}\big[(j^2-j_z^2)+(s^2-s_z^2)\big]\big|jm\omega\big\rangle = E_{rot}(r)\big|jm\omega\big\rangle. \tag{3.73}$$

This results in the r-dependent energy as

$$E_{rot}(r) = \frac{\hbar^2}{2\mu_{bc}r^2}\Big[j(j+1)-\omega^2+s(s+1)-\sigma^2\Big]. \tag{3.74}$$

After integration of the rotational eigenvalue equation over the vibrational coordinate, the diagonal part of the rotational energy is found to be

$$E_{rot}(r) = B_v\Big[j(j+1) - \omega^2 + s(s+1) - \sigma^2\Big] \tag{3.75}$$

where the rotational constant is defined as

$$B_v = \big\langle v\big|\frac{\hbar^2}{2\mu_{bc}r^2}\big|v\big\rangle. \tag{3.76}$$

The Hamiltonian described so far is the nonrelativistic one. A relativistic term due to the interaction between the spin and the orbital angular momentum of an electron, the so called spin-orbit operator, must be added to the Hamiltonian. For a single-electron configuration as in the case of NO, the approximate spin-orbit interaction is written as

$$H^{SO} = A(r)\boldsymbol{l}\cdot\boldsymbol{s} = A(r)l_z s_z + \frac{1}{2}A(r)\big[l^+ s^- + l^- s^+\big]. \tag{3.77}$$

The selection rules for the matrix elements of H^{SO} are:

$$\begin{aligned} \Delta j = 0; \qquad & \Delta\omega = 0; \qquad e \not\leftrightarrow f; \\ \Delta s = 0 \qquad & \text{or} \qquad \Delta s = \pm 1; \\ \Delta\lambda = \Delta\sigma = 0 \qquad & \text{or} \qquad \Delta\lambda = -\Delta\sigma = \pm 1. \end{aligned} \tag{3.78}$$

If the two interacting states belong to the same configuration, the diagonal part contributes ($\Delta\lambda = \Delta\sigma = 0$). If the two states differ by one spin-orbital as will be seen later for $^2\Pi \sim {}^2\Sigma$ interaction, then the off-diagonal terms of the spin-orbit operator contribute ($\Delta\lambda = -\Delta\sigma = \pm 1$). For diagonal matrix elements, the spin-orbit coupling constant, A_v, is defined as

$$\big\langle v, j\, m\, \omega\, \lambda\, s\, \sigma\, \big|H^{SO}\big|v, j\, m\, \omega\, \lambda\, s\, \sigma\, \big\rangle = A_v\lambda\sigma. \tag{3.79}$$

The total Hamiltonian for NO takes the form:

$$H = H_{el} + H_{vib} + H_{rot} + H^{SO}. \tag{3.80}$$

The off-diagonal terms of the rotational Hamiltonian $H_{rot}^{(1)}$ are related to perturbations between different electronic states

1. $(1/2\mu_{bc}r^2)[l^+s^- + l^-s^+]$ gives the spin-electronic perturbation between basis states of the same ω(homogeneous) and s, but different λ and σ. The selection rules for this perturbation are

$$\Delta\omega = 0, \;\; \Delta\lambda = -\Delta\sigma = \pm 1, \;\; \Delta s = 0.$$

2. $(1/2\mu_{bc}r^2)[j^+s^- + j^-s^+]$ is the spin-uncoupling operator which is responsible for the electronic-rotational perturbations between basis states of different ω (heterogeneous) having the same values of s and λ, but different σ. The selection rules for the spin-uncoupling operator are

$$\Delta s = 0, \;\; \Delta\omega = \Delta\sigma = \pm 1, \;\; \Delta\lambda = 0.$$

3. $(1/2\mu_{bc}r^2)[j^+l^- + j^-l^+]$ is the l-uncoupling operator which is responsible for the electronic-rotational perturbations between basis states of different ω (heterogeneous) having the same values of s and σ, but different λ. The selection rules for this operator are

$$\Delta s = 0, \;\; \Delta\omega = \Delta\lambda = \pm 1.$$

These off-diagonal terms are responsible for the phenomenon of 'λ-doubling' which is discussed in Section 3.1.3.1.

The ground state of NO is a $^2\Pi$ state that is split by spin-orbit interaction into $^2\Pi_{1/2}$ and $^2\Pi_{3/2}$ components with a separation of about 123 cm^{-1}. For NO the $^2\Pi_{1/2}$ state is lower in energy. Since the spin-orbit splitting is much larger than the rotational constant ($B_0 = 1.697$ cm^{-1} for the ground state, $B_0 = 2.06$ cm^{-1} for Rydberg states), the wavefunction can be well described in terms of Hund's case (a)

basis functions. For this case, the good quantum numbers are $j,\ s,\ \omega,\ \lambda$, and σ, with $\omega = \lambda + \sigma$. For a $^2\Pi$ state, there are four possible basis functions:

$$\left|^2\Pi_{3/2}\right\rangle = \left|n, \lambda = 1\right\rangle \left|v\right\rangle \left|j, m, \omega = \tfrac{3}{2}\right\rangle \left|s = \tfrac{1}{2}, \sigma = \tfrac{1}{2}\right\rangle \tag{3.81a}$$

$$\left|^2\Pi_{1/2}\right\rangle = \left|n, \lambda = 1\right\rangle \left|v\right\rangle \left|j, m, \omega = \tfrac{1}{2}\right\rangle \left|s = \tfrac{1}{2}, \sigma = -\tfrac{1}{2}\right\rangle \tag{3.81b}$$

$$\left|^2\Pi_{-1/2}\right\rangle = \left|n, \lambda = -1\right\rangle \left|v\right\rangle \left|j, m, \omega = -\tfrac{1}{2}\right\rangle \left|s = \tfrac{1}{2}, \sigma = \tfrac{1}{2}\right\rangle \tag{3.81c}$$

$$\left|^2\Pi_{-3/2}\right\rangle = \left|n, \lambda = -1\right\rangle \left|v\right\rangle \left|j, m, \omega = -\tfrac{3}{2}\right\rangle \left|s = \tfrac{1}{2}, \sigma = -\tfrac{1}{2}\right\rangle. \tag{3.81d}$$

At this moment, only $\omega > 0$ components are considered. The resulting Hamiltonian matrix has the form:

$$\begin{pmatrix} \left\langle^2\Pi_{3/2}\right|H\left|^2\Pi_{3/2}\right\rangle & \left\langle^2\Pi_{3/2}\right|H\left|^2\Pi_{1/2}\right\rangle \\ \left\langle^2\Pi_{1/2}\right|H\left|^2\Pi_{3/2}\right\rangle & \left\langle^2\Pi_{1/2}\right|H\left|^2\Pi_{1/2}\right\rangle \end{pmatrix}. \tag{3.82}$$

In calculating the matrix elements, it is assumed that the two substates $^2\Pi_{1/2}$ and $^2\Pi_{3/2}$ have the same potential curves and the same vibrational wavefunctions. The matrix elements of the spin-orbit part are

$$\left\langle^2\Pi_{3/2}\right|H^{SO}\left|^2\Pi_{3/2}\right\rangle = \frac{A_v}{2}, \quad \left\langle^2\Pi_{1/2}\right|H^{SO}\left|^2\Pi_{1/2}\right\rangle = -\frac{A_v}{2}, \tag{3.83}$$

and

$$\left\langle^2\Pi_{1/2}\right|H^{SO}\left|^2\Pi_{3/2}\right\rangle = 0. \tag{3.84}$$

Then, the diagonal matrix elements are

$$\left\langle^2\Pi_{3/2}\right|H\left|^2\Pi_{3/2}\right\rangle = T_\Pi^v + \frac{A_v}{2} + B_v[(j+\tfrac{1}{2})^2 - 2)] \tag{3.85}$$

and

$$\left\langle^2\Pi_{1/2}\right|H\left|^2\Pi_{1/2}\right\rangle = T_\Pi^v - \frac{A_v}{2} + B_v(j+\tfrac{1}{2})^2. \tag{3.86}$$

where T_Π^v represents the sum of E^{el} and E^{vib} for the Π state. The only nonvanishing off-diagonal element between these two substates is given by the spin-uncoupling

part of the rotational Hamiltonian. The off-diagonal matrix element of the spin-uncoupling operator is

$$\begin{aligned}
&\Big\langle v,j,\lambda,s,\sigma+1,\omega+1\Big|\Big(-\frac{1}{2\mu_{bc}r^2}j^-s^+\Big)\Big|v,j,\lambda,s,\sigma,\omega\Big\rangle \\
= \;& -\big\langle v\big|\frac{1}{2\mu_{bc}r^2}\big|v\big\rangle\big[s(s+1)-\sigma(\sigma+1)\big]^{1/2}\big[j(j+1)-\omega(\omega+1)\big]^{1/2} \\
= \;& -B_v\big[(j+\tfrac{1}{2})^2-1\big]^{1/2}. \qquad (3.87)
\end{aligned}$$

In the last line of the above equation, $\lambda=1, s=\frac{1}{2}, \sigma=-\frac{1}{2}$, and $\omega=\frac{1}{2}$ are used. The other part of the spin-uncoupling operator j^+s^- acts between $^2\Pi_{-1/2}$ and $^2\Pi_{-3/2}$ and gives the same matrix element. There are no off-diagonal matrix elements of the spin-uncoupling operator between $\omega>0$ and $\omega<0$ basis functions. The 2×2 Hamiltonian matrix is found to be

$$\begin{pmatrix}
T_\Pi^v-\frac{A_v}{2}+B_v(j+\frac{1}{2})^2 & -B_v\big[(j+\frac{1}{2})^2-1\big]^{1/2} \\
-B_v\big[(j+\frac{1}{2})^2-1\big]^{1/2} & T_\Pi^v+\frac{A_v}{2}+B_v\big[(j+\frac{1}{2})^2-2\big]
\end{pmatrix}. \qquad (3.88)$$

By diagonalizing the above matrix, the well known eigenvalues are found as [115, 116]

$$E=T_\Pi^v+B_v\big[(j+\tfrac{1}{2})^2-1\big]\pm\frac{B_v}{2}\big[Y(Y-4)+4(j+\tfrac{1}{2})^2\big]^{1/2} \qquad (3.89)$$

where

$$Y=A_v/B_v. \qquad (3.90)$$

It is customary to use F_1 and F_2 to label the different spin-orbit components with F_1 having lower energy. With this notation, the eigenvalues are

$$E(F_1) = T_\Pi^v+B_v\big[(j+\tfrac{1}{2})^2-1-\frac{X}{2}\big], \qquad (3.91a)$$

$$E(F_2) = T_\Pi^v+B_v\big[(j+\tfrac{1}{2})^2-1+\frac{X}{2}\big] \qquad (3.91b)$$

where

$$X=\big[Y(Y-4)+4(j+\tfrac{1}{2})^2\big]^{1/2}. \qquad (3.92)$$

An identical matrix is obtained for the case $\omega < 0$. Thus, the eigenvalues are the same as Eq. (3.91). As a result, the 4×4 Hamiltonian matrix in the basis set of Eqs. (3.81) is block-diagonal:

$$\begin{pmatrix} T_\Pi^v - \frac{A_v}{2} + B_v(j+\frac{1}{2})^2 & -B_v[(j+\frac{1}{2})^2-1]^{1/2} & 0 & 0 \\ -B_v[(j+\frac{1}{2})^2-1]^{1/2} & T_\Pi^v + \frac{A_v}{2} + B_v[(j+\frac{1}{2})^2-2] & 0 & 0 \\ 0 & 0 & T_\Pi^v - \frac{A_v}{2} + B_v(j+\frac{1}{2})^2 & -B_v[(j+\frac{1}{2})^2-1]^{1/2} \\ 0 & 0 & -B_v[(j+\frac{1}{2})^2-1]^{1/2} & T_\Pi^v + \frac{A_v}{2} + B_v[(j+\frac{1}{2})^2-2] \end{pmatrix}. \tag{3.93}$$

The upper left block of the matrix involves states with $\omega > 0$ and the lower right block involves states with $\omega < 0$. The eigen energies are degenerate for $\omega > 0$ and $\omega < 0$.

λ-DOUBLING

It is well known that the interaction of $^2\Pi$ states with electronic $^2\Sigma^+$ states causes each of the two spin-orbit components to be split into a doublet with a splitting of about 10^{-2} cm^{-1}. This splitting is called the 'λ-doubling'. In order to calculate the λ-doubling of the ground state, it is necessary to consider the levels of an isolated $^2\Sigma^+$ state first. The energy levels of such a state also contain contributions due to the spin-uncoupling operator. The Hund's case (a) basis function that corresponds to the $\omega = +\frac{1}{2}$ component of this state is

$$\left|^2\Sigma^+_{1/2}\right\rangle = \left|n, \lambda = 0\right\rangle \left|v\right\rangle \left|j, m, \omega = \tfrac{1}{2}\right\rangle \left|s = \tfrac{1}{2}, \sigma = \tfrac{1}{2}\right\rangle, \tag{3.94}$$

while that corresponding to the $\omega = -\frac{1}{2}$ component is given by

$$\left|^2\Sigma^+_{-1/2}\right\rangle = \left|n, \lambda = 0\right\rangle \left|v\right\rangle \left|j, m, \omega = -\tfrac{1}{2}\right\rangle \left|s = \tfrac{1}{2}, \sigma = -\tfrac{1}{2}\right\rangle. \tag{3.95}$$

The diagonal matrix elements of both components are identical:

$$\begin{aligned} & \left\langle {}^2\Sigma^+_{\pm 1/2}\middle| H \middle|{}^2\Sigma^+_{\pm 1/2}\right\rangle \\ = \;& T^v_\Sigma + B_v\big[j(j+1) - (\tfrac{1}{2})^2 + (\tfrac{1}{2})(\tfrac{3}{2}) - (\tfrac{1}{2})^2\big] \\ = \;& T^v_\Sigma + B_v(j+\tfrac{1}{2})^2 \end{aligned} \tag{3.96}$$

where T^v_Σ is the sum of the electronic and the vibrational energy of the ${}^2\Sigma^+$ state. The off-diagonal matrix element is

$$\begin{aligned} & \left\langle {}^2\Sigma^+_{1/2}\middle| -\frac{1}{2\mu_{bc}r^2}J^-S^+ \middle|{}^2\Sigma^+_{-1/2}\right\rangle, \\ = \;& -B_v\Big[j(j+1)+\tfrac{1}{4}\Big]^{1/2} \\ = \;& -B_v\big(j+\tfrac{1}{2}\big). \end{aligned} \tag{3.97}$$

This term causes the two components to be mixed completely. Collecting the diagonal and the off-diagonal elements of the Hamiltonian matrix gives

$$\begin{pmatrix} T^v_\Sigma + B_v(j+\frac{1}{2})^2 & -B_v\big(j+\frac{1}{2}\big) \\ -B_v\big(j+\frac{1}{2}\big) & T^v_\Sigma + B_v(j+\frac{1}{2})^2 \end{pmatrix}. \tag{3.98}$$

Although this matrix can be diagonalized as it is, the diagonalization can be avoided by transforming the basis functions to symmetry adapted basis functions:

$$\left|{}^2\Sigma^{+e}\right\rangle = \frac{1}{\sqrt{2}}\Big\{\left|{}^2\Sigma^+_{1/2}\right\rangle + \epsilon\left|{}^2\Sigma^+_{-1/2}\right\rangle\Big\} \tag{3.99a}$$

$$\left|{}^2\Sigma^{+f}\right\rangle = \frac{1}{\sqrt{2}}\Big\{\left|{}^2\Sigma^+_{1/2}\right\rangle - \epsilon\left|{}^2\Sigma^+_{-1/2}\right\rangle\Big\}. \tag{3.99b}$$

The Hamiltonian matrix in the transformed basis set becomes [117]

$$\begin{pmatrix} T^v_\Sigma + B_v\big[(j+\frac{1}{2})^2 - (j+\frac{1}{2})\big] & 0 \\ 0 & T^v_\Sigma + B_v\big[(j+\frac{1}{2})^2 + (j+\frac{1}{2})\big] \end{pmatrix}. \tag{3.100}$$

And the eigen energies are just the diagonal terms:

$$E(^2\Sigma^{+e}) = T_\Sigma^v + B_v\big[(j+\tfrac{1}{2})^2 - (j+\tfrac{1}{2})\big], \tag{3.101}$$

and

$$E(^2\Sigma^{+f}) = T_\Sigma^v + B_v\big[(j+\tfrac{1}{2})^2 + (j+\tfrac{1}{2})\big]. \tag{3.102}$$

Or, in a more compact form

$$E(^2\Sigma^{+e/f}) = T_\Sigma^v + B_v\big[(j+\tfrac{1}{2})^2 - \epsilon(j+\tfrac{1}{2})\big] \tag{3.103}$$

where $\epsilon = +1$ (-1) corresponds to the e (f) component.

The two components differ by $\Delta\omega = +1$, they can interact via the spin-uncoupling operator with the components of a $^2\Pi$ state. This interaction is important when the two components ($\omega > 0$ and $\omega < 0$) have the same energy. It is possible to express the Hamiltonian of the $^2\Pi$ states in terms of the symmetry adapted basis set. Then, new basis functions are formed by linear combinations of $\big|^2\Pi_{|\omega|}\big\rangle$ and $\big|^2\Pi_{-|\omega|}\big\rangle$:

$$\begin{aligned} &\big|^2\Pi, |\omega| = \tfrac{1}{2}, jm\epsilon v\big\rangle \\ = \;& \frac{1}{\sqrt{2}}\Big\{\big|n,\lambda=1\big\rangle\,\big|v\big\rangle\,\big|j,m,\omega=\tfrac{1}{2}\big\rangle\big|s=\tfrac{1}{2},\sigma=-\tfrac{1}{2}\big\rangle \\ &\quad +\epsilon\big|n,\lambda=-1\big\rangle\,\big|v\big\rangle\,\big|j,m,\omega=-\tfrac{1}{2}\big\rangle\big|s=\tfrac{1}{2},\sigma=\tfrac{1}{2}\big\rangle\Big\} \end{aligned} \tag{3.104}$$

and

$$\begin{aligned} &\big|^2\Pi, |\omega| = \tfrac{3}{2}, jm\epsilon v\big\rangle \\ = \;& \frac{1}{\sqrt{2}}\Big\{\big|n,\lambda=1\big\rangle\,\big|v\big\rangle\,\big|j,m,\omega=\tfrac{3}{2}\big\rangle\big|s=\tfrac{1}{2},\sigma=\tfrac{1}{2}\big\rangle \\ &\quad +\epsilon\big|n,\lambda=-1\big\rangle\,\big|v\big\rangle\,\big|j,m,\omega=-\tfrac{3}{2}\big\rangle\big|s=\tfrac{1}{2},\sigma=-\tfrac{1}{2}\big\rangle\Big\}. \end{aligned} \tag{3.105}$$

When the Hamiltonian matrix elements are calculated in terms of the symmetrized basis wavefunctions, the matrix element becomes

$$\begin{aligned} &\Big\langle^2\Pi, |\omega| = \tfrac{1}{2}, jm\epsilon' v\Big|\; H \;\Big|^2\Pi, |\omega| = \tfrac{1}{2}, jm\epsilon v\Big\rangle \\ = \;& \frac{1}{2}(1+\epsilon\epsilon')\Big[T_\Pi^v - \frac{A_v}{2} + B_v(j+\tfrac{1}{2})^2\Big] \end{aligned} \tag{3.106}$$

and

$$\begin{aligned} & \left\langle {}^2\Pi, |\omega| = \tfrac{3}{2}, jm\epsilon' v \right| H \left| {}^2\Pi, |\omega| = \tfrac{3}{2}, jm\epsilon v \right\rangle \\ = \; & \frac{1}{2}(1+\epsilon\epsilon')\Big[T_\Pi^v + \frac{A_v}{2} + B_v[(j+\tfrac{1}{2})^2 - 2]\Big]. \end{aligned} \tag{3.107}$$

The off-diagonal term is evaluated as

$$\begin{aligned} & \left\langle {}^2\Pi\,|\omega| = \tfrac{1}{2}, jm\epsilon' v \right| H_{rot}^{(1)} \left| {}^2\Pi\,|\omega| = \tfrac{3}{2}, jm\epsilon v \right\rangle \\ = \; & -\frac{(1+\epsilon\epsilon')}{2} B_v \Big[(j+\tfrac{1}{2})^2 - 1\Big]^{1/2} \end{aligned} \tag{3.108}$$

Since ϵ takes on the values of ± 1, it is obvious that all matrix element are zero for $\epsilon \neq \epsilon'$. Combining the diagonal and the off-diagonal terms, the matrix is the same as that for the unsymmetrized basis set:

$$\begin{pmatrix} T_\Pi^v - \frac{A_v}{2} + B_v(j+\frac{1}{2})^2 & -B_v\big[(j+\frac{1}{2})^2-1\big]^{1/2} & 0 & 0 \\ -B_v\big[(j+\frac{1}{2})^2-1\big]^{1/2} & T_\Pi^v + \frac{A_v}{2} + B_v\big[(j+\frac{1}{2})^2-2\big] & 0 & 0 \\ 0 & 0 & T_\Pi^v - \frac{A_v}{2} + B_v(j+\frac{1}{2})^2 & -B_v\big[(j+\frac{1}{2})^2-1\big]^{1/2} \\ 0 & 0 & -B_v\big[(j+\frac{1}{2})^2-1\big]^{1/2} & T_\Pi^v + \frac{A_v}{2} + B_v\big[(j+\frac{1}{2})^2-2\big] \end{pmatrix}. \tag{3.109}$$

Now, the upper left block of the matrix is associated with $\epsilon = +1$ and the lower right block with $\epsilon = -1$. Each block has identical elements. Diagonalizing the matrix gives the eigen energies which are degenerate in the symmetry quantum number ϵ. Results are the same as those calculated with only the $\omega > 0$ component.

$$\begin{aligned} E(F_1)^{e/f} &= T_\Pi^v + B_v\big[(j+\tfrac{1}{2})^2 - 1 - \frac{X}{2}\big], \\ E(F_2)^{e/f} &= T_\Pi^v + B_v\Big[(j+\tfrac{1}{2})^2 - 1 + \frac{X}{2}\big] \end{aligned} \tag{3.110}$$

where

$$X = \Big[Y(Y-4) + 4(j+\tfrac{1}{2})^2\Big]^{1/2}.$$

In order to take the interaction $^2\Sigma^+ \sim {}^2\Pi$ into account, it is necessary to assume that the potential curves of the $^2\Sigma^+$ and $^2\Pi$ are identical and that the configurations of the $^2\Sigma^+$ and $^2\Pi$ are σ^1 and π^1, respectively. There are several types of interactions:

1. $^2\Pi_{1/2} \sim {}^2\Sigma^+$ interaction
   (a) $\Delta\omega = 0$ interaction with $^2\Sigma^+$ via spin-orbit coupling
   (b) $\Delta\omega = 0$ interaction with $^2\Sigma^+$ via spin-electronic coupling
   (c) $\Delta\omega = 1$ interaction with $^2\Sigma^+$ via l-uncoupling
2. $^2\Pi_{3/2} \sim {}^2\Sigma^+$ interaction with $^2\Sigma^+$ via l-uncoupling

The matrix elements for each type of interaction are calculated as follows:

1. (a)

$$\begin{aligned}\left\langle \lambda = 1, \sigma = -\tfrac{1}{2}, \omega = \tfrac{1}{2}, v_\Pi \middle| H^{SO} \middle| \lambda = 0, \sigma = \tfrac{1}{2}, \omega = \tfrac{1}{2}, v_\Sigma \right\rangle \\ = \frac{a_+}{2} \left\langle v_\Pi \middle| v_\Sigma \right\rangle \end{aligned} \tag{3.111}$$

   where $a_+ = \left\langle \pi \middle| A(r) \boldsymbol{l}^+ \middle| \sigma \right\rangle$ and $\left\langle v_\Pi \middle| v_\Sigma \right\rangle = \delta_{v_\Pi v_\Sigma}$.

   (b)

$$\begin{aligned}\left\langle \lambda = 1, \sigma = -\tfrac{1}{2}, \omega = \tfrac{1}{2}, v_\Pi \left| \frac{\boldsymbol{l}^+ \boldsymbol{s}^-}{2\mu_{bc} r^2} \right| \lambda = 0, \sigma = \tfrac{1}{2}, \omega = \tfrac{1}{2}, v_\Sigma \right\rangle \\ = B_{v_\Pi v_\Sigma} b \end{aligned} \tag{3.112}$$

   where $b = \left\langle \pi \middle| \boldsymbol{l}^+ \middle| \sigma \right\rangle$ and $B_{v_\Pi v_\Sigma} = B_v \delta_{v_\Pi v_\Sigma}$.

   (c)

$$\begin{aligned}\left\langle \lambda = 1, \sigma = -\tfrac{1}{2}, \omega = \tfrac{1}{2}, v_\Pi \left| \frac{\boldsymbol{j}^- \boldsymbol{l}^+}{2\mu_{bc} r^2} \right| \lambda = 0, \sigma = -\tfrac{1}{2}, \omega = -\tfrac{1}{2}, v_\Sigma \right\rangle \\ = -B_{v_\Pi v_\Sigma} b\left(j + \tfrac{1}{2}\right) \end{aligned} \tag{3.113}$$

2.

$$\begin{aligned}
&\Big\langle \omega=\tfrac{3}{2},\lambda=1,\sigma=\tfrac{1}{2},v_\Pi\Big|\frac{\boldsymbol{j}^-\boldsymbol{l}^+}{2\mu_{bc}r^2}\Big|\omega=\tfrac{1}{2},\lambda=0,\sigma=\tfrac{1}{2},v_\Sigma\Big\rangle\\
=\;& -bB_v\big[j(j+1)-(\tfrac{1}{2})(\tfrac{3}{2})\big]^{1/2}\big[(\tfrac{1}{2})(\tfrac{3}{2})-(-\tfrac{1}{2})(\tfrac{1}{2})\big]^{1/2}\\
=\;& -bB_v\big[(j+\tfrac{1}{2})-1\big]^{1/2}. \qquad (3.114)
\end{aligned}$$

For e/f symmetrized basis functions, the off-diagonal ${}^2\Pi_{1/2}\sim{}^2\Sigma^+$ elements are

$$\begin{aligned}
&\big\langle {}^2\Pi^{e/f}_{1/2}\big|\big(H^{SO}+H^{(1)}_{rot}\big)\big|{}^2\Sigma^{+e/f}\big\rangle\\
=\;& \frac{1}{\sqrt{2}}\Big\{\big\langle j,\omega=-\tfrac{1}{2},\lambda=-1,\sigma=-\tfrac{1}{2},v_\Pi\big|\\
&\qquad +\epsilon\big\langle j,\omega=\tfrac{1}{2},\lambda=1,\sigma=-\tfrac{1}{2},v_\Pi\big|\Big\}\Big(H^{SO}+H^{(1)}_{rot}\Big)\\
&\times\frac{1}{\sqrt{2}}\Big\{\big|j,\omega=\tfrac{1}{2},\lambda=0,\sigma=\tfrac{1}{2},v_\Sigma\big\rangle\\
&\qquad +\epsilon'\big|j,\omega=-\tfrac{1}{2},\lambda=0,\sigma=-\tfrac{1}{2},v_\Sigma\big\rangle\Big\}\\
=\;& \frac{1+\epsilon\epsilon'}{2}\Big[\frac{a_+}{2}+bB_v-\epsilon\, bB_v\big(j+\tfrac{1}{2}\big)\Big]\\
=\;& \delta_{\epsilon\epsilon'}\Big[\frac{a_+}{2}+bB_v-\epsilon\, bB_v\big(j+\tfrac{1}{2}\big)\Big]. \qquad (3.115)
\end{aligned}$$

And the $e\sim f$ matrix elements vanish,

$$\big\langle {}^2\Pi^{e/f}_{1/2}\big|H^{SO}+H^{(1)}_{rot}\big|{}^2\Sigma^{+f/e}\big\rangle=0. \qquad (3.116)$$

The off-diagonal ${}^2\Pi_{3/2}\sim{}^2\Sigma^+$ elements are for the e/f symmetrized basis functions,

$$\big\langle {}^2\Pi^{e/f}_{3/2}\big|H^{(1)}_{rot}\big|{}^2\Sigma^{+e/f}\big\rangle=-bB_v\big[(j-\tfrac{1}{2})(j+\tfrac{3}{2})\big]^{1/2}. \qquad (3.117)$$

The e and f components are degenerate.

The matrix for the above interactions is as follows:

$$\begin{array}{c} \\ {}^2\Pi_{1/2}\\ {}^2\Pi_{3/2}\\ {}^2\Sigma^+ \end{array}
\begin{array}{c}
\begin{array}{ccc} {}^2\Pi_{1/2} & {}^2\Pi_{3/2} & {}^2\Sigma^+ \end{array}\\
\left(\begin{array}{ccc}
T^v_\Pi-\frac{A_v}{2}+B_v\big(j+\frac{1}{2}\big)^2 & -B_v\Big[(j+\frac{1}{2})^2-1\Big]^{1/2} & \frac{a_+}{2}+bB_v\Big[1-\epsilon(j+\frac{1}{2})\Big]\\
 & T^v_\Pi+\frac{A_v}{2}+B_v\Big[(j+\frac{1}{2})^2-2\Big] & -bB_v\Big[(j-\frac{1}{2})(j+\frac{3}{2})\Big]^{1/2}\\
 & & T^v_\Sigma+B_v\Big[(j+\frac{1}{2})^2-\epsilon(j+\frac{1}{2})\Big]
\end{array}\right)
\end{array}$$

(3.118)

The difference of the $^2\Pi \sim {}^2\Sigma^+$ interaction for the e and f levels give rise to the λ-doubling in a $^2\Pi$ state. Since for NO the $^2\Sigma^+$ state is sufficiently far from the $^2\Pi$ state, second-order perturbation theory can be applied to evaluate the λ-doubling. Then, the $^2\Pi^e_{1/2}$ level is lowered by

$$\Delta T^e_{1/2} = \frac{[\frac{a_+}{2} - bB_v(j-1)]^2}{E_\Pi - E_\Sigma}, \tag{3.119}$$

while the $^2\Pi^f_{1/2}$ level is lifted by

$$\Delta T^f_{1/2} = \frac{[\frac{a_+}{2} + bB_v(j+\frac{3}{2})]^2}{E_\Pi - E_\Sigma}. \tag{3.120}$$

Then, the splitting due to the λ-doubling for $^2\Pi_{1/2}$ is calculated to be

$$\begin{aligned} \Delta\nu_{fe}(^2\Pi_{1/2}) &= \Delta T^f_{1/2} - \Delta T^e_{1/2} \\ &= \frac{(a_+ bB_v + 2b^2B_v^2)[(j+\frac{3}{2}) + (j-\frac{1}{2})]}{E_\Pi - E_\Sigma} \\ &= \frac{(2j+1)(bB_v)(a_+ + 2bB_v)}{E_\Pi - E_\Sigma}. \end{aligned} \tag{3.121}$$

Since $2bB_v \ll a_+$, $\Delta\nu_{fe}(^2\Pi_{1/2})$ is approximated as

$$\Delta\nu_{fe}(^2\Pi_{1/2}) = \frac{a_+ bB_v}{E_\Pi - E_\Sigma}(j+\tfrac{1}{2}) = p(j+\tfrac{1}{2}). \tag{3.122}$$

The $^2\Sigma^+$ state e/f levels will be shifted by an equal amount but opposite to that of the $^2\Pi$ state e/f levels.

There is another mechanism by which the $^2\Pi \sim {}^2\Sigma^+$ interaction results in the λ-doubling for levels of the $^2\Pi_{3/2}$ component. The matrix element $\left\langle {}^2\Pi_{3/2}\middle|H\middle|{}^2\Pi_{1/2}\right\rangle$

can be calculated using a Van Vleck transformation [116, 118]:

$$\begin{aligned}
&\langle {}^2\Pi^e_{3/2}|\tilde{H}|{}^2\Pi^e_{1/2}\rangle \\
= \;& \langle {}^2\Pi^e_{3/2}|H|{}^2\Pi^e_{1/2}\rangle + \frac{\langle {}^2\Pi^e_{3/2}|H|{}^2\Sigma^+_e\rangle\langle {}^2\Sigma^+_e|H|{}^2\Pi^e_{1/2}\rangle}{E_\Pi - E_\Sigma} \\
= \;& -B_v\Big[(j+\tfrac{1}{2})^2-1\Big]^{1/2} - \frac{bB_v[(j+\frac{1}{2})^2-1]^{1/2}\{\frac{a_+}{2}+[1-(j+\frac{1}{2})]bB_v\}}{E_\Pi - E_\Sigma} \\
= \;& -\Big[(j+\tfrac{1}{2})^2-1\Big]^{1/2}\Big\{B_v + \frac{1}{4}\frac{2a_+bB_v}{E_\Pi-E_\Sigma} - \frac{1}{2}\frac{2b^2B_v^2}{E_\Pi-E_\Sigma}\Big(j-\tfrac{1}{2}\Big)\Big\} \\
= \;& -\Big[(j-\tfrac{1}{2})(j+\tfrac{3}{2})\Big]^{1/2}\Big\{B_v + \frac{p}{4} - \frac{q}{2}(j-\tfrac{1}{2})\Big\} \qquad (3.123)
\end{aligned}$$

where $\tilde{H}$ is the transformed Hamiltonian (see Section 3.2 in Ref. [116]). And,

$$p = \frac{2a_+bB_v}{E_\Pi - E_\Sigma}, \text{ and } q = \frac{2b^2B_v^2}{E_\Pi - E_\Sigma}.$$

Similarly,

$$\begin{aligned}
&\langle {}^2\Pi^f_{3/2}|\tilde{H}|{}^2\Pi^f_{1/2}\rangle \\
= \;& -\Big[(j-\tfrac{1}{2})(j+\tfrac{3}{2})\Big]^{1/2}\Big\{B_v + \frac{p}{4} + \frac{q}{2}(j+\tfrac{3}{2})\Big\}. \qquad (3.124)
\end{aligned}$$

Now, using second-order perturbation theory to estimate the parity-dependent effect of $\langle {}^2\Pi^{e/f}_{3/2}|\tilde{H}|{}^2\Pi^{e/f}_{1/2}\rangle$ on λ-doubling in ${}^2\Pi_{3/2}$,

$$\begin{aligned}
&\Delta\nu_{fe}({}^2\Pi_{3/2}) \\
= \;& \frac{\Big|\langle {}^2\Pi^f_{3/2}|\tilde{H}|{}^2\Pi^f_{1/2}\rangle\Big|^2 - \Big|\langle {}^2\Pi^e_{3/2}|\tilde{H}|{}^2\Pi^e_{1/2}\rangle\Big|^2}{E_{\Pi_{3/2}} - E_{\Pi_{1/2}}} \\
= \;& \frac{(j-\frac{1}{2})(j+\frac{3}{2})\Big\{\big[B_v + \frac{p}{4} + \frac{q}{2}(j+\frac{3}{2})\big]^2 - \big[B_v + \frac{p}{4} - \frac{q}{2}(j-\frac{1}{2})\big]^2\Big\}}{E_{\Pi_{3/2}} - E_{\Pi_{1/2}}} \\
= \;& \frac{2(j-\frac{1}{2})(j+\frac{1}{2})(j+\frac{3}{2})}{A_v - 2B_v}\Big(B_v + \frac{p}{4} + \frac{q}{2}\Big)q \\
\simeq \;& 2q\frac{B_v}{A_v}\Big(j-\tfrac{1}{2}\Big)\Big(j+\tfrac{1}{2}\Big)\Big(j+\tfrac{3}{2}\Big). \qquad (3.125)
\end{aligned}$$

From second-order perturbation theory, the ${}^2\Pi_{1/2}$ λ-doubling transferred to ${}^2\Pi_{3/2}$ due to spin-uncoupling is calculated as

$$p\Big(\frac{B_v}{A_v}\Big)^2\Big(j-\tfrac{1}{2}\Big)\Big(j+\tfrac{1}{2}\Big)\Big(j+\tfrac{3}{2}\Big). \qquad (3.126)$$

Finally, the total energies including λ-doubling in the symmetry adapted basis set can be written as [119]:

$$E(^2\Pi_{3/2}, v, J, \epsilon) = T_\Pi^v + \frac{A_v}{2} + B_v\Big[(j+\tfrac{1}{2})^2 - 2\Big] + \frac{\epsilon}{2}\frac{B_v}{A_v}\Big(2q + p\frac{B_v}{A_v}\Big)\Big(j-\tfrac{1}{2}\Big)\Big(j+\tfrac{1}{2}\Big)\Big(j+\tfrac{3}{2}\Big), \quad (3.127a)$$

$$E(^2\Pi_{1/2}, v, J, \epsilon) = T_\Pi^v - \frac{A_v}{2} + B_v\Big[\big(j+\tfrac{1}{2}\big)^2 - 2\Big] + \frac{\epsilon}{2}p\Big(j+\tfrac{1}{2}\Big). \quad (3.127b)$$

The λ-doubling for the F_1 component depends linearly on j while that for the F_2 component varies with the third power of j. For low values of j, the splitting is very small compared to that for the F_1 component. Therefore, the λ-doubling can only be observed in high resolution experiments. For NO, the observed λ-doubling is shown in Fig. 2.14 on page 43. The λ-doubling for the $Q_{11}(\frac{3}{2})$ line is so small that it cannot be resolved with our experimental resolution whereas that for the $Q_{11}(\frac{1}{2})$ line is recognizable for $j = \frac{3}{2}$ and $j = \frac{5}{2}$.

3.2 One- and Two-Photon Absorption Theory

3.2.1 Semiclassical Treatment and Time-dependent Perturbation Theory

In classical electrodynamics, the electromagnetic field vectors can be expressed in terms of a vector potential $\boldsymbol{A}(\boldsymbol{r}, t)$ and a scalar potential $\phi(\boldsymbol{r}, t)$ as

$$\begin{aligned} \boldsymbol{E} &= -\nabla\phi - \frac{\partial \boldsymbol{A}}{\partial t} \\ \boldsymbol{B} &= \nabla \times \boldsymbol{A}. \end{aligned} \quad (3.128)$$

The classical Hamiltonian for a system of charged particles in an electromagnetic field is given by

$$H = \sum_i \left[\frac{1}{2m_i} \left(\boldsymbol{P}_i - \frac{q_i}{c} \boldsymbol{A} \right)^2 + q_i \phi \right] + V \tag{3.129}$$

where V is the Coulomb potential. The term $\left(\boldsymbol{P}_i - \frac{q_i}{c} \boldsymbol{A} \right)^2$ is expanded as

$$\boldsymbol{P}_i^2 - \frac{q_i}{c} \boldsymbol{P}_i \cdot \boldsymbol{A} - \frac{q_i}{c} \boldsymbol{A} \cdot \boldsymbol{P}_i + \frac{q_i^2}{c^2} \boldsymbol{A}^2. \tag{3.130}$$

Since $\boldsymbol{P}_i$ is an operator, it acts on the vector potential as well as on the wavefunction:

$$\boldsymbol{P}_i \cdot \boldsymbol{A} \psi = \frac{\hbar}{i} \nabla \cdot \boldsymbol{A} \psi = \frac{\hbar}{i} \psi \, \nabla \cdot \boldsymbol{A} + \frac{\hbar}{i} \boldsymbol{A} \cdot \nabla \psi. \tag{3.131}$$

The $\boldsymbol{E}$ and $\boldsymbol{B}$ fields are invariant under gauge transformations. In free space, the scalar potential can be set to zero. The Coulomb gauge $\nabla \cdot \boldsymbol{A} = 0$ is used for the following. Then, the Hamiltonian for a molecular system interacting with an electromagnetic field is written as

$$H = \sum_i \frac{1}{2m_i} \left(\boldsymbol{P}_i^2 - \frac{2q_i}{c} \boldsymbol{A} \cdot \boldsymbol{P}_i + \frac{q_i^2}{c^2} \boldsymbol{A}^2 \right) + V. \tag{3.132}$$

For the weak field limit, the term quadratic in $\boldsymbol{A}^2$ can be neglected. Furthermore, it is assumed that the light wave interacts only with the electrons in the molecule. This yields the following approximate Hamiltonian

$$\begin{aligned} H &= \sum_i^{N_n} \frac{1}{2m_i} \boldsymbol{P}_i^2 + \sum_j^{N_e} \left[\frac{1}{2m_e} \boldsymbol{P}_j^2 + \frac{e}{m_e c} \boldsymbol{A} \cdot \boldsymbol{P}_j \right] + V \\ &= \sum_i^{N_n} \frac{1}{2m_i} \boldsymbol{P}_i^2 + \sum_j^{N_e} \frac{1}{2m_e} \boldsymbol{P}_j^2 + V + \sum_{j=1}^{N_e} \frac{e}{m_e c} \boldsymbol{A} \cdot \boldsymbol{P}_j \\ &= H_0 + H' \end{aligned} \tag{3.133}$$

where

$$H' = \sum_{j=1}^{N_e} \frac{e}{m_e c} \boldsymbol{A} \cdot \boldsymbol{P}_j. \tag{3.134}$$

The first term of the first line of Eq. (3.133) corresponds to the kinetic energy of the nuclei and the second term corresponds to that of the electrons with the charge $-e$. The perturbation term H' may be rewritten in terms of the commutator $[\boldsymbol{P}_j^2, \boldsymbol{R}_k]$:

$$[\boldsymbol{P}_j^2, \boldsymbol{R}_k] = \boldsymbol{P}_j[\boldsymbol{P}_j, \boldsymbol{R}_k] + [\boldsymbol{P}_j, \boldsymbol{R}_k]\boldsymbol{P}_j = -2\hbar i \boldsymbol{P}_j \delta_{jk}. \tag{3.135}$$

Since the potential operator depends only on the position vectors, the potential commutes with $\boldsymbol{R}_k$. Then, the commutator $[H_0, \boldsymbol{R}_k]$ becomes

$$[H_0, \boldsymbol{R}_k] = -\frac{\hbar i}{m_e}\boldsymbol{P}_k. \tag{3.136}$$

The perturbation term H' is rewritten in terms of the commutator [107],

$$H' = \frac{1}{c\hbar i}\boldsymbol{A} \cdot \Big[\ H_0, \sum_{j=1}^{N_e} e\boldsymbol{R}_j\ \Big]. \tag{3.137}$$

Because the vector potential depends explicitly on time, the perturbation H' is time-dependent. Therefore, a perturbation theory based on the time-dependent Schrödinger equation must be used to describe the interaction. Since the perturbation involves the electron dipole operator $\boldsymbol{\mu} = \sum_{j=1}^{N_e} e\boldsymbol{R}_j$, transition probabilities for one- and two-photon absorption processes are expressed in terms of transition dipole matrix elements.

The treatment of time-dependent perturbation theory is summarized as follows [107, 120]. The Hamiltonian consists of an unperturbed part H_0 and a time dependent perturbation H':

$$H = H_0 + \lambda H'(t) \tag{3.138}$$

where λ is a perturbation parameter. Later, λ will be set to 1. If $u_k^{(0)}(\boldsymbol{r})$ is a solution to the time-independent Schrödinger equation associated with the unperturbed Hamiltonian:

$$H_0 u_k^{(0)}(\boldsymbol{r}) = E_k^{(0)} u_k^{(0)}(\boldsymbol{r}), \tag{3.139}$$

then the solution to the time-dependent Schrödinger equation

$$H\Psi(\boldsymbol{r},t) = -\frac{i}{\hbar}\frac{\partial}{\partial t}\Psi(\boldsymbol{r},t) \tag{3.140}$$

can be expanded in terms of the stationary states associated with the unperturbed Hamiltonian:

$$\Psi(\boldsymbol{r},t) = \sum_k a_k(t)u_k^{(0)}(\boldsymbol{r})e^{-\frac{i}{\hbar}E_k^{(0)}t} \tag{3.141}$$

where the coefficient $a_k(t)$ are found by an iterative procedure

$$a_m(t) = a_m^{(0)}(t) + \lambda a_m^{(1)}(t) + \lambda^2 a_m^{(2)}(t) + \cdots .$$

Substituting Eq. (3.139) into the time-dependent Schrödinger equation yields

$$\sum_m (H_0 + \lambda H')a_m(t)u_m^{(0)}(\boldsymbol{r})e^{-\frac{i}{\hbar}E_m^{(0)}t} = \sum_m \left[a_m(t)u_m^{(0)}(\boldsymbol{r})E_m^{(0)} - \frac{i}{\hbar}\dot{a}_m(t)u_m^{(0)}(\boldsymbol{r})\right]e^{-\frac{i}{\hbar}E_m^{(0)}t} \tag{3.142}$$

$$\Updownarrow$$

$$\sum_m \lambda H' a_m(t)u_m^{(0)}(\boldsymbol{r})e^{-\frac{i}{\hbar}E_m^{(0)}t} = -\frac{i}{\hbar}\sum_m \dot{a}_m(t)u_m^{(0)}(\boldsymbol{r})e^{-\frac{i}{\hbar}E_m^{(0)}t}. \tag{3.143}$$

Multiplying both sides with $u_k^{(0)*}(\boldsymbol{r})e^{\frac{i}{\hbar}E_k^{(0)}t}$ and integrating over the spatial coordinate yields

$$\dot{a}_k(t) = -\frac{i}{\hbar}\sum_m \lambda H'_{km}a_m(t)e^{i\omega_{km}t} \tag{3.144}$$

where

$$\omega_{km} = (E_k^{(0)} - E_m^{(0)})/\hbar \tag{3.145}$$

and

$$H'_{km} = \int u_k^{(0)*}(\boldsymbol{r})\ H'\ u_m^{(0)}(\boldsymbol{r})d^3r = \big\langle k|H'|m\big\rangle. \tag{3.146}$$

Assume that the molecular system is initially in the quantum state $|i\rangle$, the initial condition is $a_m^{(0)} = \delta_{mi}$. The successive corrections are found by solving the equations

$$\frac{d}{dt}a_k^{(s+1)}(t) = \frac{1}{i\hbar}\sum_n H'_{km}(t)a_m^{(s)}(t)e^{-i\omega_{km}t}. \tag{3.147}$$

The first order result is

$$a_k^{(1)}(t) = \frac{1}{i\hbar}\int_0^t dt' H'_{ki}(t') e^{i\omega_{ki}t'}. \tag{3.148}$$

Using the above result, it is easy to find the second order correction

$$a_f^{(2)}(t) = \frac{1}{(i\hbar)^2}\int_0^t dt' \int_0^{t'} dt'' \sum_k H'_{ki}(t') H'_{fk}(t'') e^{i(\omega_{ki}t' + \omega_{fk}t'')}. \tag{3.149}$$

The first correction term is responsible for the one-photon absorption process while the second correction term is responsible for the non-resonant two-photon absorption process. The intensity of a spectral line involving the transition between two nondegenerate states $\big|i\big\rangle$ and $\big|f\big\rangle$ is given by

$$I(f \leftarrow i; t) = C\big|a_m(t)\big|^2 \quad \text{with} \quad a_m(0) = \delta_{mi}. \tag{3.150}$$

In the case of a degeneracy characterized by the quantum numbers M_i and M_f, the intensity is given as a sum over the individual contributions:

$$I(f \leftarrow i; t) = C \sum_{M_i, M_f} \big|a_m(t)\big|^2 \quad \text{with} \quad a_m(0) = \delta_{mi}. \tag{3.151}$$

3.2.2 One-photon Process

From the first order term, the intensity for a transition involving one-photon absorption can be calculated. In the dipole approximation, the spatial variation of the electromagnetic wave is neglected and the vector potential for a linearly polarized electromagnetic plane wave of frequency ω is written as

$$\boldsymbol{A}(\boldsymbol{r}, t) \simeq \boldsymbol{A}(t) = \frac{1}{2} A_0 \hat{e}\big(e^{+i\omega t} + e^{-i\omega t}\big). \tag{3.152}$$

Here, A_0 is the magnitude of the vector potential and $\hat{e}$ is the polarization vector. H'_{kn} can be calculated using the above vector potential:

$$\begin{aligned} H'_{ki} &= \frac{i}{c\hbar}\boldsymbol{A}(t)\cdot\big\langle k\big|\big[H_0,\sum_{j=1}^{N_e}e\boldsymbol{R}_j\big]\big|i\big\rangle \\ &= \frac{i}{c\hbar}\boldsymbol{A}(t)\cdot\Big\{\big\langle k\big|H_0\sum_{j=1}^{N_e}e\boldsymbol{R}_j\big|i\big\rangle-\big\langle k\big|\sum_{j=1}^{N_e}e\boldsymbol{R}_j\ H_0\big|i\big\rangle\Big\} \\ &= \frac{i}{c\hbar}\boldsymbol{A}(t)\cdot(E_k^{(0)}-E_i^{(0)})\big\langle k\big|\sum_{j=1}^{N_e}e\boldsymbol{R}_j\big|i\big\rangle \\ &= \frac{i\omega_{ki}}{c}\boldsymbol{A}(t)\cdot\big\langle k\big|\boldsymbol{\mu}\big|i\big\rangle. \end{aligned} \tag{3.153}$$

Substituting Eq. (3.153) into Eq. (3.148), the first order correction term becomes

$$\begin{aligned} a_k^{(1)}(t) &= \frac{1}{i\hbar}\int_0^t dt' H'_{ki}(t')e^{i\omega_{ki}t'} = \frac{\omega_{in}}{c\hbar}\big\langle k\big|\boldsymbol{\mu}\big|i\big\rangle\cdot\int_0^t dt'\boldsymbol{A}(t')e^{i\omega_{ki}t'} \\ &= \frac{\omega_{ki}}{2\hbar c}\big\langle k\big|\boldsymbol{\mu}\big|i\big\rangle\cdot A_0\hat{e}\int_0^t dt'\big[e^{i(\omega_{ki}+\omega)t')}+e^{i(\omega_{ki}-\omega)t')}\big] \\ &= \frac{\omega_{ki}}{2i\hbar c}\big\langle k\big|\boldsymbol{\mu}\big|i\big\rangle\cdot A_0\hat{e}\Big[\frac{e^{i(\omega_{ki}-\omega)t}-1}{\omega_{ki}-\omega}+\frac{e^{i(\omega_{ki}+\omega)t}-1}{\omega_{ki}+\omega}\Big]. \end{aligned} \tag{3.154}$$

The coefficient becomes important only in the case of a resonance, i.e., for $\omega=\omega_{ki}$ or $\omega=-\omega_{ki}$. Averaging the coefficient over a time which is longer than the period associated with the electromagnetic wave results in a contribution only from the term which satisfies the resonance condition. In the case of one-photon absorption, the intensity for a transition from state $\big|i\big\rangle$ to state $\big|f\big\rangle$ is given as

$$I(f\leftarrow i;t)=C\left[\frac{E_0\omega_{fi}}{2\hbar\omega}\right]^2\sum_{M_i,M_f}\big|\big\langle f\big|\hat{e}\cdot\boldsymbol{\mu}\big|i\big\rangle\big|^2\left|\frac{e^{i(\omega_{fi}-\omega)t}-1}{\omega_{fi}-\omega}\right|^2 \tag{3.155}$$

where $E_0=\omega A_0/c$. The overall intensity of the spectral line is proportional to the absolute square of the transition moment and to the intensity of the light wave which is proportional to the square of the electric field strength E_0.

3.2.3 Two-Photon Process

In the case of the interaction with two laser fields of different frequencies(ω_1 and ω_2), the corresponding first order result takes on the following form:

$$a_k^{(1)}(t) = \frac{\omega_{ki}}{2i\hbar c}\langle k|\boldsymbol{\mu}|i\rangle \cdot \Big\{A_{10}\hat{e}_1\Big[\frac{e^{i(\omega_{ki}-\omega_1)t}-1}{\omega_{ki}-\omega_1}+\frac{e^{i(\omega_{ki}+\omega_1)t}-1}{\omega_{ki}+\omega_1}\Big] + A_{20}\hat{e}_2\Big[\frac{e^{i(\omega_{ki}-\omega_2)t}-1}{\omega_{ki}-\omega_2}+\frac{e^{i(\omega_{ki}+\omega_2)t}-1}{\omega_{ki}+\omega_2}\Big]\Big\} \quad (3.156)$$

where A_{10}, A_{20} are the magnitude of the vector potential for the two laser fields and $\hat{e}_1$, $\hat{e}_2$ are their polarization vectors. Since the interaction with the molecule is assumed to be nonresonant with each of the individual photons, none of the frequencies match the difference between any two energy levels of the molecule. In this case the first order contribution will be very small while the second order contribution can be significant. Using Eq. (3.156), it is found that

$$\begin{aligned}\frac{da_f^{(2)}}{dt} &= -\frac{i}{\hbar}\sum_k H'_{fk}(t)a_k^{(1)}e^{i\omega_{fk}t} \\ &= -i\sum_k \frac{\omega_{fk}\omega_{ki}}{2\hbar^2c^2}\langle f|\boldsymbol{\mu}|k\rangle\cdot\Big\{\frac{A_{10}}{2}\hat{e}_1\Big[e^{i(\omega_{fk}+\omega_1)t}+e^{i(\omega_{fk}-\omega_1)t}\Big] \\ &\qquad +\frac{A_{20}}{2}\hat{e}_2\Big[e^{i(\omega_{fk}+\omega_2)t}+e^{i(\omega_{fk}-\omega_2)t}\Big]\Big\} \\ &\quad \times\langle k|\boldsymbol{\mu}|i\rangle\cdot\Big\{A_{10}\hat{e}_1\Big[\frac{e^{i(\omega_{ki}-\omega_1)t}-1}{\omega_{ki}-\omega_1}+\frac{e^{i(\omega_{ki}+\omega_1)t}-1}{\omega_{ki}+\omega_1}\Big] \\ &\qquad +A_{20}\hat{e}_2\Big[\frac{e^{i(\omega_{ki}-\omega_2)t}-1}{\omega_{ki}-\omega_2}+\frac{e^{i(\omega_{ki}+\omega_2)t}-1}{\omega_{ki}+\omega_2}\Big]\Big\}. \quad (3.157)\end{aligned}$$

The constant terms in the last bracket (for example, $\frac{-1}{\omega_{ki}-\omega_1}$) are not important because of the assumption that neither of the laser frequencies are resonant for a single photon.

In the above result, the terms proportional to $|A_{10}|^2$ and $|A_{20}|^2$ are responsible for single-color two-photon resonances:

$$\frac{da_f^{(2)}}{dt} = -\frac{i|A_{10}|^2}{4\hbar^2c^2}\sum_k \omega_{fk}\omega_{ki}\langle f|\hat{e}_1\cdot\boldsymbol{\mu}|k\rangle\langle k|\hat{e}_1\cdot\boldsymbol{\mu}|i\rangle\Big[e^{i(\omega_{fk}+\omega_1)t}+e^{i(\omega_{fk}-\omega_1)t}\Big]$$

$$
\begin{aligned}
&\times\left[\frac{e^{i(\omega_{ki}-\omega_1)t}}{\omega_{ki}-\omega_1}+\frac{e^{i(\omega_{ki}+\omega_1)t}}{\omega_{ki}+\omega_1}\right]\\
&-\frac{i|A_{20}|^2}{4\hbar^2c^2}\sum_k\omega_{fk}\omega_{ki}\big\langle f\big|\hat{e}_2\cdot\boldsymbol{\mu}\big|k\big\rangle\big\langle k\big|\hat{e}_2\cdot\boldsymbol{\mu}\big|i\big\rangle\left[e^{i(\omega_{fk}+\omega_2)t}+e^{i(\omega_{fk}-\omega_2)t}\right]\\
&\times\left[\frac{e^{i(\omega_{ki}-\omega_2)t}}{\omega_{ki}-\omega_2}+\frac{e^{i(\omega_{ki}+\omega_2)t}}{\omega_{ki}+\omega_2}\right]\\
=\;&-\frac{i|A_{10}|^2}{4\hbar^2c^2}\sum_k\omega_{fi}\big\langle f\big|\hat{e}_1\cdot\boldsymbol{\mu}\big|k\big\rangle\big\langle k\big|\hat{e}_1\cdot\boldsymbol{\mu}\big|i\big\rangle\left[\frac{e^{i(\omega_{fi}-2\omega_1)t}}{\omega_{ki}-\omega_1}+\frac{e^{i(\omega_{fi}+2\omega_1)t}}{\omega_{ki}+\omega_1}\right]\\
&-\frac{i|A_{20}|^2}{4\hbar^2c^2}\sum_k\omega_{fi}\big\langle f\big|\hat{e}_2\cdot\boldsymbol{\mu}\big|k\big\rangle\big\langle k\big|\hat{e}_2\cdot\boldsymbol{\mu}\big|i\big\rangle\left[\frac{e^{i(\omega_{fi}-2\omega_2)t}}{\omega_{ki}-\omega_2}+\frac{e^{i(\omega_{fi}+2\omega_2)t}}{\omega_{ki}+\omega_2}\right].
\end{aligned}
\tag{3.158}
$$

In the last line of Eq. (3.158) the first term in each bracket represents a single-color stimulated two-photon absorption while the second term represents two-photon emission.

Similarly, two-color two-photon absorption is described by the contribution involving the cross term $A_{10}A_{20}$:

$$
\begin{aligned}
&\frac{da_f^{(2)}}{dt}\\
=\;&-\frac{iA_{10}A_{20}}{4\hbar^2c^2}\sum_k\omega_{fi}\big\langle f\big|\hat{e}_1\cdot\boldsymbol{\mu}\big|k\big\rangle\big\langle k\big|\hat{e}_2\cdot\boldsymbol{\mu}\big|i\big\rangle\\
&\times\left[\frac{e^{i(\omega_{fi}-(\omega_2+\omega_1))t}}{\omega_{ki}-\omega_2}+\frac{e^{i(\omega_{fi}+(\omega_2+\omega_1))t}}{\omega_{ki}+\omega_2}+\frac{e^{i(\omega_{fi}-(\omega_2-\omega_1))t}}{\omega_{ki}-\omega_2}+\frac{e^{i(\omega_{fi}-(\omega_1-\omega_2))t}}{\omega_{ki}+\omega_2}\right]\\
&-\frac{iA_{10}A_{20}}{4\hbar^2c^2}\sum_k\omega_{fi}\big\langle f\big|\hat{e}_2\cdot\boldsymbol{\mu}\big|k\big\rangle\big\langle k\big|\hat{e}_1\cdot\boldsymbol{\mu}\big|i\big\rangle\\
&\times\left[\frac{e^{i(\omega_{fi}-(\omega_2+\omega_1))t}}{\omega_{ki}-\omega_1}+\frac{e^{i(\omega_{fi}+(\omega_2+\omega_1))t}}{\omega_{ki}+\omega_1}+\frac{e^{i(\omega_{fi}-(\omega_1-\omega_2))t}}{\omega_{ki}-\omega_1}+\frac{e^{i(\omega_{fi}-(\omega_2-\omega_1))t}}{\omega_{ki}+\omega_1}\right].
\end{aligned}
\tag{3.159}
$$

It can be noticed that resonances occur for transitions in which the sum or difference frequency corresponds to an energy difference in the molecule. The difference frequency process is referred to as a stimulated Raman pumping process and the sum frequency process is referred to as two-color two-photon absorption process.

When the two-photon absorption process is only considered, the time derivative of the second order coefficient is given by

$$\frac{da_f^{(2)}}{dt} = -\frac{iA_{10}A_{20}}{4\hbar^2c^2}\sum_k \omega_{fi}\Bigg[\big\langle f\big|\hat{e}_1\cdot\boldsymbol{\mu}\big|k\big\rangle\big\langle k\big|\hat{e}_2\cdot\boldsymbol{\mu}\big|i\big\rangle\frac{e^{i(\omega_{fi}-(\omega_2+\omega_1))t}}{\omega_{ki}-\omega_2} + \big\langle f\big|\hat{e}_2\cdot\boldsymbol{\mu}\big|k\big\rangle\big\langle k\big|\hat{e}_1\cdot\boldsymbol{\mu}\big|i\big\rangle\frac{e^{i(\omega_{fi}-(\omega_1+\omega_2))t}}{\omega_{ki}-\omega_1}\Bigg]. \quad (3.160)$$

Integration over time yields

$$a_f^{(2)} = -\frac{iA_{10}A_{20}}{4\hbar^2c^2}\frac{e^{i(\omega_{fi}-(\omega_1+\omega_2))t}-1}{\omega_{fi}-(\omega_1+\omega_2)}\sum_k \omega_{fi} \times\Bigg[\frac{\big\langle f\big|\hat{e}_1\cdot\boldsymbol{\mu}\big|k\big\rangle\big\langle k\big|\hat{e}_2\cdot\boldsymbol{\mu}\big|i\big\rangle}{\omega_{ki}-\omega_2}+\frac{\big\langle f\big|\hat{e}_2\cdot\boldsymbol{\mu}\big|k\big\rangle\big\langle k\big|\hat{e}_1\cdot\boldsymbol{\mu}\big|i\big\rangle}{\omega_{ki}-\omega_1}\Bigg]. \quad (3.161)$$

The resonance condition is $\omega_{fi}=\omega_1+\omega_2$. A similar result is found for stimulated Raman pumping.

$$a_f^{(2)} = -\frac{iA_{10}A_{20}}{4\hbar^2c^2}\frac{e^{i(\omega_{fi}-(\omega_2-\omega_1))t}-1}{\omega_{fi}-(\omega_2-\omega_1)}\sum_k \omega_{fi} \times\Bigg[\frac{\big\langle f\big|\hat{e}_1\cdot\boldsymbol{\mu}\big|k\big\rangle\big\langle k\big|\hat{e}_2\cdot\boldsymbol{\mu}\big|i\big\rangle}{\omega_{ki}-\omega_2}+\frac{\big\langle f\big|\hat{e}_2\cdot\boldsymbol{\mu}\big|k\big\rangle\big\langle k\big|\hat{e}_1\cdot\boldsymbol{\mu}\big|i\big\rangle}{\omega_{ki}+\omega_1}\Bigg]. \quad (3.162)$$

For simplicity, consider only terms with $\omega_{fi}<0, \omega_2>\omega_1$. The expression for both two-photon absorption and stimulated Raman excitation can be written in a simplified form when the two-photon transition operator T_{ab} is introduced:

$$\begin{aligned}\sum_k \frac{\big\langle f\big|\hat{e}_1\cdot\boldsymbol{\mu}\big|k\big\rangle\big\langle k\big|\hat{e}_2\cdot\boldsymbol{\mu}\big|i\big\rangle}{\omega_{ki}-\omega_2}+\frac{\big\langle f\big|\hat{e}_2\cdot\boldsymbol{\mu}\big|k\big\rangle\big\langle k\big|\hat{e}_1\cdot\boldsymbol{\mu}\big|i\big\rangle}{\omega_{ki}\pm\omega_1} &= \big\langle f\big|\sum_{abk}\hat{e}_{1a}^*\hat{e}_{1b}^*\frac{\mu_a\big|k\big\rangle\big\langle k\big|\mu_b}{\omega_{ki}-\omega_2}\big|i\big\rangle+\big\langle f\big|\sum_{abk}\hat{e}_{1b}^*\hat{e}_{1a}^*\frac{\mu_b\big|k\big\rangle\big\langle k\big|\mu_a}{\omega_{ki}\pm\omega_1}\big|i\big\rangle \\ &= \big\langle f\big|\sum_{ab}\hat{e}_{1a}^*\hat{e}_{1b}^*T_{ab}\big|i\big\rangle \end{aligned} \quad (3.163)$$

where

$$T_{ab}=\sum_k\Bigg\{\frac{\mu_a\big|k\big\rangle\big\langle k\big|\mu_b}{\omega_{ki}-\omega_2}+\frac{\mu_a\big|k\big\rangle\big\langle k\big|\mu_b}{\omega_{ki}\pm\omega_1}\Bigg\}. \quad (3.164)$$

Here, the + sign refers to the stimulated Raman process and the − sign to the two-photon absorption process. Since the line strength of a particular transition is

proportional to the square of the second order coefficient, the intensity is proportional to

$$I \propto \Big| \sum_{ab} T_{ab} \hat{e}^*_{1a} \hat{e}^*_{1b} \Big|^2. \tag{3.165}$$

The quantity $\hat{e}^*_{1a}\hat{e}^*_{1b}$ is denoted as the polarization tensor P_{ab}.

3.2.4 Application to NO

In this subsection, the theory is applied to derive the rotational structure of one- and two-photon spectra.

One-photon absorption process

As an example of a one-photon absorption process, the first overtone transition of NO $X\ ^2\Pi$ in the electronic ground state is considered. From the results of Section 3.1, the energy eigenvalues of the unperturbed NO molecule are given by Eqs.(3.127a) and (3.127b). The eigenfunction will be a linear combination of Eq.(3.104) and Eq.(3.105) with coefficients

$$A_\pm = \sqrt{\frac{1 \pm ZU}{2}} \tag{3.166}$$

where

$$Z = Y - 2$$

and

$$U = \frac{1}{X} = \Big[Y(Y-4) + 4(j+\tfrac{1}{2})^2 \Big]^{-1/2}.$$

These coefficients describe the mixing of states with $|\omega| = \frac{1}{2}$ and $|\omega| = \frac{3}{2}$. The eigenfunctions of the vibrational ground state ($v'' = 0$) are written as

$$\begin{aligned} & \Psi_i(F_1 : {}^2\Pi) \\ = \ & A^i_+ \Big| {}^2\Pi, |\omega| = \tfrac{1}{2}, J_i M_i \epsilon_i v_i \Big\rangle + A^i_- \Big| {}^2\Pi, |\omega| = \tfrac{3}{2}, J_i M_i \epsilon_i v_i \Big\rangle \end{aligned} \tag{3.167}$$

and

$$\begin{aligned} & \Psi_i(F_2 : {}^2\Pi) \\ = \; & A^i_+ \Big| {}^2\Pi, |\omega| = \tfrac{3}{2}, J_i M_i \epsilon_i v_i \Big\rangle - A^i_- \Big| {}^2\Pi, |\omega| = \tfrac{1}{2}, J_i M_i \epsilon_i v_i \Big\rangle. \end{aligned} \tag{3.168}$$

The same types of wavefunctions are used for the vibrationally excited state with $v' = 2$. The line strength for the one-photon absorption is calculated using Eq. (3.155). It is important to realize that the dot product $(\hat{e} \cdot \boldsymbol{\mu})$ is defined with respect to the sf frame while the electronic wavefunction is usually specified in a mf frame. In order to express the dipole moment operator as a transformed mf operator, one needs to express the operator in terms of spherical tensor components. For a given Cartesian vector $\boldsymbol{a} = (a_x, a_y, a_z)$, the spherical tensor components are defined as

$$a^{(1)}_0 = a_z \;\text{ and }\; a^{(1)}_\pm = \mp \frac{1}{\sqrt{2}} \big(a_x \pm i a_y \big). \tag{3.169}$$

With this definition, the dot product $\hat{e} \cdot \boldsymbol{\mu}$ takes the form:

$$\hat{e} \cdot \boldsymbol{\mu} = e^{(1)*}_0 \mu^{(1)}_0 + e^{(1)*}_{+1} \mu^{(1)}_{+1} + e^{(1)*}_{-1} \mu^{(1)}_{-1} = \sum_m e^{(1)*}_m \mu^{(1)}_m (\text{sf}). \tag{3.170}$$

The great advantage of the spherical tensor representation is that its components transform under rotation of the coordinate frame in a simple way:

$$a^{(1)}_m (\text{sf}) = \sum_k D^{(1)*}_{mk}(\alpha, \beta, \chi) a^{(1)}_k (\text{mf}) \tag{3.171}$$

with the inverse transformation

$$a^{(1)}_k (\text{mf}) = \sum_m D^{(1)}_{mk}(\alpha, \beta, \chi) a^{(1)}_m (\text{sf}). \tag{3.172}$$

Assuming that the laser field is polarized along the z direction in the space fixed frame, $\hat{e} \cdot \boldsymbol{\mu}$ becomes simply $E^{(1)*}_0 \mu^{(1)}_0 (\text{sf})$ which in turn can be expressed as $E^{(1)*}_0 \sum_k D^{(1)*}_{0k} \mu^{(1)}_k (\text{mf})$ where $\mu^{(1)}_k$ refers to the mf frame. Using the transformed mf operator, the transition matrix elements $\langle \Psi_f | \, \hat{e} \cdot \boldsymbol{\mu} \, | \Psi_i \rangle$ are evaluated. There are four types of transitions: $(F_1 \rightarrow F_1)$, $(F_1 \rightarrow F_2)$, $(F_2 \rightarrow F_1)$, and $(F_2 \rightarrow F_2)$.

For an $(F_1 \rightarrow F_1)$ transition, the transition matrix element is

$$\begin{aligned}
&\langle \Psi_f |\, \hat{e}\cdot\boldsymbol{\mu}\, |\Psi_i\rangle_{(F_1\rightarrow F_1)} \\
= \;& \Big\{ A_+^f \left\langle {}^2\Pi, |\omega| = \tfrac{1}{2}, J_f M_f \epsilon_f v_f \right| + A_-^f \left\langle {}^2\Pi, |\omega| = \tfrac{3}{2}, J_f M_f \epsilon_f v_f \right| \Big\} \\
& \quad \times \Big| \sum_k D_{0k}^{(1)*}(\alpha,\beta,\chi)\mu_k^{(1)} \Big| \\
& \times \Big\{ A_+^i \left| {}^2\Pi, |\omega| = \tfrac{1}{2}, J_i M_i \epsilon_i v_i \right\rangle + A_-^i \left| {}^2\Pi, |\omega| = \tfrac{3}{2}, J_i M_i \epsilon_i v_i \right\rangle \Big\}. \qquad (3.173)
\end{aligned}$$

The evaluation of Eq. (3.173) yields four contributions proportional to $A_+^f A_+^i$, $A_+^f A_-^i$, $A_-^f A_+^i$, and $A_-^f A_-^i$. The $A_+^f A_+^i$ term is calculated as

$$\begin{aligned}
& \left\langle {}^2\Pi, |\omega| = \tfrac{1}{2}, J_f M_f \epsilon_f v_f \right| D_{00}^{(1)*}(\alpha,\beta,\chi)\mu_0^{(1)} \left| {}^2\Pi, |\omega| = \tfrac{1}{2}, J_i M_i \epsilon_i v_i \right\rangle \\
= \;& \frac{1}{2}\Big\{ \left\langle +1, -\tfrac{1}{2}, v_f \right| \left\langle J_f, \tfrac{1}{2}, M_f \right| + \epsilon_f \left\langle -1, +\tfrac{1}{2}, v_f \right| \left\langle J_f, -\tfrac{1}{2}, M_f \right| \Big\} \\
& \times \left| D_{00}^{(1)*}(\alpha,\beta,\chi)\mu_0^{(1)} \right| \Big\{ \left| +1, -\tfrac{1}{2}, v_i \right\rangle \left| J_i, \tfrac{1}{2}, M_i \right\rangle + \epsilon_i \left| -1, +\tfrac{1}{2}, v_i \right\rangle \left| J_i, -\tfrac{1}{2}, M_i \right\rangle \Big\} \\
= \;& \frac{1}{2}\Big\{ \left\langle v_f \right| \mu_0^{(1)} \left| v_i \right\rangle \left\langle J_f, \tfrac{1}{2}, M_f \right| D_{00}^{(1)*}(\alpha,\beta,\chi) \left| J_i, \tfrac{1}{2}, M_i \right\rangle \\
& + \epsilon_f \epsilon_i \left\langle v_f \right| \mu_0^{(1)} \left| v_i \right\rangle \left\langle J_f, -\tfrac{1}{2}, M_f \right| D_{00}^{(1)*}(\alpha,\beta,\chi) \left| J_i, -\tfrac{1}{2}, M_i \right\rangle \Big\} \\
= \;& (-)^{M_i - \frac{1}{2}} \sqrt{2J_f+1}\sqrt{2J_i+1}\; \left\langle v_f \right| \mu_0^{(1)} \left| v_i \right\rangle \frac{[1+\epsilon_f\epsilon_i(-)^{J_f+J_i}]}{2} \\
& \quad \times \begin{pmatrix} J_f & 1 & J_i \\ M_f & 0 & -M_i \end{pmatrix} \begin{pmatrix} J_f & 1 & J_i \\ \frac{1}{2} & 0 & -\frac{1}{2} \end{pmatrix}. \qquad (3.174)
\end{aligned}$$

Here, for brevity $\left| -1, +\frac{1}{2}, v_i \right\rangle \left| J_i, -\frac{1}{2}, M_i \right\rangle$ denotes $\left| \Lambda = -1, \Sigma = +\frac{1}{2}, v_i \right\rangle \left| J_i, \Omega = -\frac{1}{2}, M_i \right\rangle$. $\begin{pmatrix} \cdot & \cdot & \cdot \end{pmatrix}$ is a $3j$ symbol defined in Ref. [121]. And, the relation

$$\langle \Lambda_f |\, \mu_k^{(1)}\, |\Lambda_i\rangle = \langle \Lambda_i + k |\, \mu_k^{(1)}\, |\Lambda_i\rangle\, \delta_{\Lambda_f, \Lambda_i + k} \qquad (3.175)$$

is used. Since $\Lambda_i, \Lambda_f = \pm 1$ and k is restricted to values of $0, \pm 1$ due to the property of the spherical tensor components, the only possible k value is 0 in combination with $\Lambda_i = \Lambda_f$. ΔS must be equal to 0. Thus, $\left\langle \Lambda_f, \Sigma_f, v_f \right| \mu_k^{(1)} \left| \Lambda_i, \Sigma_i, v_i \right\rangle$ is abbreviated as $\left\langle v_f \right| \mu_k^{(1)} \left| v_i \right\rangle \delta_{k0}$

Similarly, the term with $A^f_- A^i_-$ is calculated as

$$\begin{aligned}
&\left\langle {}^2\Pi, |\omega| = \tfrac{3}{2}, J_f M_f \epsilon_f v_f \middle| D^{(1)*}_{00}(\alpha,\beta,\chi)\mu^{(1)}_0 \middle| {}^2\Pi, |\omega| = \tfrac{3}{2}, J_i M_i \epsilon_i v_i \right\rangle \\
= \;& \frac{1}{2}\Big\{ \big\langle +1, +\tfrac{1}{2}, v_f \big| \big\langle J_f, \tfrac{3}{2}, M_f \big| + \epsilon_f \big\langle -1, -\tfrac{1}{2}, v_f \big| \big\langle J_f, -\tfrac{3}{2}, M_f \big| \Big\} \\
& \big| D^{(1)*}_{00}(\alpha,\beta,\chi)\mu^{(1)}_0 \big| \Big\{ \big| +1, +\tfrac{1}{2}, v_i \big\rangle \big| J_i, \tfrac{3}{2}, M_i \big\rangle + \epsilon_i \big| -1, -\tfrac{1}{2}, v_i \big\rangle \big| J_i, -\tfrac{3}{2}, M_i \big\rangle \Big\} \\
= \;& \frac{1}{2}\Big\{ \big\langle v_f \big| \mu^{(1)}_0 \big| v_i \big\rangle \big\langle J_f, \tfrac{3}{2}, M_f \big| D^{(1)*}_{00}(\alpha,\beta,\chi) \big| J_i, \tfrac{3}{2}, M_i \big\rangle \\
& + \epsilon_f \epsilon_i \big\langle v_f \big| \mu^{(1)}_0 \big| v_i \big\rangle \big\langle J_f, -\tfrac{3}{2}, M_f \big| D^{(1)*}_{00}(\alpha,\beta,\chi) \big| J_i, -\tfrac{3}{2}, M_i \big\rangle \Big\} \\
= \;& (-)^{M_i - \frac{3}{2}} \sqrt{2J_f+1}\sqrt{2J_i+1} \; \big\langle v_f \big| \mu^{(1)}_0 \big| v_i \big\rangle \; \frac{[1 + \epsilon_f \epsilon_i (-)^{J_f + J_i}]}{2} \\
& \times \begin{pmatrix} J_f & 1 & J_i \\ M_f & 0 & -M_i \end{pmatrix} \begin{pmatrix} J_f & 1 & J_i \\ \frac{3}{2} & -0 & -\frac{3}{2} \end{pmatrix}.
\end{aligned} \tag{3.176}$$

Terms with $A^f_+ A^i_-$ and $A^f_- A^i_+$ vanish due to the selection rule, $\Delta S = 0$. As a result, the transition matrix element for two levels of the F_1 component takes on the form:

$$\begin{aligned}
& \langle \Psi_f | \, \hat{e} \cdot \boldsymbol{\mu} \, | \Psi_i \rangle_{(F_1 \to F_1)} \\
= \;& (-)^{M_i - \frac{1}{2}} \sqrt{2J_f+1}\sqrt{2J_i+1} \; \big\langle v_f \big| \mu^{(1)}_0 \big| v_i \big\rangle \; \frac{[1 + \epsilon_f \epsilon_i (-)^{J_f + J_i}]}{2} \begin{pmatrix} J_f & 1 & J_i \\ M_f & 0 & -M_i \end{pmatrix} \\
& \times \left\{ A^f_+ A^i_+ \begin{pmatrix} J_f & 1 & J_i \\ \frac{1}{2} & 0 & -\frac{1}{2} \end{pmatrix} - A^f_- A^i_- \begin{pmatrix} J_f & 1 & J_i \\ \frac{3}{2} & 0 & -\frac{3}{2} \end{pmatrix} \right\}.
\end{aligned} \tag{3.177}$$

The evaluation of the other transition matrix elements $(F_1 \to F_2)$, $(F_2 \to F_1)$, and $(F_2 \to F_2)$ yields:

$$\begin{aligned}
& \langle \Psi_f | \, \hat{e} \cdot \boldsymbol{\mu} \, | \Psi_i \rangle_{(F_1 \to F_2)} \\
= \;& (-)^{M_i - \frac{1}{2}} \sqrt{2J_f+1}\sqrt{2J_i+1} \; \big\langle v_f \big| \mu^{(1)}_0 \big| v_i \big\rangle \; \frac{[1 + \epsilon_f \epsilon_i (-)^{J_f + J_i}]}{2} \begin{pmatrix} J_f & 1 & J_i \\ M_f & 0 & -M_i \end{pmatrix} \\
& \times \left\{ -A^f_- A^i_+ \begin{pmatrix} J_f & 1 & J_i \\ \frac{1}{2} & 0 & -\frac{1}{2} \end{pmatrix} - A^f_+ A^i_- \begin{pmatrix} J_f & 1 & J_i \\ \frac{3}{2} & 0 & -\frac{3}{2} \end{pmatrix} \right\},
\end{aligned} \tag{3.178}$$

$$
\begin{aligned}
&\langle\Psi_f|\,\hat{e}\cdot\boldsymbol{\mu}\,|\Psi_i\rangle_{(F_2\to F_1)} \\
&= (-)^{M_i-\frac{1}{2}}\sqrt{2J_f+1}\sqrt{2J_i+1}\;\left\langle v_f\middle|\mu_0^{(1)}\middle|v_i\right\rangle\;\frac{[1+\epsilon_f\epsilon_i(-)^{J_f+J_i}]}{2}\begin{pmatrix} J_f & 1 & J_i \\ M_f & 0 & -M_i\end{pmatrix} \\
&\times\left\{-A_+^fA_-^i\begin{pmatrix} J_f & 1 & J_i \\ \frac{1}{2} & 0 & -\frac{1}{2}\end{pmatrix}-A_-^fA_+^i\begin{pmatrix} J_f & 1 & J_i \\ \frac{3}{2} & 0 & -\frac{3}{2}\end{pmatrix}\right\},
\end{aligned}
\tag{3.179}
$$

and

$$
\begin{aligned}
&\langle\Psi_f|\,\hat{e}\cdot\boldsymbol{\mu}\,|\Psi_i\rangle_{(F_2\to F_2)} \\
&= (-)^{M_i-\frac{1}{2}}\sqrt{2J_f+1}\sqrt{2J_i+1}\;\left\langle v_f\middle|\mu_0^{(1)}\middle|v_i\right\rangle\;\frac{[1+\epsilon_f\epsilon_i(-)^{J_f+J_i}]}{2}\begin{pmatrix} J_f & 1 & J_i \\ M_f & 0 & -M_i\end{pmatrix} \\
&\times\left\{A_-^fA_-^i\begin{pmatrix} J_f & 1 & J_i \\ \frac{1}{2} & 0 & -\frac{1}{2}\end{pmatrix}-A_+^fA_+^i\begin{pmatrix} J_f & 1 & J_i \\ \frac{3}{2} & 0 & -\frac{3}{2}\end{pmatrix}\right\}.
\end{aligned}
\tag{3.180}
$$

By denoting the quantity in the bracket $\{\cdots\}$ as $S_{F_j\to F_k}(A_+^i,A_-^i,A_+^f,A_-^f;J_i,J_f)$, from Eq.(3.155) the intensity for the transition $(F_j\to F_k)$ is obtained as

$$
\begin{aligned}
I_{F_j\to F_k}(f\leftarrow i) &= C\left[\frac{E_0\omega_{fi}}{2\hbar\omega}\right]^2(2J_f+1)(2J_i+1)\Big[\frac{1+\epsilon_f\epsilon_i(-)^{J_f+J_i}}{2}\Big]^2\left|\left\langle v_f\middle|\mu_0^{(1)}\middle|v_i\right\rangle\right|^2 \\
&\quad\times\sum_{M_i,M_f}\begin{pmatrix} J_f & 1 & J_i \\ M_f & 0 & -M_i\end{pmatrix}\begin{pmatrix} J_f & 1 & J_i \\ M_f & 0 & -M_i\end{pmatrix} \\
&\quad\times\left|S_{F_j\to F_k}(A_+^i,A_-^i,A_+^f,A_-^f;J_i,J_f)\right|^2 \\
&= \frac{C'}{3}(2J_f+1)(2J_i+1)\frac{[1+\epsilon_f\epsilon_i(-)^{J_f+J_i}]}{2}\left|\left\langle v_f\middle|\mu_0^{(1)}\middle|v_i\right\rangle\right|^2 \\
&\quad\times\left|S_{F_j\to F_k}(A_+^i,A_-^i,A_+^f,A_-^f;J_i,J_f)\right|^2.
\end{aligned}
\tag{3.181}
$$

where the orthogonality property of $3j$ symbols has been used [121]:

$$
\sum_{M_i,M_f}\begin{pmatrix} J_f & 1 & J_i \\ M_f & 0 & -M_i\end{pmatrix}\begin{pmatrix} J_f & 1 & J_i \\ M_f & 0 & -M_i\end{pmatrix}=\frac{1}{3}.
\tag{3.182}
$$

Since $J_f + J_i = \Delta J + 2J_i$ and J_i is an half integer, $[1 + \epsilon_f\epsilon_i(-)^{J_f+J_i}]/2$ becomes $[1 - \epsilon_f\epsilon_i(-)^{\Delta J}]/2$ resulting in the selection rule

$$\epsilon_i \neq \epsilon_f \quad \text{for Q-branch,} \tag{3.183}$$

$$\epsilon_i = \epsilon_f \quad \text{for P- and R-branch.} \tag{3.184}$$

The intensity is proportional to the square of the vibronic transition moment which depends on the internuclear distance r. In order to investigate this dependence, the transition moment is expanded in terms of a Taylor series,

$$\mu_0^{(1)}(r) = \mu_0^{(1)}(0) + \frac{\partial\mu_0^{(1)}}{\partial r}r + \frac{1}{2}\frac{\partial^2\mu_0^{(1)}}{\partial r^2}r^2 + \cdots . \tag{3.185}$$

Remembering that the intensity is calculated for the first overtone transition, the second order term which represents the curvature of the transition moment is responsible for the nonvanishing matrix elements with $\Delta v = \pm 2$. Thus, by taking only this term into account the intensity of the first overtone transition becomes

$$\begin{aligned} I_{F_j\to F_k}(f \leftarrow i) &= \frac{C}{3}(2J_f+1)(2J_i+1)\frac{[1+\epsilon_f\epsilon_i(-)^{J_f+J_i}]}{2} \\ &\quad \times \left|\langle v_f|r^2|v_i\rangle\right|^2 \left[\frac{\partial^2\mu_0^{(1)}}{\partial r^2}\right]^2 \\ &\quad \times \left|S_{F_j\to F_k}(A_+^i, A_-^i, A_+^f, A_-^f; J_i, J_f)\right|^2 . \end{aligned} \tag{3.186}$$

Using the energy eigenvalues given in Eq. (3.127) with the set of constants (neglecting λ doubling) by Amiot *et al.* [99] and the line strength calculated according to Eq. (3.186), a spectrum is calculated and displayed in the bottom trace of Fig. 2.13.

Two-photon absorption process

As a second example, consider two-photon absorption in NO involving two different electronic states. The two photon line strength I is related to the matrix

elements of the components of the two-photon transition operator T and a polarization tensor P. Expressing both terms as spherical tensors with components $T^{(j)}_m$ and $P^{(j)}_m$ defined in a laboratory frame, S_{if} is defined as

$$S_{if} = \sum_{j,m} \big\langle f \big| T^{(j)}_m P^{(j)}_m \big| i \big\rangle. \tag{3.187}$$

Assuming that the molecular ensemble is isotropic, it is appropriate to identify the z-axis of the sf frame with the direction of the linear laser polarization. The components of the polarization tensor can be written as

$$P^{(j)}_m = \sqrt{4\pi} \begin{pmatrix} 1 & 1 & j \\ 0 & 0 & 0 \end{pmatrix} Y_{jm}(0,0), \tag{3.188}$$

where Y_{jm} is a spherical harmonic. The resulting polarization tensor has only nonvanishing components for $m = 0$. Due to the properties of the $3j$ symbol, j can take on only values j=0 and j=2. Therefore, only zeroth or second rank tensor components of the transition moment operator can contribute to the two-photon line strength. Since the wavefunctions are described in the mf frame, the tensor components must be expanded in terms of mf components.

$$S_{if} = \langle f | \sum_j | P^{(j)}_0 T^{(j)}_0 (\mathrm{sf}) | i \rangle = \sum_{j,k} P^{(j)}_0 \langle f | T^{(j)}_k (\mathrm{mf}) D^{(j)*}_{0k}(\alpha,\beta,\chi) | i \rangle. \tag{3.189}$$

Using the wavefunction from Eq. (3.72), then S_{if} becomes

$$\begin{aligned} S_{if} &= \sum_{j,k} \big\langle n_f J_f M_f \omega_f \epsilon_f \big| T^{(j)}_k D^{(j)*}_{0k}(\alpha,\beta,\chi) P^{(j)}_0 \big| n_i J_i M_i \omega_i \epsilon_i \big\rangle \\ &= \frac{1}{2} \big\langle v_f \big| v_i \big\rangle \sum_{j,k} P^{(j)}_0 \Big[\Big\{ \big\langle n_f \Lambda_f \Sigma_f \big| \big\langle J_f M_f \omega_f \big| + \epsilon_f \big\langle \eta_f - \Lambda_f - \Sigma_f \big| \big\langle J_f M_f - \omega_f \big| \Big\} \\ &\quad \times \big| T^{(j)}_k D^{(j)*}_{0k}(\alpha,\beta,\chi) \big| \\ &\quad \times \Big\{ \big| n_i \Lambda_i \Sigma_i \big\rangle \big| J_i M_i \omega_i \big\rangle + \epsilon_i \big| \eta_i - \Lambda_i - \Sigma_i \big\rangle \big| J_i M_i - \omega_i \big\rangle \Big\} \Big] \\ &= \frac{1}{2} \big\langle v_f \big| v_i \big\rangle (-)^{M_i} [J_i][J_f] \sum_{j,k} P^{(j)}_0 \end{aligned}$$

$$
\begin{aligned}
&\times\Bigg\{(-)^{-\omega_i-k}\big\langle\Lambda_f\big|T_k^{(j)}\big|\Lambda_i\big\rangle\begin{pmatrix}J_f & j & J_i\\ M_f & 0 & -M_i\end{pmatrix}\begin{pmatrix}J_f & j & J_i\\ \omega_f & -k & -\omega_i\end{pmatrix}\\
&\quad+\epsilon_i\epsilon_f(-)^{\omega_i-k}\big\langle-\Lambda_f\big|T_k^{(j)}\big|-\Lambda_i\big\rangle\begin{pmatrix}J_f & j & J_i\\ M_f & 0 & -M_i\end{pmatrix}\begin{pmatrix}J_f & j & J_i\\ -\omega_f & -k & \omega_i\end{pmatrix}\\
&\quad+\epsilon_f(-)^{-\omega_i-k}\big\langle-\Lambda_f|T_k^{(j)}|\Lambda_i\big\rangle\begin{pmatrix}J_f & j & J_i\\ M_f & 0 & -M_i\end{pmatrix}\begin{pmatrix}J_f & j & J_i\\ -\omega_f & -k & -\omega_i\end{pmatrix}\\
&\quad+\epsilon_i(-)^{\omega_i-k}\big\langle\Lambda_f\big|T_k^{(j)}\big|-\Lambda_i\big\rangle\begin{pmatrix}J_f & j & J_i\\ M_f & 0 & -M_i\end{pmatrix}\begin{pmatrix}J_f & j & J_i\\ \omega_f & -k & \omega_i\end{pmatrix}\Bigg\}\\
=\;&\frac{1}{2}\big\langle v_f\big|v_i\big\rangle(-)^{M_i}[J_i][J_f]\sum_{j,k}P_0^{(j)}\begin{pmatrix}J_f & j & J_i\\ M_f & 0 & -M_i\end{pmatrix}\\
&\times\Bigg\{(-)^{-\omega_i-k}\langle\Lambda_f|T_k^{(j)}|\Lambda_i\rangle\begin{pmatrix}J_f & j & J_i\\ \omega_f & -k & -\omega_i\end{pmatrix}\\
&\quad+(-)^{\omega_i-k+J_f+j+J_i}\epsilon_i\epsilon_f\langle-\Lambda_f|T_k^{(j)}|-\Lambda_i\rangle\begin{pmatrix}J_f & j & J_i\\ \omega_f & -k & -\omega_i\end{pmatrix}\\
&\quad+(-)^{-\omega_i-k+J_f+j+J_i}\epsilon_f\langle-\Lambda_f|T_k^{(j)}|\Lambda_i\rangle\begin{pmatrix}J_f & j & J_i\\ \omega_f & k & \omega_i\end{pmatrix}\\
&\quad+(-)^{\omega_i-k}\epsilon_i\langle-\Lambda_f|T_k^{(j)}|\Lambda_i\rangle\begin{pmatrix}J_f & j & J_i\\ \omega_f & -k & \omega_i\end{pmatrix}\Bigg\}\\
=\;&\Big[\frac{1-\epsilon_i\epsilon_f(-)^{J_i+J_f}}{2}\Big]\big\langle v_f\big|v_i\big\rangle(-)^{M_i-\omega_i}[J_i][J_f]\sum_{j,k}P_0^{(j)}(-)^{-k}\begin{pmatrix}J_f & j & J_i\\ M_f & 0 & -M_i\end{pmatrix}\\
&\times\Bigg\{\langle\Lambda_f|T_k^{(j)}|\Lambda_i\rangle\begin{pmatrix}J_f & j & J_i\\ \omega_f & -k & -\omega_i\end{pmatrix}\\
&\qquad+(-)^{J_i+J_f}\epsilon_f\langle-\Lambda_f|T_k^{(j)}|\Lambda_i\rangle\begin{pmatrix}J_f & j & J_i\\ \omega_f & k & \omega_i\end{pmatrix}\Bigg\}
\end{aligned}
\tag{3.190}
$$

where $[j]$ denotes $\sqrt{2j+1}$. From the selection rule

$$\epsilon_i = \epsilon_f (-)^{\Delta J}, \tag{3.191}$$

the rotational lines of the Q-, O-, or S-branches can be probed via a specific λ doublet component ϵ_i of a rotational level of the electronic ground state ($\epsilon_i = \epsilon_f$). The other components ($\epsilon_i \neq \epsilon_f$) must be probed on the lines of P- or R-branches.

The intensity of the two-photon transition becomes

$$\begin{aligned} I &= C \sum_{M_i M_f} \left[\frac{E_{01} E_{02}}{4\hbar^2}\right]^2 |S_{if}|^2 \\ &= C' \left[\frac{1-\epsilon_i\epsilon_f(-)^{J_i+J_f}}{2}\right]^2 (2J_i+1)(2J_f+1) \left|\langle v_f | v_i \rangle\right|^2 \\ &\quad \times \sum_{jj'} P_0^{(j)} P_0^{(j')} \sum_{M_i M_f} (-)^{2M_i} \begin{pmatrix} J_f & j & J_i \\ M_f & 0 & -M_i \end{pmatrix} \begin{pmatrix} J_f & j' & J_i \\ M_f & 0 & -M_i \end{pmatrix} \\ &\quad \times \Bigg| \langle \Lambda_f | T_k^{(j)} | \Lambda_i \rangle \begin{pmatrix} J_f & j & J_i \\ \omega_f & -k & -\omega_i \end{pmatrix} \\ &\qquad + (-)^{J_i+J_f} \epsilon_f \langle -\Lambda_f | T_k^{(j)} | \Lambda_i \rangle \begin{pmatrix} J_f & j & J_i \\ \omega_f & k & \omega_i \end{pmatrix} \Bigg|^2 . \end{aligned} \tag{3.192}$$

Using the orthogonality of the $3j$-symbols, the summation over M_i and M_f yields $\frac{1}{3}\delta_{jj'}$. Then, the intensity is calculated as

$$\begin{aligned} I &= C \left[\frac{1-\epsilon_i\epsilon_f(-)^{J_i+J_f}}{2}\right]^2 (2J_i+1)(2J_f+1) \left|\langle v_f | v_i \rangle\right|^2 \sum_j \left[P_0^{(j)}\right]^2 \\ &\quad \times \Bigg| \langle \Lambda_f | T_k^{(j)} | \Lambda_i \rangle \begin{pmatrix} J_f & j & J_i \\ \omega_f & -k & -\omega_i \end{pmatrix} \\ &\qquad + (-)^{J_i+J_f} \epsilon_f \langle -\Lambda_f | T_k^{(j)} | \Lambda_i \rangle \begin{pmatrix} J_f & j & J_i \\ \omega_f & k & \omega_i \end{pmatrix} \Bigg|^2 \\ &= C \left[\frac{1-\epsilon_i\epsilon_f(-)^{J_i+J_f}}{2}\right]^2 (2J_i+1)(2J_f+1) \left|\langle v_f | v_i \rangle\right|^2 \sum_j \end{aligned}$$

$$\times\Bigg\{\frac{1}{3}\Bigg|\langle\Lambda_f|T_0^{(0)}|\Lambda_i\rangle\begin{pmatrix}J_f & 0 & J_i\\ \omega_f & 0 & -\omega_i\end{pmatrix}$$
$$+(-)^{J_i+J_f}\epsilon_f\langle-\Lambda_f|T_0^{(0)}|\Lambda_i\rangle\begin{pmatrix}J_f & 0 & J_i\\ \omega_f & 0 & \omega_i\end{pmatrix}\Bigg|^2$$
$$+\frac{2}{15}\Bigg|\langle\Lambda_f|T_k^{(2)}|\Lambda_i\rangle\begin{pmatrix}J_f & 2 & J_i\\ \omega_f & -k & -\omega_i\end{pmatrix}$$
$$+(-)^{J_i+J_f}\epsilon_f\langle-\Lambda_f|T_k^{(2)}|\Lambda_i\rangle\begin{pmatrix}J_f & 2 & J_i\\ \omega_f & k & \omega_i\end{pmatrix}\Bigg|^2\Bigg\}. \quad (3.193)$$

In the last line of the above equation, from Eq. (3.188)

$$P_0^{(0)}=\frac{1}{\sqrt{3}}\ \text{ and }\ P_0^{(2)}=\sqrt{\frac{2}{15}} \quad (3.194)$$

are used. From Eq. (3.193), it follows that the spectrum consists of the sum of two independent spectra due to $T_0^{(0)}$ and $T_k^{(2)}$. As in the case of a one-photon transition, the two-photon transition matrix elements determine the selection rules for the total angular momentum and its projection. Moreover, they specify the nonvanishing tensor component related to the electronic matrix elements $\langle \pm\Lambda_f|T_k^{(j)}|\Lambda_i\rangle$ for the specific states. If the electronic wave function is approximated by a single electron wave function, it can be shown that $T_k^{(j)} \sim e^{ik\phi}$. Approximate selection rules for the orbital angular momentum projection can be obtained as follows:

$$\begin{aligned}\langle\Lambda_f|T_k^{(j)}|\Lambda\rangle &= \langle\Lambda_f+k|T_k^{(j)}|\Lambda\rangle\delta_{\Lambda_f,k+\Lambda_i},\\ \langle-\Lambda_f|T_k^{(j)}|\Lambda\rangle &= \langle\Lambda_f+k|T_k^{(j)}|\Lambda\rangle\delta_{\Lambda_f,-(k+\Lambda_i)}.\end{aligned} \quad (3.195)$$

Since the orbital angular momentum quantum number is positive, the condition for a nonvanishing contribution of a tensor component is found to be $k=\Lambda_f-\Lambda_i$ or $k=-(\Lambda_f+\Lambda_i)$. For NO, the possible two-photon transitions from the ground state ($X\ ^2\Pi$) to the low lying Rydberg state are listed in Table 3.2 [122]. The transitions

Table 3.2: Non-vanishing spherical tensor components $T_k^{(j)}$ of the two-photon transitions from the $X^2\Pi$ to various Rydberg states [122].

	ω	Λ	j	k	$T_k^{(j)}$
$X^2\Pi$	$\frac{1}{2}, \frac{3}{2}$	1			
$D, H^2\Sigma$	$\frac{1}{2}$	0	2	-1	$T_{-1}^{(2)}$
$C, H'^2\Pi$	$\frac{1}{2}, \frac{3}{2}$	1	0	0	$T_0^{(0)}$
			2	0,-2	$T_0^{(2)}, T_{-2}^{(2)}$
$F^2\Delta$	$\frac{3}{2}, \frac{5}{2}$	2	2	+1	$T_1^{(2)}$
$^2\Phi$	$\frac{3}{2}, \frac{5}{2}$	3	2	+2	$T_2^{(2)}$

to Σ, Δ, or Φ states are carried by a single component of the second rank tensor while transitions to Π states involve contributions from different tensor components.

3.3 Theory of NO-X (X=Ar, Ne)

In this section, the theoretical description of van der Waals complexes including an open shell diatom will be discussed.

3.3.1 Correlation Diagram: Energy levels for Bending Motions

The interaction for an NO-X complex depends on the Jacobi coordinates R, r, θ as defined in Fig. 3.2(a). R represents the length of $\boldsymbol{R}$ which describes a vector from the cm of the nuclei of the diatom to the atom nucleus. r represents the distance between the nuclei of the diatom. And, θ denotes the angle between $\boldsymbol{R}$

and $\boldsymbol{r}$. For the following discussion, it is assumed that the vibration of the diatom is neglected. In order to describe the electronic structure of the interaction, it is important to distinguish three different coordinate frames as shown in Fig. 3.2(b): a space fixed(sf) frame, a body fixed(bf) frame and a molecule fixed(mf) frame. In the sf frame, the origin is located at the cm of all three nuclei. The bf(2) frame is defined by rotating the z axis of the sf frame through two Euler angles α and β onto the direction of $\boldsymbol{R}$. Note that the diatom does not lie in the xz nor yz planes. In this frame, the orientation of the diatom vector $\boldsymbol{r}$ is represented by the polar angles θ and ϕ. The mf frame is defined by rotating the bf frame through the angles θ and ϕ so that the vector $\boldsymbol{r}$ lies along the z axis of mf frame. In this frame, all nuclei lie in the xz plane. For clarity, the total angular momentum of the atom-diatom system and its projections as well as those of the diatom must be defined carefully. As shown in Fig. 3.2(c), $\boldsymbol{J}$ is the total angular momentum of the atom-diatom system and M and P are its projections onto the z-axes of the sf and bf(2) frames, respectively. And, $\boldsymbol{j}$ is the total angular momentum of the diatom and P and ω are its projection onto the z-axes of the bf(2) and mf frames, respectively. Since the end-over-end rotational angular momentum of the complex, $\boldsymbol{L}$, is perpendicular to the triatom plane, P is the projection of both J and j onto the z-axes of the bf(2) z-axis. Finally, $\boldsymbol{l}$ is the electron orbital momentum of the diatom.

The energy level pattern of the complex can be understood by defining the following bender Hamiltonian

$$H_{bend} = B(\boldsymbol{J}^2 + \boldsymbol{j}^2 - J_z^2 - j_z^2) + H_{BC}^{(0)} + V_{int} \tag{3.196}$$

where B is the rotational constant of the NO-X complex. $H_{BC}^{(0)}$ is the zeroth order term of the H_{BC} in Eq. (3.51). The total wavefunction is approximated as a product of functions describing the overall rotation of the complex, the rotation of the diatom

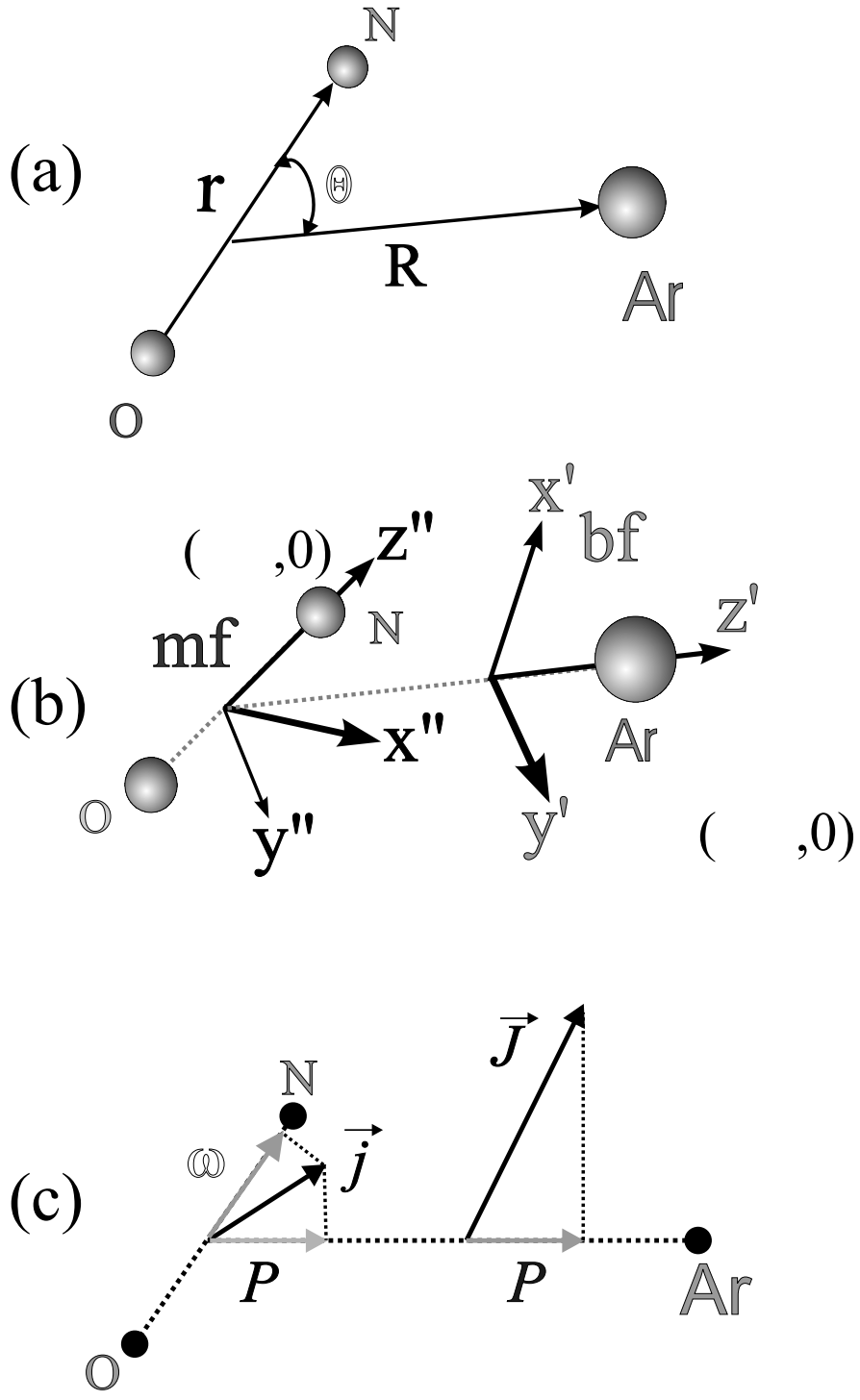

Figure 3.2: (a) Jacobi coordinates, (b) definition of the coordinate frames, (c) total angular momenta and their projections onto the bf(2) and mf frames.

within the complex, and the electronic structure of the diatom including spin:

$$\Psi^{JM}_{Pj\omega}(\alpha,\beta,\phi,\theta,r,\boldsymbol{\rho}_{k_{bc}}) = \sqrt{\frac{2J+1}{4\pi}} D^{(J)^*}_{MP}(\alpha,\beta,0) \sqrt{\frac{2J+1}{4\pi}} D^{(j)^*}_{P\omega}(\phi,\theta,0)\ \psi^{el}_{n\lambda}\ \Gamma_{s\sigma}. \tag{3.197}$$

Details are discussed in Section 3.3.4. The matrix elements of the intermolecular potential between different electronic states are obtained by integrating over the electronic wavefunction:

$$V_{\lambda\lambda'}(R,r,\theta) = \left\langle n\lambda \middle| V_{int} \middle| n\lambda' \right\rangle \tag{3.198}$$

The potential energy surfaces $V_{\lambda\lambda'}(R,\theta)$ may be expanded in terms of rotation matrices:

$$\left\langle n\lambda \middle| V_{int} \middle| n\lambda' \right\rangle = D^{(\tilde{l})^*}_{0\ \lambda-\lambda'}(0,\theta,0) V_{\tilde{l}\ \lambda-\lambda'}(R,r). \tag{3.199}$$

For Π states, λ and λ' are equal to either 1 or -1. Π states have off-diagonal terms $V_{\tilde{l}2}$ for $\tilde{l} \geq 2$ as well as diagonal $V_{\tilde{l}0}$ terms. The off-diagonal terms do not exist for Σ states. Since the off-diagonal terms cause only higher order perturbations, they are neglected in a first approximation. Though the potential terms depend on the coordinate r and R, at this point only the rotational and the angular motion are of interest. As a zeroth order approximation the bender Hamiltonian may be considered vibrationally averaged over r and R. The coefficient of the first potential term, V_{00} simply shifts all levels of the complex by a constant amount relative to the levels of the free diatom. The anisotropic terms, V_{10}, V_{20} etc., cause additional shifts and splittings of the observed levels.

According to Hutson [123], the anisotropy of the diagonal terms of the interaction potential play an important role in determining the energy level structure of the complex. Depending on the relative magnitudes of B, b (the rotational constant of the diatom) and V_{aniso} (dominant anisotropic term), there are three different cases labeled 1, 2, and 3 in order of increasing anisotropy. For case 1, the anisotropy

is so small that $V_{aniso} < B \ll b$. The diatom is almost rotating freely within the complex. The orbital angular momentum $\boldsymbol{L}$ associated with the end-over-end rotation is well defined and the total angular momentum of the diatom is conserved. In this situation, it is convenient to use a space fixed(sf) description.

For case 2, the anisotropy is larger than B but still smaller than b ($B < V_{aniso} < b$). The orbital angular momentum is not conserved whereas the angular momentum of the diatom is still a good quantum number. Thus, it is appropriate to use the eigenfunctions of the diatom. In this case, it is necessary to consider Coriolis coupling terms which connect states of the same J and j but with ω differing by ± 1. For this purpose, it is convenient to use two angle embedding of the body fixed frame (bf(2)) defined by two Euler angles α and β with respect to a sf frame.

For real van der Waals molecules, it is necessary to go beyond the case 2 limit. The case 2 may break down if the anisotropy is high enough to cause significant mixing of states with different j. An odd-order anisotropy can be effective in causing the change over from case 2 to case 3. The case 3 occurs when the potential anisotropy is large compared to b, so that the complex is a nearly rigid molecule executing torsional oscillations. While P is still nearly conserved, j and l are no longer good quantum numbers. Different diatom rotor states will be coupled by the interaction potential, but it is still feasible to expand the wavefunction in terms of a bf(2) basis set. A basis set of vibrational wavefunctions located at the equilibrium geometry may be used. Appropriate basis sets are different for linear and T-shaped configuration.

As the anisotropy increases, the complex becomes more rigid. In the limit, $V_{ansio} \gg \ b > B$, the rotational level structure can be approximated by that of a rigid rotor Hamiltonian. In this case, the Hamiltonian is derived using three angle embedding (bf(3)). The bf(3) frame is defined with the vector $\boldsymbol{R}$ along the z-axis and the complex lies in the xz plane. This approach has been successfully applied to

the analysis of the rotational structure of the NO-X complexes in various strongly bound Rydberg states [69, 70].

In order to understand the couplings between the overall rotation and the bending motion, a Hamiltonian H'_{bend} involving an effective anisotropy is considered:

$$\begin{aligned} H'_{bend} &= bj^2 + V_{10}D_{00}^{(1)*}(0,\theta,0) + V_{20}D_{00}^{(2)*}(0,\theta,0) \\ &= b\Big\{\frac{1}{\sin\theta}\frac{\theta}{\partial\theta}\sin\theta + \frac{1}{\sin^2\theta}\frac{\partial^2}{\partial\phi^2}\Big\} + V_{10}D_{00}^{(1)*}(0,\theta,0) + V_{20}D_{00}^{(2)*}(0,\theta,0). \end{aligned} \tag{3.200}$$

This Hamiltonian does not include the end-over-end rotation of the complex which allows one to determine correlation diagrams that scale only with the diatom rotational constant b [21]. Using the basis set of Eq. (3.197) the matrix elements of H'_{bend} are found as

$$\begin{aligned} \big\langle jP\omega\big|H'_{bend}\big|j'P\omega\big\rangle &= bj(j+1)\delta_{jj'} \\ &\quad + V_{10}(2j+1)(-)^{P-\omega}\begin{pmatrix} j & 1 & j' \\ -P & 0 & P \end{pmatrix}\begin{pmatrix} j & 1 & j' \\ -\omega & 0 & \omega \end{pmatrix} \\ &\quad + V_{20}(2j+1)(-)^{P-\omega}\begin{pmatrix} j & 2 & j' \\ -P & 0 & P \end{pmatrix}\begin{pmatrix} j & 2 & j' \\ -\omega & 0 & \omega \end{pmatrix}. \end{aligned} \tag{3.201}$$

The value of ω is chosen as the lowest value: $\omega = \frac{1}{2}$ for $^2\Pi_{1/2}$ states and $\omega = 0$ for $^1\Sigma$ states. In order to determine the eigenvalues the matrix H'_{bend} is diagonalized using a basis set involving different diatom states. For $^1\Sigma$ states the matrix is diagonalized for each value of P $(= 0 - 4)$ and includes j values from 0 up to 11 while for $^2\Pi_{1/2}$ states the matrix is diagonalized for each value of P $(= \frac{1}{2} - \frac{9}{2})$ and includes j values from $\frac{1}{2}$ up to $\frac{21}{2}$. Correlation diagrams are plotted in Figs. 3.3 and 3.4 as a function of V_{20} with $V_{10} = 0$ (part (a)), $V_{10} = 2b$ (part (b)) for a $^1\Sigma$ state and a $^2\Pi_{1/2}$ state, respectively.

For a $^1\Sigma$ state, Fig. 3.3(a) corresponds to a homonuclear diatom ($V_{10} = 0$) while Fig. 3.3(b) refers to a heteronuclear diatom with $V_{10} = 2b$. For a large negative value of V_{20}, the energy levels are those of a linear triatomic molecule with potential minima at $\theta = 0°$ and $\theta = 180°$. For $V_{10} = 0$, all levels are doubly degenerate since the potential well has two identical minima. For example, for $V_{20} = -50b$ in the correlation diagram Fig. 3.3(a) the energies for $j = 0$ and $j = 1$ are degenerate. Probabilities of finding the complex in each well are equal. Figure 3.5(a) shows the associated probabilities for these two energy levels with symmetric(II) and antisymmetric(I) wavefunctions. But, as soon as a V_{10} term is introduced, the well depths are no longer identical resulting in the lifting of the degeneracy. In order to show this, the wavefunctions for $V_{10} \neq 0$ ($V_{10} = 0.01b,\ 2b$) are plotted in Fig. 3.6. Even with a small value of V_{10}, the degeneracy is lifted, locating the system in one well.

For only small deviations from the linear geometry, the angular part of H'_{bend} can be approximated as

$$b\Big\{\frac{\partial^2}{\partial\theta^2} + \frac{1}{\theta}\frac{\partial}{\partial\theta} + \frac{1}{\theta^2}\frac{\partial^2}{\partial\phi^2}\Big\} + V_{10}D_{00}^{(1)*}(0,\theta,0) + V_{20}D_{00}^{(2)*}(0,\theta,0). \tag{3.202}$$

The quantity in brackets is just the two dimensional Laplacian in polar coordinates. By transforming θ and ϕ to Cartesian coordinates defined as

$$\begin{aligned} x &= \sin\theta\cos\phi \\ y &= \sin\theta\sin\phi, \end{aligned} \tag{3.203}$$

the Hamiltonian becomes

$$b\Big\{\frac{\partial^2}{\partial x^2} + \frac{\partial^2}{\partial y^2}\Big\} + V_{10}D_{00}^{(1)*}(0,\theta,0) + V_{20}D_{00}^{(2)*}(0,\theta,0). \tag{3.204}$$

For small amplitude motion, the potential can be approximated by a quadratic term in θ. In this case, the bending vibrational levels are equally spaced with the vth level

having a degeneracy of $(v+1)$ corresponding to the states with vibrational quantum number $K = v, v-2, \cdots, -v$.

For a large positive value of V_{20}, the energy levels correspond to those of a T-shaped complex. The wavefunction and the probability distribution for this configuration are shown in Fig.(3.5a). Depending on the values of V_{10} the maximum probability is found near $\theta = 90°$. The bending Hamiltonian for values near 90° decouples into a purely vibrational and a purely rotational term.

$$b\Big\{\frac{\partial^2}{\partial\theta^2} + \frac{\partial^2}{\partial\phi^2}\Big\} + V_{10}D_{00}^{(1)*}(0,\theta,0) + V_{20}D_{00}^{(2)*}(0,\theta,0). \tag{3.205}$$

Since the potential matrix elements do not depend on ϕ, the contribution to the rotational energy is found to be approximately given by bP^2. Within the rigid rotor model, this term represents the energy associated with the a-axis rotation. For $V_{10} = 0$, the A rotational constant of the complex is equal to the diatom rotational constant b. But, when the V_{10} term is large, its effect is to tip the equilibrium geometry away from $\theta = 90°$ so that the A rotational constant of the complex is larger than b. Figure 3.5(a)I-IV shows how the maximum in the probability distribution deviates from the T-shaped geometry depending on different values of $V_{10} = -25b,\ 0,\ 25b,\ 50b$, respectively.

For a $^2\Pi_{1/2}$ state, the V_{20} anisotropy splits each state into $j + \frac{1}{2}$ components with different values of P. For the $^1\Sigma$ state, the first $3j$ symbol in Eq. (3.201) is zero if $j = j'$ and the V_{10} anisotropy does not make a contribution to the diagonal matrix elements. On the other hand, for a $^2\Pi_{1/2}$ state this argument is no longer valid. Now, the V_{10} anisotropy causes first order splittings even for $V_{20} = 0$ shifting the $+\omega$ and $-\omega$ level by equal amounts but in opposite directions. Regarding the geometry of the complex, a similar argument may be applied as in the case of the $^1\Sigma$ state: a large negative value of V_{20} corresponds to the linear geometry and a large positive value of the V_{20} corresponds to the T-shaped geometry. In the T-shaped

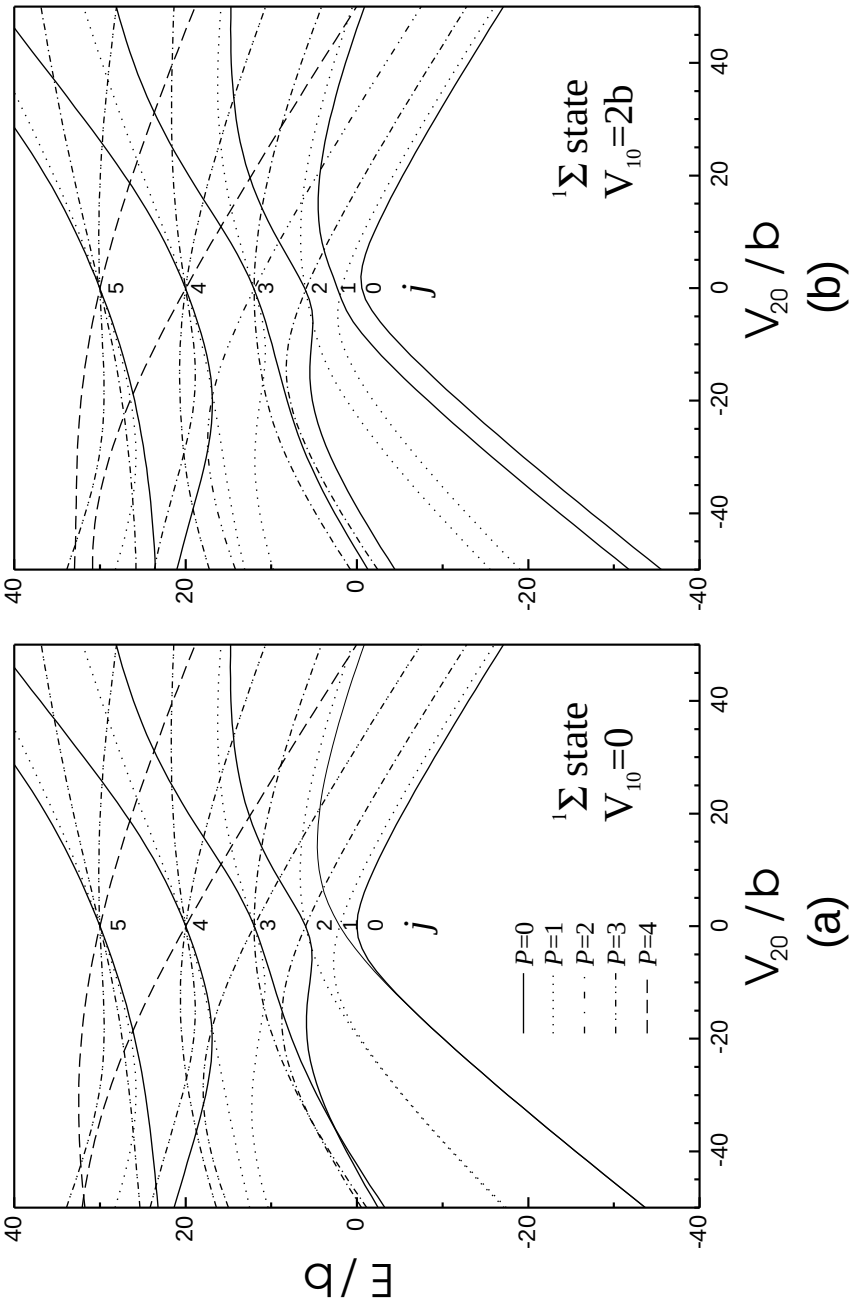

Figure 3.3: Correlation diagrams for complexes containing diatoms in $^1\Sigma$ states. Parts (a) and (b) depict the bending levels as a function of the V_{20} anisotropy for a homonuclear diatom ($V_{10} = 0$) and a heteronuclear diatom ($V_{10} = 2b$), respectively. Different types of lines are assigned for different P quantum numbers.

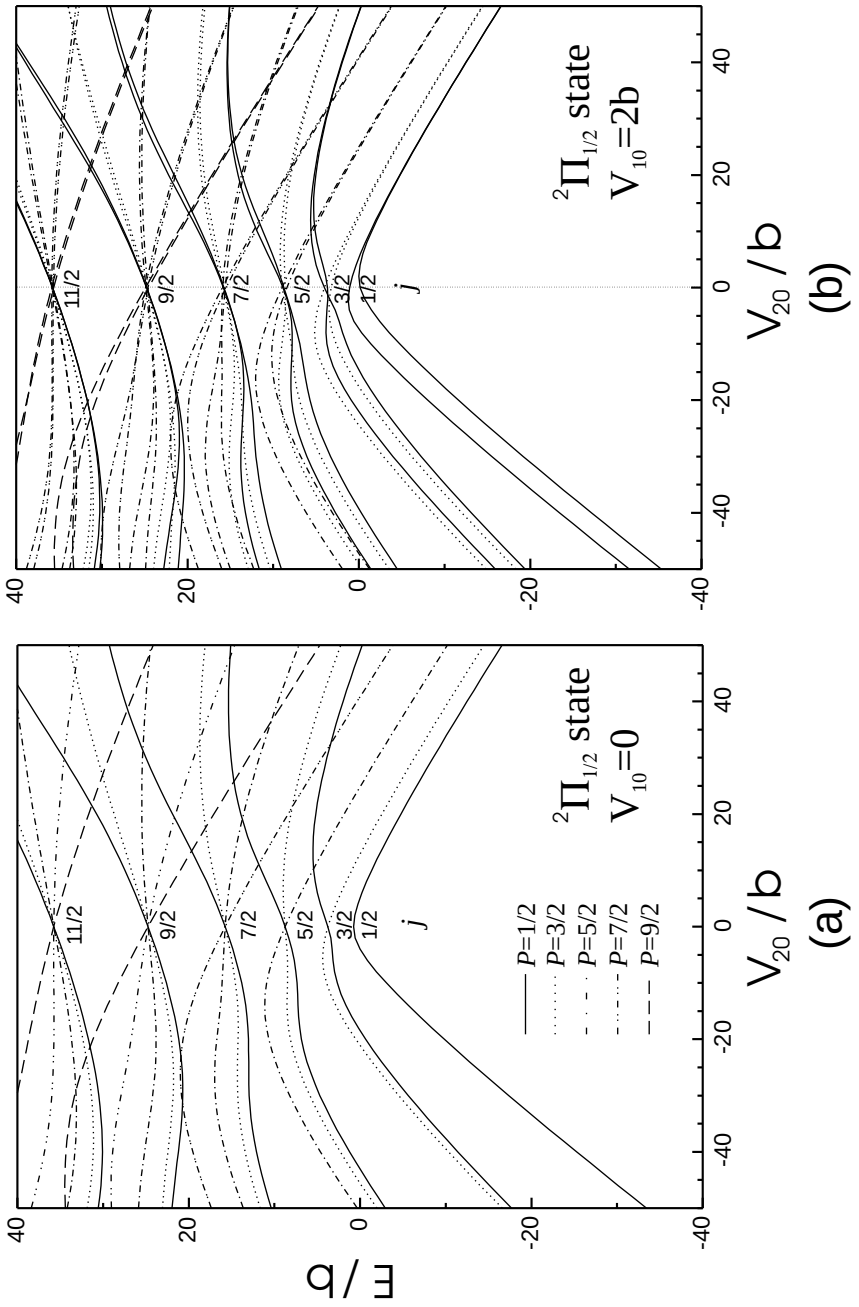

Figure 3.4: Correlation diagram for complexes containing diatoms in $^2\Pi_{1/2}$ states. Parts (a) and (b) depict the bending levels as a function of the V_{20} anisotropy for a homonuclear diatom ($V_{10} = 0$) and a heteronuclear diatom ($V_{10} = 2b$), respectively. Different types of lines are assigned for different P quantum numbers.

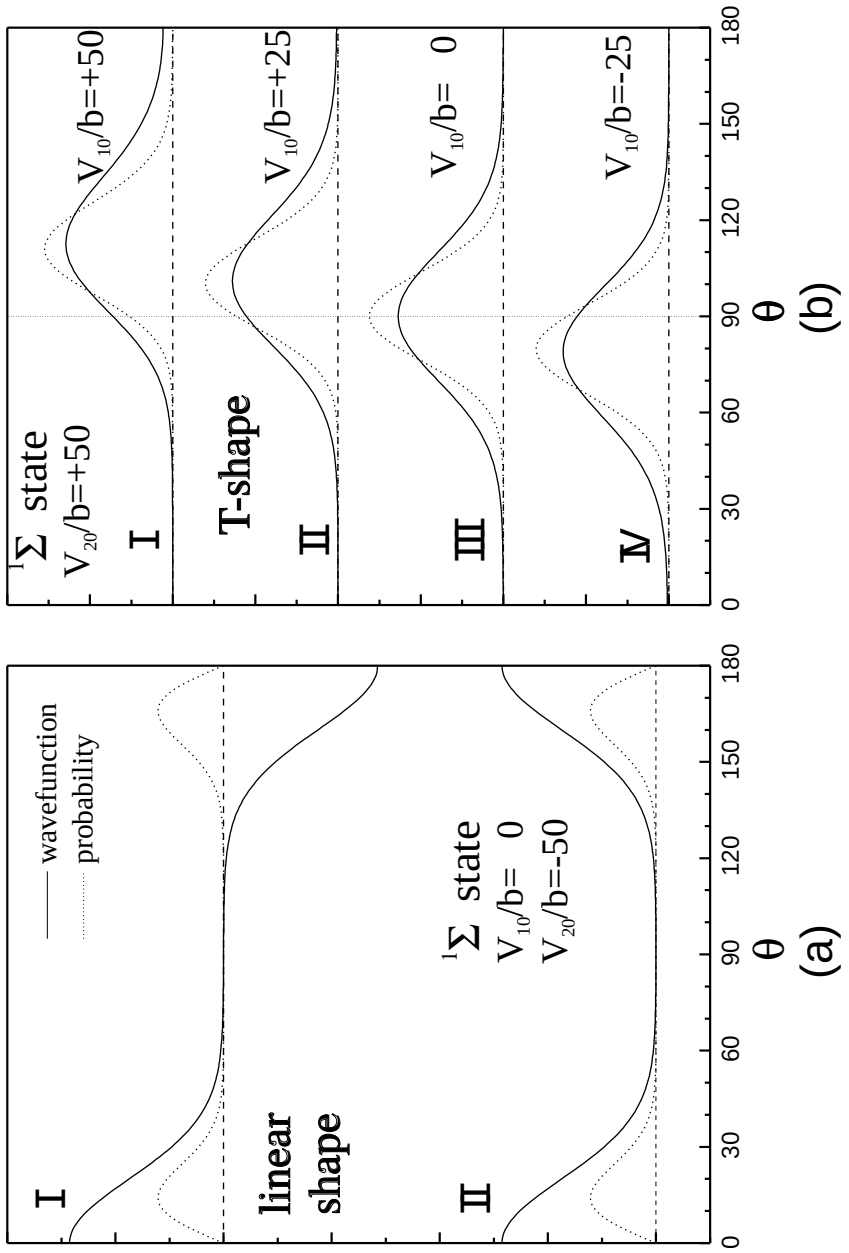

Figure 3.5: Wavefunctions and probabilities for $^1\Sigma$ state. Part (a) represents a linear geometry with $V_{20} = -50b$, $V_{10} = 0$. For a homonuclear diatom the potential well has two symmetric minima and the energy levels are degenerate. The wavefunctions for the degenerate levels are linear combinations of the wavefunctions for each well, yielding a symmetric ((a)I) and an antisymmetric ((a)II) function, but with identical probabilities. Part (b) shows the deviation from the T-shaped geometry depending on different values of the V_{10} anisotropy with the fixed valued of $V_{20} = +50b$.

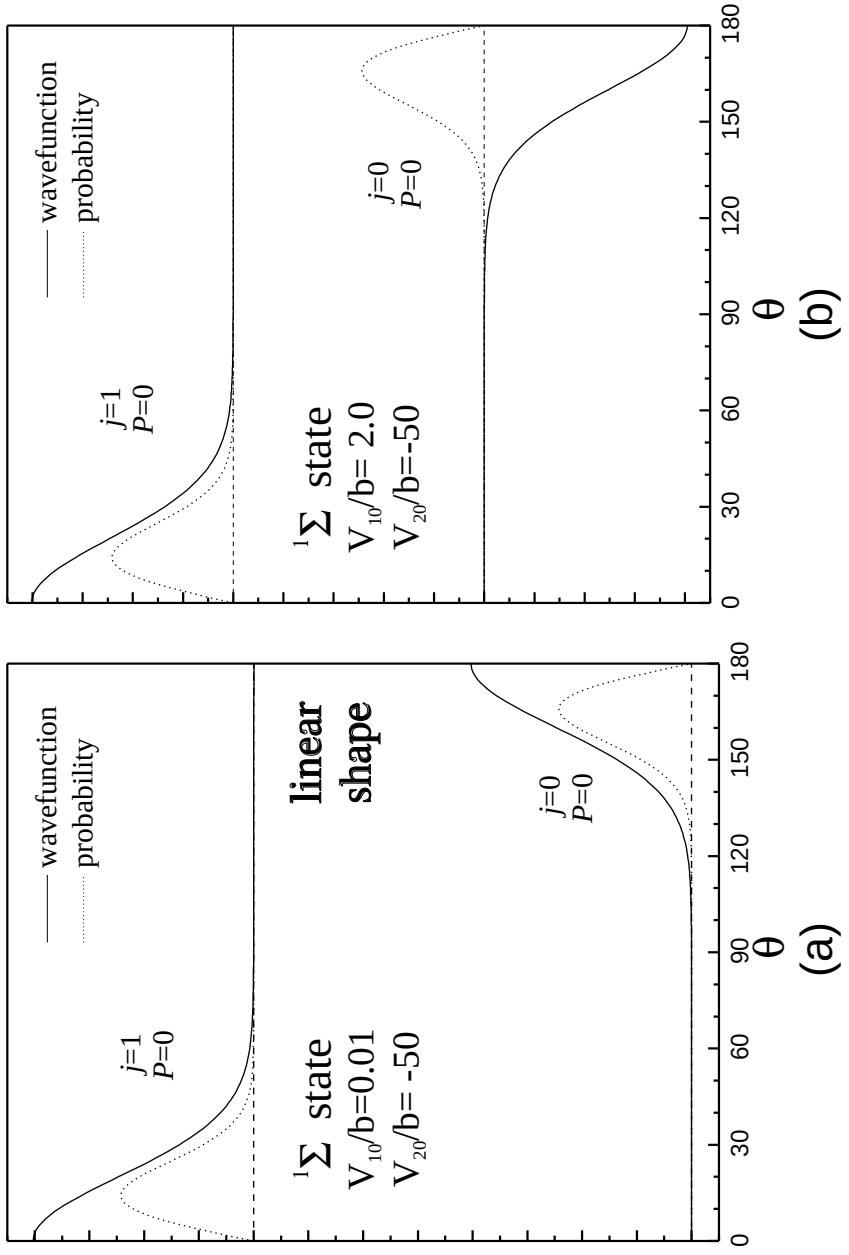

Figure 3.6: Wavefunctions and probabilities for a complex with a diatom in a $^1\Sigma$ state. As soon as V_{10} is introduced into the potential, the symmetry is broken. The wavefunctions and the probabilities are calculated with $V_{10} = 0.01b$ (a) $V_{10} = 2.0b$ (b). The probabilities for both cases are essentially identical.

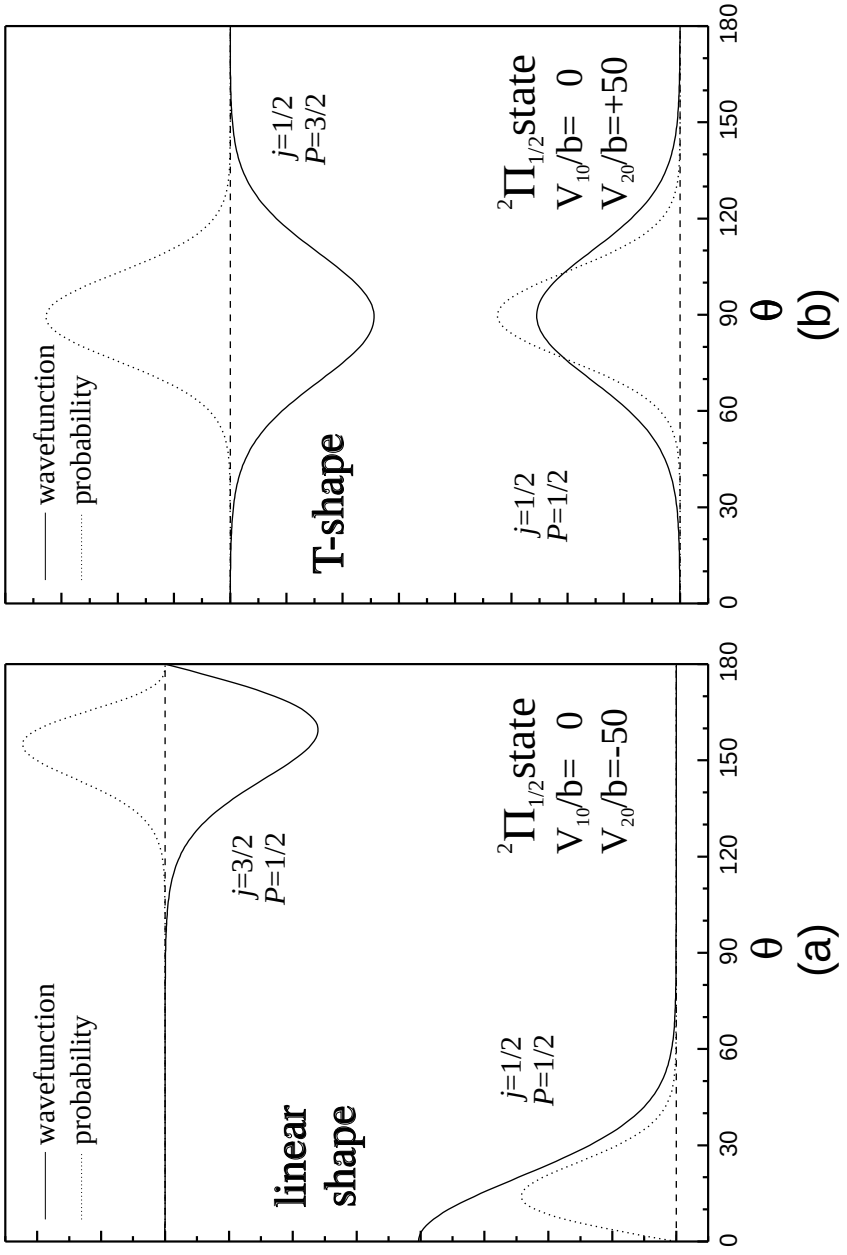

Figure 3.7: Wavefunctions and probabilities for a complex with a diatom in a $^2\Pi_{1/2}$ state. Parts (a) and (b) are for linear and T-shaped geometry, respectively.

geometry, the degree of deviation from the $\theta = 90°$ depends on the value of V_{10}. The correlation diagram for $^2\Pi_{3/2}$ state is essentially identical to that of a $^2\Pi_{1/2}$ state, except that the lowest allowed j value is now $\frac{3}{2}$. Examples of open shell complexes with linear and T-shaped geometries are the rare gas complexes of OH ($^2\Pi_{3/2}$ ground state) and NO ($^2\Pi_{1/2}$ ground state), respectively.

3.3.2 Hamiltonian of NO-X (X=Ar, Ne)

The position vectors of the particles in the sf frame are given by $\boldsymbol{R}_a$, $\boldsymbol{R}_b$, $\boldsymbol{R}_c$ (nuclei), and $\boldsymbol{R}_{k_a}$, $\boldsymbol{R}_{k_{bc}}$ (electrons). The kinetic energy of the complex is written as

$$T = \frac{1}{2}m_a\dot{\boldsymbol{R}}_a^2 + \frac{1}{2}\sum_{k_a=1}^{N_a} m_e\dot{\boldsymbol{R}}_{k_a}^2 + \frac{1}{2}m_b\dot{\boldsymbol{R}}_b^2 + \frac{1}{2}m_c\dot{\boldsymbol{R}}_c^2 + \frac{1}{2}\sum_{k_{bc}=1}^{N_{bc}} m_e\dot{\boldsymbol{R}}_{k_{bc}}^2. \tag{3.206}$$

The atom (denoted a) contains N_a electrons while the diatom (denoted bc) contains N_{bc} electrons. In order to partition the kinetic energy into contributions due to the two fragments and due to the relative motion of the two fragments, the position of the particles must be described with respect to two sf frames centered in the cm of the atom and the diatom, respectively:

$$\boldsymbol{R}_a = \boldsymbol{R}_{cm}^a + \boldsymbol{r}_a, \quad \text{and} \quad \boldsymbol{R}_{k_a} = \boldsymbol{R}_{cm}^a + \boldsymbol{r}_{k_a},$$

$$\boldsymbol{R}_b = \boldsymbol{R}_{cm}^{bc} + \boldsymbol{r}_b, \quad \boldsymbol{R}_c = \boldsymbol{R}_{cm}^{bc} + \boldsymbol{r}_c, \quad \text{and} \quad \boldsymbol{R}_{k_{bc}} = \boldsymbol{R}_{cm}^{bc} + \boldsymbol{r}_{k_{bc}}. \tag{3.207}$$

The relative position of the cm of the two fragments is defined as

$$\boldsymbol{R} = \boldsymbol{R}_{cm}^a - \boldsymbol{R}_{cm}^{bc}. \tag{3.208}$$

Using the definitions in Eq. (3.207) and (3.208) and the cm condition, the kinetic energy is separated into three contributions:

$$\begin{aligned} T &= \frac{1}{2}m_a\dot{\boldsymbol{r}}_a^2 + \frac{1}{2}\sum_{k_a=1}^{N_a} m_e\dot{\boldsymbol{r}}_{k_a}^2 + \frac{1}{2}m_b\dot{\boldsymbol{r}}_b^2 + \frac{1}{2}m_c\dot{\boldsymbol{r}}_c^2 + \frac{1}{2}\sum_{k_{bc}=1}^{N_{bc}} m_e\dot{\boldsymbol{r}}_{k_{bc}}^2 + \frac{1}{2}\mu\dot{\boldsymbol{R}}^2 \\ &= T_A + T_{BC} + T_{rel}. \end{aligned} \tag{3.209}$$

Note that the kinetic energy associated with the cm motion of the complex is ignored here. The first and second term in Eq. (3.209) represent the kinetic energy of the atom, T_A. The next three terms correspond to the kinetic energy of the diatom, T_{AB}. The last term represents the kinetic energy associated with the relative motion of the two fragments. μ denotes the reduced mass of the complex. Note that the coordinates used so far are not completely independent. In order to express the kinetic energy in terms of a set of independent generalized coordinates a sf nuclear cm frame is introduced for each fragment. The transformation of the coordinates for the diatom becomes

$$\boldsymbol{r}_b = -\frac{m_e}{M_{tot}^{bc}} \sum_{k_{bc}}^{N_{bc}} \boldsymbol{\xi}_{k_{bc}} + \frac{m_c}{m_{bc}} \boldsymbol{r}, \quad \boldsymbol{r}_c = -\frac{m_e}{M_{tot}^{bc}} \sum_{k_{bc}}^{N_{bc}} \boldsymbol{\xi}_{k_{bc}} - \frac{m_b}{m_{bc}} \boldsymbol{r} \tag{3.210}$$

$$\text{and} \qquad \boldsymbol{r}_{j_{bc}} = -\frac{m_e}{M_{tot}^{bc}} \sum_{k_{bc}}^{N_{bc}} \boldsymbol{\xi}_{k_{bc}} + \boldsymbol{\xi}_{j_{bc}}. \tag{3.211}$$

Similarly, for the atom

$$\boldsymbol{r}_a = -\frac{m_e}{M_{tot}^{a}} \sum_{k_a}^{N_a} \boldsymbol{\xi}_{k_a} \qquad \text{and} \qquad \boldsymbol{r}_{j_a} = -\frac{m_e}{M_{tot}^{a}} \sum_{k_a}^{N_a} \boldsymbol{\xi}_{k_a} + \boldsymbol{\xi}_{j_a}. \tag{3.212}$$

$\boldsymbol{\xi}_{k_a}$ and $\boldsymbol{\xi}_{k_{bc}}$ represent the electron coordinates of the atom and the diatom in the sf nuclear cm frame, respectively. The kinetic energy in the nuclear cm frames takes the form of

$$\begin{aligned} T &= \frac{1}{2}\mu \dot{\boldsymbol{R}}^2 + \frac{1}{2}\mu_{bc}\dot{\boldsymbol{r}}^2 + \frac{1}{2}\sum_{k_{bc}=1}^{N_{bc}} m_e \dot{\boldsymbol{\xi}}_{k_{bc}}^2 - \frac{1}{2}\frac{m_e^2}{M_{bc}^{tot}} \left(\sum_{j_{bc}=1}^{N_{bc}} \dot{\boldsymbol{\xi}}_{j_{bc}} \right)^2 \\ &\quad + \frac{1}{2}\sum_{k_a=1}^{N_a} m_e \dot{\boldsymbol{\xi}}_{k_a}^2 - \frac{1}{2}\frac{m_e^2}{M_{a}^{tot}} \left(\sum_{j_a=1}^{N_a} \dot{\boldsymbol{\xi}}_{j_a} \right)^2 . \end{aligned} \tag{3.213}$$

μ_{bc} denotes the reduced mass of the diatom. Due to the mass ratio, the mass polarization terms which are the fourth and sixth terms in Eq. (3.213) are very small, and will be neglected henceforth. The kinetic energy is reduced to

$$\begin{aligned} T &= \frac{1}{2}\sum_{k_a=1}^{N_a} m_e \dot{\boldsymbol{\xi}}_{k_a}^2 + \frac{1}{2}\mu_{bc}\dot{\boldsymbol{r}}^2 + \frac{1}{2}\sum_{k_{bc}=1}^{N_{bc}} m_e \dot{\boldsymbol{\xi}}_{k_{bc}}^2 + \frac{1}{2}\mu \dot{\boldsymbol{R}}^2 \\ &= T_A + T_{BC} + T_{int}. \end{aligned} \tag{3.214}$$

The second and third term correspond to the kinetic energy of the diatom.

The potential energy is the sum of the Coulomb interaction energy between all particles (including nuclei and electrons). After successive transformations using Eqs. (3.207), (3.210)-(3.212), the potential energy is given by

$$
\begin{aligned}
V &= \frac{Z_b Z_c e^2}{|\boldsymbol{r}_b - \boldsymbol{r}_c|} - \sum_{k_{bc}} \frac{Z_b e^2}{|\boldsymbol{r}_b - \boldsymbol{r}_{k_{bc}}|} - \sum_{k_{bc}} \frac{Z_c e^2}{|\boldsymbol{r}_c - \boldsymbol{r}_{k_{bc}}|} + \sum_{k_{bc}<j_{bc}} \frac{e^2}{|\boldsymbol{r}_{k_{bc}} - \boldsymbol{r}_{j_{bc}}|} && \text{(3.215a)} \\
&\quad - \sum_{k_a} \frac{Z_a e^2}{|\boldsymbol{r}_a - \boldsymbol{r}_{k_a}|} + \sum_{k_a<j_a} \frac{e^2}{|\boldsymbol{r}_{k_a} - \boldsymbol{r}_{j_a}|} && \text{(3.215b)} \\
&\quad + \frac{Z_a Z_b e^2}{|\boldsymbol{R} + \boldsymbol{r}_a - \boldsymbol{r}_b|} + \frac{Z_a Z_c e^2}{|\boldsymbol{R} + \boldsymbol{r}_a - \boldsymbol{r}_c|} - \sum_{k_{bc}} \frac{Z_a e^2}{|\boldsymbol{R} + \boldsymbol{r}_a - \boldsymbol{r}_{k_{bc}}|} \\
&\quad - \sum_{k_a} \frac{Z_b e^2}{|\boldsymbol{R} + \boldsymbol{r}_{k_a} - \boldsymbol{r}_b|} - \sum_{k_a} \frac{Z_c e^2}{|\boldsymbol{R} + \boldsymbol{r}_{k_a} - \boldsymbol{r}_c|} + \sum_{k_a, k_{bc}} \frac{e^2}{|\boldsymbol{R} + \boldsymbol{r}_{k_a} - \boldsymbol{r}_{k_{bc}}|} && \text{(3.215c)} \\
&= V_{BC} + V_A + V_{int}.
\end{aligned}
$$

The first four terms, Eq. (3.215a), represent the potential energy of the diatom. The fifth and sixth terms, Eq. (3.215b), are the potential energy of the atom. The remaining terms define the interaction potential. The interaction potential will be described in detail in Section 3.3.2.

The bf(2) representation of the Hamiltonian is derived by transforming all coordinates to the bf(2) frame as follows:

$$
\boldsymbol{R}^{bf} = \mathsf{C}(\alpha,\beta)\boldsymbol{R}^{sf} = \begin{pmatrix} 0 \\ 0 \\ R \end{pmatrix}, \quad \boldsymbol{r}^{bf} = \mathsf{C}(\alpha,\beta)\boldsymbol{r}^{sf} = r \begin{pmatrix} \sin\beta\cos\alpha \\ \sin\beta\sin\alpha \\ \cos\beta \end{pmatrix},
$$

and

$$
\boldsymbol{\eta}_{k_a} = \mathsf{C}(\alpha,\beta)\boldsymbol{\xi}_{k_a}, \quad \boldsymbol{\eta}_{k_{bc}} = \mathsf{C}(\alpha,\beta)\boldsymbol{\xi}_{k_{bc}}. \tag{3.216}
$$

Velocity vectors projected onto the bf(2) axes are calculated using Eq. (3.23):

$$
\mathsf{C}(\alpha,\beta)\dot{\boldsymbol{r}}^{sf} = \dot{\boldsymbol{r}}^{bf} + \boldsymbol{\omega} \times \boldsymbol{r}^{bf}, \tag{3.217}
$$

$$
\mathsf{C}(\alpha,\beta)\dot{\boldsymbol{\xi}}_{k_a} = \dot{\boldsymbol{\eta}}_{k_a} + \boldsymbol{\omega} \times \boldsymbol{\eta}_{k_a}, \tag{3.218}
$$

$$\mathsf{C}(\alpha,\beta)\dot{\boldsymbol{\xi}}_{k_{bc}} = \dot{\boldsymbol{\eta}}_{k_{bc}} + \boldsymbol{\omega}\times\boldsymbol{\eta}_{k_{bc}}. \tag{3.219}$$

The kinetic energy in terms of the generalized coordinates $(R,\alpha,\beta,\boldsymbol{r}^{bf},\boldsymbol{\eta}_{k_a},\boldsymbol{\eta}_{k_{bc}})$ is written as

$$\begin{aligned} T &= \frac{\mu}{2}\big(\dot{R}^2 + R^2\dot{\beta}^2 + R^2\dot{\alpha}^2\sin^2\beta\big) + \frac{\mu_{bc}}{2}\big(\dot{\boldsymbol{r}}^{bf} + \boldsymbol{\omega}\times\boldsymbol{r}^{bf}\big)^2 \\ &\quad + \frac{m_e}{2}\sum_{k_{bc}}^{N_{bc}}\big(\dot{\boldsymbol{\eta}}_{k_{bc}} + \boldsymbol{\omega}\times\boldsymbol{\eta}_{k_{bc}}\big)^2 + \frac{m_e}{2}\sum_{k_a}^{N_a}\big(\dot{\boldsymbol{\eta}}_{k_a} + \boldsymbol{\omega}\times\boldsymbol{\eta}_{k_a}\big)^2. \end{aligned} \tag{3.220}$$

In order to derive the classical Hamiltonian, it is necessary to find the momenta conjugate to the generalized coordinates. The conjugate momenta $\boldsymbol{P}_R,\ \boldsymbol{p}_r,\ \boldsymbol{p}_{k_a}$, and $\boldsymbol{p}_{k_{bc}}$ are found easily:

$$\boldsymbol{P}_R = \nabla_{\dot{\boldsymbol{R}}}T = \mu\big(\dot{\boldsymbol{R}}^{bf} + \boldsymbol{\omega}\times\boldsymbol{R}^{bf}\big), \tag{3.221a}$$

$$\boldsymbol{p}_r = \nabla_{\dot{\boldsymbol{r}}}T = \mu_{bc}\big(\dot{\boldsymbol{r}}^{bf} + \boldsymbol{\omega}\times\boldsymbol{r}^{bf}\big), \tag{3.221b}$$

$$\boldsymbol{p}_{k_a} = \nabla_{\dot{\boldsymbol{\eta}}_{k_a}}T = m_e\big(\dot{\boldsymbol{\eta}}_{k_a} + \boldsymbol{\omega}\times\boldsymbol{\eta}_{k_a}\big), \tag{3.221c}$$

$$\boldsymbol{p}_{k_{bc}} = \nabla_{\dot{\boldsymbol{\eta}}_{k_{bc}}}T = m_e\big(\dot{\boldsymbol{\eta}}_{k_{bc}} + \boldsymbol{\omega}\times\boldsymbol{\eta}_{k_{bc}}\big). \tag{3.221d}$$

The total angular momentum projected onto the bf(2) frame, $\boldsymbol{J}^{bf}$, is given by the gradient of the kinetic energy with respect to $\boldsymbol{\omega}$. For an arbitrary position vector $\boldsymbol{a}^{bf}$, the following relationship holds:

$$\nabla_{\boldsymbol{\omega}}\Big[\frac{m}{2}\big(\dot{\boldsymbol{a}}^{bf} + \boldsymbol{\omega}\times\boldsymbol{a}^{bf}\big)^2\Big] = m\boldsymbol{a}^{bf}\times\big(\dot{\boldsymbol{a}}^{bf} + \boldsymbol{\omega}\times\boldsymbol{a}^{bf}\big) = \boldsymbol{a}^{bf}\times\boldsymbol{p}_a. \tag{3.222}$$

Using Eq. (3.222), the gradient of the kinetic energy with respect to $\boldsymbol{\omega}$ is calculated as

$$\begin{aligned} \nabla_{\boldsymbol{\omega}}T &= \boldsymbol{R}^{bf}\times\boldsymbol{P}_R + \boldsymbol{r}^{bf}\times\boldsymbol{p}_r + \sum_{k_a}\boldsymbol{\eta}_{k_a}\times\boldsymbol{p}_{k_a} + \sum_{k_{bc}}\boldsymbol{\eta}_{k_{bc}}\times\boldsymbol{p}_{k_{bc}} \\ &= \boldsymbol{L}^{bf} + \boldsymbol{j}_{bc}^{bf} + \boldsymbol{j}_a^{bf}. \end{aligned} \tag{3.223}$$

The orbital angular momentum and the internal angular momentum are defined as $\boldsymbol{L}$ and $\boldsymbol{j}_{bc}^{bf}$, respectively. $\boldsymbol{j}_a^{bf}$ represents the orbital angular momentum of the

atom. In order to verify that the above expression is equivalent to the total angular momentum calculated for the sf frame but projected onto the bf(2) frame, it is necessary to evaluate the total angular momentum. The total angular momentum is defined in the sf frame as

$$\boldsymbol{J}^{sf} = m_b \boldsymbol{R}_b \times \dot{\boldsymbol{R}}_b + m_c \boldsymbol{R}_c \times \dot{\boldsymbol{R}}_c + m_e \sum_{j_{bc}} \boldsymbol{R}_{j_{bc}} \times \dot{\boldsymbol{R}}_{j_{bc}} + m_a \boldsymbol{R}_a \times \dot{\boldsymbol{R}}_a + m_e \sum_{j_a} \boldsymbol{R}_{j_a} \times \dot{\boldsymbol{R}}_{j_a}. \tag{3.224}$$

After the transformations of the coordinates using Eqs. (3.207), (3.210)-(3.212), $\boldsymbol{J}^{sf}$ becomes

$$\boldsymbol{J}^{sf} = \mu \boldsymbol{R}^{sf} \times \dot{\boldsymbol{R}}^{sf} + \mu_{bc} \boldsymbol{r}^{sf} \times \dot{\boldsymbol{r}}^{sf} + m_e \sum_{k_{bc}}^{N_{bc}} \boldsymbol{\xi}^{sf} \times \dot{\boldsymbol{\xi}}^{sf} + m_e \sum_{k_a}^{N_a} \boldsymbol{\xi}^{sf} \times \dot{\boldsymbol{\xi}}^{sf}. \tag{3.225}$$

When $\boldsymbol{J}^{sf}$ is transformed to the bf frame, $\boldsymbol{J}^{bf}$ is

$$\begin{aligned} \boldsymbol{J}^{bf} &= \mathsf{C}\boldsymbol{J}^{sf} \\ &= \mu \mathsf{C}\boldsymbol{R}^{sf} \times \mathsf{C}\dot{\boldsymbol{R}}^{bf} + \mu \mathsf{C}\boldsymbol{r}^{sf} \times \mathsf{C}\dot{\boldsymbol{r}}^{bf} + m_e \sum_{k_a} \mathsf{C}\boldsymbol{\xi}_{k_a} \times \mathsf{C}\dot{\boldsymbol{\xi}}_{k_a} + m_e \sum_{k_{bc}} \mathsf{C}\boldsymbol{\xi}_{k_{bc}} \times \mathsf{C}\dot{\boldsymbol{\xi}}_{k_{bc}} \\ &= \boldsymbol{R}^{bf} \times \boldsymbol{P}_R + \left(\boldsymbol{r}^{bf} \times \boldsymbol{p}_r + \sum_{k_a} \boldsymbol{\eta}_{k_{bc}} \times \boldsymbol{p}_{k_{bc}} \right) + \sum_{k_{bc}} \boldsymbol{\eta}_{k_a} \times \boldsymbol{p}_{k_a}. \end{aligned} \tag{3.226}$$

This result is exactly the same as Eq. (3.223) meaning that $\nabla_{\boldsymbol{\omega}} T = \boldsymbol{J}^{bf}$.

In the same way as Eqs. (3.29) and (3.30) for the diatom, the momenta conjugate to α and β are obtained by applying the chain rule,

$$J_\alpha = \frac{\partial T}{\partial \dot{\alpha}} = \mu R^2 \dot{\alpha} \sin^2 \beta - \sin \beta \left(j^{bf}_{bc\ x} + j^{bf}_{a\ x} \right) + \cos \beta \left(j^{bf}_{bc\ z} + j^{bf}_{a\ z} \right) \tag{3.227a}$$

and

$$J_\beta = \frac{\partial T}{\partial \dot{\beta}} = \mu R^2 \dot{\beta} + j^{bf}_{bc\ y} + j^{bf}_{a\ y}. \tag{3.227b}$$

Using Eqs. (3.226) and (3.227), the components of the total angular momentum projected onto the bf(2) frame are

$$J^{bf}_x = -\csc \beta\ J_\alpha + \cot \beta \left(j^{bf}_{bc\ z} + j^{bf}_{a\ z} \right),$$

$$
\begin{aligned}
J_y^{bf} &= J_\beta, \\
J_z^{bf} &= j_{bc\ z}^{bf} + j_{a\ z}^{bf}.
\end{aligned} \tag{3.228}
$$

The kinetic energy in terms of the generalized coordinates and their conjugate momenta is expressed as

$$
\begin{aligned}
T &= \frac{1}{2\mu}\boldsymbol{P}_R^2 + \frac{1}{2\mu R^2}\Big[\left(J_x^{bf} - j_{bc\ x}^{bf} - j_{a\ x}^{bf}\right)^2 + \left(J_y^{bf} - j_{bc\ y}^{bf} - j_{a\ y}^{bf}\right)^2\Big] \\
&\quad + T_{BC} + \frac{1}{2m_e}\sum_{k_a}\boldsymbol{p}_{k_a}^2
\end{aligned} \tag{3.229}
$$

where

$$
T_{BC} = \frac{1}{2\mu_{bc}}\boldsymbol{p}_r^2 + \frac{1}{2m_e}\sum_{k_{bc}}\boldsymbol{p}_{k_{bc}}^2.
$$

Since the atom of interest is a rare gas atom such as Ar and Ne, it is appropriate to assume that the atom is structureless, i.e., $\boldsymbol{j}_a^{bf} = 0$. In order to derive the quantum mechanical Hamiltonian, the Podolsky trick [108] is applied yielding

$$
\begin{aligned}
H &= T_R + \frac{1}{2\mu R^2}\Big[(J_x^{bf} - j_{bc\ x}^{bf})^2 + \frac{1}{\sin\beta}(J_y^{bf} - j_{bc\ y}^{bf})\sin(J_y^{bf} - j_{bc\ y}^{bf})\Big] \\
&\quad + H_A + H_{BC} + T_{BC} + V_{int}(R, \theta, \boldsymbol{r}, \boldsymbol{\eta}_{k_{bc}}, \boldsymbol{\eta}_{k_a})
\end{aligned} \tag{3.230}
$$

where

$$
\begin{aligned}
T_R &= -\frac{\hbar^2}{2\mu R^2}\frac{\partial}{\partial R}R^2\frac{\partial}{\partial R}, \\
H_{BC} &= -\frac{\hbar^2}{2\mu_{bc}}\nabla_r^2 - \sum_{k_{bc}}\frac{\hbar^2}{2m_e}\nabla_{k_{bc}}^2 + V_{BC}(\boldsymbol{r}, \boldsymbol{\eta}_{k_{bc}}), \\
H_A &= -\sum_{k_a}\frac{\hbar^2}{2m_e}\nabla_{k_a}^2 + V_A(\boldsymbol{\eta}_{k_a}).
\end{aligned} \tag{3.231}
$$

To describe the bound state levels of the NO-X (X=Ar, Ne) complex, it is convenient to expand the complete wavefunction in terms of products of wavefunctions which describe the electronic-rotational states of the NO molecule and angular momentum functions which describe the orbital (end-over-end) rotation of the NO-X complex. Since the Hamiltonian of the diatom in Eq. (3.230) is given in terms

of bf(2) coordinates, it is not possible to use the diatomic wavefunctions which are given in a mf frame as discussed in Section 3.1. To remedy this situation, a mf frame is introduced by rotating the bf(2) frame through angles θ and ϕ. These angles describe the orientation of the internuclear axis of the diatom with respect to the bf(2) frame. The transformation is described by a matrix $\mathsf{C}_d(\theta,\phi)$:

$$\boldsymbol{r}^{mf} = \mathsf{C}_d(\phi,\theta)\boldsymbol{r}^{bf} = \begin{pmatrix} 0 \\ 0 \\ r \end{pmatrix}, \quad \boldsymbol{\rho}_{k_{bc}} = \mathsf{C}_d(\phi,\theta)\boldsymbol{\eta}_{k_{bc}}. \tag{3.232}$$

The kinetic energy of the diatom in the mf takes the form of

$$T_{BC} = \frac{\mu_{bc}}{2}\Big[\dot{\boldsymbol{r}}^{mf} + (\boldsymbol{\omega}_d + \mathsf{C}_d\boldsymbol{\omega}) \times \boldsymbol{r}^{mf}\Big]^2 + \frac{m_e}{2}\sum_{k_{bc}}^{N_a}\Big[\dot{\boldsymbol{\rho}}_{k_{bc}} + (\boldsymbol{\omega}_d + \mathsf{C}_d\boldsymbol{\omega}) \times \boldsymbol{\rho}_{k_{bc}}\Big]^2. \tag{3.233}$$

The effect of the second transformation is to replace the original angular velocity $\boldsymbol{\omega}$ by $\boldsymbol{\omega}_r = \boldsymbol{\omega}_d + \mathsf{C}_d\boldsymbol{\omega}$. The projection of the body fixed diatomic angular momentum onto the molecule fixed frame is given by the expression

$$\boldsymbol{j}_{bc}^{mf} = \mathsf{C}_d\boldsymbol{j}_{bc}^{bf} = \nabla_{\boldsymbol{\omega}_r} T_{BC} = \boldsymbol{r}^{mf} \times \boldsymbol{p}_r + \boldsymbol{l} \tag{3.234}$$

where $\boldsymbol{l} = \sum_{k_{bc}} \boldsymbol{\rho}_{k_{bc}} \times \boldsymbol{p}_{k_{bc}}$ defines the orbital angular momentum of the electrons in terms of the mf frame. In complete analogy to Eq. (3.227), the conjugate momenta are

$$\begin{aligned} j_\phi &= \sin\theta\,\left(j_x^{mf} - l_x\right) - \sin\theta\, l_x + \cos\theta\, l_x, \\ j_\theta &= j_y^{mf}. \end{aligned} \tag{3.235}$$

Then, the expression for the kinetic energy T_{BC} in the mf frame becomes

$$\begin{aligned} T_{BC} &= -\frac{\hbar^2}{2\mu_{bc}r^2}\frac{\partial}{\partial r}r^2\frac{\partial}{\partial r} + \frac{1}{2\mu r^2}\Big[\left(j_x^{mf} - l_x\right)^2 + \frac{1}{\sin\theta}\left(j_y^{mf} - l_y\right)\sin\theta\left(j_y^{mf} - l_y\right)\Big] \\ &\quad -\sum_{k_{bc}}^{N_{bc}}\frac{\hbar^2}{2m_e}\nabla_{k_{bc}}^2. \end{aligned} \tag{3.236}$$

In this form, the eigenfunctions of the diatom can be used to describe the NO-X complex. However, this Hamiltonian involves nonstandard angular momentum operators. In order to derive an isomorphic Hamiltonian, it is necessary to apply two unitary transformations:

$$U = \exp\left(\frac{i}{\hbar} j^{bf}_{bc\ z}\chi\right) \qquad \text{for the triatom} \tag{3.237}$$

$$U_d = \exp\left(\frac{i}{\hbar} l_z \chi_d\right) \qquad \text{for the diatom.} \tag{3.238}$$

After some algebra, the final expression for the isomorphic triatomic Hamiltonian is obtained as

$$\begin{aligned} H &= T_R + \frac{1}{2\mu R^2}\left[(J^{bf}_x - j^{bf}_{bc\ x})^2 + (J^{bf}_y - j^{bf}_{bc\ y})^2\right] \\ &\quad + V_{int}(R, \theta, \boldsymbol{r}, \boldsymbol{\rho}_{k_{bc}}, \boldsymbol{\eta}_{k_a}) + H_{BC} + H_A \end{aligned} \tag{3.239}$$

where

$$\begin{aligned} T_R &= -\frac{\hbar^2}{2\mu R^2}\frac{\partial}{\partial R}R^2\frac{\partial}{\partial R}, \\ H_{BC} &= -\frac{1}{2\mu_{bc} r^2}\frac{\partial}{\partial r}r^2\frac{\partial}{\partial r} + \frac{\hbar^2}{2\mu r^2}\left[\left(j^{mf}_x - l_x\right)^2 + \left(j^{mf}_y - l_y\right)^2\right] \\ &\quad - \sum_{k_{bc}} \frac{\hbar^2}{2m_e}\nabla^2_{k_{bc}} + V_{BC}(\boldsymbol{r}, \boldsymbol{\eta}_{k_{bc}}), \\ H_A &= -\sum_{k_a} \frac{\hbar^2}{2m_e}\nabla^2_{k_a} + V_A(\boldsymbol{\eta}_{k_a}). \end{aligned}$$

3.3.3 The Interaction Potential

In this section, the interaction potential, $V_{int}(R, \theta, \boldsymbol{r}, \boldsymbol{\rho}_{k_{bc}}, \boldsymbol{\eta}_{k_a})$ (see Eq. (3.215c)), is described in detail [107, 124]. As a representative term of the interaction, let us consider the repulsive term between an electron k_{bc} and an electron k_a in the bf(2)

frame at a distance: $|\boldsymbol{R}+\boldsymbol{r}_{k_a}-\boldsymbol{r}_{\boldsymbol{k_{bc}}}|$. The inverse distance can be expanded in terms of unnormalized spherical harmonics, $C_{\tilde{l}m}(\hat{X})$ [125]:

$$\begin{aligned}\frac{1}{|\boldsymbol{R}+\boldsymbol{r}_{k_a}-\boldsymbol{r}_{\boldsymbol{k_{bc}}}|} &= \sum_{\tilde{l},l_1,l_2}\sum_{m,m_1,m_2} A_{l_1l_2}(R,\eta_{k_a},\eta_{k_{bc}})\langle\tilde{l}ml_1m_1 \mid l_2m_2\rangle \\ &\quad\times C_{\tilde{l}m}(\hat{\eta}_{k_{bc}})C_{l_1m_1}(\hat{\eta}_{k_a})C^*_{l_2m_2}(\hat{R}) \qquad (3.240)\end{aligned}$$

where $\langle\tilde{l}ml_1m_1 \mid l_2m_2\rangle$ is a Clebsch-Gordan coefficient [121]. The quantities with hats designate the orientation of the vectors. Since $\hat{R}=(0,0)$ in the bf(2) frame, only terms with m_2=0 contribute to the expansion due to the property $Y_{lm}(0,\phi)=\sqrt{(2l+1)/4\pi}\times\delta_{m0}$. In the case that the electron k_a belongs to an atom in a ^1S state, only contributions with $m_1=0$ terms survive. Eq. (3.240) is averaged over the electronic coordinates of the atom:

$$\frac{1}{|\boldsymbol{R}+\boldsymbol{r}_{k_a}-\boldsymbol{r}_{\boldsymbol{k_{bc}}}|}=\sum_{\tilde{l},l_1,l_2} A_{l_1l_2}(R,\eta_{k_a},\eta_{k_{bc}})\langle\tilde{l}0l_10 \mid l_20\rangle C_{\tilde{l}0}(\hat{\eta}_{k_{bc}})C_{l_10}(\hat{\eta}_{k_a}). \qquad (3.241)$$

The coordinates of the electrons in the diatom $\boldsymbol{\eta}_{k_{bc}}$ must be expressed in terms of the mf coordinates in order to be able to use the wavefunctions of the diatom discussed in Section 3.1.2. The coordinates are transformed by use of Eq. (3.232). Using the transformation properties of spherical tensors under the rotation through angles $(\theta,\ \phi,\ 0)$, the unnormalized spherical harmonics are transformed as

$$C_{\tilde{l}0}(\hat{\eta}_{k_{bc}})=\sum_p D^{(\tilde{l})*}_{0p}(\phi,\ \theta,\ 0)C_{\tilde{l}p}(\hat{\rho}_{k_{bc}})=D^{(\tilde{l})*}_{0p}(0,\ \theta,\ 0)C_{\tilde{l}p}(\hat{\rho}_{k_{bc}}). \qquad (3.242)$$

Substituting the above result into Eq. (3.241), the interaction potential becomes

$$\begin{aligned}V_{int} &= \frac{1}{|\boldsymbol{R}+\boldsymbol{r}_{k_a}-\boldsymbol{r}_{\boldsymbol{k_{bc}}}|}+\cdots\cdots \\ &= \sum_{\tilde{l},l_1,l_2,p} A_{l_1l_2}(R,\eta_{k_a},\rho_{k_{bc}})\langle\tilde{l}0l_10 \mid l_20\rangle C_{l_10}(\hat{\eta}_{k_a})D^{(\tilde{l})*}_{0p}(0,\ \theta,\ 0)C_{\tilde{l}p}(\hat{\rho}_{k_{bc}}).\end{aligned} \qquad (3.243)$$

It can be shown that the interaction potential does not depend on the azimuthal angle ϕ. The matrix elements of the interaction potential involving the diatomic

wavefunctions $|n\lambda\rangle$ are

$$V^{int}_{\lambda\lambda'}(R,r,\theta) = \langle n\lambda|V_{int}|n\lambda'\rangle = \sum_{\tilde{l}} D^{(\tilde{l})*}_{0\ \lambda-\lambda'}(0,\theta,0)V_{\tilde{l}\ \lambda-\lambda'}(R,r). \tag{3.244}$$

Since the diatom wavefunctions with λ and $-\lambda$ are degenerate, it is more convenient to use wavefunctions with a well defined parity:

$$\big|n|\lambda|\epsilon\big\rangle = \frac{1}{\sqrt{2}}\Big\{|n\ \lambda\rangle + \epsilon|n\ -\lambda\rangle\Big\}. \tag{3.245}$$

Using the symmetrized wavefunctions as basis set, the potential matrix which is diagonal in ϵ is found to be

$$\begin{aligned} V^{int}_{|\lambda|\epsilon\epsilon'} &= \Big\langle n|\lambda|\epsilon\Big|V_{int}\Big|n|\lambda|\epsilon\Big\rangle \\ &= \delta_{\epsilon\epsilon'}\sum_{\tilde{l}}\left(D^{(\tilde{l})*}_{00}(0,\theta,0)V_{\tilde{l}0}(R,r) + \epsilon D^{(\tilde{l})*}_{0\ 2\lambda}(0,\theta,0)V_{\tilde{l}\ 2\lambda}(R,r)\right). \end{aligned} \tag{3.246}$$

The eigenvalues of the electronic Hamiltonian define two potential surfaces of $A'(\epsilon = +1)$ and $A''(\epsilon = -1)$ reflection symmetry (see Fig. **??**): $V^{int}_{|\lambda|}(A';R,r,\theta)$ and $V^{int}_{|\lambda|}(A'';R,r,\theta)$, respectively. The diagonal elements in λ represent the average of the two adiabatic potentials of A' and A'' reflection symmetry which are given in terms of Legendre polynomials:

$$V_{ave} = \frac{1}{2}\big[V^{int}_{|\lambda|}(A';R,r,\theta) + V^{int}_{|\lambda|}(A'';R,r,\theta)\big] = \sum_{\tilde{l}} D^{(\tilde{l})*}_{00}(0,\theta,0)V_{\tilde{l}0}(R,r). \tag{3.247}$$

The off-diagonal elements are related to the difference of the potentials which are given in terms of associated Legendre polynomials:

$$V_{diff} = \frac{1}{2}\big[V^{int}_{|\lambda|}(A';R,r,\theta) - V^{int}_{|\lambda|}(A'';R,r,\theta)\big] = \sum_{\tilde{l}} D^{(\tilde{l})*}_{0\ \lambda-\lambda'}(0,\theta,0)V_{\tilde{l}\ \lambda-\lambda'}(R,r). \tag{3.248}$$

As will be discussed below, the odd-expansion terms of the average potential, V_{ave}, are closely related to the ω splitting while the difference potential, V_{diff}, is responsible for the P-type doubling.

3.3.4 Close Coupled Equations

The complete eigenfunctions of the total Hamiltonian in Eq. (3.239) can be expanded in terms of products of diatom states and total angular momentum eigenfunctions:

$$\Psi^{JM}_{Pj\omega}(\alpha,\beta,\phi,\theta,r,\boldsymbol{\rho}_{k_{bc}}) = \sqrt{\frac{2J+1}{4\pi}} D^{(J)*}_{MP}(\alpha,\beta,0)\sqrt{\frac{2j+1}{4\pi}} D^{(j)*}_{P\omega}(\phi,\theta,0)\ \psi^{el}_{n\lambda}\ \Gamma_{s\sigma} \tag{3.249}$$

or, in a shorthand form

$$|JMPj\omega\rangle = |JMP\rangle|jP\omega\rangle|n\lambda\rangle|s\sigma\rangle \quad \text{with} \quad \omega = \lambda + \sigma. \tag{3.250}$$

In Eq. (3.249), $D^{(J)*}_{MP}(\alpha,\beta,0)$ and $D^{(j)*}_{P\omega}(\phi,\theta,0)$ represent a total angular momentum eigenfunction of the complex and the diatom, respectively. $\psi^{el}_{n\lambda}$ represents the electronic wavefunction while $\Gamma_{s\sigma}$ represents the spin wavefunction. Here, the eigenfunction of the atom, $|^1S\,\rangle$, is not included explicitly.

The levels corresponding to (P,ω) and $(-P,-\omega)$ are degenerate when the first order energy correction due to the electrostatic potential is considered (see below in Eq. (3.265)). Thus, it is convenient to combine these states into two new basis states with a well defined parity:

$$\begin{aligned} &\Psi^{JM}_{P\zeta j\omega}(\alpha,\beta,\phi,\theta,r,\boldsymbol{\rho}_{k_{bc}}) = |JMP\zeta j\omega\rangle \\ = \ &\frac{1}{\sqrt{2}}\Big\{|JMP\rangle|jP\omega\rangle|n\lambda\rangle|s\sigma\rangle + \zeta|JM\ -P\rangle|j\ -P\ -\omega\rangle|n\ -\lambda\rangle|s\ -\sigma\rangle\Big\} \end{aligned} \tag{3.251}$$

where the symmetry quantum number ζ takes on the values ± 1. It is related to the overall parity of the basis state: $\eta = \zeta(-)^{J-s}$. The degeneracy in ζ is removed by Coriolis interaction involving states with $P = \frac{1}{2}$. This lifting of the degeneracy is called the P-type doubling in analogy to the λ-doubling in the diatom discussed in Section 3.1.3. For linear complexes such as OH-Ar, ω is a nearly good quantum number and the energy levels are split into different P-components. In this case, ω

is restricted to positive values and P takes on signed values. On the other hand, for T-shaped complexes such as NO-Ar, the main contribution of the rotational energy is determined by P^2 while the splitting of the different (P,ω)-states is small. In this case, it is more appropriate to restrict the quantum number P to positive values and to treat ω as a signed quantum number.

Assuming that the intramolecular distance r does not change, the total wavefunction is expanded in terms of the basis set defined in Eq. (3.251):

$$\Psi_{tot}^{JMv\zeta} = \sum_{P'j'\omega'} \frac{1}{R} X_{P'j'\omega'}^{Jv\zeta}(R)|JMP'\zeta j'\omega'\rangle. \tag{3.252}$$

The matrix representation of the complete Hamiltonian in this basis contains several important off-diagonal contributions.

$$H_{tot} = T_R + H_{rot}^{(0)} + H_{BC}^{(0)} + H_A + H_{rot}^{(1)} + H_{BC}^{(1)} + V_{int} \tag{3.253}$$

where

$$\begin{aligned} T_R &= -\frac{\hbar^2}{2\mu R^2}\frac{\partial}{\partial R}R^2\frac{\partial}{\partial R}, \\ H_{rot}^{(0)} &= \frac{1}{2\mu R^2}(\boldsymbol{J}^2 + \boldsymbol{j}^2 - J_z^2 - j_z^2), \\ H_{rot}^{(1)} &= -\frac{1}{2\mu R^2}(j_+J_- + j_-J_+), \\ H_{BC}^{(1)} &= -\frac{1}{2\mu_{bc}r^2}(j_+^{mf}s_- + j_-^{mf}s_+). \end{aligned} \tag{3.254}$$

Here, the identity

$$\begin{aligned} & (J_x^{bf} - j_{bc\ x}^{bf})^2 + (J_y^{bf} - j_{bc\ y}^{bf})^2 \\ = \ & (\boldsymbol{J}^2 + \boldsymbol{j}^2 - J_z^2 - j_z^2) - (j_+J_- + j_-J_+) \end{aligned} \tag{3.255}$$

has been used. For a structureless atom, H_A contributes a constant energy shift and will be neglected. By substituting the wavefunction into the Schrödinger equation and integrating over all coordinates except the R-dependent part, a set of close

coupled equations for the radial coefficient $X^{Jv\zeta}_{P'j'\omega'}(R)$ is obtained:

$$\left\{ -\frac{\hbar^2}{2\mu}\frac{d^2}{dR^2} + B(R)\Big(J(J+1)+j(j+1)-2P^2\Big) - \Big[E^{Jv\zeta}_{tot} - E^{(BC)}_{j\omega}\Big] \right\} X^{Jv\zeta}_{P'j'\omega'}(R)$$
$$= -\sum_{P'j'\omega'} X^{Jv\zeta}_{P'j'\omega'}(R)\big\langle JMP\zeta j\omega\big|H^{(1)}_{rot} + H^{(1)}_{BC} + V^{e.s}_{int}\big|JMP\zeta j\omega\big\rangle. \quad (3.256)$$

The off-diagonal terms due to Coriolis coupling, the spin-uncoupling, and the interaction potential are collected on the right hand side of Eq. (3.256).

Since $\boldsymbol{j}^{bf}$ represents the transformed mf operator, it obeys normal commutation rules. The operator j^{bf}_{+}(or j^{bf}_{-}) acts as a raising (or lowering) operator. On the other hand, the operator $\boldsymbol{J}^{bf}$ obeys anomalous commutation rules. This means that the operator J^{bf}_{-} (or J^{bf}_{+}) acts as a raising (or lowering) operator. When the Coriolis coupling terms are evaluated, three contributions are found:

$$\begin{aligned} &\big\langle JMP\zeta j\omega\big|H^{(1)}_{rot}\big|JMP'\zeta' j'\omega'\big\rangle \\ = \;& -\delta_{jj'}\delta_{\zeta\zeta'}B(R)\Big\{F(P')\delta_{P,P'+1}\delta_{\omega\omega'} + F(P'-1)\delta_{P,P'-1}\delta_{\omega\omega'} + \zeta F(P')\delta_{P,1-P'}\delta_{\omega,-\omega'}\Big\} \end{aligned} \quad (3.257)$$

where

$$F(P) = \sqrt{[J(J+1)-P(P+1)][j(j+1)-P(P+1)]}.$$

The matrix representation of $H^{(1)}_{rot}$ is diagonal in j. The first two terms in Eq. (3.257) are responsible for coupling of states with $\Delta P = \pm 1$, $\Delta\omega = 0$ while the third term is only possible for $P = P' = \frac{1}{2}$ $\omega' = -\omega$. This term depends on the quantum number ζ giving rise to the P-type doubling.

The spin-uncoupling operator only acts on the diatom part of the wavefunction. The matrix elements of this operator are calculated as

$$\begin{aligned} &\big\langle JMP\zeta j\omega\big|H^{(1)}_{BC}\big|JMP'\zeta' j'\omega'\big\rangle \\ = \;& -\delta_{jj'}\delta_{PP'}\delta_{\zeta\zeta'}\delta_{\lambda\lambda'}\; b\Big\{f(\omega'-1)\delta_{\omega,\omega'-1}\delta_{\sigma,\sigma'-1} + f(\omega')\delta_{\omega,\omega'+1}\delta_{\sigma,\sigma'+1}\Big\} \end{aligned} \quad (3.258)$$

where

$$f(\omega) = \sqrt{[j(j+1) - \omega(\omega+1)]}.$$

Its matrix representation is diagonal in j, P, ζ, and λ. The off-diagonal terms only exist for states which differ in ω and σ by one unit: $\Delta\omega = \Delta\sigma = \pm 1$.

The third off-diagonal term is due to the interaction potential whose matrix elements are evaluated as

$$\begin{aligned} & \left\langle JMP\zeta j\omega \middle| V_{int} \middle| JMP'\zeta' j'\omega' \right\rangle \\ = \; & \delta_{PP'}\delta_{\zeta\zeta'}[j][j'] \sum_{\tilde{l}} (-)^{P-\omega} \begin{pmatrix} j & \tilde{l} & j' \\ -P & 0 & P \end{pmatrix} \begin{pmatrix} j & \tilde{l} & j' \\ -\omega & \lambda - \lambda' & \omega \end{pmatrix} V_{\tilde{l}\,\lambda-\lambda'}(R). \end{aligned} \tag{3.259}$$

The interaction potential matrix is diagonal in P and ζ and its elements do not even depend on J, M, and ζ. The average potential mixes different diatom rotor states ($\Delta j \neq 0$) with the same projection quantum ($\Delta\omega = 0$) while the difference potential mixes states with $\Delta j \neq 0$ and $\Delta\omega = \pm 2$. The latter terms contribute to the P-type doubling.

The diagonal elements of the potential matrix are:

$$\begin{aligned} & \left\langle JMP\zeta j\omega \middle| V_{int}^{e.s} \middle| JMP\zeta j\omega \right\rangle \\ = \; & [j]^2 \sum_{\tilde{l}=0} (-)^{P-\omega} \begin{pmatrix} j & \tilde{l} & j' \\ -P & 0 & P \end{pmatrix} \begin{pmatrix} j & \tilde{l} & j' \\ -\omega & 0 & \omega \end{pmatrix} V_{\tilde{l}0}(R) \\ = \; & V_{00} + [j]^2 \sum_{\tilde{l}=1} (-)^{P-\omega} \begin{pmatrix} j & \tilde{l} & j' \\ -P & 0 & P \end{pmatrix} \begin{pmatrix} j & \tilde{l} & j' \\ -\omega & 0 & \omega \end{pmatrix} V_{\tilde{l}0}(R). \end{aligned} \tag{3.260}$$

The leading term V_{00}, which is the isotropic term, can be used to define a zeroth order stretching Hamiltonian:

$$\Big\{ -\frac{\hbar^2}{2\mu}\frac{d^2}{dR^2} + V_{00}(R) \Big\} U_{v_s}(R) = E^{(0)}_{vib\,v_s} U_{v_s}(R) \tag{3.261}$$

where the stretching vibrational energy is defined as

$$E^{(0)}_{vib\,v_s} = E^{JM}_{tot} - E^{(BC)}_{tot} - B\big(J(J+1) + j(j+1) - 2P^2\big). \tag{3.262}$$

The eigenfunctions to the stretching Hamiltonian can be used to define a new basis set which includes the dependence on the coordinate R:

$$\Psi^{JMv}_{tot} = \sum_{P'\zeta'j'\omega'v'_s} C^{JMv}_{P'\zeta'j'\omega'v'_s} \frac{1}{R}\big|v'_s\big\rangle\big|JMP'\zeta'j'\omega'\big\rangle. \tag{3.263}$$

Using this basis set, the first order energy correction due to the higher order expansion terms of the potential is obtained:

$$\begin{aligned} E^{JPv_s}_{tot\,j\omega} &= E^{(0)}_{vib\,v_s} + E^{(BC)}_{j\omega} + B\big(J(J+1) + j(j+1) - 2P^2\big) \\ &\quad + (2j+1)\sum_{\tilde{l}=1}(-)^{P-\omega} \begin{pmatrix} j & \tilde{l} & j' \\ -P & 0 & P \end{pmatrix} \begin{pmatrix} j & \tilde{l} & j' \\ -\omega & 0 & \omega \end{pmatrix} \big\langle v_s\big|V_{\tilde{l}0}(R)\big|v_s\big\rangle. \end{aligned} \tag{3.264}$$

The first three terms are degenerate in P and ω. The splitting of the degenerate level is caused in first order by the electrostatic potential. Considering the leading term of the potential anisotropy ($\tilde{l} = 1$), it is found that the correction depends only on the sign of the product $P \times \omega$. When the signs of both P and ω are reversed, the last term in Eq. (3.264) does not change:

$$\begin{aligned} & (-)^{-P+\omega} \begin{pmatrix} j & 1 & j' \\ P & 0 & -P \end{pmatrix} \begin{pmatrix} j & 1 & j' \\ \omega & 0 & -\omega \end{pmatrix} \\ = \; & (-)^{-P+\omega+2P-2\omega} \begin{pmatrix} j & 1 & j' \\ -P & 0 & P \end{pmatrix} \begin{pmatrix} j & 1 & j' \\ -\omega & 0 & \omega \end{pmatrix} \\ = \; & (-)^{P-\omega} \begin{pmatrix} j & \tilde{l} & j' \\ -P & 0 & P \end{pmatrix} \begin{pmatrix} j & \tilde{l} & j' \\ -\omega & 0 & \omega \end{pmatrix}. \end{aligned} \tag{3.265}$$

3.3.5 Centrifugal Decoupling and Adiabatic Bender Approximation

In order to decouple the rotational motion from the bending vibration efficiently, it is convenient to define a zeroth order bending Hamiltonian H_{bend} by retaining only contributions from the rotational part, the diatomic Hamiltonian and the interaction potential:

$$H_{bend} = H_{rot}^{(0)} + H_{BC}^{(0)} + V_{int}^{e.s}. \tag{3.266}$$

The matrix elements of H_{bend} are diagonal in P and independent of ζ whereas they depend on the stretching coordinate R as a parameter. Therefore, the expansion of the eigenfunctions of the bending Hamiltonian in terms of the $P\omega$ basis set is restricted to states which differ only in the quantum number for j and ω:

$$\Psi_{bend}^{JMP\zeta n} = \sum_{j',\omega'} W_{j'\omega'}^{JPn}(R)|JMP\zeta j'\omega'\rangle. \tag{3.267}$$

The coefficients $W_{j'\omega'}^{JPn}(R)$ are determined by diagonalizing the R-dependent matrix associated with the following eigenvalue problem:

$$\sum_{j'\omega'} \Bigg\{ \Big[B(R)\Big(J(J+1) + j(j+1) - 2P^2\Big) + E_{jw}^{(BC)}\Big]\delta_{jj'}\delta_{\omega\omega'} + \langle JMP\zeta j\omega|V_{int}|JMP\zeta j'\omega'\rangle \Bigg\} W_{j'\omega'}^{JPn}(R) = E_{bend}^{JPn}(R) W_{j'\omega'}^{JPn}(R). \tag{3.268}$$

Although the contribution due to the end-over-end rotation of the complex depends on J, the rotational energy is much smaller than the energy associated with the internuclear vibrations of the fragments. It is neglected in a first approximation by replacing J by $\bar{l}$:

$$B(R)J(J+1) = B(R)\bar{l}(\bar{l}+1). \tag{3.269}$$

The eigenvalue $E_{bend}^{Pn}(R)$ represents the total energy of the system minus the energies associated with the stretching vibration and the end-over-end rotation. When R approaches infinity, the bending vibration vanishes and the total energy approaches

the energy of a free rotor state of the diatom. Then, it is convenient to define an adiabatic bender potential as

$$V_{bend}^{Pn}(R) = E_{bend}^{Pn}(R) - E_{j\omega}^{(BC)} - B(R)\bar{l}(\bar{l}+1). \tag{3.270}$$

This adiabatic potential serves as the potential energy for the intermolecular stretching vibration. The complete eigenfunctions are expanded in terms of the bender eigenfunctions,

$$\begin{aligned}\Psi_{tot}^{JMv\zeta} &= \sum_{Pn} \frac{1}{R} U_{Pn}^{Jv\zeta}(R) \Psi_{bend}^{JMP\zeta n} \\ &= \sum_{Pn} \sum_{j'\omega'} \frac{1}{R} U_{Pn}^{Jv\zeta}(R) W_{j'\omega'}^{Pn}(R) |JMP\zeta j'\omega'\rangle. \end{aligned} \tag{3.271}$$

Substitution into the complete Schrödinger equation results in a set of close coupled equations:

$$\Big\{T_R + H_{bend} + B(R)\Big(\boldsymbol{J}^2 - \bar{l}(\bar{l}+1)\Big) - E_{tot}^{Jv\zeta}\Big\}\Psi_{tot}^{JMv\zeta} = -H_{rot}^{(1)}\Psi_{tot}^{JMv\zeta}$$

$$\Updownarrow$$

$$\begin{aligned}&\sum_{Pn}\Bigg\{T_R \frac{1}{R} U_{Pn}^{Jv\zeta}(R)\Psi_{bend}^{JMP\zeta n} \\ &+ \frac{1}{R} U_{Pn}^{Jv\zeta}(R)\Psi_{bend}^{JMP\zeta n}\Big[E_{bend}^{Pn}(R) + B(R)J(J+1) - B(R)\bar{l}(\bar{l}+1) - E_{tot}^{Jv\zeta}\Big]\Bigg\} \\ &= -\sum_{pn} H_{rot}^{(1)} \frac{1}{R} U_{Pn}^{Jv\zeta}(R)\Psi_{bend}^{JMP\zeta n}. \end{aligned} \tag{3.272}$$

The energy eigenvalue can be viewed as a sum of fragment energy plus the rovibrational energy associated with the intermolecular mode

$$E_{tot}^{Jv\zeta} = E_{r.v.}^{Jv\zeta} + E_{j\omega}^{(BC)}.$$

When the adiabatic bender potential in Eq. (3.270) is introduced into Eq. (3.272):

$$\begin{aligned}\sum_{Pn}\Bigg\{T_R \frac{1}{R} U_{Pn}^{Jv\zeta}(R)\Psi_{bend}^{JMP\zeta n} &+ \frac{1}{R} U_{Pn}^{Jv\zeta}(R)\Psi_{bend}^{JMP\zeta n}\Big[V_{bend}^{Pn}(R) - E_{r.v.}^{Jv\zeta}\Big]\Bigg\} \\ &= -\sum_{pn} H_{rot}^{(1)} \frac{1}{R} U_{Pn}^{Jv\zeta}(R)\Psi_{bend}^{JMP\zeta n}. \end{aligned} \tag{3.273}$$

The Coriolis coupling term on the right hand side is responsible for mixing states which differ in P. It is responsible for removing the degeneracy of levels which differ in ζ. This coupling term is neglected in the centrifugal decoupling (CD) approximation. At this level of approximation, P is a good quantum number. Because the P-type doubling is caused by the Coriolis coupling term, energy levels at the CD level must be degenerate in the symmetry quantum number ζ. The complete CD wavefunction takes the form:

$$\begin{aligned}\Psi_{tot}^{JMPv\zeta} &= \sum_{n} \frac{1}{R} U_{Pn}^{Jv}(R) \Psi_{bend}^{JMP\zeta n} \\ &= \sum_{nj'\omega'} \frac{1}{R} U_{Pn}^{Jv}(R) W_{j'\omega'}^{Pn}(R) |JMP\eta j'\omega'\rangle. \end{aligned} \tag{3.274}$$

Additionally, there are non-adiabatic couplings mediated by the kinetic energy operator for the stretching motion, T_R. Since the bender wavefunctions depend on R, non-adiabatic coupling terms are found in the form:

$$\frac{1}{R} U_{Pn}^{Jv}(R) \left\langle \Psi_{bend}^{JMP\zeta n} \middle| T_R \middle| \Psi_{bend}^{JMP\zeta n'} \right\rangle_{\theta, \boldsymbol{\eta}_{k_{bc}}}. \tag{3.275}$$

The matrix element represents integration over all coordinates $(\theta, \boldsymbol{\eta}_{k_{bc}})$ except the stretching coordinate R. In an adiabatic bender (AB) calculation, these couplings are neglected in addition to the Coriolis coupling term. In this case, the complete wavefunction is approximated as a product of a bending and a stretching wavefunction.

$$\Psi_{tot}^{JMPv\eta} = \frac{1}{R} U_{Pn}^{Jv}(R) \Psi_{bend}^{JMP\zeta n}. \tag{3.276}$$

The stretching wavefunction is a solution to a one-dimensional Schrödinger equation:

$$-\frac{\hbar^2}{2\mu} \frac{d^2}{dR^2} U_{Pn}^{Jv}(R) + \Big[V_{bend}^{Pn}(R) + B(R) J(J+1) \Big] U_{Pn}^{Jv}(R) = E_{r.v.}^{Jv} U_{Pn}^{Jv}(R). \tag{3.277}$$

Since the bending potentials correlate with different diatom states, the energy eigenvalues to this equation contain the energy due to intermolecular stretching

vibration, bending vibration, and the overall rotation of the complex. For instance, the potentials correlating with $j = \frac{3}{2}$ and $\omega = \pm\frac{1}{2}$ split under the electrostatic potential into bender potentials with $P = \frac{1}{2}$ and $P = \frac{3}{2}$. Because the main portion of the rotational energy is determined by J, the bender potentials corresponding to a particular value of P are expected to lie close to each other as shown .

3.3.6 Perturbation Theory

Ideally, an experimental spectrum needs to be compared with the results of a complete *ab initio* treatment. But, calculating an *ab initio* potential energy surface (PES) is very complicated and for many systems potential energy surfaces (PESs) are not available. In order to gain further insight into the energy level structure of the complex and to calculate a spectrum without detailed information on the PESs, an empirical Hamiltonian is introduced.

Perturbation theory is applied to construct this Hamiltonian. This approach was developed by Green and Lester [23]. The first order energy correction was obtained in Eq. (3.264).

$$\begin{aligned} E_{tot\ j\omega}^{JPv_s} &= E_{vib\ v_s}^{(0)} + E_{j\omega}^{(BC)} + B\big(J(J+1) + j(j+1) - 2P^2\big) \\ &\quad + (2j+1)\sum_{\tilde{l}=1}(-)^{P-\omega} \begin{pmatrix} j & \tilde{l} & j' \\ -P & 0 & P \end{pmatrix} \begin{pmatrix} j & \tilde{l} & j' \\ -\omega & 0 & \omega \end{pmatrix} \big\langle v_s \big| V_{\tilde{l}0}(R) \big| v_s \big\rangle. \end{aligned}$$

For a given P value the main contribution to the ω splitting comes from the leading term $V_{10}(R)$. By replacing $+\omega$ by -ω,

$$(-)^{\omega} \begin{pmatrix} j & 1 & j \\ \omega & 0 & -\omega \end{pmatrix} V_{10}(R) = -(-)^{-\omega} \begin{pmatrix} j & 1 & j \\ -\omega & 0 & \omega \end{pmatrix} V_{10}(R). \tag{3.278}$$

In first order, the two ω levels are shifted by the same amount but in opposite directions. The splitting is proportional to $2\big\langle v_s \big| V_{10} \big| v_s \big\rangle$. But, the contribution due

to the term $V_{20}(R)$ is independent of the sign of P and ω, it cannot remove the degeneracy of the $\pm\omega$ levels.

Even though the degeneracy of the $\pm\omega$ levels is removed, each level is still two-fold degenerate in the quantum number ζ. Also, the P-type doubling can be explained within the framework of perturbation theory. Since the last term in Eq. (3.257) for the Coriolis coupling is linear in ζ, this term must be responsible for the P-type doubling.

For this term, the selection rule for ω is $\omega' = -\omega''$, which means that other ω-changing perturbations such as spin uncoupling and the difference potential must be implemented for the perturbation treatment. The lowest bound levels for NO-Ar and NO-Ne involve basis states with $\omega = \pm\frac{1}{2}$ and $P = \frac{1}{2}$. The splitting can be explained by a mechanism involving the difference potential and the spin uncoupling operator.

$$\langle J\tfrac{1}{2}\eta j\tfrac{1}{2}|H^{(1)}_{rot}|J\tfrac{1}{2}\eta' j' -\tfrac{1}{2}\rangle\langle J\tfrac{1}{2}\eta j -\tfrac{1}{2}|V_{diff}|J\tfrac{1}{2}\eta' j'\tfrac{3}{2}\rangle\langle J\tfrac{1}{2}\eta j\tfrac{3}{2}|H^{(1)}_{BC}|J\tfrac{1}{2}\eta' j'\tfrac{1}{2}\rangle$$
$$= C_1\left(J+\frac{1}{2}\right). \tag{3.279}$$

In summary, the ω splitting is closely related to the odd expansion terms of the average potential V_{ave} while the P-type doubling requires contributions from the difference potential V_{diff}.

With this in mind, the energy levels of the NO-X complex are approximated by the following formula:

$$\begin{aligned} E^{JPv_s}_{tot\,\omega} &= E_{Pv_vv_s} + BJ(J+1) - D\big[J(J+1)\big]^2 + \cdots \\ &\quad -\frac{P\omega}{|P\omega|}\Big\{V_0 + V_1(J+\tfrac{1}{2}) + V_2(J+\tfrac{1}{2})^2 + \cdots \\ &\qquad +\zeta\Big[C_0 + C_1(J+\tfrac{1}{2}) + C_2(J+\tfrac{1}{2})^2 + \cdots\Big]\Big\}. \end{aligned} \tag{3.280}$$

According to Eq. (3.280), the main contribution to the individual levels is due to an energy which represents the rotational energy of the complex around the

a-axis and the intermolecular bending and stretching vibration. The next two terms describe the end-over-end rotation of the complex and the centrifugal distortion. The electrostatic intermolecular interaction causes two types of splittings: the ω-splitting and the P-type doubling. Although the projection ω of the diatom total angular momentum j is not a rigorously good quantum number, there is a constant electrostatic splitting of the rotational lines into two ω components due to the influence of the average potential which is proportional to V_0. As can be seen in Eq. (3.279), using third order perturbation theory, the P-type doubling is proportional to C_1 which in turn is related to the difference potential. All other terms in Eq. (3.280) such as V_1, V_2 and C_0 etc. are empirical constants introduced to increase the flexibility of the model so that the *ab initio* results are reproduced more accurately. Applications of the heuristic Hamiltonian are discussed in detail in Chapter 4.

3.3.7 One-Photon line strength

Simulation of IR spectra of the NO-X complex requires knowledge of the rovibrational energies and the transition line strengths. For the former the heuristic Hamiltonian is used while the intensity is calculated using a procedure discussed in this section. One-photon line strengths are calculated using Eq. (3.151). The NO molecule acts as one-photon absorption chromophore. The wavefunctions of the NO molecule depend on the electronic coordinates defined in the mf frame. Therefore, the components of the dipole moment operator need to be expressed in terms of its mf components. Using the transformation properties of the spherical tensor operators, the dipole moment is transformed as follows:

$$\mu_m^{(1)}(\text{lab}) = \sum_k \mu_k^{(1)}(\text{bf}) D_{mk}^{(1)*}(\hat{R}) = \sum_{k\tilde{k}} \mu_k^{(1)}(\text{bf}) D_{k\tilde{k}}^{(1)*}(\hat{r}) D_{mk}^{(1)*}(\hat{R}) \tag{3.281}$$

with

$$\hat{R} = (\alpha, \beta, 0) \quad \text{and} \quad \hat{r} = (\phi, \theta, 0).$$

In the experiment, the direction of the laser polarization is chosen to lie along the z-axis of the laboratory frame. In this case, the only non-vanishing component is $e_0^{(0)} = E_z$. Since the IR transition in NO involves two Π states, the transition moment must be parallel to the internuclear axis contributing the only nonvanishing components $\mu_0^{(1)}(\mathrm{mf})$:

$$\mu_0^{(1)}(\mathrm{lab}) = \sum_k \mu_0^{(1)}(\mathrm{mf}) D_{k0}^{(1)*}(\hat{r}) D_{0k}^{(1)*}(\hat{R}). \tag{3.282}$$

Using the transformed mf transition moment operator, it is found that

$$\begin{aligned} \tilde{S}_{if} &= \sum_{n'j'\omega'} \sum_{n''j''\omega''} \sum_k \left\langle J'M'P'\zeta'j'\omega' \middle| \mu_0^{(1)}(\mathrm{mf}) D_{k0}^{(1)*}(\hat{r}) D_{0k}^{(1)*}(\hat{R}) \middle| J''M''P''\zeta''j''\omega'' \right\rangle \\ &\quad \times \left\langle U_{P'n'}^{J'v'}(R) W_{j'\omega'}^{P'n'}(R) \frac{1}{R^2} U_{P''n''}^{J''v''}(R) W_{j''\omega''}^{P''n''}(R) \right\rangle. \end{aligned} \tag{3.283}$$

The matrix elements contain an integral which involves electronic and angular coordinates as wells as a Franck-Condon type integral over the stretching coordinate R. The latter integral can only be evaluated after the different coefficients, $U_{Pn}^{Jv}(R)$ and $W_{j\omega}^{Pn}(R)$, are known. However, the angular integral can be calculated analytically. Using the $P\omega$ signed basis set and $\lambda = 1$, the angular integral becomes

$$\begin{aligned} &\sum_k \left\langle J'M'P'\zeta'j'\omega' \middle| \mu_0^{(1)}(\mathrm{mf}) D_{k0}^{(1)*}(\hat{r}) D_{0k}^{(1)*}(\hat{R}) \middle| J''M''P''\zeta''j''\omega'' \right\rangle \\ &= \delta_{M'M''}[J'][J''][j'][j''](-)^{M'-\omega'} \mu_0^{(1)} \begin{pmatrix} J' & 1 & J'' \\ M' & 0 & -M'' \end{pmatrix} \begin{pmatrix} j' & 1 & j'' \\ \omega' & 0 & -\omega' \end{pmatrix} \\ &\quad \times \frac{1 + \zeta'\zeta''(-)^{J'+J''}}{2} \sum_k \left\{ \delta_{\omega'\omega''} \begin{pmatrix} J' & 1 & J'' \\ P' & -k & -P'' \end{pmatrix} \begin{pmatrix} j' & 1 & j'' \\ P' & -k & -P'' \end{pmatrix} \right. \\ &\qquad \left. + \zeta'' \, \delta_{\omega',-\omega''} \begin{pmatrix} J' & 1 & J'' \\ P' & -k & P'' \end{pmatrix} \begin{pmatrix} j' & 1 & j'' \\ P' & -k & P'' \end{pmatrix} \right\}. \end{aligned} \tag{3.284}$$

For brevity, $\mu_0^{(1)}$ denotes $\langle 0|\mu_0^{(1)}(\mathrm{mf})|2\rangle$. The properties of the $3j$ symbol provide the one-photon selection rule $\Delta J = 0, \pm 1$. Since the total parity of the wavefunction is defined by $\eta = \zeta(-)^{J-1/2}$, the parity selection rule $\eta' = -\eta''$ is found from

$$1 + \zeta'\zeta''(-)^{J'+J''} = 1 - \eta'\eta'' \tag{3.285}$$

as expected for a one-photon transition. The second term in the brackets in Eq. (3.284) only contributes for $k = 1$ and $P' = P'' = \frac{1}{2}$ resulting in a perpendicular transition. On the other hand, the first term in the brackets gives rise to a parallel($\|$) transition ($k = 0, \Delta P = 0$) or a perpendicular($\perp$) transition ($k = 1, \Delta P = \pm 1$). The parallel component is responsible for transitions between basis states with large probability for $\omega' = \omega''$ while the perpendicular component connects states which are dominated by expansion terms with $\omega' = -\omega''$. Since under molecular beam conditions only the lowest level $P = \frac{1}{2}$ is populated, transitions are restricted to ($P'' = \frac{1}{2} \rightarrow P' = \frac{1}{2}$) and ($P'' = \frac{1}{2} \rightarrow P' = \frac{3}{2}$). For convenience, let us define an R-dependent transition moment function:

$$\mu_{n'n''}^{(1\|)}(R) = \sum_{j'\omega' j''} [j'][j''](-)^{-\omega} \begin{pmatrix} j' & 1 & j'' \\ \omega' & 0 & -\omega' \end{pmatrix} \begin{pmatrix} j' & 1 & j'' \\ \frac{1}{2} & 0 & -\frac{1}{2} \end{pmatrix} W_{j'\omega'}^{P'n'} W_{j''\omega'}^{P''n''}, \tag{3.286}$$

and

$$\mu_{n'n''}^{(1\perp)}(R) = \sum_{j'\omega' j''} [j'][j''](-)^{-\omega} \begin{pmatrix} j' & 1 & j'' \\ \omega' & 0 & -\omega' \end{pmatrix} \begin{pmatrix} j' & 1 & j'' \\ \frac{1}{2} & -1 & \frac{1}{2} \end{pmatrix} W_{j'\omega'}^{P'n'} W_{j''-\omega'}^{P''n''}. \tag{3.287}$$

Then, the intensity is given by a superposition of contributions due to two components:

$$\begin{aligned} I(\tfrac{1}{2} \rightarrow \tfrac{1}{2}) = \frac{[J']^2[J'']^2}{3} \left[\mu_0^{(1)}\right]^2 \frac{1 + \zeta'\zeta''(-)^{J'+J''}}{2} \\ \times \left| \begin{pmatrix} J' & 1 & J'' \\ \frac{1}{2} & 0 & -\frac{1}{2} \end{pmatrix} \sum_{n'n''} \langle U_{P'n'}^{J'v'}(R) \mu_{n'n''}^{(1\|)}(R) U_{P''n''}^{J''v''}(R) \frac{1}{R^2} \rangle \right. \\ \left. + \zeta'' \begin{pmatrix} J' & 1 & J'' \\ \frac{1}{2} & -1 & \frac{1}{2} \end{pmatrix} \sum_{n'n''} \langle U_{P'n'}^{J'v'}(R) \mu_{n'n''}^{(1\perp)}(R) U_{P''n''}^{J''v''}(R) \frac{1}{R^2} \rangle \right|^2. \end{aligned} \tag{3.288}$$

Similarly, for the transition ($P'' = \frac{1}{2} \rightarrow P' = \frac{3}{2}$) an R-dependent transition moment function is defined as

$$\mu^{(3)}_{n'n''}(R) = \sum_{j'\omega' j''} [j'][j''](-)^{-\omega} \begin{pmatrix} j' & 1 & j'' \\ \omega' & 0 & -\omega' \end{pmatrix} \begin{pmatrix} j' & 1 & j'' \\ \frac{3}{2} & -1 & -\frac{1}{2} \end{pmatrix} W^{P'n'}_{j'\omega'} W^{P''n''}_{j''\omega'}. \quad (3.289)$$

The intensity for this transition is given as

$$I(\tfrac{1}{2} \rightarrow \tfrac{3}{2}) = \frac{[J']^2[J'']^2}{3} \left[\mu_0^{(1)}\right]^2 \frac{1 + \zeta'\zeta''(-)^{J'+J''}}{2} \begin{pmatrix} J' & 1 & J'' \\ \frac{3}{2} & -1 & -\frac{1}{2} \end{pmatrix}^2 \times \left| \sum_{n'n''} \left\langle U^{J'v'}_{P'n'}(R) \mu^{(3)}_{n'n''}(R) U^{J''v''}_{P''n''}(R) \frac{1}{R^2} \right\rangle \right|^2. \quad (3.290)$$

In order to simulate the rotational structure for transitions between different vibrational levels without explicit knowledge of the complete wavefunction, an approximate line strength is calculated based on the adiabatic bender treatment. In this case the intensity is governed by a vibrational transition moment for the stretching vibration and a purely rotational contribution. Then, the involved matrix elements for the R-dependent transition moments $\mu^{(1\|)}_{n'n''}$, $\mu^{(1\perp)}_{n'n''}$, and $\mu^{(3)}_{n'n''}$ are simply incorporated into overall scaling factors $C_{\omega'\omega''}$:

$$I(\tfrac{1}{2} \rightarrow \tfrac{1}{2}) = \frac{[J']^2[J'']^2}{3} \left[\mu_0^{(1)}\right]^2 \frac{1 + \zeta'\zeta''(-)^{J'+J''}}{2} \times \left| \begin{pmatrix} J' & 1 & J'' \\ \frac{1}{2} & 0 & -\frac{1}{2} \end{pmatrix} C^{\|}_{\omega'\omega''} + \zeta'' \begin{pmatrix} J' & 1 & J'' \\ \frac{1}{2} & -1 & \frac{1}{2} \end{pmatrix} C^{\perp}_{\omega'\omega''} \right|^2. \quad (3.291)$$

and

$$I(\tfrac{1}{2} \rightarrow \tfrac{3}{2}) = \frac{[J']^2[J'']^2}{3} \left[\mu_0^{(1)}\right]^2 \frac{1 + \zeta'\zeta''(-)^{J'+J''}}{2} \begin{pmatrix} J' & 1 & J'' \\ \frac{3}{2} & -1 & -\frac{1}{2} \end{pmatrix}^2 \left| C^{(3)}_{\omega'\omega''} \right|^2. \quad (3.292)$$

These results are used to calculate several spectra discussed in Chapter 4.

Chapter 4

Results and Discussions

4.1 NO-Ne system

In order measure the rotationally resolved IR spectrum of the NO-Ne complex associated with the first overtone transition in NO($X\,^2\Pi$) in an IR-UV double resonance experiment, (2+1) REMPI involving the Rydberg states $\tilde{C}\ ^2\Pi$, $\tilde{E}\,^2\Sigma^+$, $\tilde{F}\,^2\Delta$, $\tilde{H}\,^2\Sigma^+$, $\tilde{H}'\,^2\Pi$ was used. To perform the IR-UV double resonance experiment, understanding the above states spectroscopically is a prerequisite. In preparation of the IR-UV double resonance experiment, a single color (2+1) REMPI experiment was performed. Several band systems of the NO-Ne complex correlating with the vibrational bands $\tilde{C}\,^2\Pi(v' = 1 - 4)$ and with the vibrationless levels of the states $\tilde{E}\,^2\Sigma^+$, $\tilde{F}\,^2\Delta$, and $\tilde{H}'\,^2\Pi$ [70] are found. In the first subsection, the above states are described briefly. The second subsection will describe the experimental results and analysis. Note that in order to distinguish states for the complex from those of the monomer a tilde is put on top the state index (e.g. $\tilde{C}\ \Pi$) for the complex.

4.1.1 REMPI spectroscopy of NO-Ne

$\tilde{C}\ ^2\Pi - \tilde{X}\ ^2\Pi$ Transition

For the NO-Ne band systems, the vibrational assignments are consistent with a dominant progression in the intermolecular stretching vibration and a T-shaped

vibrationally averaged structure. The findings are also consistent with the results obtained for other NO($\tilde{C}$)-X complexes [70, 122, 126]. The dominance of the stretching progression indicates a significant reduction in the NO-X bond distance. Furthermore, the blue satellites which accompany the members of the stretching progression are identified as partially resolved rotational structures rather than hot bands or excitation to different bending levels. Additional weak bands are assigned to members of a progression in the bending vibration. The weak intensity of the members of this progression provides additional evidence for a near T-shaped configuration resulting in unfavorable Franck-Condon factors for transitions with $\Delta v_b \neq 0$. Recorded REMPI spectra for the $\tilde{C}\,^2\Pi(v' = 1 - 4) - \tilde{X}\,^2\Pi$ transition of the NO-Ne complex are displayed in Fig. 4.1 where the origins of the individual band systems are aligned for clarity. The positions of the bands are listed in Table 4.1 together with a comparison of term values and spectroscopic constants. The columns from the second to the fourth represent the term values of the monomer. The second column refers to the position of the observed bands while the third and the fourth columns represent the term value after applying a first-order and second-order deperturbation procedure, respectively [106]. The frequency shift with respect to the monomer value in the sixth column is listed together with the term values for each observed cluster band in the fifth entry. Since the $C\,^2\Pi - X\,^2\Pi$ two-photon transition in the monomer is carried by two tensor components $T_0^{(0)}$(mf) and $T_0^{(2)}$(mf) (see Table 3.2), the corresponding spectrum is a superposition of two different spectra. The $T_0^{(0)}$(mf) component consists of Q-branches which are not resolved with the experimental resolution. Upon transformation to the principal axis (PA) system, the second rank tensor component will be responsible for perpendicular transitions with $\Delta P = 0, \pm 1, \pm 2$. In the case of a perfect symmetric top, it is expected that unresolved P-branches are located at positions $(A - B)\Delta(P^2)$. Since under molecular beam conditions only levels with $P'' = \frac{1}{2}$ are populated,

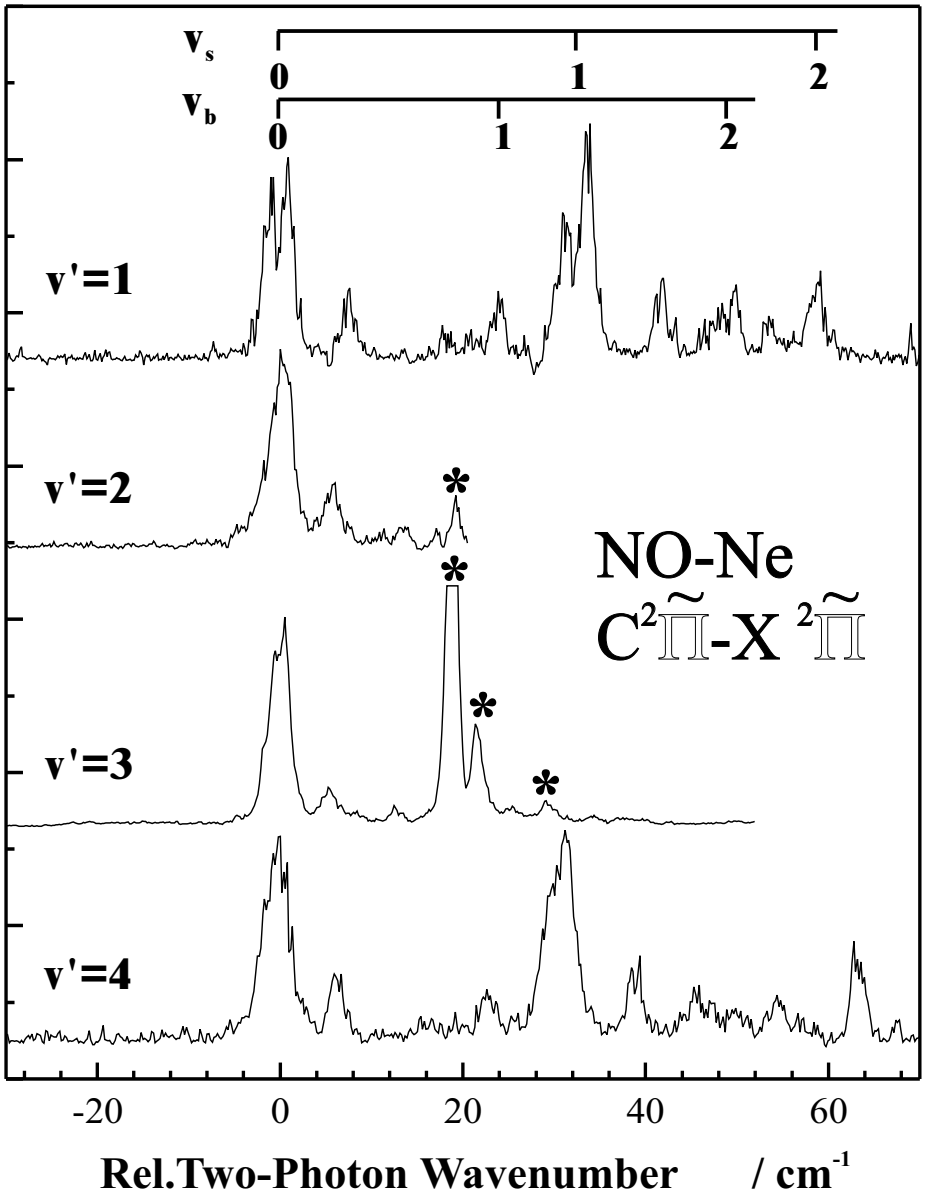

Figure 4.1: Spectra of the $\tilde{C}\,^2\Pi(v' = 1 - 4) - \tilde{X}$ transition in NO-Ne. Features marked with an asterisk are artifacts caused by baseline shifts due to strong monomer transitions. For clarity the origins of the individual band systems are aligned. The correct positions of the band systems are listed in Table 4.1.

Table 4.1: Comparison of term values and spectroscopic constants (in cm^{-1}) for vibrational bands of NO($\tilde{C}\,^2\Pi(v')$)-Ne with the corresponding monomer values. The second column refers to the position of the observed bands while the third and the fourth columns represent the term values after applying a first-order and a second-order deperturbation procedure, respectively. The frequency shift ($\Delta\nu$) with respect to the monomer value in the sixth column is listed together with the term values for each observed cluster band in the fifth entry. ν_s denotes the stretching frequency.

$\tilde{C}(v')$	NO(0)[a]	NO(1)[a]	NO(2)[a]	NO-Ne	$\Delta\nu(1)$	ν_s
0	52373	52372	52380	52287[b]	-85	34
1	54690	54697	54742	54612[c]	-85	33
2	57081	56958	57108	57044[c]	+86	?
3	59208	59420	59378	59188[d]	-232	?
4	61732	61741	61677	61656[c]	-85	31

[a]Reference [106]
[b]Reference [66]
[c]Reference [70]
[d]Reference [72]

two-photon transitions to the levels with $P' = \frac{1}{2}$, $P' = \frac{3}{2}$, and $P' = \frac{5}{2}$ are possible. Therefore, the unresolved rotational branches are predicted to be located on the blue side of the rotationless origin at frequencies $2(A - B)$ and $6(A - B)$. Since for a near T-shaped complex the a-inertial axis coincides approximately with the internuclear axis, the rotational A constant is given approximately by the rotational constant b_{NO} of the monomer while the rotational constant B is very small and can be neglected. Using typical values for the NO monomer Rydberg states, spacings of about 4 cm^{-1} and 12 cm^{-1} are predicted. In Fig. 4.1, there are two small peaks at 5 cm^{-1} and 12.5 cm^{-1} for the v'=3 band system. For NO-Ar, the positions are at 4.8 cm^{-1} and 13 cm^{-1} [122].

The slight increase in the experimentally observed values for the A constant as compared to b_{NO} reflects either a deviation from the T-shaped configuration or a change in the rotational constant b_{NO} in the complex. Although the latter explanation seems to be unlikely at first, one must remember that in the monomer the state $C\,^2\Pi(v')$ interacts strongly with the valence state $B\,^2\Pi(v')$. Therefore, the observed excited monomer levels must be regarded as mixtures which contain at least these two unperturbed states. The degree of mixing depends on the energy mismatch between the two unperturbed states. It is conceivable that in the complex the energy mismatch is changed causing a reduction in the B-state admixture. Since the B-state is characterized by a much smaller rotational constant, the effective rotational constant of NO, b_{NO}, can actually increase.

Evidence for this state mixing upon complexation can be deduced from a comparison of the intermolecular vibrational frequencies with the observed frequency shifts for the band origins. The frequency shifts and observed frequencies for the bands with $v' = 0, 1$, and 4 are very similar, indicating that the intermolecular interaction changes very little as function of NO vibration. On the other hand, the shift found for the level $v' = 3$ is further to the red and the shift found for the level $v' = 2$ is even to the blue. This unusual behavior in the frequency shifts becomes clear when the observed monomer band positions are examined assuming the validity of the BO approximation. Within the BO approximation, the dissociation energy of the complex in the excited state can be derived from the relation: $D_0' = D_0'' - \Delta\nu$ where $\Delta\nu$ is the observed frequency shift. Alternatively, an estimate of the binding energy of the complex can be obtained from the observed intermolecular stretching frequencies. For example, ω_e and $\chi_e\omega_e$ can be estimated from the fundamental and overtones. In terms of these parameters, the binding energy of a Morse potential is given by $D_e = \omega_e^2/4\chi_e\omega_e$.

Table 4.2: Comparison of term values (in cm^{-1}) for the vibrational bands NO($\tilde{C}\,^2\Pi(v')$)−X with the values for the monomer state $B\,^2\Pi$. The term values of NO for the different vibrational levels of the B state obtained in a first-order deperturbation procedure are listed in the second column while the term values of NO-Ne for the different vibrational levels of the $\tilde{C}$-state obtained experimentally are listed in the fourth column. The energy mismatch (ΔE) is given in the third column.

$B(v')$	NO(1)[a]	ΔE	NO-Ne	$\tilde{C}(v')$
6	51425	862	52287[b]	0
9	54203	409	54612[c]	1
12	56878	166	57044[c]	2
14	58564	624	59188[d]	3
17	61103	553	61656[c]	4

[a]Reference [106]
[b]Reference [66]
[c]Reference [70]
[d]Reference [72]

For the levels $v' = 0, 1$, and 4, two stretching bands are observed while only the first member of the intermolecular stretching progression is observed for $v' = 2$ and 3 due to strong baseline shifts resulting from resonances associated with monomer transitions. For the levels $v' = 0, 1$, and 4, the vibrational frequencies for the bending and stretching mode are 24 cm^{-1} and 33 cm^{-1}, respectively. In Table 4.2, the term values of NO for the different vibrational levels of the B state obtained in the first-order deperturbation procedure are listed in the second column while the term value of NO-Ne for the different vibrational levels of the $\tilde{C}$-state obtained experimentally are listed in the fourth column. The energy mismatch (ΔE) is given in the third column. In the Table, there is a strong variation in the mismatch for the different term values. The smallest value is found for the level $\tilde{C}\,^2\Pi(v' = 2)$.

There is no evidence for strong predissociation for any of the detected NO-Ne band systems while in the NO-Ar case predissociation behavior is evident when the energy mismatch is small (see Section 4.2.1). In order to rationalize the predissociation behavior for NO-Ne, it should be remembered that in the monomer the levels with $v' = 2$ and $v' = 3$ are most strongly perturbed by the B-state. Therefore, upon complexation there must be a strong effect on the state mixing in these levels. Furthermore, the dissociation energy in the NO-Ne complex is comparable to the magnitude of the perturbation matrix elements for the $B - C$ state interaction. Therefore, it is conceivable that the corresponding $\tilde{B}$-state level is shifted up in energy, effectively closing this channel. This notion is consistent with the fact that in the second-order deperturbation process the level $\tilde{B}\,^2\Pi(v' = 12)$ is pushed up further to 56899 cm^{-1}.

$\tilde{H}^+\,^2\Sigma,\ \tilde{H}'\,^2\Pi - \tilde{X}\,^2\Pi$ Transition

Overview spectra of the two-photon transitions to the Rydberg states $\tilde{F}\,^2\Sigma$, $\tilde{H}\,^2\Sigma$, and $\tilde{H}'\,^2\Pi$ for NO-Ne (trace (b)) and NO-Ar (trace (a)) in the wavelength region around 320 nm are shown in Fig. 4.2. These states are derived from an electron configuration involving a $3d$ electron. Trace (c) in Fig. 4.2 shows the corresponding monomer spectrum recorded under similar molecular beam conditions. The $\tilde{H}$-state spectrum is shifted by about 235 cm^{-1} to the red of the corresponding monomer transition. The spectrum shows almost no rotationally resolved structure. This is consistent with the fact that the corresponding monomer transition is dominated by a zeroth rank tensor component allowing only rotational Q-branches. The absence of rotational structures indicates that the transition accesses mainly the Π component [103]. The observed spectrum is dominated by a long vibrational progression assigned to the stretching vibration, consistent with a shortening of

the NO-Ne bond length. Except for the first and second member, small satellites are seen to the red of the stretching vibration peaks. These are assigned as combination bands having one quantum of stretching vibration and up to three quanta of bending vibration. Assuming a Morse potential with harmonic constant (ω_e=74 cm^{-1}) and anharmonic constant ($\chi_e\omega_e$=4.9 cm^{-1}), the binding energy is estimated to be approximately 280 cm^{-1} . This value is in good agreement with the value 270 cm^{-1} calculated from the experimentally observed red shift combined with the theoretical ground state dissociation energy D_e=35 cm^{-1} of Ref. [15]. The comparison of the measured energy with the calculated bond energy D_e=345 cm^{-1} of the corresponding NO$^+$-Ne complex suggests that the interaction in the $\tilde{H}$-state is dominated by ionic interactions [127]. This result is also consistent with the observed vibrational stretching and bending frequencies (v_s=74 cm^{-1} and v_b=42 cm^{-1}) which are close to the values determined by Lee *et al.* for the ionic complex (v_s=82 cm^{-1} and v_b=41 cm^{-1}) [127]. The observed Q-branches show a small splitting consistent with a deviation in the vibrationally averaged structure from a near T-shaped configuration. The deduced Jacobi angle of 60° is smaller than the value determined for the equilibrium configuration of the cation complex in the *ab-initio* calculation by Wright and co-workers [127].

$\tilde{F}\,^2\Delta - \tilde{X}\,^2\Pi$ Transition

In the NO monomer, the two-photon transition for $F\,^2\Delta - X\,^2\Pi$ is carried by a single second rank tensor component $T_1^{(2)}$. When this component is transformed to the PA system, all possible second rank tensor components are expected to contribute. Consequently, the band systems of the complex correlating with the $\tilde{F}\,^2\Delta$ are expected to have a complicated rotational structure. As shown in Fig. 4.2, the $\tilde{F}$-state spectrum is shifted by 100 cm^{-1} to the red of the corresponding

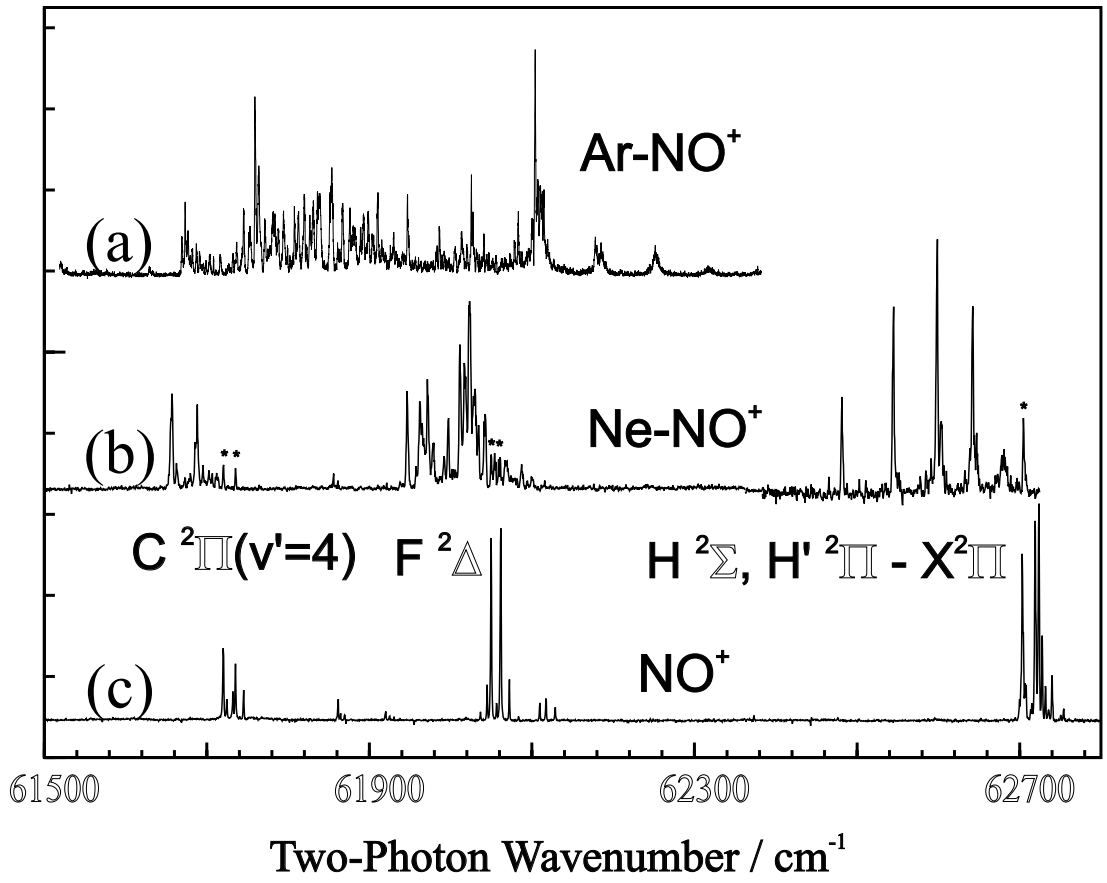

Figure 4.2: Overview spectrum for the region of excitation to the states derived from the $3d$ complex. The spectra are recorded by monitoring the appropriate parent ion masses.

monomer band. Although the vibrational progression is not clear, most likely the spectrum consists of two band systems with partially resolved rotational structures. The spectrum could be analyzed assuming two different vibrationally averaged structures: a near T-shaped geometry (85°) and a 30° geometry with an energy difference of about 5 cm^1. Assuming that the excitation of the two vibrational levels involve the intermolcular stretching coordinate, the spectrum could be reproduced. Since the calculation is based on the rigid rotor model, the assignment should be considered as tentative.

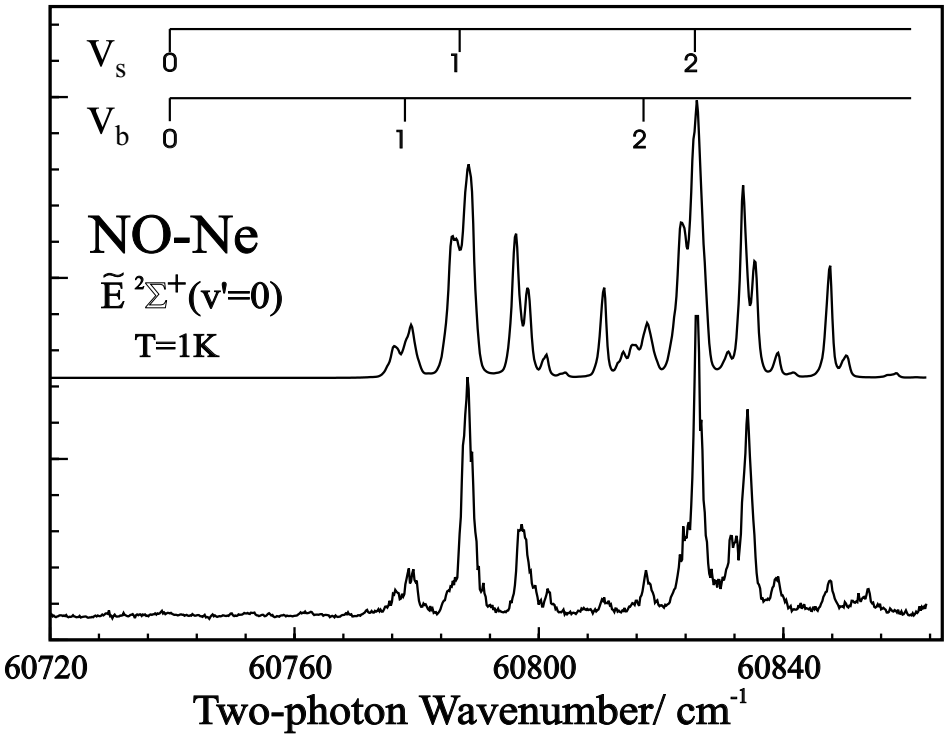

Figure 4.3: (2+1) REMPI spectrum of the NO-Ne complex probing an electronic state correlating with $E\,^2\Sigma^+$. The bottom spectrum is the observed one while the top spectrum is the calculated one.

$\tilde{E}\,^2\Sigma^+ - \tilde{X}\,^2\Pi$ Transition

The spectrum for the $\tilde{E}\,^2\Sigma^+ - \tilde{X}\,^2\Pi$ transition is shown in Fig. 4.3. The bottom spectrum is the observed one while the top spectrum is the calculated one. The spectrum is dominated by two members of the stretching progression. A small satellite band observed to the red of the stretching progression is assigned to the intermolecular bending mode. For a consistent interpretation, the first band must be regarded as the second member of the stretching progression. This assignment locates the origin for this band system at 60738 cm^{-1} with stretching and bending

frequencies of about 50 cm^{-1} and 39 cm^{-1} , respectively. Even though the radius for the Rydberg orbital increases to 6.26 Å which might result in a large increase of the binding energy for the NO-Ne complex, the E-state is derived from a $4s$ orbital which allows for a considerable probability of finding the electron in the core region, shielding partially the electric charge of NO^+.

4.1.2 Infrared-Ultraviolet spectroscopy of NO-Ne

Experimental Results

In order to find the first overtone transition of the complex, a depletion spectrum was recorded with the UV laser fixed to the second vibronic band of the $\tilde{C}(v' = 1)-\tilde{X}$ transition shown in Fig. 4.1. Compared to the depletion measured for the NO monomer in Fig. 2.27 on page 62, the depletion signal found for the NO-Ne complex is considerably reduced due to the mismatch in the linewidths of the two lasers. Figure 4.4 shows a depletion spectrum (top) together with a room temperature photoacoustic spectrum (bottom). The strongest depletion feature of about 15% is found near the $Q_{11}(\frac{1}{2})$ monomer line at 3724 cm^{-1}. Even though the signal-to-noise ratio is poor, the features indicated as arrows represent different rotational lines of band A (the vibrationless band of the first overtone transition. See Fig. 4.10). This becomes obvious in Fig. 4.5 where the depletion spectrum (top) is compared with the hot band spectrum (bottom) of band A. Dominant depletion features coincide with lines of the bottom spectrum.

(2+1) REMPI spectra of the hot band transition are recorded by stabilizing the IR laser onto one of the observed depletion features and scanning the UV laser through the hot band region of interest. Figure 4.6 displays the hot band transition to the $\tilde{E}$-state. Unfortunately, this transition coincides with the vibronic band

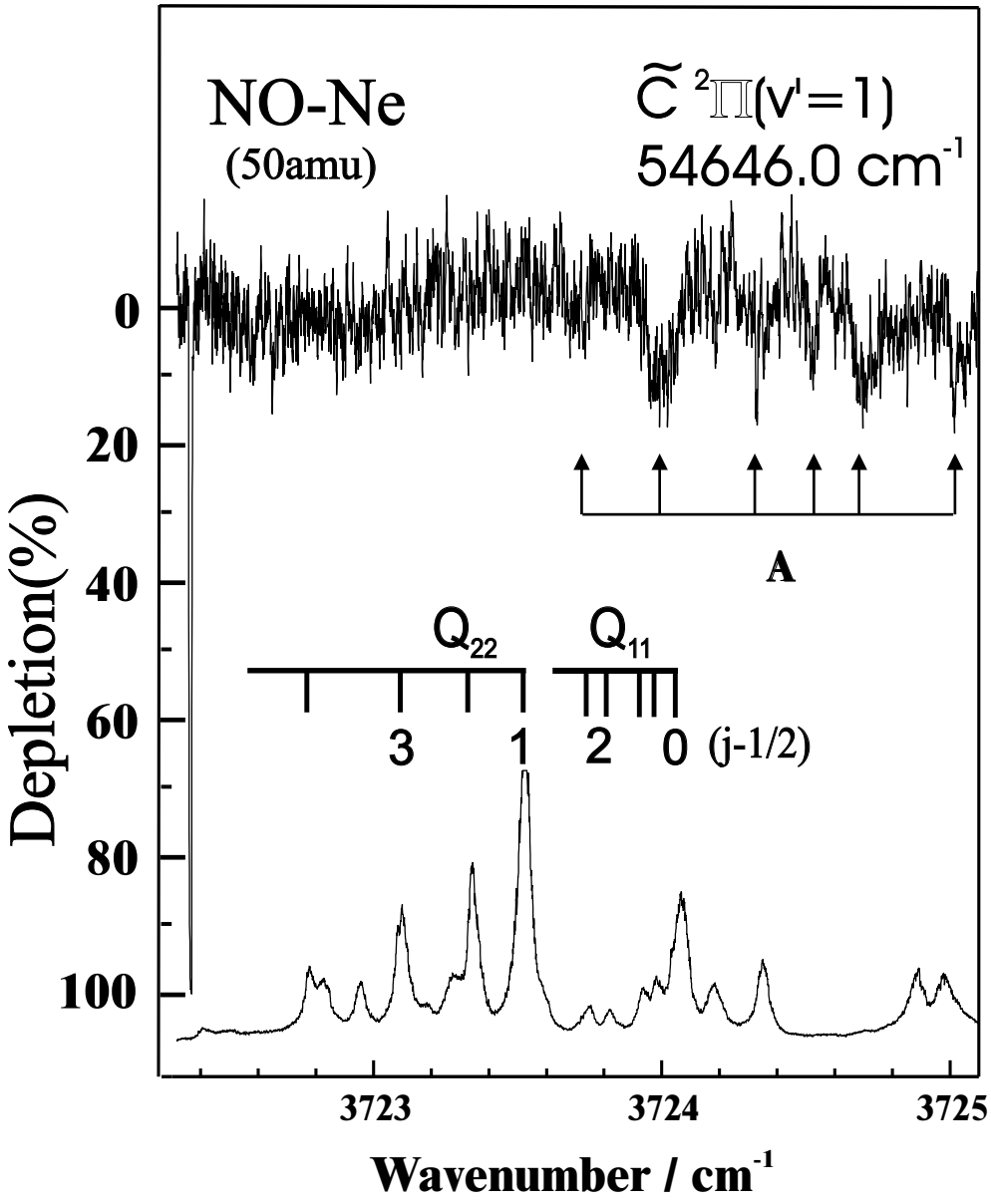

Figure 4.4: Depletion of the NO-Ne REMPI signal as a function of the IR frequency. The REMPI laser is fixed to a vibronic feature of the $\tilde{C}(v' = 1) - \tilde{X}$ band system of the complex corresponding to a two-photon resonance of 54646.0 cm^{-1} . The bottom trace shows the room temperature photoacoustic spectrum. Depletion features are marked with arrows. Rotational lines are labeled with $(j - \frac{1}{2})$. The Q_{11} lines show the λ-doublets.

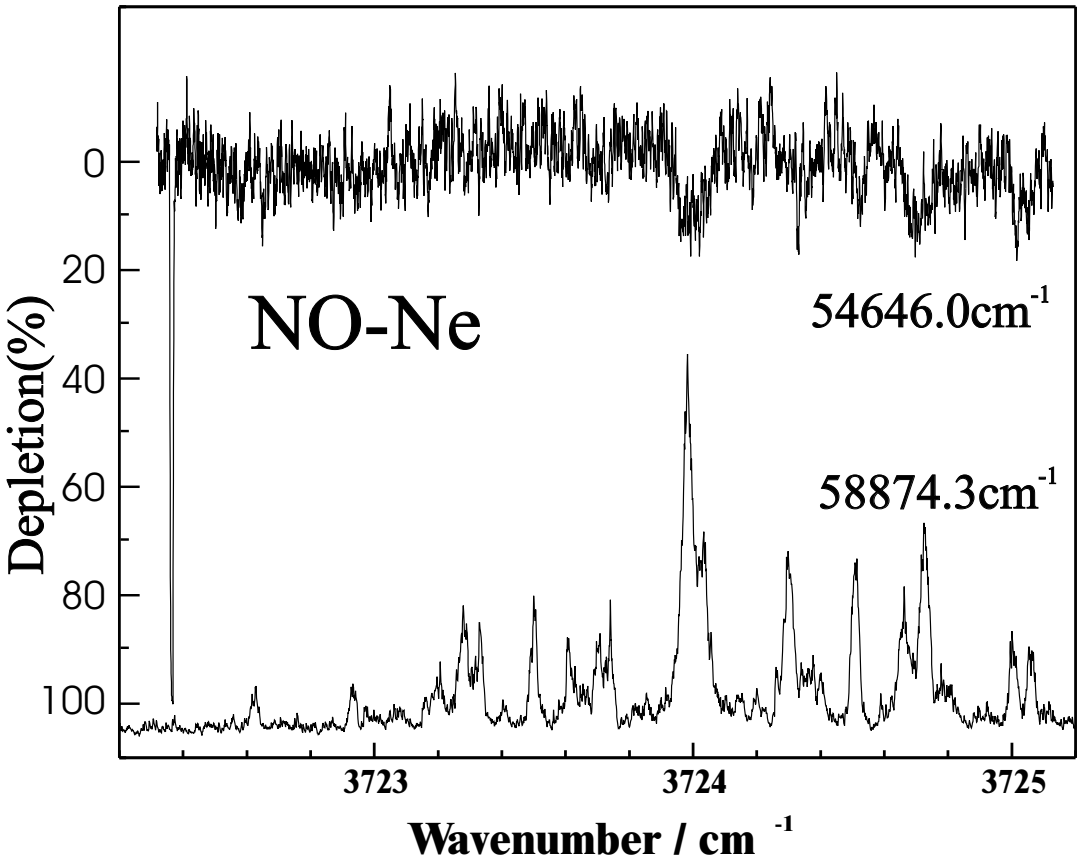

Figure 4.5: The depletion features represent different rotational lines of band A. Top spectrum is the same as the top trace in Fig. 4.4. Thee bottom spectrum is an IR spectrum of band A.

$C\,^2\Pi(v' = 2) - X\,^2\Pi(v'' = 0)$ of the monomer, resulting in serious baseline shifts at several frequencies (marked with asterisks). Furthermore, a part of the spectrum overlaps the single color spectrum associated with the $\tilde{C}\,^2\Pi(v' = 2) - \tilde{X}\,^2\Pi(v'' = 0)$ transition in the NO-Ne complex (dotted box area). Nonetheless, two hot band transitions have been identified at 57088.1 cm^{-1} and 57107.3 cm^{-1} and are marked with arrows. On the other hand, none of these problems have been encountered for the hot band regions of the $\tilde{F}$- and $\tilde{H}$-states as shown in Figs. 4.7−4.9. A careful comparison confirms that the rovibrational structures are very similar to the ones found for the corresponding origin bands. This is seen in Figs. 4.7−4.9 where

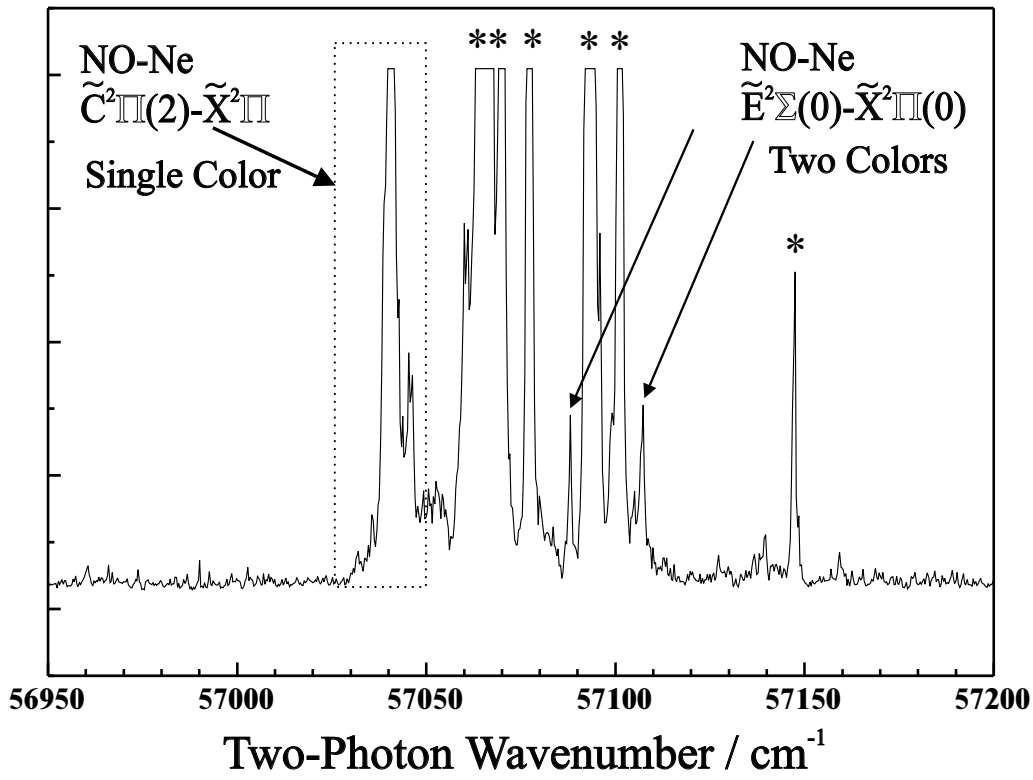

Figure 4.6: IR-REMPI double resonance spectrum of NO-Ne. The UV laser is scanned over the region of the hot band transition $\tilde{E}\,^2\Sigma(v'=0) - \tilde{X}\,^2\Pi(v''=2)$ of the complex while the IR laser is fixed to the maximum depletion signal. Features marked with an asterisk are due to monomer transitions resulting in serious baseline shifts. The dotted box area is due to the single color $\tilde{C}\,^2\Pi(v'=2) - \tilde{X}\,^2\Pi(v''=0)$ transition of the NO-Ne complex. Hot band transitions corresponding to a double resonance are identified at 57088.1 cm^{-1} and 57107.3 cm^{-1} and are marked with arrows.

the hot band spectra are compared with the single color spectra shifted to the red by the amount of the NO vibrational excitation. For the origin bands and the hot band transitions, the same levels of the excited potential surface are accessed. Thus, any difference in the rovibrational structure must be attributed to differences in the population of the intermolecular vibrational levels of the overtone system and to the resulting changes in FC factors for excitation to the Rydberg state. By pumping a combination band which involves one or more quanta of intermolecular stretching

and bending vibration, it is expected that changes in FC factors allow one to access different intermolecular vibrational levels in the excited state. For instance, Fig. 4.8 shows the hot band transition in which the IR laser excites to a combination band involving intermolecular bending and stretching vibration. In comparison to Fig. 4.7, Fig. 4.8 shows different rovibronic structures especially at larger frequencies. These are most likely due to excitation of higher bending levels in the excited state.

Once the hot band spectra have been identified, the UV laser is fixed to one of the frequencies marked with arrows in Figs. 4.7−4.9 and then the IR laser is scanned through the overtone region. Figure 4.10 shows a comparison of the IR spectra recorded by detecting the vibrationally excited complex through the $\tilde{E}$-, $\tilde{F}$-, and $\tilde{H}$-states. Up to 4 bands are observed and labeled as A, B, C, and D in order of increasing frequency. They are located at 3724.02 cm^{-1}, 3727.87 cm^{-1}, 3732.56 cm^{-1}, and 3739.20 cm^{-1}, respectively. The positions of the resonances recorded with different UV frequencies coincide very well. On the other hand, the intensity varies from spectrum to spectrum. These differences must be due to the rovibronic structure of the (2+1) REMPI spectra of the various Rydberg states and to the fact that the UV laser frequency is kept fixed while the IR laser is scanned. As can be seen in Figs. 4.6−4.9, the two-photon excitation spectra to the $\tilde{E}$- and $\tilde{F}$-states show a dense cluster of rovibrational bands while the $\tilde{H}$-state spectrum is dominated by well separated sharp Q-branches. Therefore, while scanning the IR laser, the REMPI laser is more likely to be out of resonance in the case of $\tilde{H}$-state detection. On the other hand, for the $\tilde{F}$-state the complete hot band manifold is shifted according to the change in the IR laser frequency. In other words, although the fixed UV laser probes different resonances in this manifold, the IR absorption is effectively detected over a wide range. This phenomenon is quite obvious in the high frequency parts of the spectra displayed in Fig. 4.10. In the case of $\tilde{H}$-state detection, only bands A and B are detected. But, when $\tilde{F}$-state detection is applied,

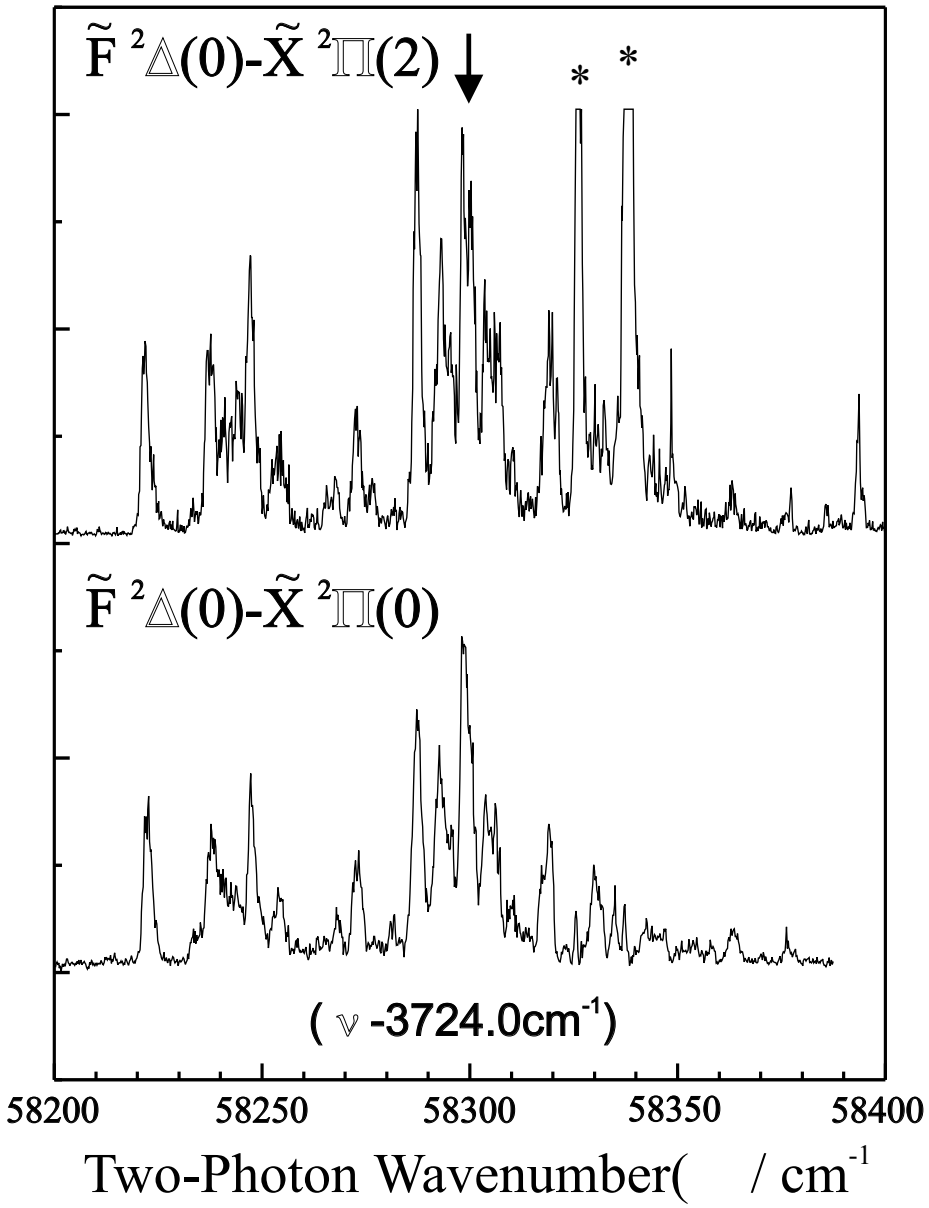

Figure 4.7: Hot band spectrum (top) to an excited state of the NO-Ne complex correlating with the NO F-state. The IR laser is locked to the maximum feature of band A (see Fig. 4.10 on page 174). Lines marked with an asterisk resulted from a baseline distortion due to a strong monomer signal. The bottom spectrum represents the single color REMPI spectrum corresponding to the origin band of the complex. This spectrum is shifted by the amount of IR excitation.

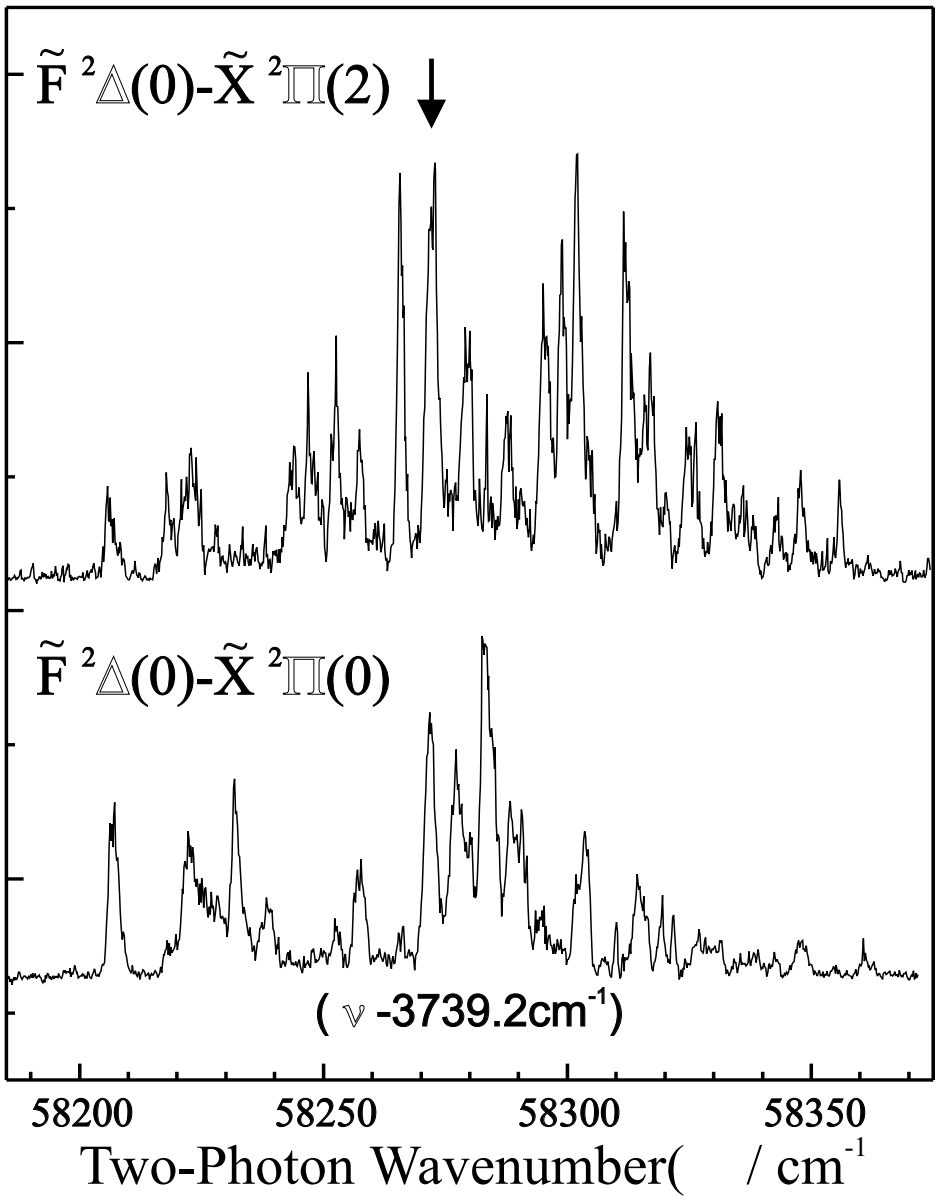

Figure 4.8: Hot band spectrum (top) to an excited state of the NO-Ne complex correlating with the NO F-state. The IR laser is locked to the maximum feature of band D at 3739.2 cm^{-1}. The bottom spectrum represents the single color REMPI spectrum corresponding to the origin band of the complex. This spectrum is shifted by the amount of IR excitation.

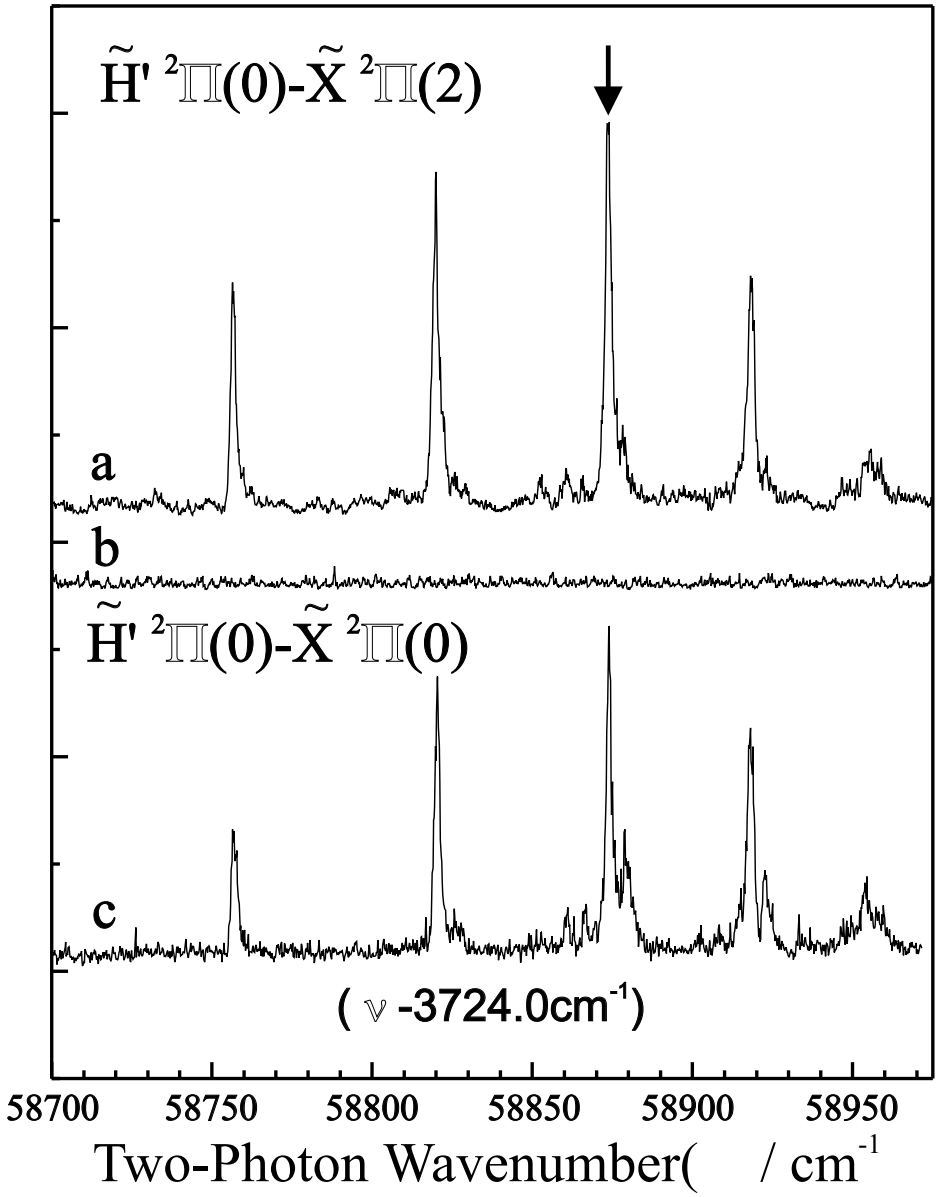

Figure 4.9: Hot band spectrum (trace (a)) to an excited state of the NO-Ne complex correlating with the NO H-state. The IR laser is locked to the maximum feature of band A (see Fig. 4.10 on page 174). Under these conditions no background signal (trace (b)) is observed. Trace c represents the single color REMPI spectrum corresponding to the origin band of the complex. This spectrum is shifted by the amount of IR excitation.

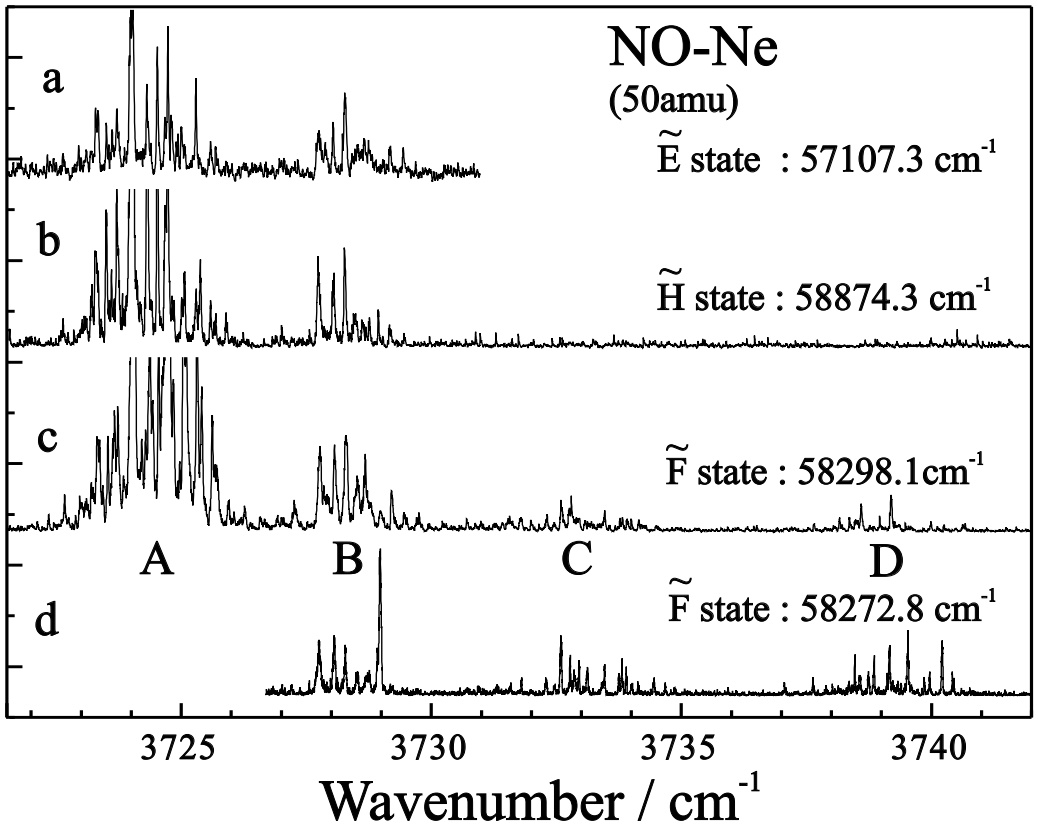

Figure 4.10: Overview spectra of the NO-Ne complex recorded at the indicated two-photon frequencies corresponding to the hot band systems of the $\tilde{E}$-, $\tilde{H}$-, and $\tilde{F}$-states.

two additional bands C and D are detected. Even though they are weak, once the bands are identified, the IR laser is stabilized onto a feature of the new bands and the UV laser is scanned to find the associated hot band spectrum. This provides new UV frequencies for the IR detection. As an example, part (d) of Fig. 4.10 shows a spectrum recorded through $\tilde{F}$-state detection but now at the UV frequency suitable for detection of band D.

Analysis

Figure 4.11 shows the adiabatic bender (AB) potentials for the NO-Ne complex calculated with CCSD(T) potential energy surfaces (PESs) by Alexander [15]. Corresponding relative energies are tabulated in Table 4.3. n labels the AB state. Solid curves and dashed curves correspond to $P = \frac{1}{2}$ and $P = \frac{3}{2}$, respectively. The potential curves appear in closely spaced pairs (for example, n=1,2 pair or n=3,4 pair). These pairs correspond to the ω-doublets. Because the Coriolis coupling is neglected in the AB approximation, the P-type doubling does not appear in the potential curves. Since the minimum configuration for the NO-Ne complex is a near T-shaped geometry, the difference potential term, V_{diff}, is small. Thus, states with positive and negative values of $P \times \omega$ lie very close in energy. According to the theoretical calculation, band A is assigned to the lowest vibrational level of the complex $(v_s, v_b) = (0, 0)$ (or $P = \frac{1}{2}, n = 1, 2$) in Fig. 4.11, while band B corresponds to excitation to the (0,1) level (or $P = \frac{3}{2}, n = 1, 2$). Here, v_s and v_b are the intermolecular stretching and bending vibrational quantum numbers, respectively. Band C corresponds to transition to $P = \frac{1}{2}$, n=3,4 levels with (0,2) and band D corresponds to transition to the $P = \frac{1}{2}, n = 1, 2$ levels with excitation of one stretching quantum (1,0).

From the heuristic Hamiltonian

$$\begin{aligned} E^{JPv_s}_{tot\,\omega} &= E_{Pv_vv_s} + BJ(J+1) - D\big[J(J+1)\big]^2 + \cdots \\ &\quad -\frac{P\omega}{|P\omega|}\Big\{V_0 + V_1(J+\tfrac{1}{2}) + V_2(J+\tfrac{1}{2})^2 + \cdots \\ &\qquad +\zeta\Big[C_0 + C_1(J+\tfrac{1}{2}) + C_2(J+\tfrac{1}{2})^2 + \cdots\Big]\Big\}, \end{aligned} \tag{3.280}$$

it is found that the rotational lines are split into two ω-components and that these ω-components are split again into two components depending on the sign of ζ. The following parity selection rule was derived for the one-photon transition (Eq. (3.285)):

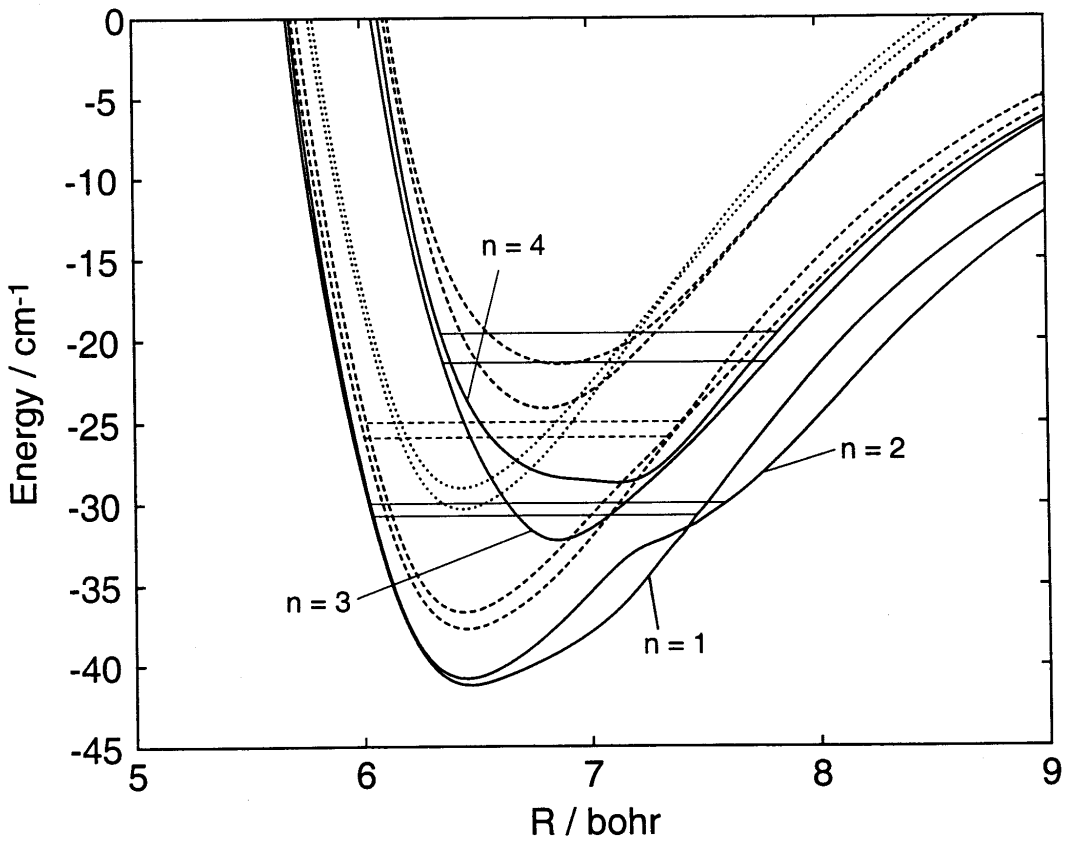

Figure 4.11: Adiabatic bender potentials for the NO-Ne complex. The figure is excerpted from Ref.[15]. The solid and dashed curves correspond to $P = \frac{1}{2}$ and $P = \frac{3}{2}$, respectively. n labels the adiabatic bender states. The position of the lowest vibrational level in each AB potential is shown by horizontal lines.

$\zeta'\zeta''(-)^{2J''+\Delta J} = 1$. In order to understand the structure of the observed spectra, the energy levels and allowed one-photon transitions are illustrated in Fig. 4.12. In considering the transitions, one should note that the ordering of the P-type doublets in the $\omega = -\frac{1}{2}$ level is reversed as compared to the $\omega = \frac{1}{2}$ level. According to the selection rule, Q-branch lines can only occur between levels which differ in the symmetry quantum number ζ while lines of the different P- and R-branches exist if the symmetry quantum number is conserved. Due to the ω-splitting terms, there

Table 4.3: Relative energies (in cm^{-1}) of the lowest bound-states of the NO-Ne complex [15].

J	P	n^{d}	$v_s{}^{e}$	CC[a]		CD[b]	AB[c]	Band[g]	Data Table
				$\eta^{f}=+1$	$\eta=-1$				
1/2	1/2	1	0	0	0.007	0	0	A	4.4
		2	0	0.86	0.84	0.76	0.76		
		3	0	7.72	7.70	7.46	9.36	C	4.6
		4	0	9.19	9.22	9.07	11.15		
		1	1	14.66	14.41	14.18	16.84	D	4.7
		2	1	14.85	15.07	14.53	15.46		
3/2	1/2	1	0	0.31	0.29	0.22	0.33		
		2	0	1.18	1.21	0.98	1.08		
		3	0	7.97	8.01	7.66	9.66		
		4	0	9.54	9.49	9.26	11.44		
		1	1	14.51	14.83	14.37	17.12		
		2	1	15.45	15.18	14.72	15.73		
	3/2	1	0	4.28	4.28	3.72	5.18	B	4.5
		2	0	5.30	5.30	4.14	6.11		
		3	0	16.79	16.78	20.59	17.71		
		4	0	17.06	17.06	21.20	19.12		

[a]Close-coupled calculations.
[b]Centrifugal-decoupled calculations.
[c]Adiabatic-bender calculations.
[d]Adiabatic-bender state index.
[e]Nominal stretching quantum number
[f]Parity. $\eta = \zeta(-)^{J-1/2}$.
[g]Bands A, B, C, and D correspond to the transition from the lowest state to the indicated states.

$$\eta'' \Delta J_{\omega''}^{\omega'}$$

Selection rule: $(\zeta'\zeta'' \ (-)^{2J''+\Delta J} = 1)$

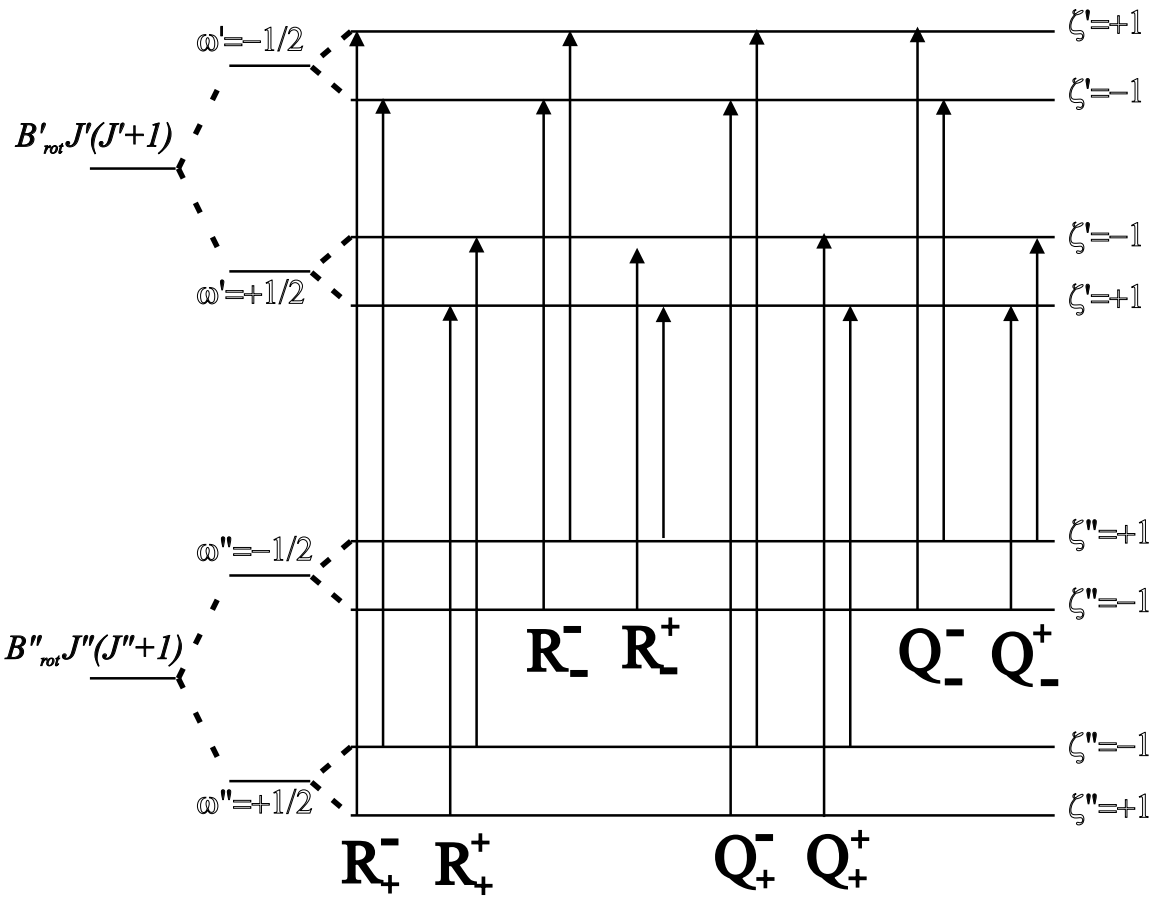

Figure 4.12: One-photon transitions between different rotational levels of the NO-X complex.

are four different types of transitions within each P-, Q-, and R-branch depending on $\Delta\omega = 0, \pm 1$. Individual lines are conveniently labeled as ${}_{\mathrm{sign}(\zeta)}(\Delta J)^{\mathrm{sign}(\omega')}_{\mathrm{sign}(\omega'')}(J)$. For instance, ${}_{+}Q^{-}_{+}(J)$ represents a transition from a level with $\omega = +\frac{1}{2}, \zeta = +1$ to a level with $\omega = -\frac{1}{2}, \zeta = -1$. From the diagram, it is evident that the ω splitting of the excited level is reflected in the difference between ${}_{\pm}(\Delta J)^{-}_{+}$ and ${}_{\pm}(\Delta J)^{+}_{+}$ lines. Similarly, the ω splitting of the ground state is found from the difference between ${}_{\pm}(\Delta J)^{-}_{+}$ and ${}_{\pm}(\Delta J)^{+}_{+}$ lines. Furthermore, the spacing between Q^{+}_{+} branches and Q^{-}_{+} branches provide information about the ω-splitting in the excited state. In the same manner, the spacing between ${}_{+}Q^{+}_{+}$ branches and ${}_{-}Q^{+}_{+}$ reveals the J-independent P-type doubling.

Using the heuristic Hamiltonian, the different spectroscopic constants are determined by a least squares fit from the energy levels calculated by Alexander in a full quantum mechanical bound state calculation. Tables 4.4−4.7 list the total energy levels for the vibrational levels $((v_s, v_b) = (0,0), P = \frac{1}{2}, n = 1,2)$, $((0,1), P = \frac{3}{2}, n = 1,2)$, $((0,2), P = \frac{1}{2}, n = 3,4)$, and $((1,0), P = \frac{1}{2}, n = 1,2)$, respectively. The determined constants are compiled in Table 4.8. The results of the fit are displayed in Figs. 4.13 and 4.14. Figure 4.13 displays the energies as a function of $J(J+1)$. Clearly, the energies depend on $J(J+1)$, indicating that the main contribution to the energy is given by the rotational term. In the figure, no centrifugal distortion is noticeable, which is consistent with a very small centrifugal constant.

In Fig. 4.14 the ω splitting is plotted as a function of $J + \frac{1}{2}$. It is dominated by a constant term and a term quadratic in $(J + \frac{1}{2})$. The fit indicates a small contribution from a term proportional to $(J + \frac{1}{2})^4$. It is important to verify that the empirical Hamiltonian can reproduce the results from the *ab initio* calculation. Figure 4.15 shows two different calculated spectra. Trace (a) is a spectrum based on the *ab initio* calculation. Spectrum (b) is generated by fitting the bound state energies of the *ab initio* calculation to the heuristic Hamiltonian in a least squares fit (Table

Table 4.4: Relative position of the $P = \frac{1}{2}, n = 1, 2$ level as a function of J (in cm^{-1}). Results are from the calculation based on the CCSD(T) PES's by Alexander [132].

J_{tot}	$\eta^a = +1$		$\eta = -1$	
	$\omega = +\frac{1}{2}$	$\omega = -\frac{1}{2}$	$\omega = +\frac{1}{2}$	$\omega = -\frac{1}{2}$
1/2	0	0.858	0.007	0.841
3/2	0.306	1.178	0.294	1.210
5/2	0.789	1.788	0.803	1.742
7/2	1.510	2.525	1.479	2.592
9/2	2.380	3.608	2.413	3.529
11/2	3.518	4.748	3.485	4.835
13/2	4.797	6.274	4.830	6.179
15/2	6.340	7.814	6.309	7.916
17/2	8.022	9.758	8.051	9.651
19/2	9.931	11.795	9.958	11.684

[a]Parity. $\eta = \zeta(-)^{J-1/2}$.

Table 4.5: Relative position of the $P = \frac{3}{2}, n = 1, 2$ level as a function of J (in cm^{-1}). Results are from the calculation based on the CCSD(T) PES's by Alexander [132].

J_{tot}	$\eta^a = +1$		$\eta = -1$	
	$\omega = +\frac{1}{2}$	$\omega = -\frac{1}{2}$	$\omega = +\frac{1}{2}$	$\omega = -\frac{1}{2}$
1/2	-	-	-	-
3/2	4.281	5.297	4.281	5.298
5/2	4.795	5.824	4.796	5.822
7/2	5.512	6.558	5.508	6.565
9/2	6.428	7.507	6.435	7.493
11/2	7.558	8.627	7.547	8.651
13/2	8.863	10.001	8.880	9.962
15/2	10.396	11.481	10.370	11.538
17/2	12.065	13.263	12.100	13.185
19/2	13.941	15.170	13.986	15.071

[a]Parity. $\eta = \zeta(-)^{J-1/2}$.

Table 4.6: Relative position of the $P = \frac{1}{2}, n = 3, 4$ level as a function of J (in cm^{-1}). Results are from the calculation based on the CCSD(T) PES's by Alexander [132].

J_{tot}	$\eta^a = +1$		$\eta = -1$	
	$\omega = +\frac{1}{2}$	$\omega = -\frac{1}{2}$	$\omega = +\frac{1}{2}$	$\omega = -\frac{1}{2}$
1/2	7.719	9.186	7.700	9.214
3/2	7.969	9.543	8.006	9.489
5/2	8.478	10.001	8.429	10.076
7/2	9.098	10.810	9.131	10.735
9/2	9.983	11.651	9.951	11.735
11/2	11.007	12.847	11.032	12.758
13/2	12.285	14.048	12.271	14.137
15/2	13.744	15.591	13.741	15.509
17/2	15.407	17.132	15.430	17.201
19/2	17.288	18.908	17.333	18.957

[a]Parity. $\eta = \zeta(-)^{J-1/2}$.

Table 4.7: Relative position of $P = \frac{1}{2}, n = 1, 2$ level with one quantum of the bending vibration as a function of J (in cm^{-1}). Results are from the calculation based on the CCSD(T) PES's by Alexander [132].

J_{tot}	$\eta^a = +1$		$\eta = -1$	
	$\omega = +\frac{1}{2}$	$\omega = -\frac{1}{2}$	$\omega = +\frac{1}{2}$	$\omega = -\frac{1}{2}$
1/2	14.660	14.413	14.847	15.068
3/2	14.512	14.832	15.445	15.178
5/2	15.121	14.789	15.733	15.983
7/2	15.293	15.588	16.696	16.510
9/2	16.251	15.965	17.424	17.582
11/2	16.856	17.122	18.657	18.525
13/2	18.217	17.989	19.822	19.929
15/2	19.369	19.537	21.394	21.310
17/2	21.093	20.991	22.994	23.056
19/2	22.880	22.837	24.872	24.912

[a]Parity. $\eta = \zeta(-)^{J-1/2}$.

Table 4.8: Spectroscopic constants (in cm^{-1}) of the heuristic Hamiltonian in Eq. (3.280) for the electronic ground state levels of the NO-Ne complex based on Alexander's calculation. Note the different values of C_0 and C_1 for $\omega = \pm 1$.

Band	P	$E_{v_b v_s P}$	B	D $\times 10^{-5}$	V_0	V_2 $\times 10^{-3}$	V_4 $\times 10^{-5}$	C_0 $\times 10^{-2}$	C_1 $\times 10^{-3}$
A	$\frac{1}{2}$	0	0.1070	1.75	0.422	6.94	-2.22	0.60^a	1.85^a
								0.81^b	5.28^b
B	$\frac{3}{2}$	4.051	0.1045	2.83	0.504	1.34	-5.74	0.15^a	-0.14^a
								0.39^b	-0.33^b
C	$\frac{1}{2}$	8.034	0.0994	1.78	0.743	6.00	-5.35	-1.43^a	0.00^a
								-2.44^b	0.00^b
D	$\frac{1}{2}$	14.322	0.0850	7.48	0.259	18.83	-1.77	-16.46^a	1.32^a
								-11.75^b	1.11^b

$^a\omega = +\frac{1}{2}$

$^b\omega = -\frac{1}{2}$

Table 4.9: Spectroscopic constants (in cm^{-1}) for the electronic ground state levels of the NO-Ne complex fitted to the experimental spectra.

Band	P	$E_{v_b v_s P}$	B	D $\times 10^{-5}$	V_0	V_2 $\times 10^{-3}$	V_4 $\times 10^{-5}$	C_0 $\times 10^{-2}$	C_1 $\times 10^{-3}$
A	$\frac{1}{2}$	0	0.1130		0.33	6.80		0.4	6.0
B	$\frac{3}{2}$	3.83	0.1100		0.45	1.0		0.0	0.0
C	$\frac{1}{2}$	8.54	0.0995		0.59	-1.0		2.0	2.0
D	$\frac{1}{2}$	15.18	0.0780		0.27	25.0		-13.0	0.0

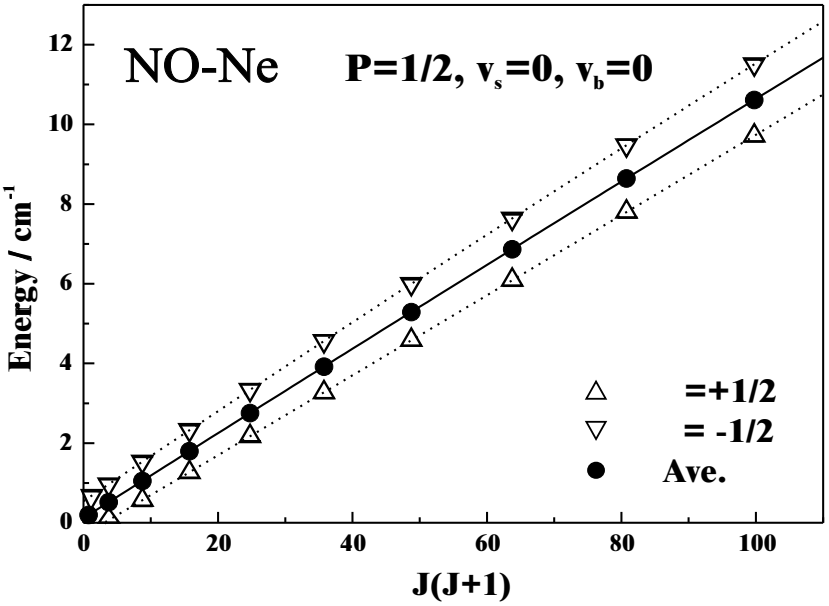

Figure 4.13: Bound state energies for the vibrational ground state of the NO-Ne complex as a function of $J(J+1)$. The open triangles represent the energy averaged over the two P-type components for $\omega = \pm\frac{1}{2}$. The solid circles represent the rotational energy.

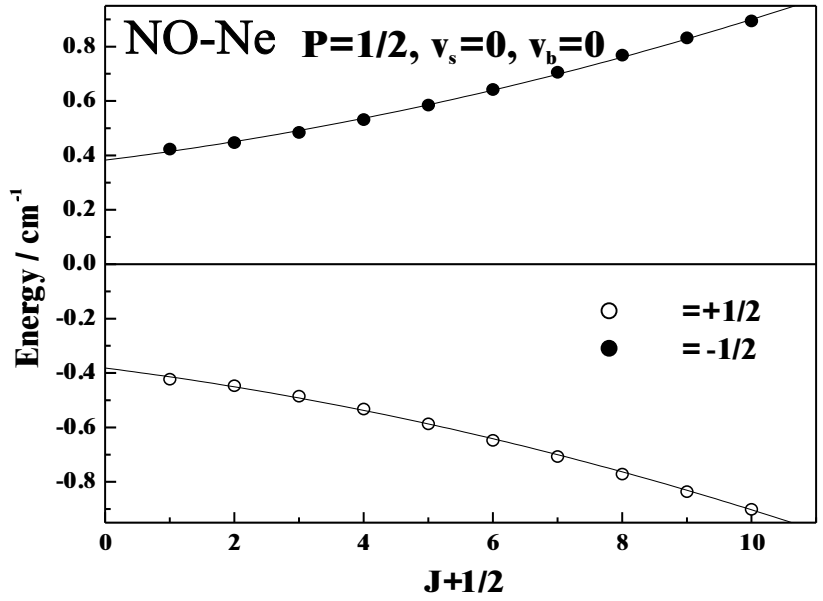

Figure 4.14: The ω-splitting of the rotational energy levels for the ground vibrational state of NO-Ne for $\omega = \pm\frac{1}{2}$.

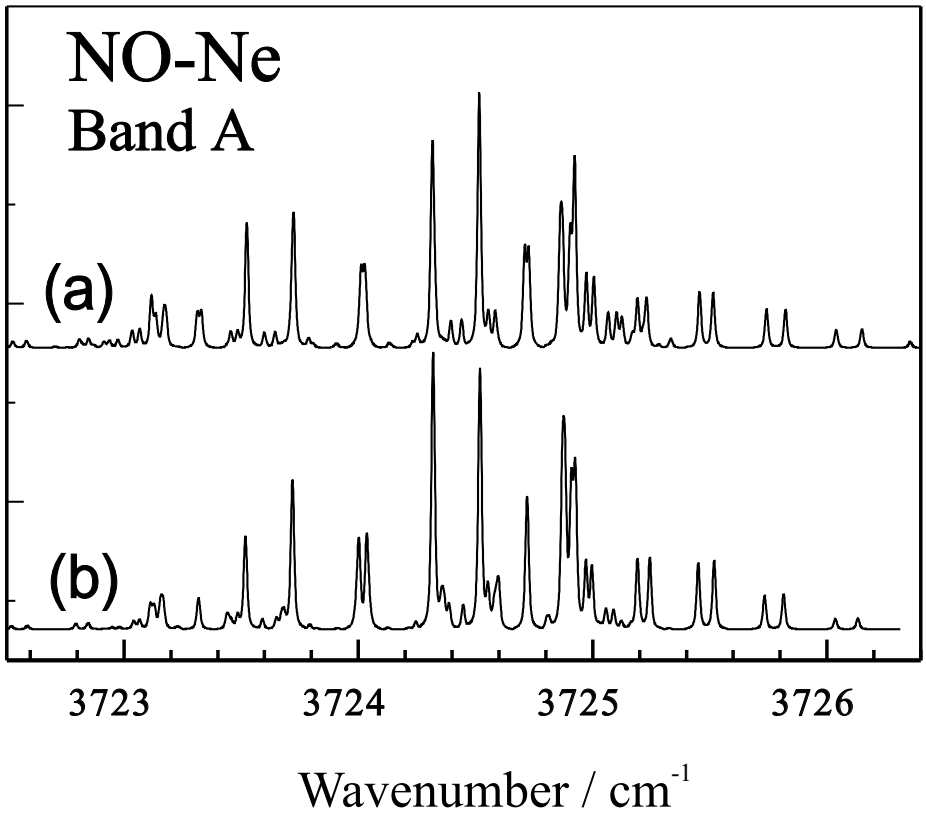

Figure 4.15: Comparison of two predicted spectra. Part (a) is the simulation from the *ab initio* calculation. Part (b) is the simulation using the heuristic Hamiltonian with parameters corresponding to the best fit of the *ab initio* energy levels. Both Spectra are calculated assuming a temperature of 1 K and for the linewidth a 0.01 cm^{-1} Lorentzian component and a 0.01 cm^{-1} Gaussian component.

4.8) with the assumption that the intensity arises from a purely parallel transition with a constant FC factor. The overall agreement between the calculated spectra (a) and (b) is excellent except for minor differences in the intensities. This agreement confirms that the Hamiltonian in Eq. (3.280) can be used to fit the experimental spectra.

Figure 4.16 shows a calculated spectrum (a) and the different branches (b−d). In this way, it is straightforward to assign individual rotation lines. The assignment is shown in Fig. 4.17. Observed and calculated spectra in the region of band

A are displayed in Fig. 4.17. Spectrum (a) is the experimental spectrum measured under molecular beam conditions. The theoretical spectrum (b) is calculated from the energy levels represented by Eq. (3.280) using the constants of Table 4.9 and assuming a temperature of 1 K and a linewidth with a 0.01 cm^{-1} Lorentzian component and a 0.01 cm^{-1} Gaussian component (all predicted spectra are calculated assuming these parameters). Different rotational lines belonging to different branches are labeled with $(J - \frac{1}{2})$. The two parity components are indicated for the branches R^-_+, R^+_- ,P^-_+, and P^+_-. Because under molecular beam conditions the temperature is low and because for the NO-X complexes levels with $\omega = +\frac{1}{2}$ are lower in energy, lines originating from these levels are expected to be dominant in the spectrum. For example, lines of the branches ${}_{\pm}R^-_+(J)$ are clearly visible. Each line of this branch is split due to the P-type doubling (Fig. 4.17). As can be seen in Table 4.9, the ω-splitting is comparable to the rotational energy for small values of J. As a result, branches other than ${}_{\pm}R^-_+(J)$ are heavily mixed in the center of the band. The P-type doubling is resolved for branches with $\Delta\omega = \pm 1$. Furthermore, Fig. 4.17 shows that the P-type doubling of the R^-_+ branches is clearly J-dependent since the spacing increases as J.

Figure 4.18 shows the observed spectrum of band A and different calculated spectra. Spectrum (b) is the experimental spectrum with the UV frequency fixed to the two-photon resonance at 58874.3 cm^{-1} of the $\tilde{H} - \tilde{X}$ transition. Part (c) is the same spectrum as Fig. 4.16(b). Comparison of spectra (c) with the experimental spectrum shows good agreements in the overall rotational structure except discrepancies for a few line positions. Using the heuristic Hamiltonian of Eq. (3.280), it is possible to improve the agreement with the observed spectrum by slightly changing the parameters. Part (a) in Fig. 4.18 is a spectrum based on constants determined in a fit to the experimental spectrum. Table 4.9 lists the set of constants derived in this fit. In the process of fitting band A, constants for both the ground state

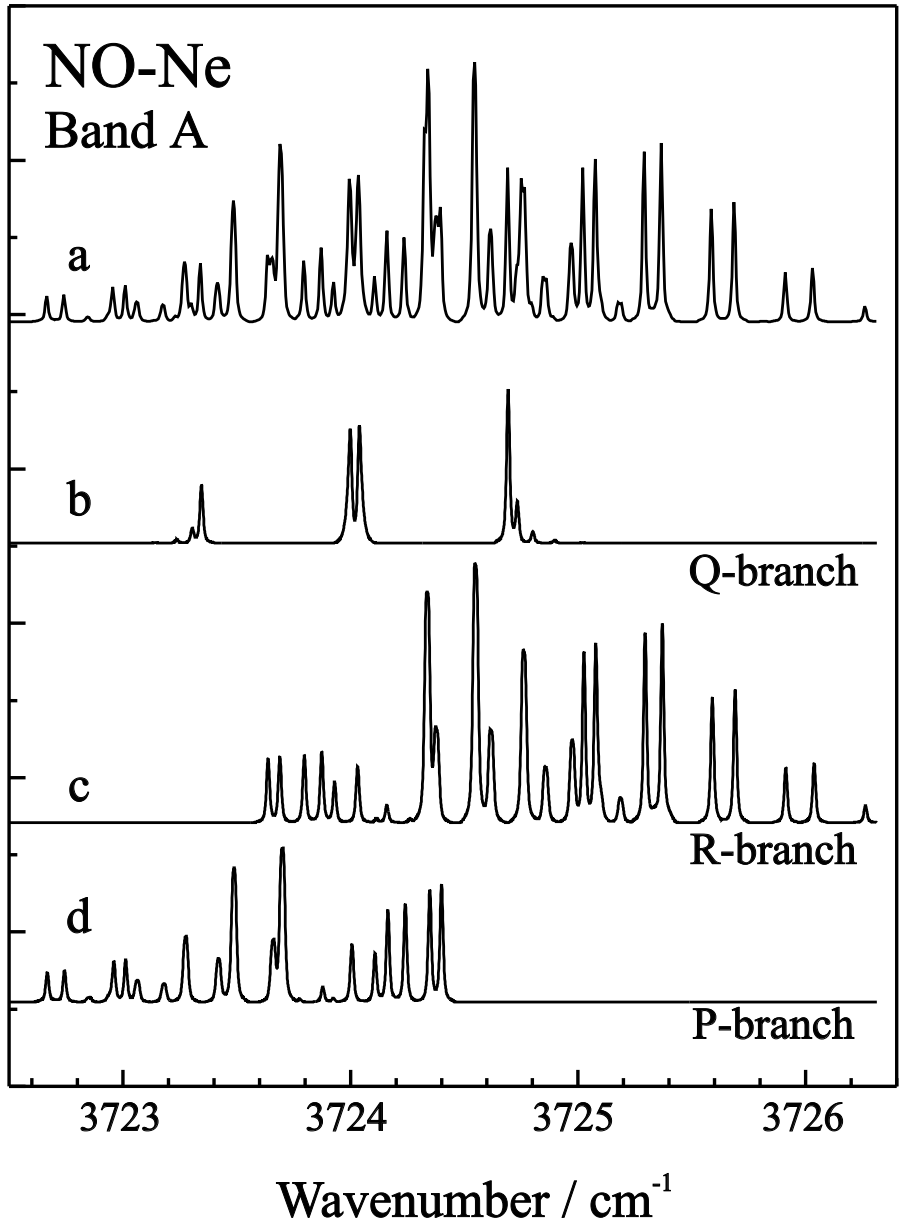

Figure 4.16: Spectrum calculated with constants in Table 4.9. Spectrum (a) shows all branches. Parts (b), (c), and (d) represent spectra for Q-, R-, and P-branches, respectively.

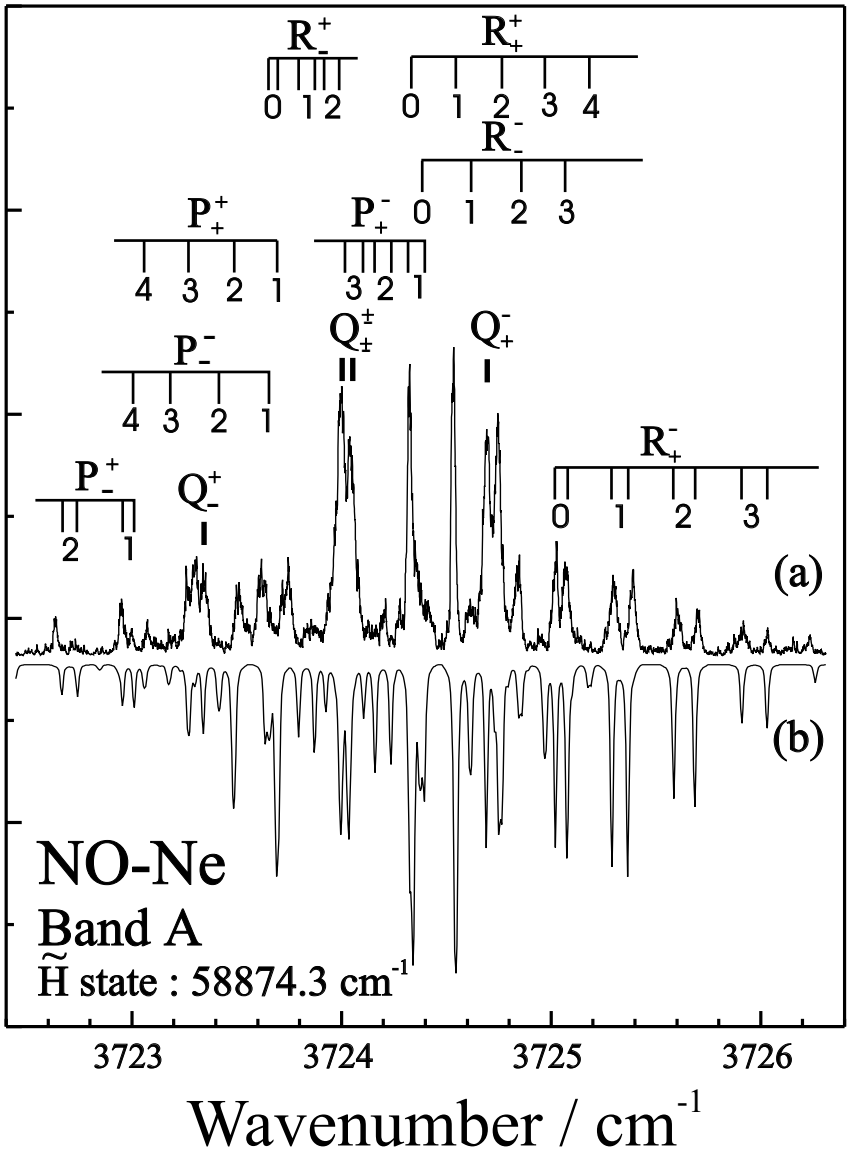

Figure 4.17: Comparison of observed and calculated spectra in the region of band A. The theoretical spectrum is calculated from the energy levels represented by Eq. (3.280) using the constants of Table 4.9 and assuming a temperature of 1 K and a linewidth with a 0.01 cm^{-1} Lorentzian component and a 0.01 cm^{-1} Gaussian component. The intensities are determined from an approximate line strength calculation as discussed in the text. The P-type doubling is resolved for branches with $\Delta\omega = \pm 1$. The UV laser is fixed to the indicated two-photon frequency corresponding to $\tilde{H}$-state detection. Different rotational lines belonging to different branches are labeled with $J - \frac{1}{2}$. The two parity components are indicated for the branches R_+^-, R_-^+, P_+^-, and P_-^+. Rotational lines are labeled with $(J - \frac{1}{2})$.

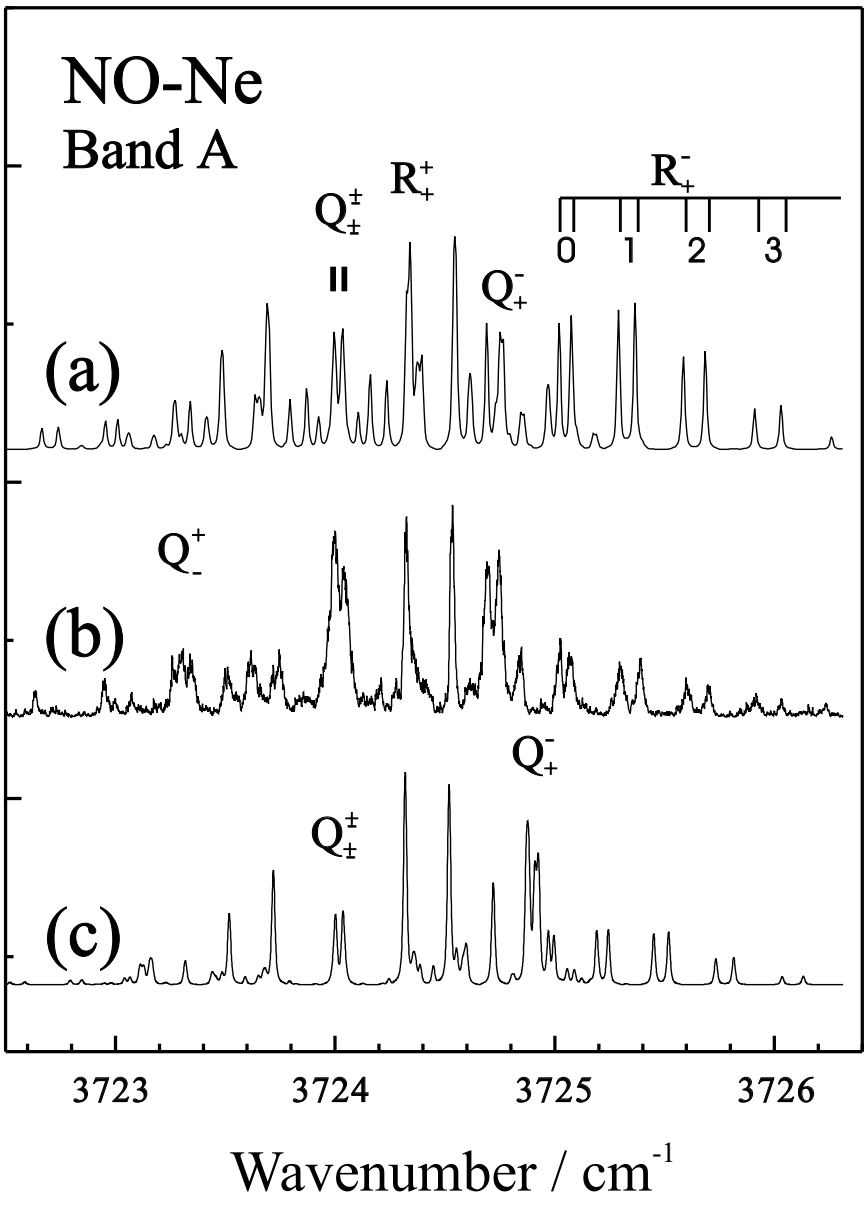

Figure 4.18: Comparison of predicted spectra with the experimental spectrum (b) of the first overtone transition in the NO-Ne complex. Part (a) is generated using the heuristic Hamiltonian. Part (c) is the simulation using the heuristic Hamiltonian with parameters corresponding to the best fit of the *ab initio* energy levels. Spectra (a) and (c) are calculated assuming a temperature of 1 K and for the linewidth a 0.01 cm^{-1} Lorentzian component and a 0.01 cm^{-1} Gaussian component. Rotational lines are labeled with $(J - \frac{1}{2})$.

and the excited state in Table 4.9 are not determined independently. In comparing spectra (a) and (c), it turns out that the *ab initio* calculation predicts too large an ω-splitting. In the best fit, the constant V_0 is decreased from 0.422 cm^{-1} to 0.33 cm^{-1} while the rotational constant is increased from 0.1070 cm^{-1} to 0.113 cm^{-1}. The splittings predicted by the *ab initio* calculation for the R_+^--branch manifold are too small. Therefore, in the *ab initio* calculation the J-dependent P-type doubling is slightly underestimated.

Figure 4.19 shows the comparison of spectra for band B which represents the transition to the first excited bending level associated with $P = \frac{3}{2}$. The spectrum calculated from the *ab initio* results is shifted by 0.221 cm^{-1} to lower frequencies to match the experimental spectrum. This implies that for the predicted origin of this band the $E_{v_s v_s P}$ parameter in Table 4.8 is slightly too large. Also, the rotational constant predicted by the *ab initio* treatment is slightly too small (0.1045 cm^{-1} vs. 0.11 cm^{-1}) while the ω-splitting is predicted correctly. From the theoretical study in Chapter 2, it is expected that the P-type doubling is more pronounced when the transition is between levels with $P = \frac{1}{2}$. Therefore, in the best fit of this band, the constants C_0 and C_1 were not included. From the fit, the bending vibrational energy is found to be 3.83 cm^{-1}. The transition frequency for this band is approximately derived as $b_{NO}(P_f^2 - P_i^2) = 2b_{NO}$, where b_{NO} represents the rotational constant for the NO monomer. The expected vibrational frequency is 3.4 cm^{-1} which is slightly smaller than the observed value. This discrepancy may be due to the deviation from the T-shaped geometry resulting in an increased effective rotational constant. In Fig. 4.20 the calculated spectrum is compared with different experimental spectra. The differences in the intensities reflect dependence of the detection sensitivity on the UV frequency. On the other hand, the agreement between line positions in the different spectra is very satisfactory.

Band C represents the transition to the second excited bending level with $P = \frac{1}{2}$. Trace (c) of Fig. 4.21 is based on the *ab initio* results shifted by 0.506 cm^{-1} to the blue. The rotational constant for the best fit does not change dramatically as compared to the *ab initio* calculation. A J-dependent P-type doubling constant is added in the fit although it was not necessary for fitting the results of the *ab initio* calculation. In Fig. 4.22, traces (b) and (c) are recorded with different UV frequencies. Again, the positions are well reproduced although the intensities are different.

For band D, the simulation based on the heuristic Hamiltonian reproduces the experimental spectrum far less satisfactorily than those for other bands. This band corresponds to excitation of one quantum of intermolecular stretching vibration with a stretching frequency of 15.18 cm^{-1} resulting in a substantial decrease in the rotational constant (0.078 cm^{-1}). The ω-splitting is considerably decreased while Coriolis coupling is increased dramatically. As can be seen in Fig. 4.23, one line of the $R(\frac{1}{2})$ doublet lies even higher in frequency than a line from the $R(\frac{3}{2})$. This makes the unambiguous fitting of constants very difficult. Therefore, except for the rotational constant the other constants are kept very close to the ones found for the *ab initio* result.

The comparison of the constants for different bands listed in Table 4.9 shows several interesting trends. The rotational constant B decreases with increasing intermolecular vibrational excitation reflecting the larger delocalization of the wavefunction. Especially for band D, the large reduction of B reflects the increased averaged Jacobi distance upon excitation of the intermolecular stretching vibration. Differences in the relative amounts of bending and stretching motion can be used to rationalize the variation of the ω-splitting constants V_0. Qualitatively, the ω-splitting can be interpreted as reflecting the degree of electronic orbital angular momentum quenching, i.e., the lifting of the degeneracy between electronic states

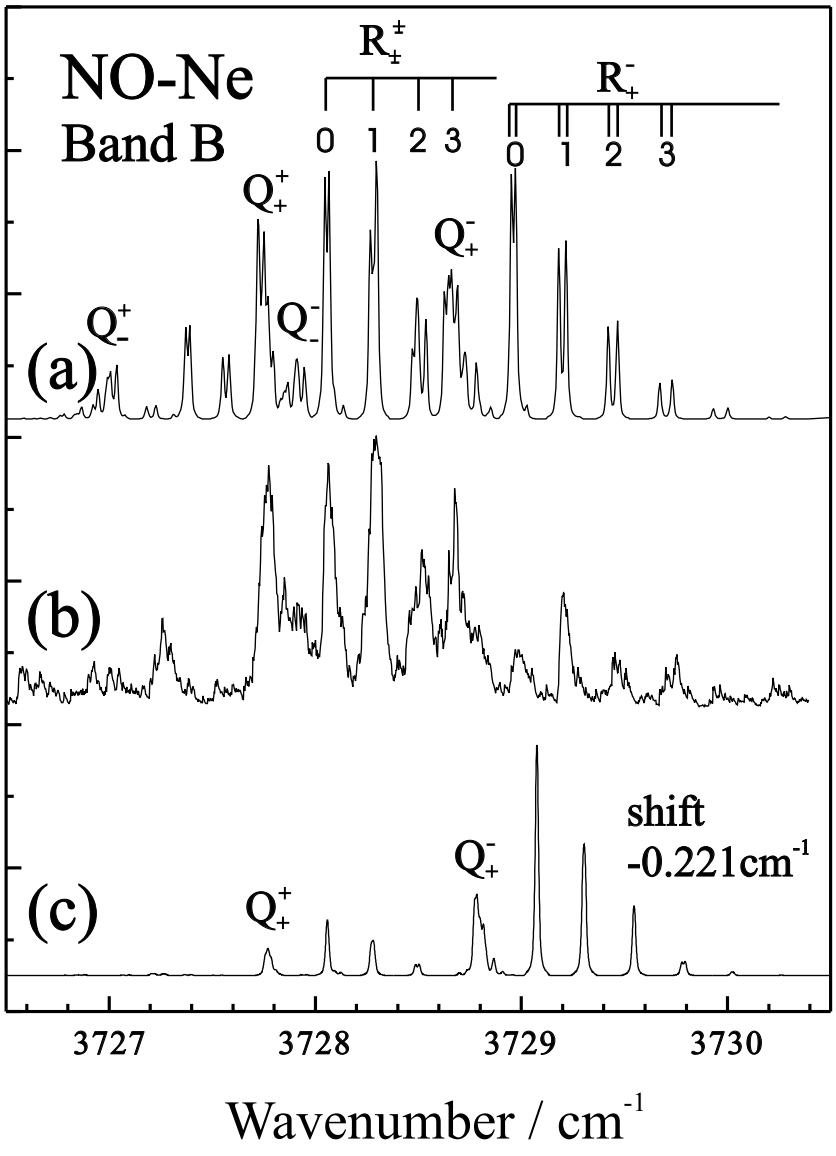

Figure 4.19: Comparison of predicted and experimental spectra of band B. Trace (a) is the spectrum generated using the heuristic Hamiltonian and the constants listed in Table 4.9. Trace (b) is the experimental spectrum. Trace (c) is the simulation based on the *ab initio* calculation. Spectra (a) and (c) are calculated assuming a temperature of 1 K and for the linewidth a 0.01 cm^{-1} Lorentzian component and a 0.01 cm^{-1} Gaussian component. Rotational lines are labeled with $(J - \frac{1}{2})$.

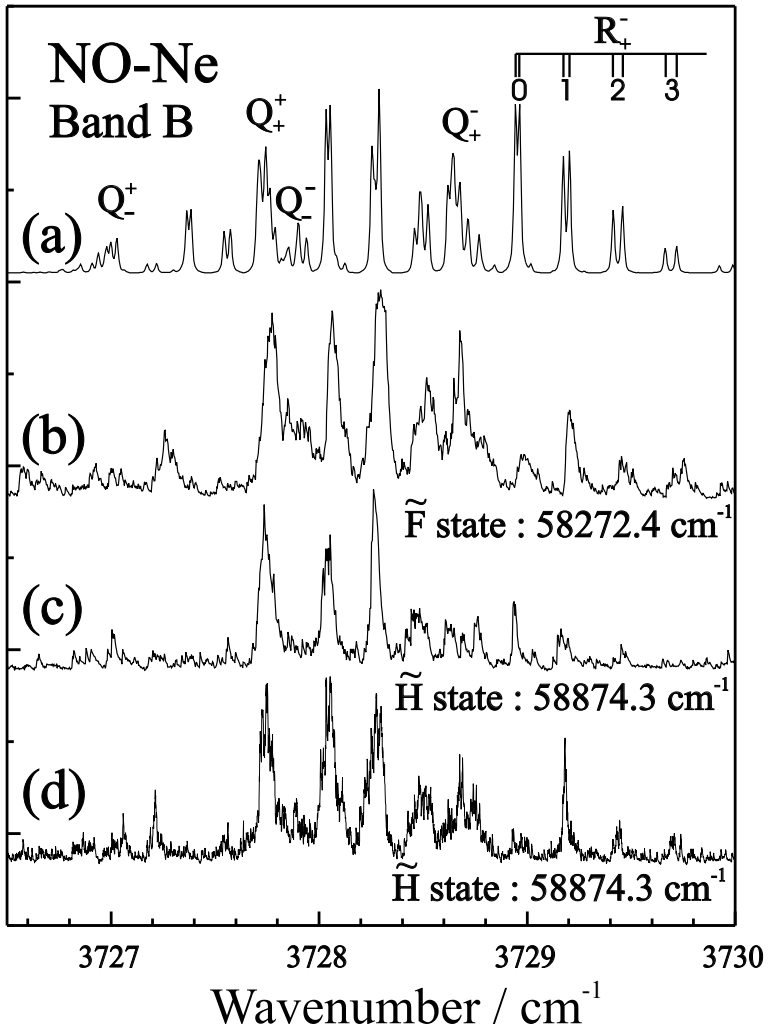

Figure 4.20: Comparison of the calculated spectra for band B with different observed spectra detected at the indicated two-photon frequencies. Different rotational lines belonging to several branches are labeled with $(J - \frac{1}{2})$. The two parity components are indicated for the R_+^- branch.

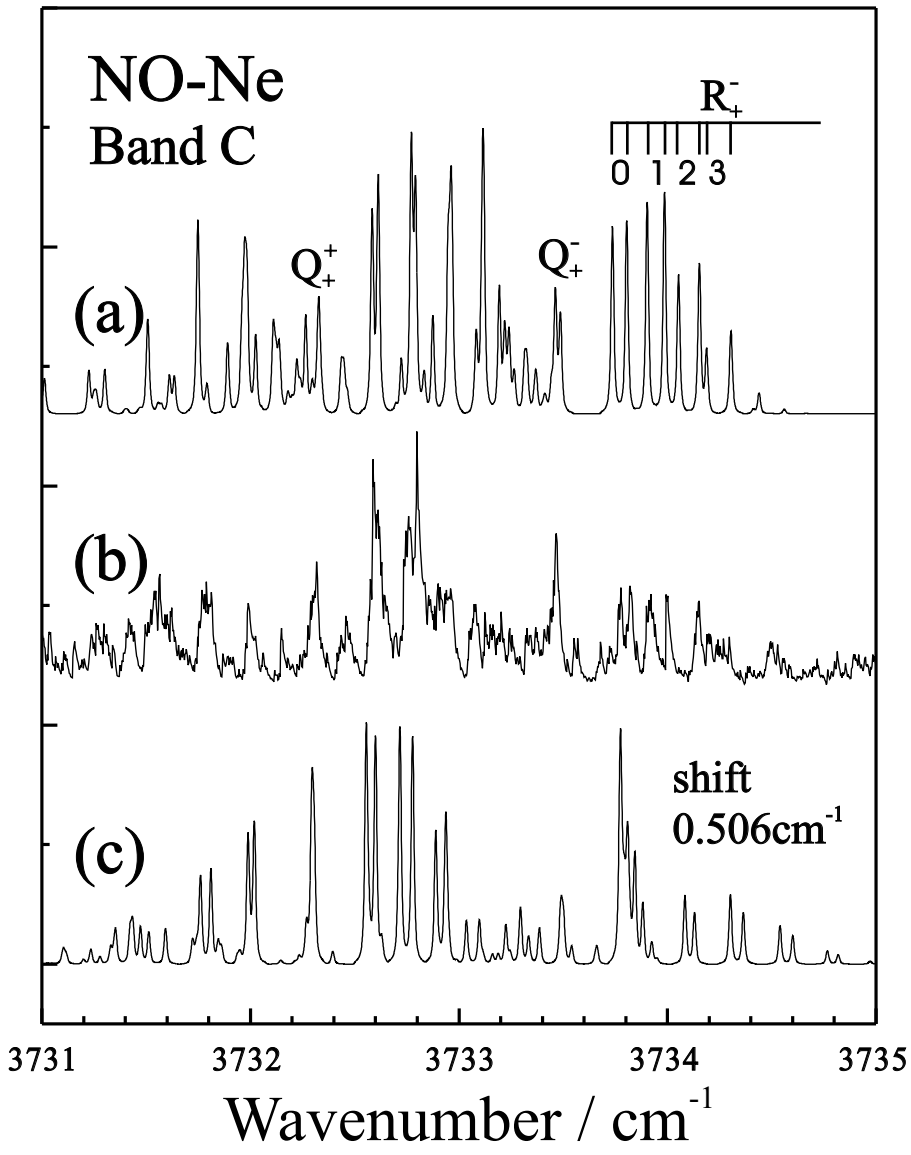

Figure 4.21: Comparison of predicted and experimental spectra of band C. Trace (a) is the spectrum generated using the heuristic Hamiltonian with constants from Table 4.9. Trace (b) is the experimental spectrum. Trace (c) is the simulation from the *ab initio* calculation. Spectra (a) and (c) are calculated assuming a temperature of 1 K and for the linewidth a 0.01 cm^{-1} Lorentzian component and a 0.01cm^{-1} Gaussian component. Rotational lines are labeled with $(J - \frac{1}{2})$.

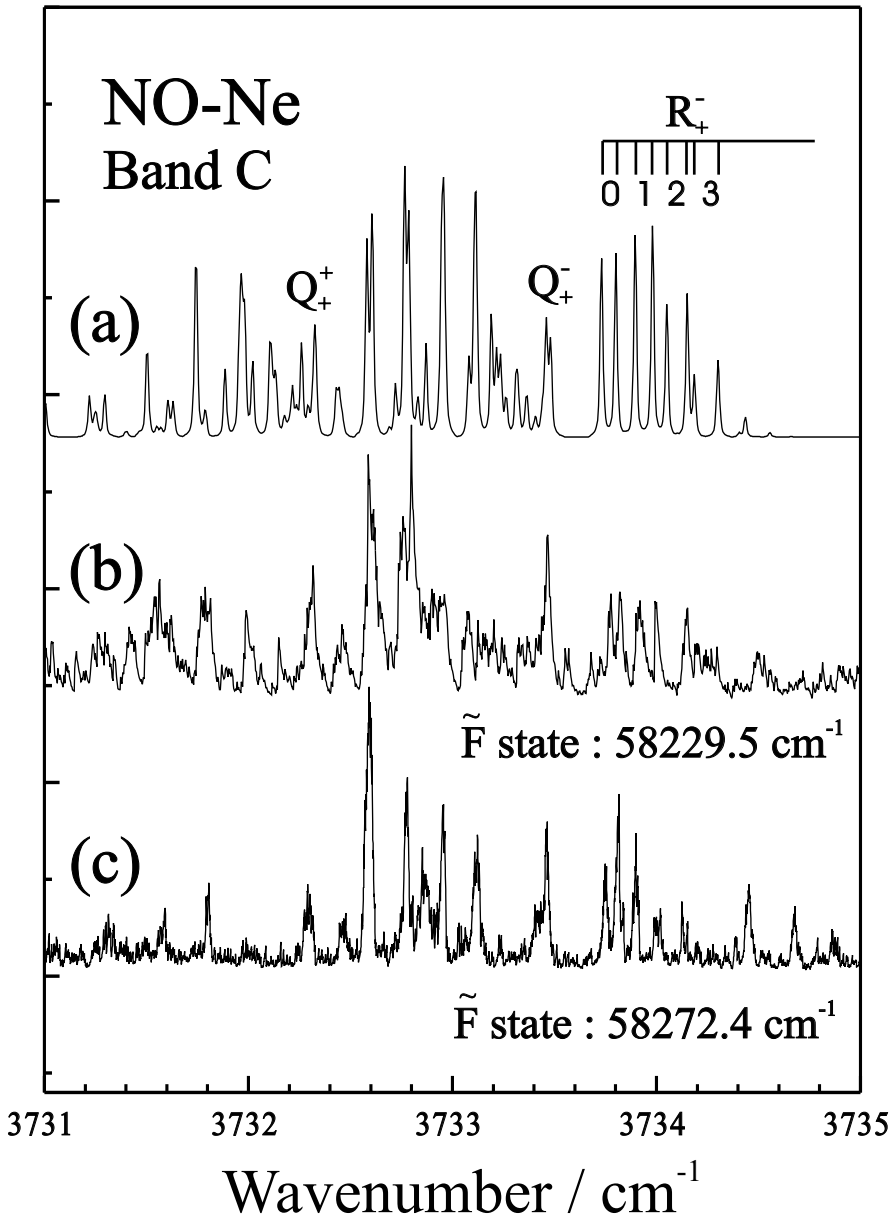

Figure 4.22: Comparison of observed and calculated spectra for band C. The UV laser is fixed to the indicated two-photon frequencies. Different rotational lines belonging to several branches are labeled with $(J - \frac{1}{2})$. The two parity components are indicated for the R_+^- branch. Rotational lines are labeled with $(J - \frac{1}{2})$.

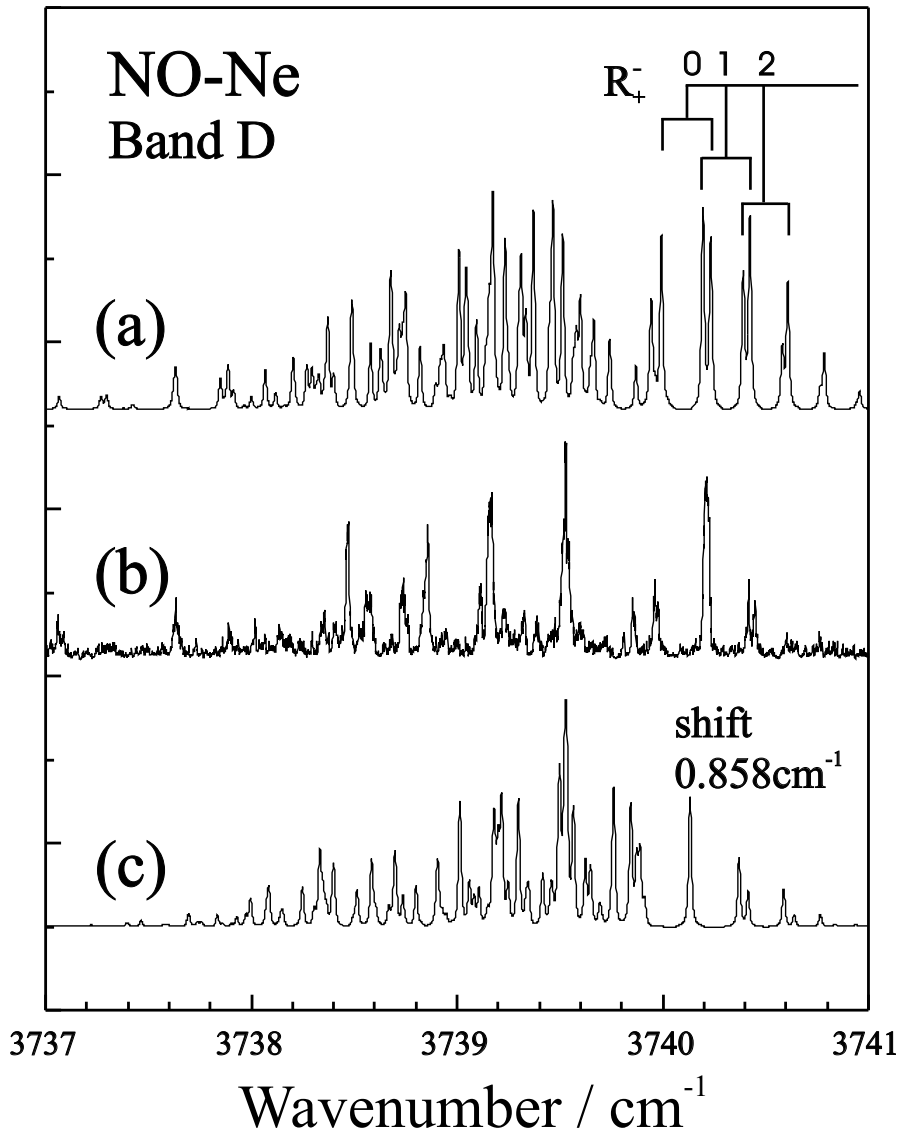

Figure 4.23: Comparison of observed and calculated spectra for band D. The UV laser is fixed to the indicated two-photon frequency corresponding to F-state detection. Different rotational lines belonging to several branches are labeled with $(J-\frac{1}{2})$. The two parity components are indicated for the R_+^- branch. Spectra (a) and (c) are calculated assuming a temperature of 1 K and for the linewidth a 0.01 cm^{-1} Lorentzian component and a 0.01 cm^{-1} Gaussian component. Rotational lines are labeled with $(J-\frac{1}{2})$.

with electronic orbital angular momentum projection $\lambda = \pm 1$. Excitation of the intermolecular stretching vibration will increase the average Jacobi distance R and, consequently, it will cause a decrease in the splitting. On the other hand, excitation of the bending vibration allows the Ne atom to approach the NO moiety more closely at intermediate Jacobi distances resulting in a more dramatic quenching of the angular momentum. For levels with $P = \frac{1}{2}$, the Coriolis coupling increases substantially with increasing vibrational excitation. This reflects the extreme floppiness of the NO-Ne complex.

4.2 NO-Ar system

As a benchmark system for the interaction of an open-shell diatom with a closed shell atom, the NO-Ar complex has been studied with the new IR-REMPI double resonance technique developed as part of this thesis. In the IR-REMPI double resonance experiment, the states $E\,^2\Sigma^+$, $F\,^2\Delta$, and $H'\,^2\Pi$ were used to detect the IR absorption through hot band spectra. To have a better understanding of the experiment, the different low lying Rydberg states of the complex are summarized in the first subsection. The second subsection contains the experimental results and analysis of the IR-REMPI double resonance experiment.

4.2.1 REMPI spectroscopy of NO-Ar

$\tilde{A}\,^2\Sigma^+ - \tilde{X}\,^2\Pi$ Transition

For the state $\tilde{A}\,^2\Sigma^+$ of NO-Ar, the origin band is located at 44242 cm^{-1} blue shifted by 43 cm^{-1}, suggesting that the interaction with the cationic core is weak. This behavior is understandable because the A-state of the monomer has a large quantum defect resulting in an expectation value for the radius of the Rydberg

orbital smaller than the van der Waals radius. The Rydberg electron resides in an orbital which screens effectively the charge of the NO^+ core. Due to the very weak bond, it is not possible to apply the rigid rotor model in describing the rovibrational structure for this system. Large amplitude bending motion will be coupled to the rotational motion of the complex. McQuaid *et al.* applied a hindered rotor model to assign several features in the spectrum to the excitation of different bending levels [62]. They concluded that the effective bending Hamiltonian is dominated by a V_{20} term while the V_{10} term is very small. But, the data were not sufficient to distinguish between a global minimum for the linear or the T-shaped geometry. Recently, Lozeille *et al.* employed the same hindered rotor model [128]. According to their analysis, the observed spectrum is a composite of at least two band systems: excitation to the vibrationless origin band and to the first intermolecular stretching level. Additional bands are assigned to the excitation of combination bands involving different bending levels. For the vibrational ground state of the $\tilde{A}$ state, a negative anisotropy term results in a linear configuration (see Section 3.3.1). In the first excited stretching level, the anisotropy is dominated by a positive V_{20}-term moving the global minimum of the $\tilde{A}$-state surface to the T-shaped geometry. The rotational structure should be regarded as an almost free rotation of the NO within the molecular plane or out of plane rotation representing a axis rotation.

$\tilde{C}\,^2\Pi - \tilde{X}\,^2\Pi$ Transition

As in the case of NO-Ne, bands systems correlating with the NO vibrational level ($v' = 0 - 4$) have been measured for NO-Ar. The vibrational structure is dominated by a progression in the stretching vibration. The blue satellites of the stretching progression are identified as partially resolved rotational structures. The weak progression in the bending vibration confirms the near T-shaped vibrationally

Table 4.10: Comparison of term values and spectroscopic constants (in cm^{-1}) for the vibrational bands of NO($\tilde{C}\,^2\Pi(v')$)-Ar with the corresponding monomer values. The second column refers to the position of the observed bands while the third and the fourth columns represent the term values after applying a first-order and a second-order deperturbation procedure, respectively. The frequency shift ($\Delta\nu$) with respect to the monomer value in the sixth enrtry is listed together with the term values for each cluster band in the fifth entry. ν_s denotes the stretching frequency.

$\tilde{C}(v')$	NO(0)[a]	NO(1)[a]	NO(2)[a]	NO-Ar	$\Delta\nu(1)$	ν_s
0	52373	52372	52380	52050[b]	-332	56
1	54690	54697	54742	54373[c]	-324	56
2	57081	56958	57108	56578[c]	-390	48
3	59208	59420	59378	59046[d]	-374	44
4	61732	61741	61677	61428[c]	-313	54

[a]Reference [106]
[b]Reference [66]
[c]Reference [122]
[d]Reference [72]

averaged structure. Figure 4.24 shows recorded spectra for the $\tilde{C}\,^2\Pi(v' = 1-4) - \tilde{X}\,^2\Pi$ transition of the NO-Ar complex. The origins of the individual band systems are aligned for comparison. Positions of the band systems are listed in Table 4.10 together with term values and spectroscopic constants.

The rotational analysis shows that the experimentally observed rotational A constant as compared to b_{NO} is slightly increased. This fact also indicates evidence for complexation-induced changes in the state mixing. As in the case of NO-Ne, the frequency shift of the band system and the observed vibrational frequencies for the bands with $v' = 0, 1$, and 4 are very similar. On the other hand, the bands associated with $v' = 2, 3$ are further redshifted.

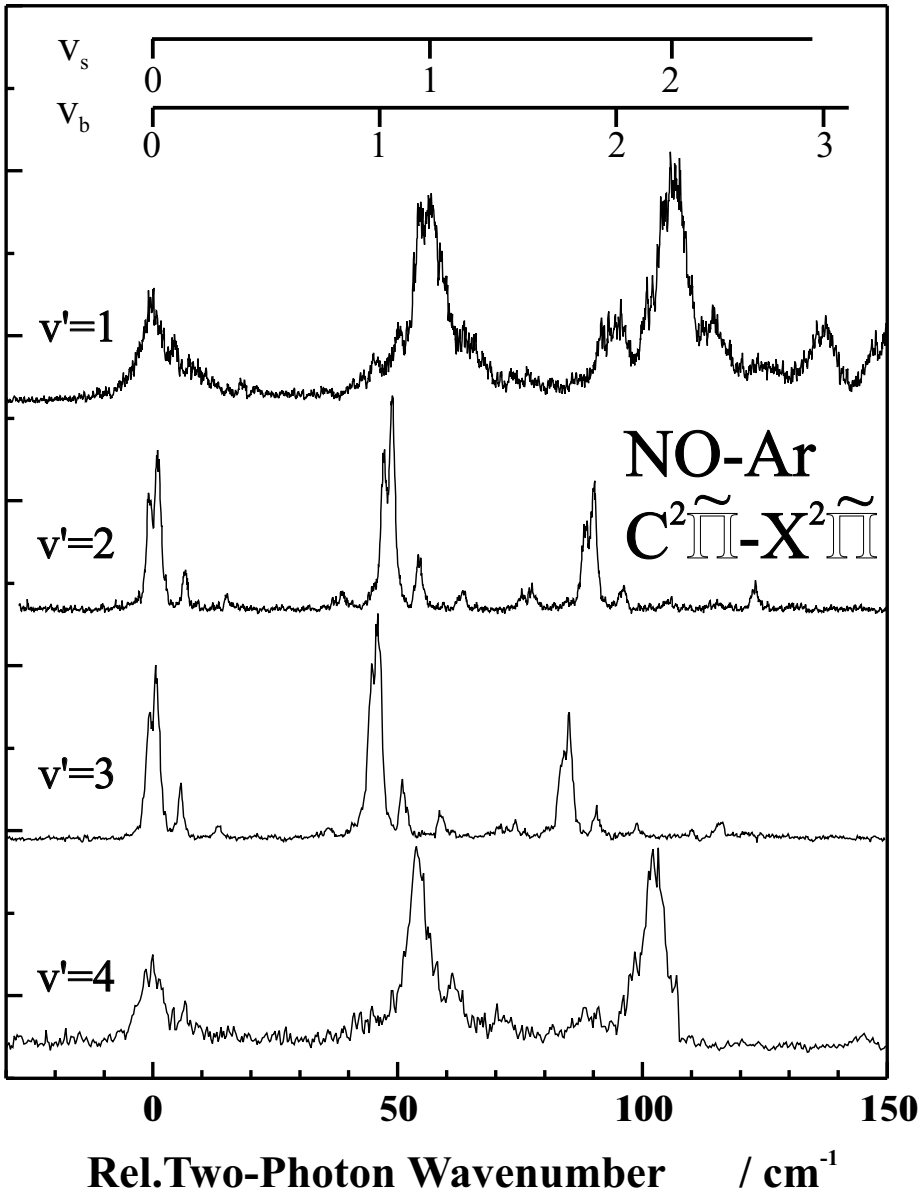

Figure 4.24: Spectra of the $\tilde{C}\,^2\Pi(v' = 1 - 4) - \tilde{X}$ transition in NO-Ar. The spectra recorded for $v' = 2$ and $v' = 3$ do not show any indication of lifetime broadening due to predissociation. Correct positions of the band systems are listed in Table 4.10.

Table 4.11: Comparison of term values (in cm^{-1}) for the vibrational bands of $NO(\tilde{C}\,^2\Pi(v')) - X$ with the values for the monomer state $B\,^2\Pi$. The term value of NO for the different vibrational levels of the B state obtained in a first-order deperturbation procedure is listed in the second column while the term value of NO-Ne for the different vibrational levels the $\tilde{C}$-state obtained experimentally is listed in the fourth column together with energy mismatch (ΔE) in the third column.

$B(v')$	NO(1)[a]	ΔE	NO-Ar	$\tilde{C}(v')$
6	51425	615	52040[b]	0
9	54203	170	54373[c]	1
11	55984	584	56578[c]	2
14	58564	482	59046[d]	3
17	61103	325	61428[c]	4

[a]Reference [106]
[b]Reference [66]
[c]Reference [122]
[d]Reference [72]

When the vibrational frequencies are compared, the observed stretching vibration frequencies are noticeably smaller for the vibrational levels v'=2 and v'=3 than for the levels $v' = 0, 1$ and 4 (46 cm^{-1} vs. 55 cm^{-1}). These reduced values of the stretching frequency suggest a decrease in the dissociation energy, contradicting the values derived from the increased red shifts. The data strongly support complexation-induced changes of the homogeneous interaction between the C- and the B-states of the NO moiety within the complex.

As can be seen in Fig. 4.24, unlike the NO-Ne complex the band system correlating with $NO(C\,^2\Pi(v' = 1))$-Ar exhibits considerable broadening due to predissociation [77]. Although the signal for this band is relatively weak, the intensity of the bands assigned to the bending vibration is significantly increased most

likely due to a weak coupling to the stretching coordinate. These findings have been confirmed by Tsuji *et al.* in their recent studies [68]. These authors suggest predissociation via a lower lying vibrational level of the $\tilde{B}$-state as the dominant mechanism. Because most of the $\tilde{C}$-state vibrational levels are heavily mixed, differences in the predissociation behavior are attributed to the difference in FC factors between bound state wavefunctions and the continuum state wavefunctions associated with the $\tilde{B}$-state. In Table 4.11, the term values for the different vibrational levels of the B-state obtained in a first order deperturbation procedure are listed [106]. The energy mismatch (ΔE) controlling the FC factor is given by the energy difference. For the $C\,^2\Pi$ state, ΔE is at a minimum for v'=1 indicating a rapid predissociation process. Along the same line of reasoning, it is expected that the (v'=4) level exhibits an increased predissociation rate. This is confirmed by the observed (v'=4) band which is broadened and shows diminished intensity. This behavior is quite different from the case for NO-Ne. For NO-Ne, in Table 4.2 the smallest value for the energy mismatch is found for the level $\tilde{C}\,^2\Pi(v'=2)$ which is almost resonant with the B-state level $v'=12$. But, Figure 4.1 does not show any evidence for the predissociation behavior. The strong effects for the state mixing in these levels upon complexation are expected for NO-Ne.

$\tilde{D}\,^2\Sigma^+ - \tilde{X}\,^2\Pi$ Transition

The $\tilde{D}\,^2\Sigma^+ - \tilde{X}\,^2\Pi$ spectra for NO-Ar were reported by Miller and Cheng [66] and Tsuji *et al.* [68]. The spectra are dominated by a long progression in the stretching vibration. Although the observed vibrational frequency (68.7 cm^{-1}) is very similar to the one found for the stretching vibration of the $\tilde{C}$-state (60 cm^{-1}), the dissociation energy deduced from the observed red shift is increased by more than a factor of two. It is interesting to note that the binding energy of 1044 cm^{-1} for

the NO($\tilde{D}(v'=0)$)-Ar state is surprisingly large, even larger than the D_0 value of NO^+-Ar (940 cm^{-1}). In this respect, the system in the $\tilde{D}$-state closely resembles the strongly bound cation whose stretching frequency (94 cm^{-1}) is substantially larger than the one found for the $\tilde{C}$-state (60 cm^{-1}) and the $\tilde{D}$-state (69 cm^{-1}). On the other hand, the expectation values for the radius of the Rydberg orbitals in the two states are very similar (3.38Å vs. 3.53Å) [129]. Consequently, one would expect similar Rydberg behavior for the interaction in these states.

$\tilde{F}\,^2\Delta,\ \tilde{H}\,^2\Sigma^+,\ \tilde{H}'\,^2\Pi - \tilde{X}\,^2\Pi$ Transition

The overview spectrum of NO-Ar at 320 nm region is shown in Fig. 4.2 on page 164. Band systems involving the $\tilde{F}$-state and the $\tilde{H}$-state are observed to be shifted to the red. The $\tilde{H}$-state is shifted so far to the red that it overlaps the band system of the $\tilde{F}$-state resulting in a complicated rovibronic structure. In comparison with the one-color REMPI spectrum (Fig. 4.25(c)) the IR-REMPI experiment shows a possibility to analyze the $\tilde{H}'$-state spectrum. Parts (a) and (b) are IR-REMPI double resonance spectra. Part (b) is recorded with the IR frequency fixed to a frequency for the first overtone without any intermolecular vibration $(v_s, v_b) = (0, 0)$ while part (a) is recorded with the IR laser tuned to the transition to the first intermolecular bending level $(v_s, v_b) = (0, 1)$. For comparison, spectrum (a) is shifted to the blue by 15 cm^{-1}. Spectrum (a) shows only strong lines in the region of the $\tilde{F}$-state while part (b) is almost identical to part (c) except that spectrum (c) is shifted to lower frequency by 3724 cm^{-1}. As a possible explanation, the FC factor for excitation to the $\tilde{H}$-state from the first bending level is thought to be very small, consistent with the assumption that the excited state has a near T-shaped configuration similar to the ground state configuration. On the other hand, as shown in part (a), the transition to the $\tilde{F}$-state is allowed if the following

assumption is made: This state strongly deviates from the T-shaped geometry so that the FC factor with the first excited bending wavefunction of the ground state does not vanish. If this explanation is correct, the missing lines of part (a), as compared to parts (b) and (c), can be assigned to the progression in the stretching vibration of the $\tilde{H}$-state located at 61940 cm^{-1} [72]. With this assumption, the $\tilde{H}$-state structure looks very similar to the one found for NO-Ne. The different stretching vibrational bands do not show a resolved rotational structure consistent with a zeroth rank tensor component carrying the two-photon transition. From the vibrational analysis, ω_e=80 cm^{-1}, $\chi_e\omega_e$=2 cm^{-1} are found. Assuming a Morse potential, these data give a dissociation energy consistent with the value of D'=867 cm^{-1} derived from the red shift of the band system. In both (b) and (c), the first three members of the progression are sharp and the intensity increases dramatically with increasing vibrational excitation reflecting the increase in FC factor. But, the intensities of the higher members are very weak and broadened due to the predissociation. The most probable mechanism is dissociation to the continuum of the $\tilde{F}$-state. A possible schematic view of the potential of those states is shown in Fig. 4.26. The $\tilde{H}$-state potential lies 273 cm^{-1} higher than the one for the $\tilde{F}$-state which has a binding energy of 465 cm^{-1}. Using the derived spectroscopic constants and in the absence of a barrier, dissociation becomes possible for stretching levels $\tilde{H}(v' \geq 3)$. This line of reasoning agrees with the experimental observation. As the IR-REMPI spectrum suggests, if the $\tilde{F}$-state has a vibrationally averaged structure which deviates considerably from the T-shaped geometry, intense transitions to excited bending levels are anticipated. In this case, the hindered rotor model is more appropriate [123].

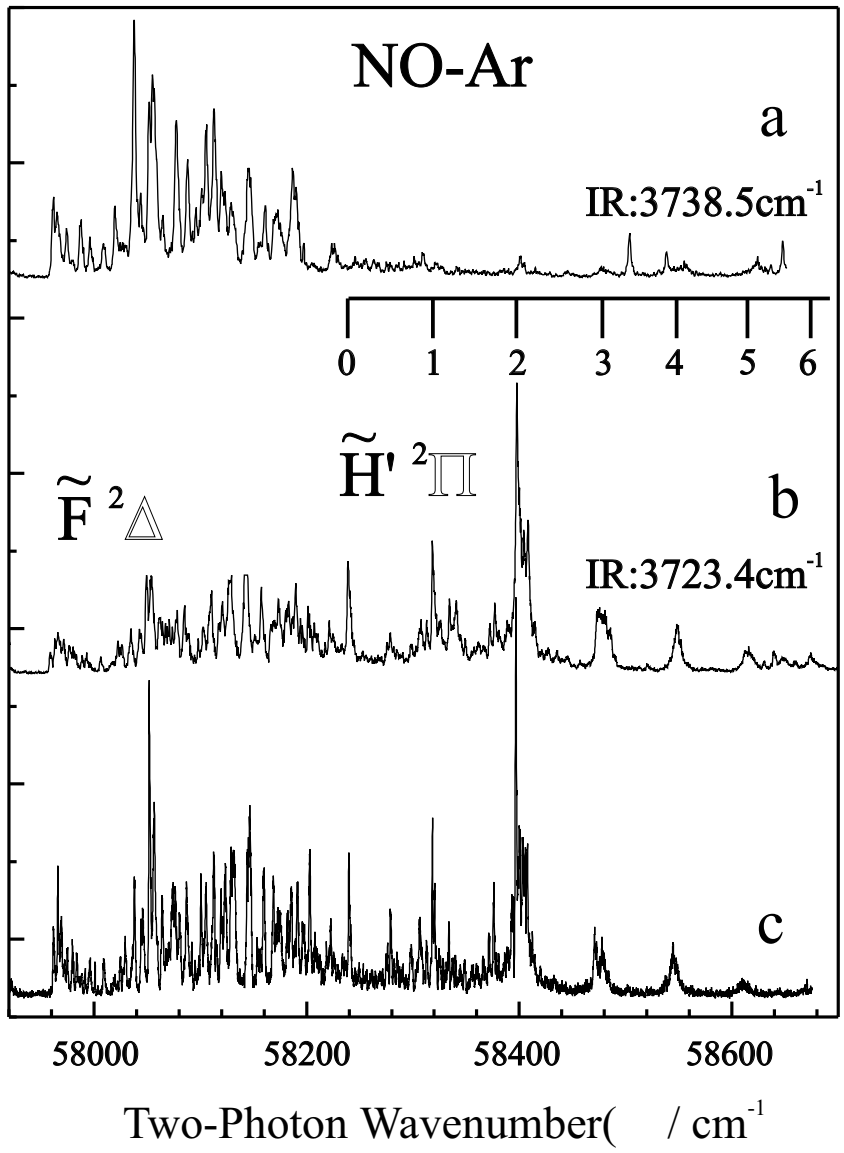

Figure 4.25: (2+1) REMPI spectra of the $\tilde{F} - \tilde{X}$ and $\tilde{H} - \tilde{X}$ transitions in NO($v'' = 2$)-Ar. Part (c) represents the one-color REMPI spectrum for NO($v'' = 2$)-Ar shifted by 3724 cm^{-1}. The top two spectra are IR-REMPI double resonance spectra recorded at the indicated IR frequencies. Spectrum (a) is shifted to the blue by the amount of 15 cm^{-1} for comparison.

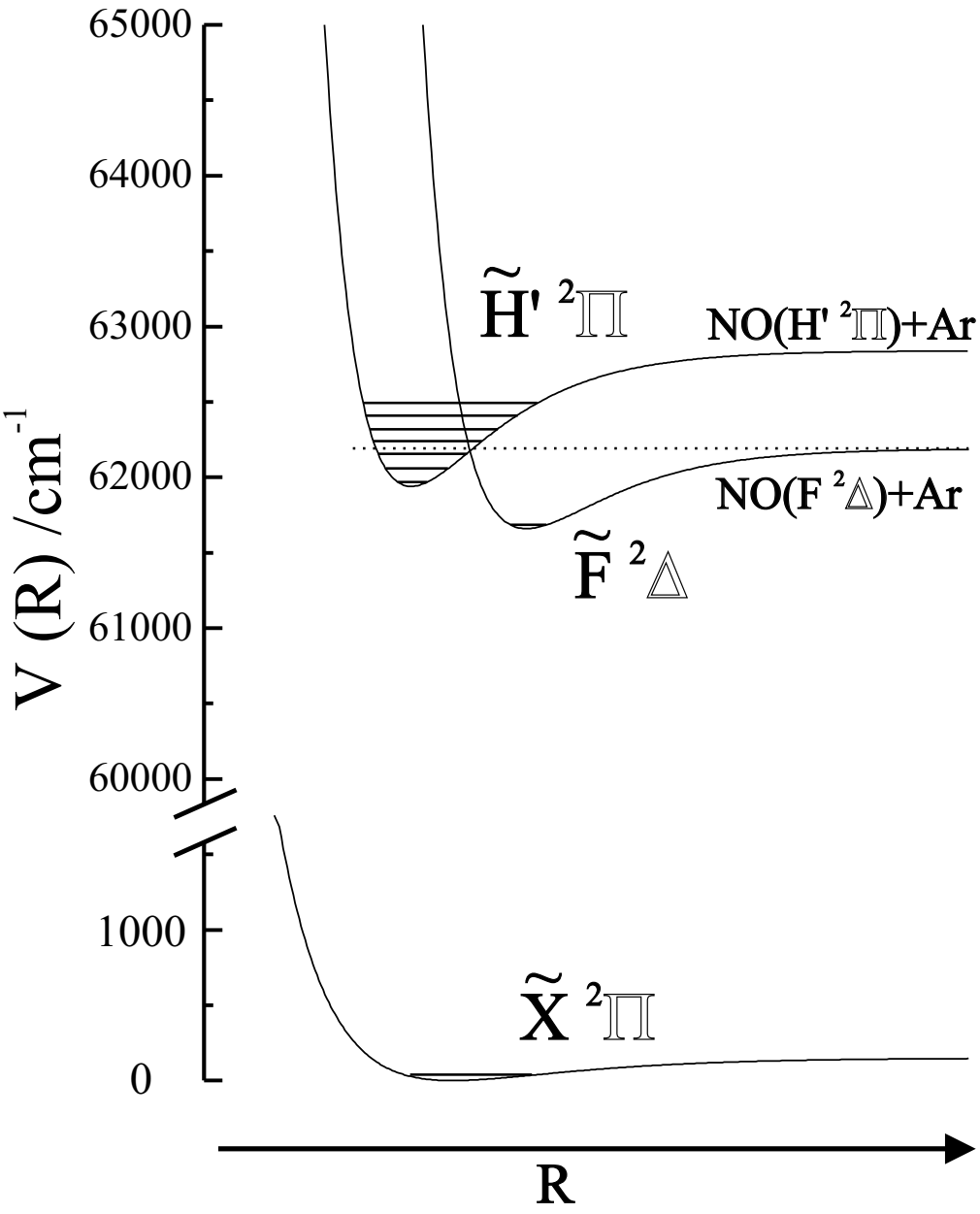

Figure 4.26: Schematic of the potential energy curves and vibrational levels for the states $\tilde{F}$ and $\tilde{H}$ for the NO-Ar complex.

$\tilde{E}\,^2\Sigma^+ - \tilde{X}\,^2\Pi$ Transition

In the NO monomer, the rotational structure of the two-photon $\tilde{E} - \tilde{X}$ transition is determined by a single tensor component $T^{(2)}_{-1}$ [49]. The comparison of the rotational contour with the experimental spectrum suggests that the Jacobi angle θ deviates from a perfect T-shaped structure by about 25° in either direction [122]. The experimental spectrum is dominated by the stretching vibration with a frequency of 86.4 cm^{-1}. This value is very similar to the one found for the cationic complex [130]. Significant deviation from the T-shaped structure of the complex allows the substantial increase in the FC factor, resulting in a relatively strong bending progression and even combination bands. The frequency of the bending mode is about 54 cm^{-1}. From the red shift, the dissociation energy is derived as 578.5 cm^{-1} considerably smaller than that of cationic complex. As pointed out for NO-Ne, the $\tilde{E}$-state is derived from the $4s$ orbital which allows for some electron density in the core region, thus effectively shielding the nuclear charge. In summary, the interaction in these Rydberg states is very sensitive to the spatial orientation of the orbital as well as its spatial extent.

4.2.2 Infrared-Ultraviolet spectroscopy of NO-Ar

Experimental Results

The experimental procedure to find the first overtone transition of NO-Ar is similar to the procedure applied for NO-Ne. A depletion signal for NO-Ar was found by fixing the UV laser to the second feature of $\tilde{C}\,^2\Pi(v' = 2) - \tilde{X},\ (v_s, v_b) = (1, 0)$ in Fig. 4.24 and scanning the IR laser over the wavelength region of the first overtone. As can be seen in Fig. 2.29, a depletion of 20% is found at a frequency of 3723.4 cm^{-1}. And a weaker signal is identified at 3727.2 cm^{-1}. The cluster

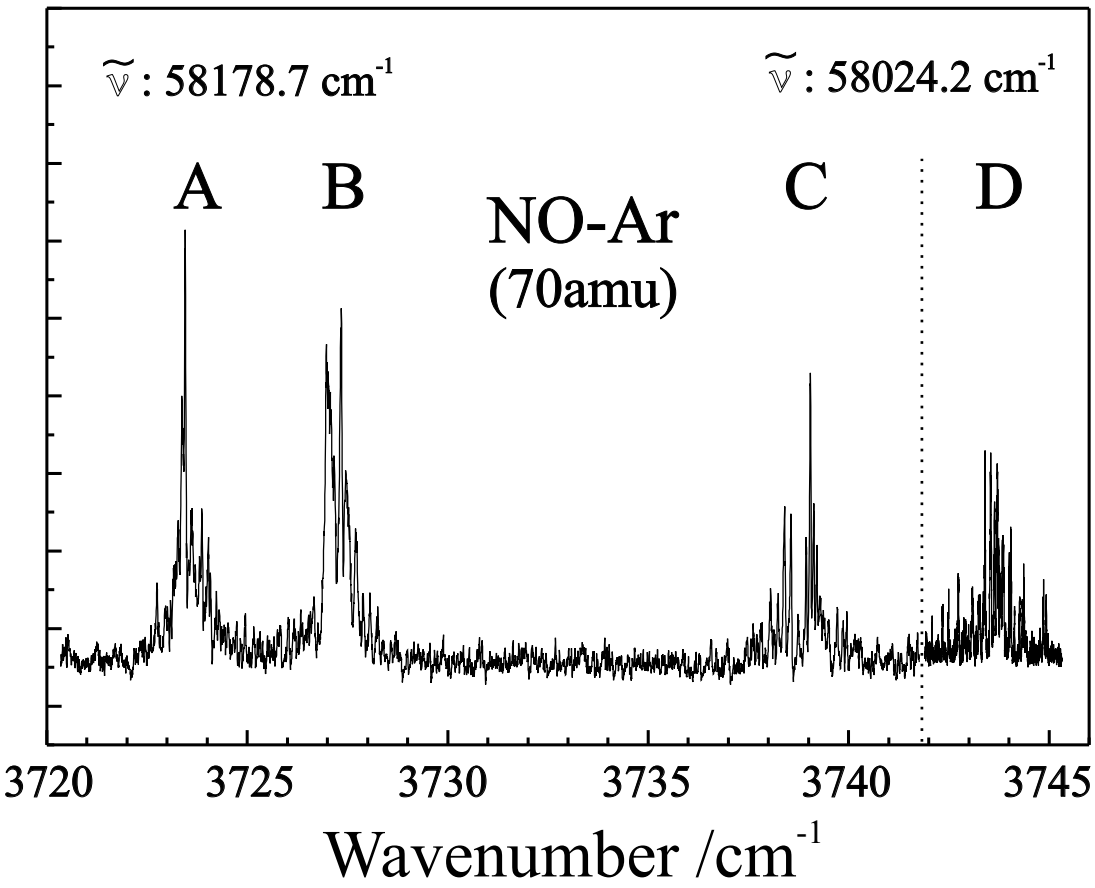

Figure 4.27: IR overview spectra of the NO-Ar complex are labeled A, B, C, and D in order of increasing frequency. Bands A, B, and C are recorded at the two-photon frequency of 58178.7 cm^{-1} while band D is recorded at 58024.2 cm^{-1}.

band is red-shifted about 0.45 cm^{-1}, which indicates that the binding energy for the vibrationally excited complex is increased by this amount and that the NO stretching vibration remains unchanged upon complexation. To confirm the double resonance, the IR laser frequency is stabilized on this frequency and the UV laser is scanned. Figure 2.30 shows the resulting IR-REMPI double resonance spectrum in the region of the hot band $\tilde{E} - \tilde{X}$ transition. The bottom part shows the one color (2+1) REMPI spectrum of the $\tilde{E} - \tilde{X}$ transition. It is shifted by the amount of IR photon frequency to match the spectrum with the top part. As can be seen

in Fig. 2.31, the intensity of a band system is very sensitive to the UV frequency probed even though the position of a band system is reproducible. As shown in Fig. 4.27, four band systems, labeled as A, B, C, and D in order of increasing frequency, are detected. They are located at 3723.4 cm^{-1}, 3727.2 cm^{-1}, 3738.5 cm^{-1}, and 3743.4 cm^{-1}, respectively. Bands A, B, and C, are measured with the UV frequency fixed to the two-photon frequency 58178.7 cm^{-1} whereas band D is measured with the UV laser fixed to the frequency corresponding to 58178.7 cm^{-1}.

Analysis

While the experiment was being performed, Alexander independently performed the bound state calculations based on a CCSD(T) PESs [45, 46]. Band A, which is the vibrationless band of the first overtone transition, is well reproduced [12] by the simple rigid-rotor model of Howard and co-workers [19]. On the other hand, it was not possible to reproduce satisfactorily the spectrum of band B with this rigid-rotor model [12]. Therefore, a joint theoretical-experimental investigation was performed between two groups [13]. This section will describe the results of the joint studies.

Figure 4.28 shows adiabatic potentials for the NO-Ar complex based on the CCSD(T) PES's [13, 46]. The curves appear in closely spaced pairs, indicating two curves of different signs of $P \times \omega$ similar to the case of the NO-Ne complex. Examination of the adiabatic wavefunctions shows that in the well region the eigenfunctions are dominated by signed $P \times \omega$ states. Figure 4.28 displays the identification of the lowest adiabatic bender (AB) states listed in the column of AB calculation of Table 4.12. Since for NO-Ar the minimum in the potential energy surface occurs at a near T-shaped geometry, the AB potential with positive and negative values of $P \times \omega$ lie very close in energy as seen in Fig. 4.28. On the other hand, two minima in the PES occur at the linear geometry with substantial differences in the OH-Ar and HO-Ar

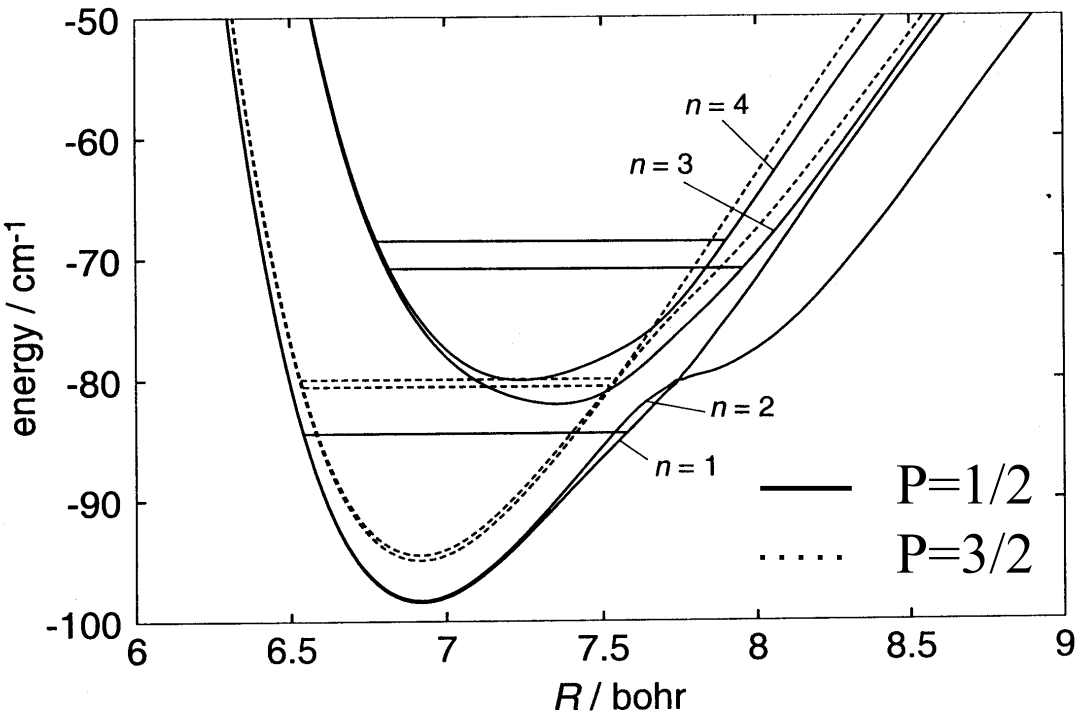

Figure 4.28: Adiabatic bender potential curves for the NO-Ar complex. The figure is excerpted from Ref.[13] The solid and dashed curves correspond to $P = \frac{1}{2}$ and $P = \frac{3}{2}$, respectively. n labels the AB states. The position of the lowest vibrational level in each AB potential is shown by a horizontal line

well depth. In this case, the states with $P \times \omega$ positive and $P \times \omega$ negative differ significantly in energy [11].

The contour plots of the probability densities calculated by Alexander are displayed in Figs. 4.29−4.33. Figure 4.29 presents the probability distributions of the lowest two states with $P = \frac{1}{2}$ (labeled as n=1,2). The solid curve corresponds to the n=1 state and the dashed line represents the n=2 state. These two states are compact and nodeless indicating $(v_s, v_b) = (0, 0)$. Figure 4.30 shows the probability distribution of the lowest two states ($n = 1, 2$) with $P = \frac{3}{2}$. The wavefunctions

Table 4.12: Relative energies (in cm^{-1}) of the lowest bound states of the NO-Ar complex [15].

J	P	n^d	v_s^e	CC[a]		CD[b]	AB[c]	Figure	Band[g]	Data Table
				$\eta^f = +1$	$\eta = -1$					
1/2	1/2	1	0	0	0.021	0	0	4.29	A	4.13
		2	0	0.217	0.192	0.193	0.003			
		3	0	13.77	13.77	13.78	13.56	4.31	C	4.15
		4	0	14.94	14.94	14.93	15.79			
		1	1	19.78	19.58	19.65	19.95	4.33	D	
		2	1	19.98	20.12	20.00	23.12			
3/2	1/2	1	0	0.211	0.177	0.211	0.209			
		2	0	0.415	0.454	0.404	0.215			
		3	0	13.95	13.94	13.97	13.76			
		4	0	15.14	15.15	15.12	15.99			
		1	1	19.62	19.90	19.84	20.15			
		2	1	20.53	20.14	20.21	22.65			
	3/2	1	0	3.72	3.72	3.72	4.02	4.30	B	4.14
		2	0	4.16	4.16	4.14	4.18			
		3	0	20.73	20.68	20.59	20.35	4.32	D	
		4	0	21.24	21.24	21.20	22.16			

[a]Close-coupled calculations.
[b]Centrifugal-decoupled calculations.
[c]Adiabatic-bender calculations.
[d]Adiabatic-bender state index.
[e]Nominal stretching quantum number: equal to the number of node in the vibrational wavefunction (see Figs. 4.29−4.33).
[f]Parity. $\eta = \zeta(-)^{J-1/2}$.
[g]Bands A, B, C, and D correspond to the transition from the lowest state to the indicated states.

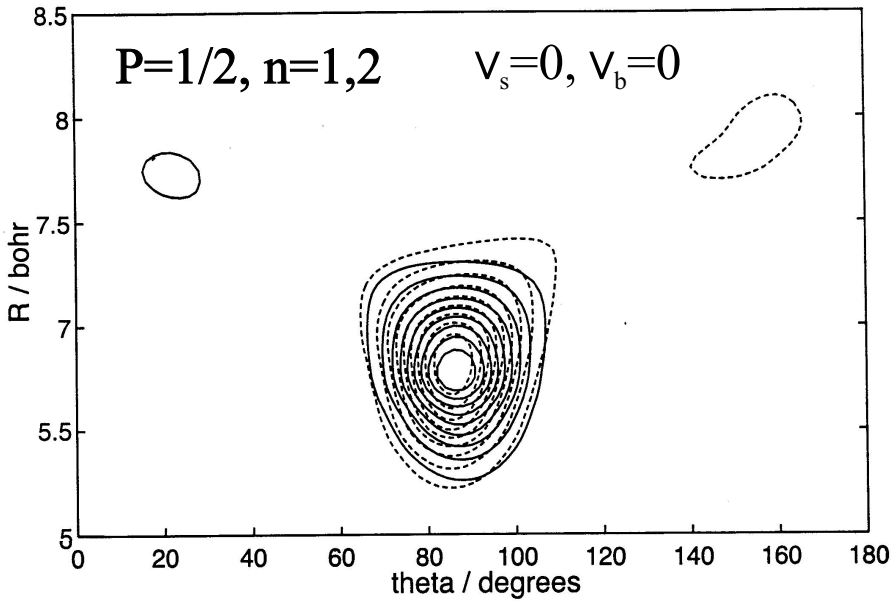

Figure 4.29: Plot of the distribution function describing the probability of finding the Ar atom at the Jacobi coordinates (R, θ) for the $P = \frac{1}{2}$ states of the NO-Ar complex excerpted from Ref. [13]. The solid curves represent probabilities for the $n = 1$ state while the dashed curves refer to those for the $n = 2$ state. The wavefunctions are nodeless, representing a vibrationless state. Results are from the calculation based on the CCSD(T) PES's.

have one node at 90° indicating that one bending quantum is excited. Figure 4.31 shows the probability distributions of the next two states (n=3,4) with $P = \frac{1}{2}$. The wavefunctions have a node in the angular degree of freedom corresponding to the excitation of one bending quantum.

Because it was possible to reproduce the *ab initio* spectra for NO-Ne with the heuristic Hamiltonian, a similar Hamiltonian is applied to generate spectra for NO-Ar. The next two states ($n = 3, 4$) with $P = \frac{3}{2}$, displayed in Fig. 4.32, have two nodes in the angular degree of freedom indicating two quanta of excitation in the bending mode. Finally, the probability distribution for the fifth and sixth $P = \frac{1}{2}$ states are shown in Fig. 4.33. As listed in Table 4.12, these states correspond

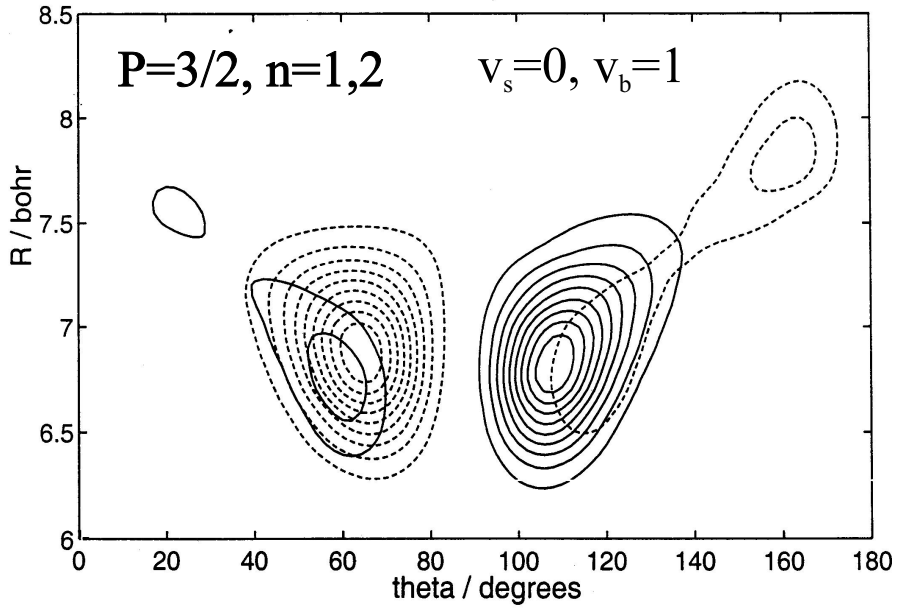

Figure 4.30: Plot of the distribution function describing the probability of finding the Ar atom at the Jacobi coordinates (R, θ) for the $P = \frac{3}{2}$ states of the NO-Ar complex excerpted from Ref. [13]. The solid curves represent probabilities for the $n = 1$ state while the dashed curves refer to those for the $n = 2$ state. The wavefunctions have one node in angle θ representing that one quantum of bending vibration is excited. Results are from calculation based on the CCSD(T) PES's.

to the first vibrationally excited ($v_s = 1$) state of the adiabatic bender potential ($P = \frac{1}{2}, n = 1, 2$). The probability distribution shows clear evidence of a radial node in the stretching coordinate and two angular nodes in the bending coordinate. Using the energy levels provided by Alexander (Tables 4.13−4.15) [132], spectroscopic constants are determined in a least squares fit. The results are listed in Table 4.17 and are plotted in Figs. 4.34−4.36. Table 4.16 shows the centrifugal decoupling (CD) results for the lowest three levels. In the CD approximation, Coriolis coupling is neglected so that the only levels with different ω values are listed. Most energy levels are reproduced within 0.01 cm^{-1}. Slightly larger deviations occur for several levels with $J = \frac{1}{2}$. The main contribution to the energy is given by the rotational

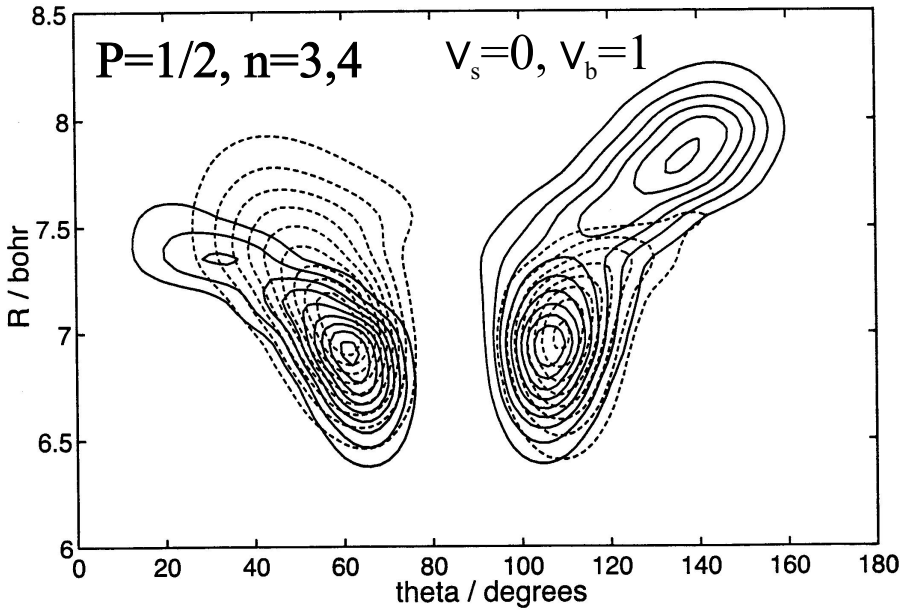

Figure 4.31: Plot of the distribution function describing the probability of finding the Ar atome at the Jacobi coordinates (R, θ) for the $P = \frac{1}{2}$ states of the NO-Ar complex excerpted from Ref. [13]. The solid curves represent probabilities for the $n = 3$ state while the dashed curves refer to those for the $n = 4$ state. The wavefunctions have one node in angle θ representing that one quantum of bending vibration is excited. Results are from calculation based on the CCSD(T) PES's.

energy which is displayed in Fig. 4.34. In comparison to NO-Ne, no centrifugal distortion is observed. Figure 4.35 displays the ω-splitting of rotational levels for the ground vibrational state of NO-Ar as function of J. Within the CD approximation, the splitting is independent of J, which is consistent with the result of first-order perturbation theory. However, the full calculation yields a pronounced linear J-dependence of the splitting. From the difference between the CD calculation and the full calculation, it is clear that the J-dependence in the ω-splitting originates from Coriolis coupling. This deduction is confirmed by the analysis of the rotational levels for the bending states corresponding to $P = \frac{3}{2}$ as shown in Fig. 4.36. Since

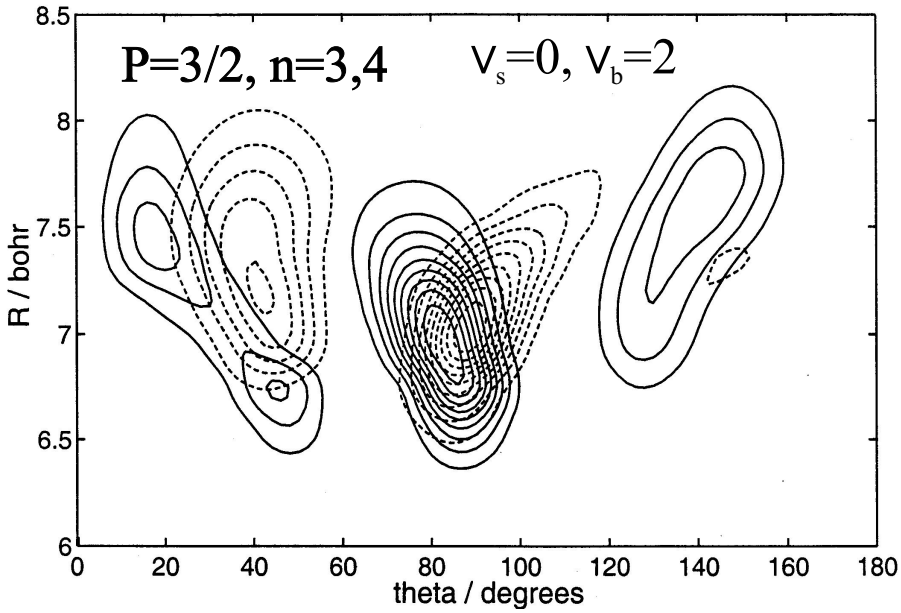

Figure 4.32: Plot of the distribution function describing the probability of finding the Ar atom at the Jacobi coordinates $(R, \theta)$for the $P = \frac{3}{2}$ states of the NO-Ar complex excerpted from Ref. [13]. The solid curve represents probabilities for the $n = 3$ state while the dashed curve refers to those for the $n = 4$ state. The wavefunctions have two nodes in angle θ representing that two quanta of bending vibration is excited. Results are from calculation based on the CCSD(T) PES's.

for these states Coriolis coupling can only contribute in higher order, the ω-splitting is nearly constant.

Figure 4.37 shows an experimental spectrum (part (a)) and several simulated spectra ((b)−(d)). Part (a) corresponds to the experimental spectrum. Parts (c) and (d) show calculated spectra using the line strength for a parallel transition and a perpendicular transition, respectively. Part (b) is calculated assuming an equal mixture of parallel and perpendicular transition moments in order to achieve better agreement with the experimental spectrum (see Eq. (3.291)). The spectra are dominated by two Q-branches (Q_-^- and Q_+^+) which are split due to the constant term of the P-type doubling. The R_+^- branch shows a J-dependent P-type doubling. At

Table 4.13: Relative position of the $P = \frac{1}{2}, n = 1, 2$ levels as a function of J (in cm^{-1}). Results are from the calculation based on the CCSD(T) PES's by Alexander [132].

$P = 1/2$, $v_s = 0$, $v_b = 0$

J	η^a=+1		η=-1	
	$\omega = +\frac{1}{2}$	$\omega = -\frac{1}{2}$	$\omega = +\frac{1}{2}$	$\omega = -\frac{1}{2}$
1/2	0	0.217	0.021	0.192
3/2	0.211	0.415	0.177	0.454
5/2	0.486	0.834	0.525	0.786
7/2	0.972	1.301	0.931	1.354
9/2	1.512	2.011	1.554	1.955
11/2	2.271	2.747	2.230	2.805
13/2	3.085	3.736	3.125	3.675
15/2	4.116	4.740	4.077	4.802
17/2	5.205	6.004	5.243	5.940
19/2	6.507	7.274	6.470	7.340

[a]Parity. $\eta = \zeta(-)^{J-1/2}$.

Table 4.14: Relative position of the $P = \frac{3}{2}, n = 1, 2$ levels as a function of J (in cm^{-1}). Results are from calculation based on the CCSD(T) PES's by Alexander [132].

$P = 3/2$, $v_s = 0$, $v_b = 1$

J	η^a=+1		η=-1	
	$\omega = +\frac{1}{2}$	$\omega = -\frac{1}{2}$	$\omega = +\frac{1}{2}$	$\omega = -\frac{1}{2}$
3/2	3.719	4.161	3.719	4.161
5/2	4.064	4.506	4.064	4.506
7/2	4.546	4.990	4.547	4.989
9/2	5.168	5.610	5.167	5.611
11/2	5.924	6.370	5.927	6.368
13/2	6.824	7.263	6.819	7.267
15/2	7.851	8.301	7.858	8.296
17/2	9.029	9.465	9.019	9.472
19/2	10.324	10.780	10.336	10.770

[a]Parity. $\eta = \zeta(-)^{J-1/2}$.

Table 4.15: Relative position of the $P = \frac{1}{2}, n = 3, 4$ levels as a function of J (in cm^{-1}). Results are from calculation based on the CCSD(T) PES's by Alexander [132].

$P = 1/2$, $v_s = 1$, $v_b = 0$

J	η^a=+1		η=-1	
	$\omega = +\frac{1}{2}$	$\omega = -\frac{1}{2}$	$\omega = +\frac{1}{2}$	$\omega = -\frac{1}{2}$
1/2	13.769	14.942	13.771	14.940
3/2	13.948	15.142	13.943	15.145
5/2	14.235	15.482	14.242	15.479
7/2	14.655	15.949	14.646	15.952
9/2	15.176	16.552	15.186	16.551
11/2	15.838	17.284	15.827	17.281
13/2	16.599	18.137	16.610	18.144
15/2	17.503	19.132	17.493	19.118

[a]Parity. $\eta = \zeta(-)^{J-1/2}$.

Table 4.16: Centrifugal decoupling results (in cm^{-1}) for $P = \frac{1}{2}, n = 1, 2$,$P = \frac{3}{2}, n =$, 2, and $P = \frac{1}{2}, n = 3, 4$ level. Results are from calculation based on the CCSD(T) PES's by Alexander [132]. In the CD approximation, Coriolis coupling is neglected so that the only levels with different ω values are listed.

J_{tot}	$P = 1/2$		$P = 3/2$		$P = 1/2$	
	$v_s = 0, v_b = 0$		$v_s = 0, v_b = 1$		$v_s = 1, v_b = 0$	
1/2	0	0.193	-	-	13.781	14.934
3/2	0.211	0.404	3.717	4.137	13.970	15.118
5/2	0.562	0.755	4.069	4.489	14.285	15.424
7/2	1.053	1.246	4.562	4.981	14.726	15.853
9/2	1.684	1.878	5.195	5.615	15.293	16.404
11/2	2.456	2.650	5.969	6.388	15.984	17.075
13/2	3.366	3.561	6.883	7.301	16.801	17.868
15/2	4.416	4.612	7.936	8.354	17.743	18.781
17/2	5.605	5.801	9.129	9.547	18.809	19.813
19/2	6.932	7.129	10.461	10.878	19.999	20.963
21/2	8.398	8.595	11.932	12.347	21.313	22.230

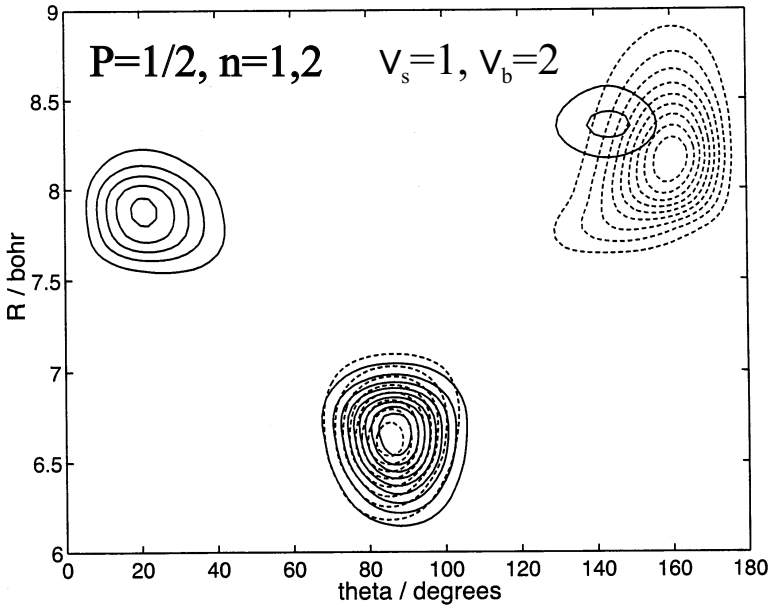

Figure 4.33: Plot of the distribution function describing the probability of finding the Ar atom at the Jacobi coordinates (R, θ) for the $P = \frac{1}{2}$ states of the NO-Ar complex excerpted from Ref. [13] with one quantum of the stretching vibration excited. The solid curve represents probabilities for the $n = 1$ state while the dashed curve refers to those for the $n = 2$ state. The wavefunctions have two nodes in angle θ representing that two quanta of bending vibration is excited, with $v_s = 1$. Results are from calculation based on the CCSD(T) PES's.

the low molecular beam temperature of about 1 K, mainly the lower ω-component is populated resulting in weak branches for transitions originating from the upper ω-component. Figure 4.38 shows the comparison of the experimental spectrum with calculated spectra based on the fit to the experimental spectrum and the fit to the *ab initio* energy levels. The overall agreement is excellent although a careful examination reveals a slightly larger value for the P-type doubling constant.

Band B involves the transition to the state $P = \frac{3}{2}, n = 1, 2$ which has one quantum of bending vibrational excitation as shown in Fig. 4.30. No P-type doubling is observed as expected for this perpendicular transition. The associated vibra-

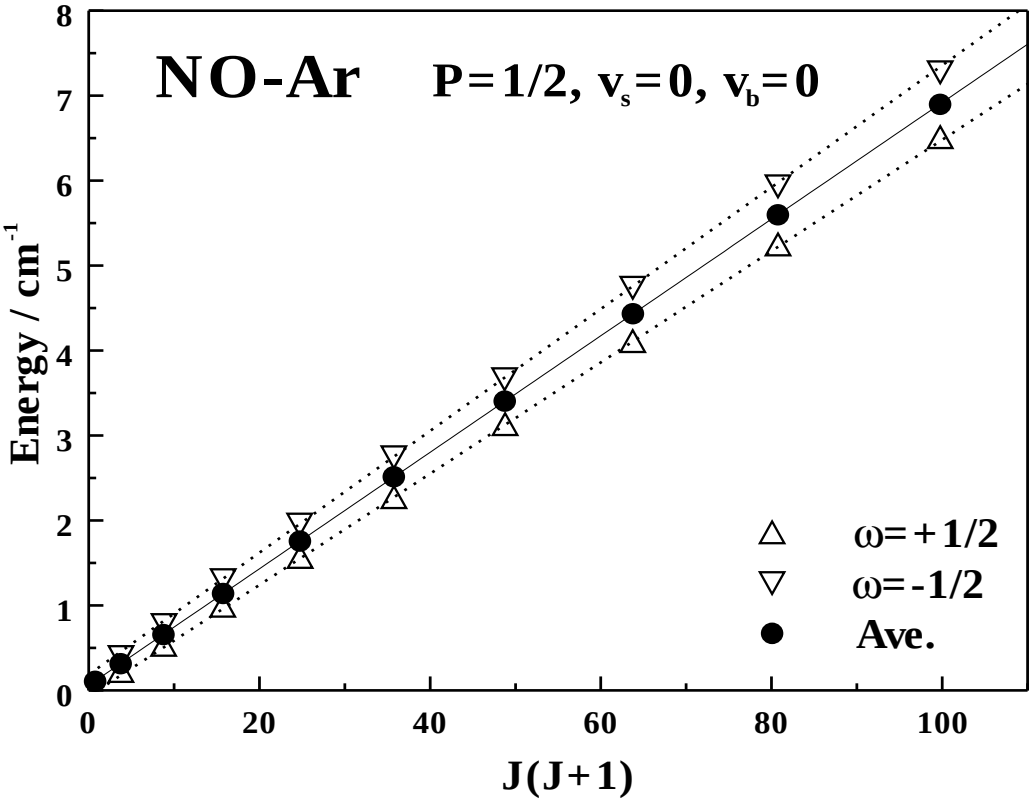

Figure 4.34: Bound state energies for the vibrational ground state of the NO-Ar complex as a function of $J(J+1)$. The open triangles represent the energy averaged over the two P-type components for $\omega = \pm\frac{1}{2}$. The solid circles represent the rotational energy.

tional energy $b_{NO}(\Delta P)^2$ is predicted by the *ab initio* calculation within 0.1 cm^{-1}. The fitted constants show that in the *ab initio* calculation the constants B and V_0 are slightly overestimated. Since the rotational constant reflects the vibrationally averaged structure, a decrease in the rotational constant can result from a change towards a more T-shaped configuration or from a lengthening of the intermolecular distance. The former effect is also consistent with the smaller value found for the ω-splitting constant.

For the parallel band C, again better agreement in the intensity distribution is found if an equal mixture of parallel and perpendicular components for the trans-

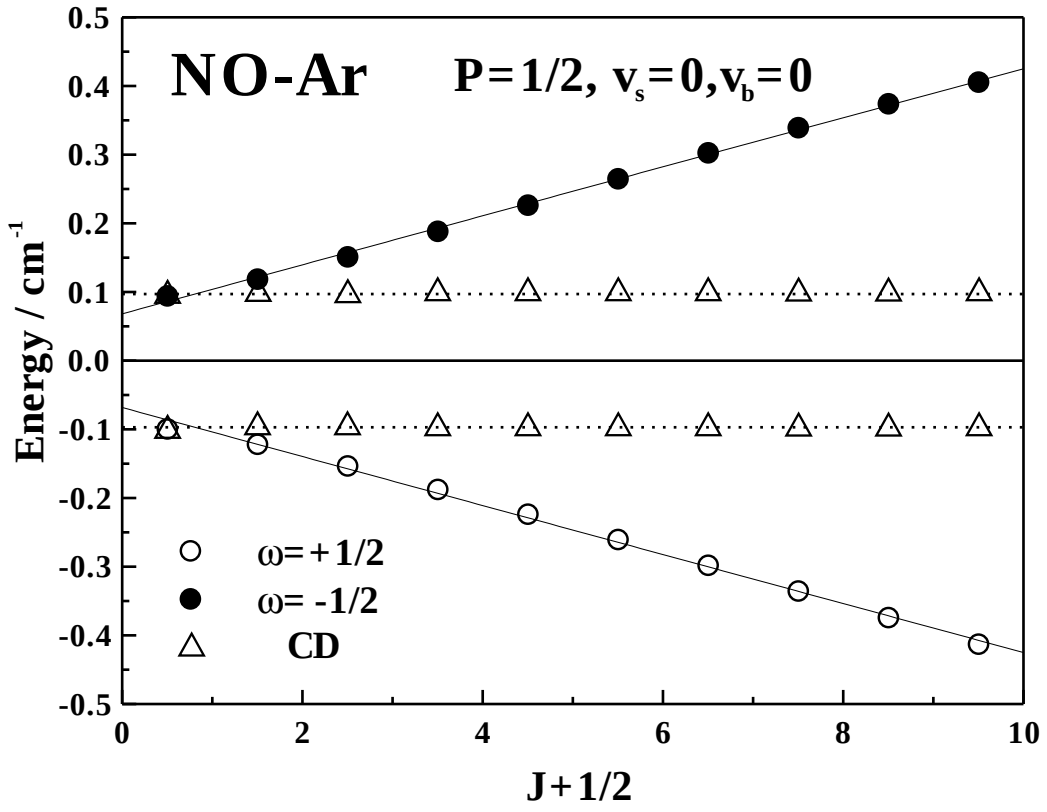

Figure 4.35: The ω-splitting of the rotational energy levels for the ground vibrational state of NO-Ar for $\omega = \pm\frac{1}{2}$. Circles represent the results for the different ω levels. The triangles are the results for the CD approximation.

formed transition moment is assumed. The origin of this band is found at a higher frequency than predicted in the *ab initio* calculation. From the position of the two Q-branches (Q_-^- and Q_+^+), it is clear that the ω-splitting predicted by the *ab initio* calculation is too large while the P-type doubling constants is too small.

Figure 4.41 shows the comparison of predicted and experimental spectra of band D. Band D corresponds to the excitation of two states; the first excited state of the $P = \frac{1}{2}, n$=1,2 AB potential which corresponds to the first van der Waals stretching mode and the second pair of the $P = \frac{3}{2}, n$=3,4 AB potential. It may well be that the FC factors for the UV detection step differ significantly for excitation out of these

Table 4.17: Spectroscopic constants (in cm^{-1}) of the heuristic Hamiltonian given in Eq. (3.280) for the electronic ground state levels of the NO-Ar complex based on Alexanders's calculation [132].

Band	P	$E_{v_b v_s P}$	B	V_0	V_1 $\times 10^{-2}$	V_2 $\times 10^{-2}$	C_0
A	$\frac{1}{2}$	0	0.0686	0.050	3.57	0.00	2.26
B	$\frac{3}{2}$	3.683	0.0689	0.221	0.00	0.00	0.00
C	$\frac{1}{2}$	14.310	0.0628	0.577	0.00	0.93	0.05

Table 4.18: Fitted Spectroscopic constants (in cm^{-1}) for the electronic ground state levels of the NO-Ar complex.

Band	P	$E_{v_b v_s P}$	B	V_0	V_1 $\times 10^{-2}$	V_2 $\times 10^{-2}$	C_0
A	$\frac{1}{2}$	0	0.068	0.045	3.6		2.0
B	$\frac{3}{2}$	3.580	0.068	0.19	0.0		0.0
C	$\frac{1}{2}$	15.302	0.063	0.43	2.6		1.2

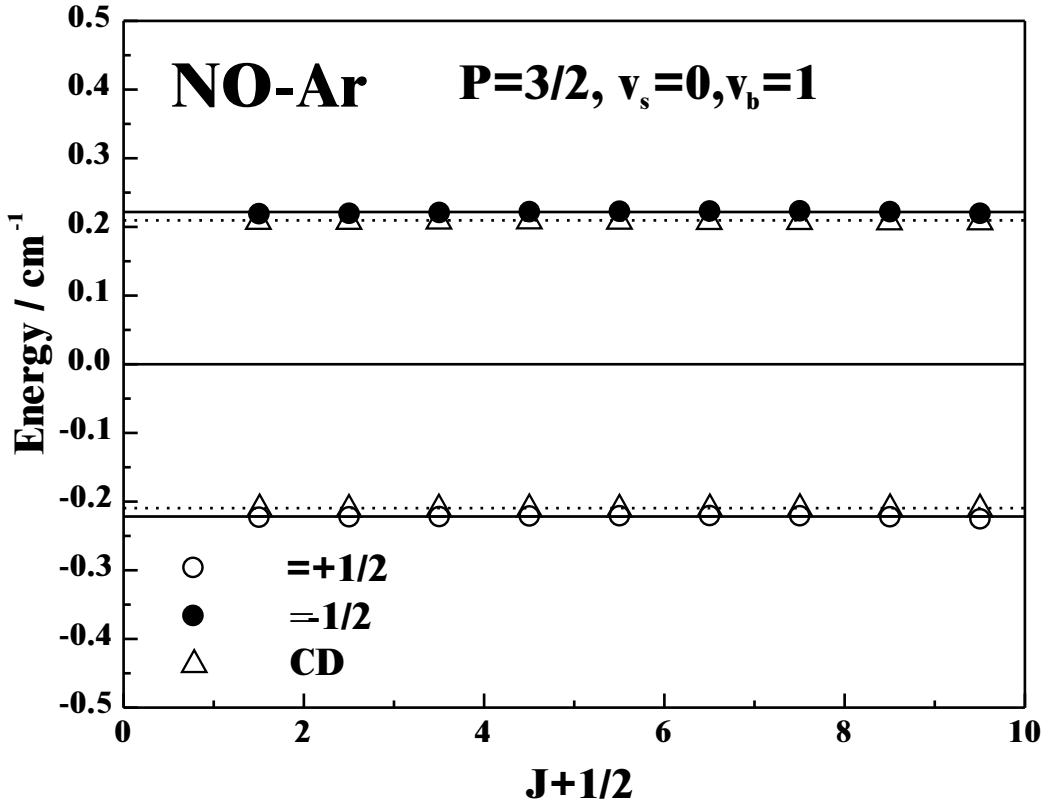

Figure 4.36: The ω-splitting of the rotational energy levels for the ground vibrational state of NO-Ar for $\omega = \pm\frac{3}{2}$. Circles represent the results for the different ω levels. The triangles are the results for the CD approximation.

two different van der Waals modes. This may be part of the reason for the poorer agreement with the simulated spectrum for band D as compared with bands A−C. The black boxes in Fig. 4.41 indicate regions of strong water absorption.

Because band B involves one quantum of bending vibrational excitation, it was not possible to reproduce satisfactorily the spectrum with the rigid-rotor treatment [12]. Similarly, the complicated structures of bands C and D reflect the more delocalized probability of the rovibronic states involved. In this case, quantum number could only be assigned reliably by analyzing the calculated wavefunctions. In this sense, the theoretical work combined with the experimental results allows for a syn-

ergy effect which provides a much better understanding of the molecular interaction and dynamics. The heuristic Hamiltonian which reproduces the spectra obtained by the *ab initio* calculation not only helps to assign the lines of different branches, but it also helps to gain additional physical insight about the different splittings and interactions. This approach will also be very helpful for those open shell complexes for which no set of PESs are available.

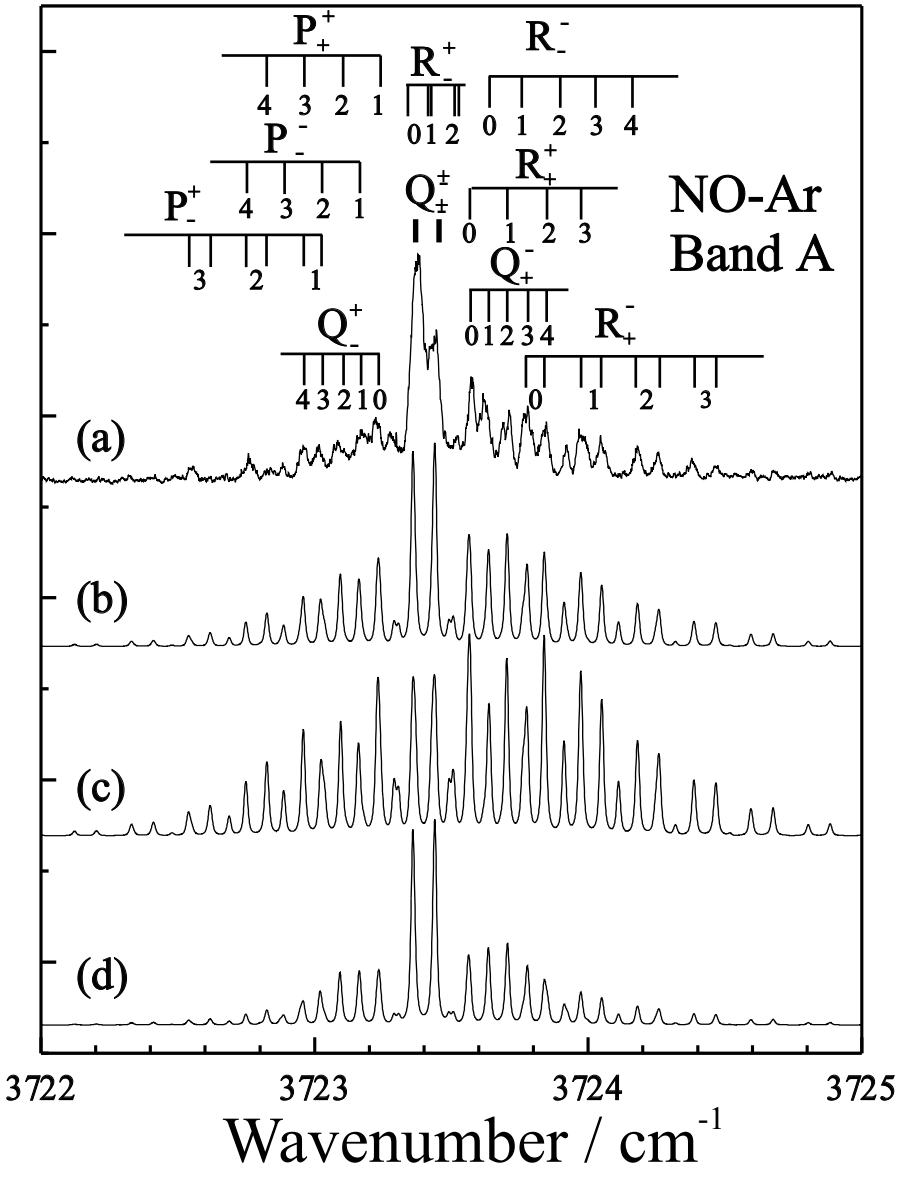

Figure 4.37: Comparison of band A with simulated spectra assuming different types of transition moments. Spectrum (a) is the observed one while spectra (b), (c), and (d) are calculated assuming a temperature of 1 K and for the linewidth a 0.01 cm^{-1} Lorentzian component and a 0.01 cm^{-1} Gaussian component. Rotational lines are labeled with $(J - \frac{1}{2})$.

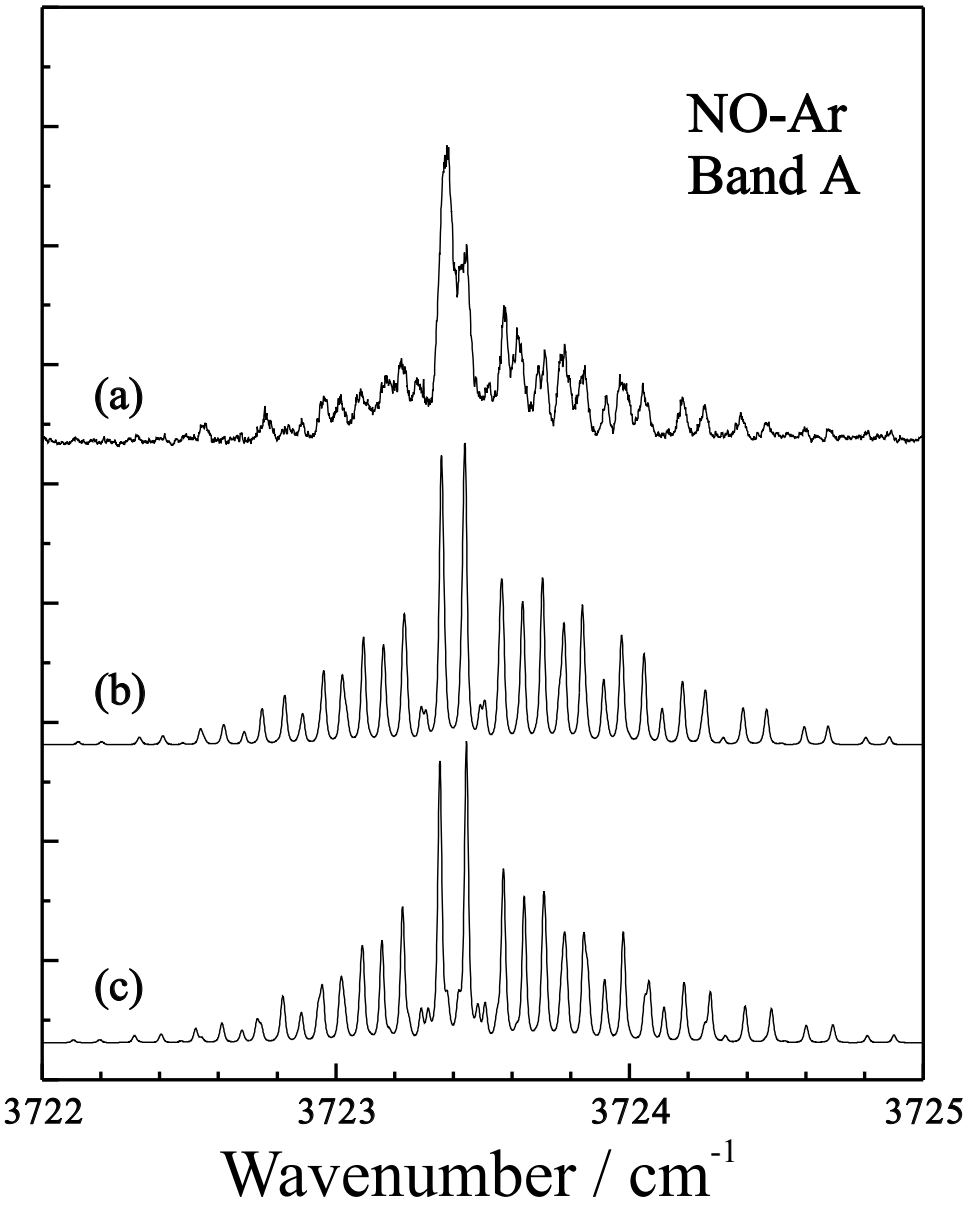

Figure 4.38: Comparison of band A with simulated spectra based on the results of (c) the *ab initio* treatment and (b) and the results of the fit of the experimental spectrum. Spectra (b) and (c) are calculated assuming a temperature of 1 K and for the linewidth a 0.01 cm^{-1} Lorentzian component and a 0.01 cm^{-1} Gaussian component.

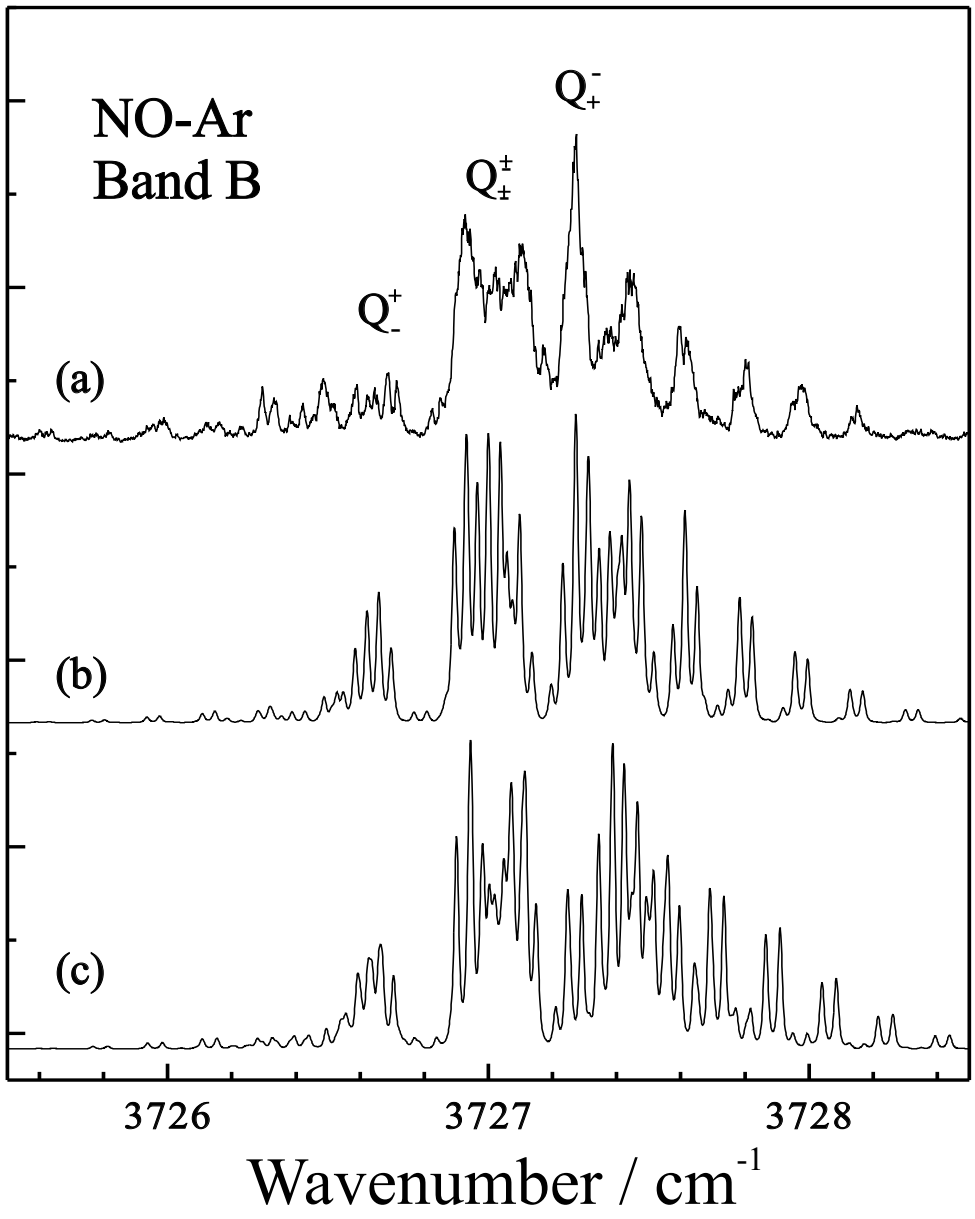

Figure 4.39: Comparison of band B with simulated spectra based on the results of (c) the *ab initio* treatment and (b) and the results of the fit of the experimental spectrum. Spectra (b) and (c) are calculated assuming a temperature of 1 K and for the linewidth a 0.01 cm^{-1} Lorentzian component and a 0.01 cm^{-1} Gaussian component.

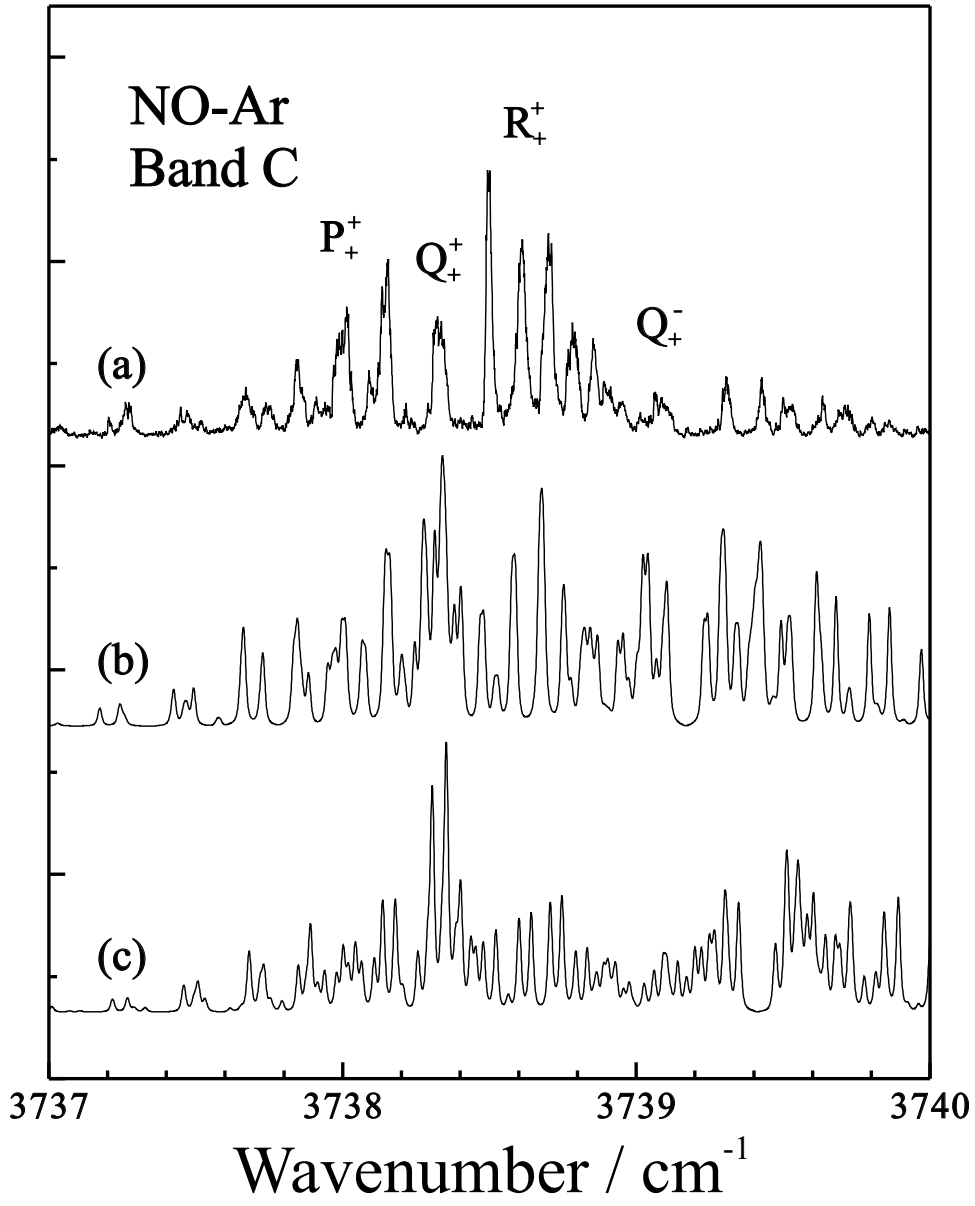

Figure 4.40: Comparison of band C with simulated spectra based on the results of (c) the *ab initio* treatment and (b) and the results of the fit of the experimental spectrum. Spectra (b) and (c) are calculated assuming a temperature of 1 K and for the linewidth a 0.01 cm^{-1} Lorentzian component and a 0.01 cm^{-1} Gaussian component.

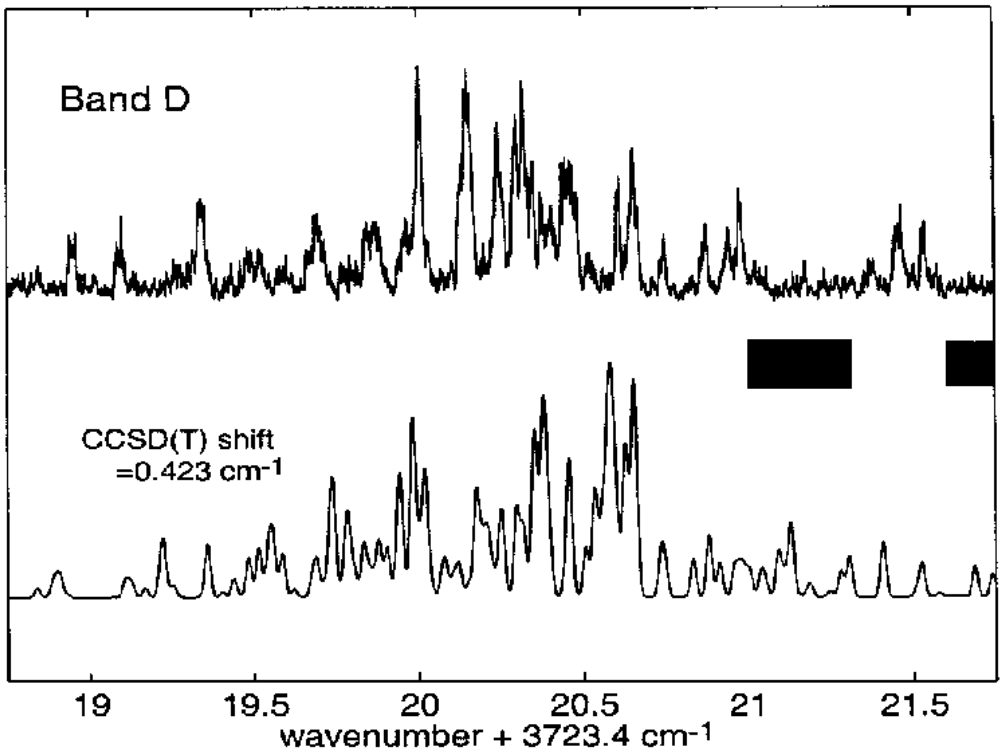

Figure 4.41: Comparison of predicted and experimental spectra of band D. The two black boxes indicate the spectral region where strong water absorption masks the presence of NO-Ar lines.

Chapter 5

Conclusion

In this thesis, the measurement of the first overtone spectra of the NO-Ne and NO-Ar complexes has been achieved using a new type of IR-REMPI double resonance technique. The use of a single longitudinal mode OPO made it possible to excite the first overtone transition associated with the N-O stretching vibration. In combination with REMPI detection, it was possible to measure different bending-stretching intermolecular vibrational levels with rotational resolution for the first time.

The small frequency shifts of the origin band (0.45 cm^{-1} to the red for NO-Ar and 0.17 cm^{-1} to the blue for NO-Ne) indicate that the NO stretching vibration does not change much upon complexation. For both complexes, four band systems were measured. For NO-Ar, Alexander's *ab initio* potential surface assigns bands A, B, C and D to the excitation of the levels $(P = \frac{1}{2}, (v_s, v_b) = (0,0))$, $(P = \frac{3}{2}, (0,1))$, $(P = \frac{1}{2}, (0,1))$ and $(P = \frac{1}{2}, (1,2)$ and $P = \frac{3}{2}, (0,2))$, respectively. And for NO-Ne, the assignments are $(P = \frac{1}{2}, (0,0))$, $(P = \frac{3}{2}, (0,1))$, $(P = \frac{1}{2}, (0,2))$, and $(P = \frac{1}{2}, (1,0))$, respectively. Since the observed spectra are sensitive to details of the potential surfaces, they provide an important test for current *ab initio* treatments of these systems. Potential energy surfaces for NO-Ar and NO-Ne calculated at the CCSD(T) level predict the bound level energies within a fraction of a wavenumber, thus achieving spectroscopic accuracy.

Although the *ab initio* studies enabled a complete comparison and assignment of the experimental spectra, the development of an empirical Hamiltonian based on

perturbation theory allows one to gain additional physical insight. In this model, the complex is described as a near symmetric top molecule whose energy levels are split due to electrostatic splitting (ω-splitting) and Coriolis coupling (P-type doubling). The latter involves contributions from the difference potential while the former is closely related to the odd expansion terms of the average potential. This Hamiltonian is used to improve the spectroscopic constants predicted by *ab initio* treatment. The results are not only consistent with a near T-shaped structure of the complex, but they also give clear indication of the large amplitude motion present in the complex.

So far the main information on the ground state interaction of the NO-X complexes relied on collision experiments which could not resolve uncertainties in connection with the existing *ab initio* PESs. The experimental results of this thesis provide a very stringent test for these PESs. The excellent agreement between results obtained in IR-REMPI double resonance experiment and the *ab initio* results encourages further exploration of the weak interactions involving van der Waals complexes using the IR-REMPI double resonance technique.

Bibliography

[1] Chem. Rev. **88** (1988); *ibid.*, **94** (1994); *ibid.*, **100** (2000).

[2] Faraday Discuss. Chem. Soc. **73** (1982); *ibid.*, **97** (1994);

[3] D. J. Nesbitt, Chem. Res. **88**, 843 (1988).

[4] Y. P. Zeng, S. W. Sharpe, D. Reifschneider, C. Wittig, and R. A. Beaudet, J. Chem. Phys. **93**, 183 (1990).

[5] R. E. Miller, in *Laser Techniques in Chemistry*, edited by A. B. Myers and T. R. Rizzo (Wiley, New York, 1995), Vol. 23, p. 43.

[6] D. J. Nesbitt, Annu. Rev. Phys. Chem. **45**, 367 (1994).

[7] Y. Matsumoto, T. Ebata, and N. Mikami, J. Chem. Phys. **109**, 6303 (1998).

[8] R. N. Pribble and T. S. Zwier, Faraday Discuss. **97**, 229 (1994).

[9] S. Djafari, H.-D. Barth, K. Buchold, and B. Brutchy, J. Chem. Phys. **107**, 10573 (1997).

[10] K. Liu, M. Dulligan, I. Bezel, A. Kollessov, and C. Wittig, J .Chem. Phys. **108**, 9614 (1998).

[11] R. T. Bonn, M. D. Wheeler, and M. I. Lester, J. Chem. Phys. **112**, 4942 (2000).

[12] Y. Kim, K. Patton, J. Fleniken, and H. Meyer, Chem. Phys. Lett. **318**, 522 (2000).

[13] Y. Kim, J. Fleniken, H. Meyer, P. J. Dagdigian, and M. H. Alexander, J. Phys. Chem. **113**, 73 (2000).

[14] Y. Kim, J. Fleniken, and H. Meyer, J. Phys. Chem. **114**, 5578(2001).

[15] M. H. Alexander, P. Soldan, T. G. Wright, Y. Kim, H. Meyer, P. J. Dagdigian, and E. P. F. Lee, J. Phys. Chem. **114**, 5588 (2001).

[16] E. Miescher and K. P. Huber, Int. Rev. Sci., Phys. Chem. Ser. 2, Vol. 3, edited by A. D. Buckingham and D. A. Ramsey, p. 37 (Butterworths, London, 1973).

[17] Z. Bacic and R. E. Miller, J. Phys. Chem. **100**, 12945 (1996).

[18] R. J. Saykally, Acc. Chem. Res. **22**, 295 (1989).

[19] P. D. A. Mills, C. M. Western and B. J. Howard, J. Phys. Chem. **90**, 3331 (1986).

[20] W. M. Fawzy and J. T. Hougen, J. Mol. Spectrosc. **137**, 154 (1989).

[21] M. L. Dubernet, D. Flower, and J. M. Hutson, J. Chem. Phys. **94**, 7602 (1991).

[22] M. T. Berry, M. R. Brustein, J. R. Adamo, and M. I. Lester, J. Phys. Chem. **92**, 5551 (1988).

[23] W. H. Green and M. I. Lester, J. Chem. Phys. **96**, 2573 (1992).

[24] B. C. Chang, L. Yu, D. Cullin, B. Rehfuss, J. Williamson, T. A. Miller, W. M. Fawzy, X. Zheng, S. Fei, and M. C. Heaven, J. Chem. Phys. **95**, 7086 (1991).

[25] J. M. Bowman, B. Gazdy, P. Shafer, and M. C. Heaven, J. Phys. Chem. **94**, 2226 (1990).

[26] C. Chakravarty, D. C. Clary, A. D. Esposti, and H. J. Werner, J. Chem. Phys. **93**, 3367 (1990).

[27] Y. Lin, S. K. Kulkarni, and M. C. Heaven, J. Phys. Chem. **94**, 1720 (1990).

[28] B. C. Chang, J. R. Dunlop, and T. A. Miller, Chem. Phys. Lett. **207**, 35 (1993).

[29] Y. Ohshima, M. Iida, and Y. Endo, J. Chem. Phys. **95**, 7001 (1991).

[30] Y. Endo, H. Kohguchi, Y. Ohshima, Faraday Discuss. **97**, 341 (1994).

[31] C. Chakravarty and D. C. Clary, J. Chem. Phys. **97**, 4149 (1991).

[32] A. Degli-Eposti and H. J. Werner, J. Chem. Phys. **93**, 3351 (1990).

[33] M. D. Wheeler, M. W. Todd, D. T. Anderson, and M. I. Lester, J. Chem. Phys. **110**, 6732 (1999).

[34] R. A. Loomis and M. I. Lester, J. Chem. Phys. **103**, 4371 (1995).

[35] G. C. Nielson, G. A. Parker, and R. T. Pack, **64**, 2055 (1976).

[36] G. C. Nielson, G. A. Parker, and R. T. Pack, **66**, 1396 (1977).

[37] S. Green and R. N. Zare, Chem. Phys. **7**, 62 (1977).

[38] M. H. Alexander, J. Chem. Phys. **76**, 5974 (1982).

[39] M. H. Alexander, Chem. Phys. **92**, 337 (1985).

[40] T. Orlikowski and M. H. Alexander, J. Chem. Phys. **79**, 6006 (1983).

[41] G. C. Corey and M. H. Alexander, J. Chem. Phys. **85**, 5652 (1986).

[42] M. H. Alexander, J. Chem. Phys. **99**, 7725 (1993).

[43] M. Yang and M. H. Alexander, J. Chem. Phys. **103**, 6973 (1995).

[44] M. Islam, I. W. M. Smith, and M. H. Alexander, Chem. Phys. Lett. **305**, 311 (1999).

[45] M. H. Alexander, J. Chem. Phys. **111**, 7426 (1999).

[46] M. H. Alexander, J. Chem. Phys. **111**, 7435 (1999).

[47] E. P. F. Lee and T. G. Wright, J. Chem. Phys. **109**, 157 (1998).

[48] J. Klos, G. Chalasinski, M. T. Berry, R. Bukowski, and S. M. Cybulski, J. Chem. Phys. **112**, 2195 (2000).

[49] H. Meyer, J. Chem. Phys. **102**, 3151 (1995).

[50] H. H. W. Thuis, S. Stolte, and J. Reuss, Chem. Phys. **43**, 351 (1979).

[51] H. H. W. Thuis, S. Stolte, J. Reuss, J. J. H. van der Biesen, and C. C. H. van der Meijdenberg, Chem. Phys. **52**, 211 (1980).

[52] A. S. Sudbø and M. M. T. Loy, Chem. Phys. Lett. **82**, 135 (1981); J. Chem. Phys. **76**, 3646 (1982).

[53] P. Andresen, H. Joswig, H. Pauly, and R. Schinke, J. Chem. Phys. **77**, 2204 (1982).

[54] H. Joswig, P. Andresen, and R. Shinke, J. Chem. Phys. **85**, 1904.(1986).

[55] S. D. Jons, J. E. Shirley, M. T. Vonk, C. F. Giese and R. W. Gentry, J. Chem. Phys. **97**, 7831 (1992).

[56] S. D. Jons, J. E. Shirley, M. T. Vonk, C. F. Giese and R. W. Gentry, J. Chem. Phys. **105**, 5397 (1996).

[57] S. E. Novick, P. B. Davies, T. R. Dyke, and W. Klemperer, J. Am. Chem. Soc. **95**, 8547 (1976).

[58] E. M. Carrasquillo, P. R. R. Langride-Smith, and D. H. Levy, in *Laser Spectroscopy V: Proceedings of the Fifth International Conference, Jasper Park*, Alberta, Canada, June 29-July 3, 1981, edited by A. R. W. McKellar, T. Oka, and B. P. Stoicheff (Springer, Berlin, 1981).

[59] P. R. R. Langride-Smith, E. M. Carrasquillo, and D. H. Levy, J. Chem. Phys. **74**, 6514 (1981).

[60] J. C. Miller, J. Chem. Phys. **90**, 4031 (1989).

[61] K. Tsuji, K. Shibuya, and K. Obi, J Chem. Phys. **100**, 5541 (1994).

[62] M. J. McQuaid, G. W. Lemire, and R. C. Sausa, Chem. Phys. Lett. **227**, 54 (1994).

[63] N. Shafizadeh, Ph. Brechignac, M. Dyndgaard, J. H. Fillion, D. Gauyacq, B. Levy, J. C. Miller, T. Pino, and M. Raoult, J. Chem. Phys. **108**, 9313 (1998).

[64] P. Mack, J. M. Dyke, and T. G. Wright, J. Chem. Soc. Faraday Trans. **94**, 629 (1998).

[65] K. Sato, Y. Achiba, and K. Kimura, J. Chem. Phys. **81**, 57 (1984).

[66] J. C. Miller and W. C. Cheng, J. Phys. Chem. **89**, 1647 (1985).

[67] J. C. Miller, J. Chem. Phys. **86**, 3166 (1987).

[68] K. Tsuji, K. Aiuchi, K. Shibuya, and K. Obi, Chem. Phys. **231**, 279 (1998).

[69] H. Meyer, J. Phys. Chem. **107**, 7732 (1997).

[70] J. Fleniken, Y. Kim, and H. Meyer, J. Phys. Chem. **109**, 8940 (1998).

[71] K. Tsuji, K. Shibuya, and K. Obi, Laser. Chem. **15**, 157 (1995).

[72] Y. Kim and H. Meyer, Int. Reviews in Phys. Chem. **20**, 219 (2001).

[73] P. D. A. Mills, C. M. Western and B. J. Howard, J. Phys. Chem. **90**, 4961 (1986).

[74] M. T. Berry, R. A. Loomis, L. C. Giancarlo, and M. I. Lester, J. Chem. Phys. **96**, 7890 (1992).

[75] D. T. Anderson, R. L. Schwartz, M. W. Todd, and M. I. Lester, J. Chem. Phys. **109**, 3461 (1998).

[76] H. Meyer, J. Chem. Phys. **101**, 6686 (1994).

[77] H. Meyer, J. Chem. Phys. **101**, 6697 (1994).

[78] LAS Pulsed Dye Laser user's manual for LDL 205.

[79] CONTINUUM POWERLITE 3000 user's manual.

[80] Single-Frequency Injection-Seeding Laser user's manual.

[81] S. E. Harris, *Tunable Optical Parametric Oscillators*, **Proc. IEEE 57**, 2096 (1969).

[82] R. L. Byer, Parametric Oscillators, *Laser Spectroscopy*, edited by R. G. Brewer and A. Mooradian, 77 (Plenum, New York, 1973).

[83] R. L. Byer, Optical Paramteric Oscillators in *Quantum Electronics: A Trestise*, edited by H. Rabin, C. L. Tang, Academic, New York, Vol. I, Part B, 587 (1975).

[84] R. L. Byer and R. L. Herbst, Parametric Oscillation and Mixing, in *Nonelinear Infrared Generation*, edited by Y. R. Shen, 81 (Springer-Verlag, Berlin, 1997).

[85] S. J. Brosnan and R. L. Byer, Optical Parametric Oscillator Threshold and Linewidth Studies, *IEEE. J. Quant. Electron.* **QE-15:** 415 (1979).

[86] B. J. Orr, M. J. Johnson, and J. G. Haub, Spectroscopic Applications of Tunable Optical Parametric Oscillators, *Tunable Laser Applications*, edited by F. J. Duarte, 11 (Marcel Dekker, Inc., New York, 1995).

[87] N. P. Barnes, Optical Parameteric Oscillators, *Tunable Laser Handbook*, edited by F. J. Duarte, 293 (Academic Press, Inc., San Diego, 1995).

[88] J. Zhang, J. Y. Huang, and Y. R. Shen, *Optical Parametric Generation and Amplification*, (Harwood Academic Publishers, 1995).

[89] J. F. Nye, *Physical Properies of Crystals*, (Oxford Univ. Press, London and New York, 1960).

[90] R. A. Baumgartner and R. L. Byer, Optical Parametric Amplification, *IEEE. J. Quant. Electron.* **QE-15:** 432 (1979).

[91] V. G. Dmitriev, G. G. Gurzadyn, and D. N. Nikogosyan, *Handbook of Nonlinear Optical Crystals*, (Springer-Verlag, Berlin, 1991).

[92] W. Demtröder, *Laser Spectroscopy*, 2nd Ed., (Springer-Verlag, Berlin, Heidelberg, New York, 1998).

[93] A. Yariv, in *Quantum Electronics*, 3rd Ed., (John Wiley & Sons, 1989).

[94] A. Yariv and W. H. Louisell, Theory of Optical Parametric Oscillators, *IEEE. J. Quant. Electron.* **QE-2:** 418 (1979).

[95] W. R. Bosenberg and D. R. Guyer, Appl. Phys. Lett. **61**, 387 (1992).

[96] W. R. Bosenberg and D. R. Guyer, J. Opt. Soc. Am. B, **10**, 1716 (1993).

[97] D. R. Guyer, private communication.

[98] Y. Kim, J. Fleniken, and H. Meyer, J. Chem. Phys. **109**, 3401 (1998).

[99] C. Amiot, R. Bacis, and G. Guelachvili, Can. J. Phys. **56**, 251 (1978).

[100] J. Fleniken, Y. Kim, and H. Meyer, Chem. Phys. Lett. **318**, 529 (2000).

[101] E. Hecht, *Optics*, 3rd Ed., (Addison-Wesley, 1998).

[102] J. W. C. Johns, J. Reid, and D. W. Lepard, J. Mol. Spectrosc. **65**, 155 (1977).

[103] K. P. Huber and E. Miescher, Helv. Phys. Acta. **36**, 257 (1963).

[104] Ch. Jungen, J. Cmem. Phys., **53**, 4168 (1970).

[105] K. P. Huber and G. Herzberg, *Molecular Spectra and Molecular Structure IV, Constants of Diatomic Molecules* (Van Nostrand Reinhold, New York, 1979).

[106] A. Lagerquist and E. Miescher Hel. Phys. Acta, **31**, 221 (1958).

[107] Lectures note on *Molecular Physics* by H. Meyer (1999).

[108] B. Podolsky, Phys. Rev. **32**, 812 (1928).

[109] P. R. Bunker and P. Jensen, *Molecular Symmetry and Spectroscopy*, 2nd Ed., (NRC Research Press, Ottawa, 1998).

[110] J. T. Hougen, J. Chem. Phys. **36**, 519 (1962).

[111] P. R. Bunker and D. Papoušek, J. Mol. Spectrosc. **102**, 419 (1969).

[112] J. K. G. Watson, Mol. phys. **19**, 465 (1970).

[113] B. J. Howard and R. E. Moss, Mol. Phys. **20**,147 (1971).

[114] D. M. Brink and G. R. Satchler, *Angular Momemtum*, (Oxford Univ. Press, London and New York, 1979).

[115] E. L. Hill and J. H. Van Vleck, Phys. Rev. **32**, 250 (1928).

[116] H. Lefebvre-Brion and R. W. Field, *Perturbations in the Spectra of Diatomic Molecules*, (Academic, New York, 1986).

[117] P. F. Bernath, *Spectra of Atoms and Molecules*, (Oxford Univ. Press, New York Oxford, 1995).

[118] J. H. Van Vleck, Phys. Rev. **33**, 467 (1929).

[119] J. T. Hougen, Monogr. 115(1070), Nat. Bur. Stand. (US) Washington D.C.

[120] W. S. Struve, *Fundamentals of Molecular Spectroscopy*, (John Wiley & Sons, New York, 1989).

[121] R. N. Zare, *Angular Momentum*, (John Wiley & Sons, New York, 1988).

[122] H. Meyer, J. Phys. Chem. **107**, 7722 (1997).

[123] J. M. Hutson, in *Advances in Molecular Vibration and Collision Dynamics*, edited by J. M. Bowman and M. A. Ratner, Vol. **IA**, p. 1 (JAI, Greenwich, CT,1991).

[124] M. H. Alexander, Chem. Phys. **92**, 337 (1985).

[125] C. G. Gray, Can. J. Phys. **54**, 505 (1976).

[126] P. Mack, J. M. Dyke, D. M. Smith, T. G. Wright, and H. Meyer, J. Chem. Phys. **109**, 4361 (1998).

[127] E.P.F. Lee, P. Soldan, and T.G. Wright, J. Phys. Chem. **102**, 6858 (1999).

[128] J. Lozeille, S. D. Gamblin, S. E Daire, T. G Wright, and D. M. Smith, J. Chem. Phys. **113**, 7224 (2000).

[129] J. D. Barr, J. M. Dyke, D. M. Smith, and T. G. Wright, J. Electron Spectros. **97**, 159 (1998).

[130] I. Fourré, and M Raout, Chem. Phys. **199**, 215 (1995).

[131] M. Takahashi, J. Chem. Phys. **96**, 2594 (1992).

[132] M. H. Alexander, private communication.